1978

Adsorption Of Metal Ions By Calcite And Iron Sulphides: A Quantitative X-ray Photoelectron Spectroscopy Study

James Robert Brown

Recommended Citation

Brown, James Robert, "Adsorption Of Metal Ions By Calcite And Iron Sulphides: A Quantitative X-ray Photoelectron Spectroscopy Study" (1978). *Digitized Theses*. 1086.
https://ir.lib.uwo.ca/digitizedtheses/1086

National Library of Canada

Cataloguing Branch
Canadian Theses Division

Ottawa, Canada
K1A 0N4

Bibliothèque nationale du Canada

Direction du catalogage
Division des thèses canadiennes

NOTICE

The quality of this microfiche is heavily dependent upon the quality of the original thesis submitted for microfilming. Every effort has been made to ensure the highest quality of reproduction possible.

If pages are missing, contact the university which granted the degree.

Some pages may have indistinct print especially if the original pages were typed with a poor typewriter ribbon or if the university sent us a poor photocopy.

Previously copyrighted materials (journal articles, published tests, etc.) are not filmed.

Reproduction in full or in part of this film is governed by the Canadian Copyright Act, R.S.C. 1970, c. C-30. Please read the authorization forms which accompany this thesis.

THIS DISSERTATION
HAS BEEN MICROFILMED
EXACTLY AS RECEIVED

AVIS

La qualité de cette microfiche dépend grandement de la qualité de la thèse soumise au microfilmage. Nous avons tout fait pour assurer une qualité supérieure de reproduction.

S'il manque des pages, veuillez communiquer avec l'université qui a conféré le grade.

La qualité d'impression de certaines pages peut laisser à désirer, surtout si les pages originales ont été dactylographiées à l'aide d'un ruban usé ou si l'université nous a fait parvenir une photocopie de mauvaise qualité.

Les documents qui font déjà l'objet d'un droit d'auteur (articles de revue, examens publiés, etc.) ne sont pas microfilmés.

La reproduction, même partielle, de ce microfilm est soumise à la Loi canadienne sur le droit d'auteur, SRC 1970, c. C-30. Veuillez prendre connaissance des formules d'autorisation qui accompagnent cette thèse.

LA THÈSE A ÉTÉ
MICROFILMÉE TELLE QUE
NOUS L'AVONS REÇUE

NL-339 (3/77)

ADSORPTION OF METAL IONS BY CALCITE AND IRON SULPHIDES: A QUANTITATIVE X-RAY PHOTOELECTRON SPECTROSCOPY STUDY

by

James Robert Brown

Department of Geology

Submitted in partial fulfillment
of the requirements for the degree of
Doctor of Philosophy

Faculty of Graduate Studies
The University of Western Ontario
London, Ontario
March, 1978

To Barbara with endearing love.

ABSTRACT

Extensive sorption on mineral surfaces has been examined using the relatively new technique of x-ray photoelectron spectroscopy (ESCA), combined with atomic absorption methods as analytical probes. The ESCA technique has extremely useful properties for fundamental studies of ion sorption on solid surfaces, i.e. qualitative and quantitative trace metal surface analysis. Two mineral systems were examined: 1) Ba^{2+} adsorption on single calcite crystals and 2) Hg^{2+}, Hg° adsorption on cut and/or polished highly pure slabs of pyrrhotite (FeS) and pyrite (FeS_2) ore. Initially, reasonable measures of the sorption capacity (X_m) of these two mineral sorbents were determined. This was accomplished by monitoring the uptake of metal ions exposed to powdered samples of large surface area using atomic absorption methods. Estimates of the surface area of iron sulphide and calcite powder were calculated from these adsorption results. The powdered study results fit well to the Langmuir equation.

Using x-ray photoelectron spectroscopy as the surface sensitive technique, linear reproducible calibration plots for monolayer and sub-monolayer amounts ($\leq 6 \times 10^{-7}$ gm/cm^2) of barium and lead ions on cleaved calcite surfaces were obtained. The slopes of these linear plots are equated to theoretical estimates. The effects of surface contamination and analyser variation (transmission function) with kinetic energies were also examined using these plots. Linear, reproducible calibration plots of mercury and chlorine ions on iron sulphide plates were also produced and verified the usefulness of the technique for monolayer and sub-monolayer detection of sorbed species. An estimate of

the mercury and chlorine atom escape depths ($\lambda_{Hg} \sim 7$ Å, $\lambda_{Cl} \sim 25$ Å) was calculated from the calibration plots determined. Qualitative calibration plots for lanthanum, barium and nickel ions on precipitated amorphorus pyrolusite (MnO_2) plates were also determined. The results of the calibration studies indicated other metals will give calibration results similar to these plots. The results strongly indicate that ESCA will be a very useful analytical probe for direct surface analysis of trace elements down to $\simeq 10^{-9}$ gm/cm^2. These calibration plots were then used for semi-quantitative and quantitative analysis of trace metals adsorbed from aqueous solution by the aforementioned mineral surfaces. In all cases, monolayer coverage ($\sim 10^{15}$ ions/cm^2) was observed after reaction times ranging from minutes for mercury uptake by iron sulphide to days for barium adsorption on calcite. These adsorption reactions were also found to be very specific, as counter-ions such as Cl^- or ClO_4^- were not adsorbed.

Variation in pH and chloride concentration was found to affect the rate of mercury adsorption on iron sulphides. Iron sulphide (FeS) ore has the ability to very specifically cleanse solutions containing trace mercuric ion species and mercury atoms. In situ pilot studies should now be examined to best apply this finding.

The mechanism (hydroxylation, ageing etc.) of adsorption onto mineral surfaces is discussed in detail. This study has lead to a better, albeit small, understanding of the adsorption mechanism and a greater understanding of aqueous reactions involving metal ions in contact with mineral surfaces. The importance of the adsorption process to waste water treatment, mining flotation processing, nuclear waste disposal and in improving our knowledge of ore body deposition and trace element incorporation into various mineral phases is shown. Adsorption, desorption, leaching and diffusion of metal species on the surfaces of minerals must be more fully studied if one is to prevent or temporarily postpone ecological suicide.

ACKNOWLEDGEMENTS

I would like to thank the many people who have shown interest, offered suggestions and added to my education during this study. Foremost, I thank Dr. W.S. Fyfe for allowing me the opportunity to study under his direction in the Department of Geology and Dr. G.M. Bancroft for his invaluable advice, encouragement and liberal use of his ESCA facilities in the Chemistry Department.

Barbara, my wife, was instrumental in the completion of this thesis and I thank her for her understanding, patience, love and frequent psycho-analysis sessions.

My thanks are due to the technical staff of the departments of Geology and Chemistry, especially Mr. R. Lazier who helped immeasurably with the technical problems of ESCA analysis, and Mr. J. Forth who cut and polished many of the mineral samples.

I wish to thank my friends and contemporaries in Graduate School particularly Barbara Kronberg, David Creber, John Tse and T.K. Sham for helpful comments and encouragement given throughout this project.

I'm grateful to Ms. M. Pierce who worked as my Research Assistant during the summer of 1975, crushing and sieving the limestone samples used in this study.

Grateful acknowledgement is made for financial assistance received from the Geology Department, Chemistry Department and the National Research Council of Canada for Post-Graduate Scholarship awards issued throughout this work.

Finally, I wish to thank Carol Aarssen for a fast and accurate job of typing this manuscript.

TABLE OF CONTENTS

Page

TITLE PAGE i

CERTIFICATE OF EXAMINATION ii

DEDICATION iii

ABSTRACT iv

ACKNOWLEDGEMENTS vii

TABLE OF CONTENTS viii

LIST OF TABLES xi

LIST OF FIGURES xiii

NOMENCLATURE xvii

CHAPTER 1 - GENERAL INTRODUCTION 1

1.1 Introduction 1

1.2 References 5

CHAPTER 2 - INSTRUMENTATION AND ADSORPTION THEORY 9

2.1 Analytical Methods 9

2.1.1 Atomic Absorption Spectrophotometry (AAS) . . 9

2.1.2 X-Ray Photoelectron Spectroscopy (XPS) . . . 9

2.2 Adsorption Theory - "The Solid-Solution Interface" . 14

2.2.1 Introduction 14

2.2.2 Interpretation of Sorption Reactions - "The Langmuir Isotherm" 16

2.2.3 Other Sorption Models 19

2.3 References 29

CHAPTER 3 - ESCA CALIBRATION STUDIES 33

3.1 Introduction 33

3.2 Experimental 34

Page

3.3 Results and Discussion 36

3.3.1 Barium Analysis on Calcite ($CaCO_3$) 36

3.3.2 Mercury Analysis on Iron Sulphide (FeS) 54

3.3.3 Barium, Lanthanum and Nickel Analysis on Manganese Dioxide (MnO_2) 64

3.4 References 71

CHAPTER 4 - BARIUM SORPTION ON CALCITE 73

4.1 Introduction 73

4.2 Powdered Calcite - A.A.S. Study 75

4.2.1 Experimental 75

4.2.1.1 Powdered Calcite 75

4.2.1.2 Crushed Limestone 78

4.2.2 Discussion 80

4.2.2.1 Powdered Calcite 80

4.2.2.2 Crushed Limestone 89

4.3 Single Crystal Calcite - XPS Study 94

4.3.1 Experimental 94

4.3.2 Discussion 96

4.4 Conclusion 104

4.5 References 108

CHAPTER 5 - MERCURY SORPTION ON IRON SULPHIDES 111

5.1 Introduction 111

5.2 Powdered Iron Sulphide - A.A.S. Study 112

5.2.1 Experimental 112

5.2.2 Discussion 115

Page

5.3 Polished Iron Sulphide Plates - XPS Study 129
  5.3.1 Experimental 129
  5.3.2 Discussion 132
5.4 Conclusion 152
5.5 References 156
CHAPTER 6 - CONCLUDING REMARKS 158
APPENDIX A.1 - WASHING (DIPPING) PROCEDURE USED FOR ESCA STUDIES 160
APPENDIX A.2 - CALCITE SURFACE REACTIONS STUDIED BY ESCA 164
APPENDIX A.3 - ADSORPTION OF METAL IONS ON MnO_2 175
APPENDIX A.4 - CALCITE DATA 180
  A.4.1 Calcite-H_2O-CO_2 Equilibria 181
  A.4.2 Calcite-$Ba(ClO_4)_2$-H_2O-CO_2 Equilibria . . . 184
  A.4.3 Calcite Crystal Chemistry 185
  A.4.4 Calcite Surface Area Calculations 188
APPENDIX A.5 - IRON SULPHIDE DATA 190
  A.5.1 FeS-H_2O Equilibria 191
  A.5.2 FeS-$HgCl_2$-H_2O Equilibria 193
  A.5.3 Iron Sulphide Crystal Chemistry 194
    A.5.3.1 $Fe_{1-X}S$ 194
    A.5.3.2 FeS_2 197
  A.5.4 Crushed FeS Surface Area Calculation . . . 197
APPENDIX A.6 - PUBLICATIONS 199
  A.6.1 Quantitative X-Ray Photoelectron Spectroscopy (ESCA): Studies of Ba^{2+} Sorption on Calcite 200
  A.6.2 Calibration Studies for Quantitative X-Ray Photoelectron Spectroscopy of Ions 215
VITA 220

LIST OF TABLES

Table	Description	Page
1	Barium Perchlorate XPS Calibration Data.	42
2	Barium Chloride XPS Calibration Data.	44
3	Lead Nitrate XPS Calibration Data.	47
4	$HgCl_2$ XPS Calibration Data.	55
5	Fresh $HgCl_2$ XPS Calibration Data.	59
6	Powdered Calcite-Ba^{2+} Adsorption Results.	81
7	Thermodynamic Data Calculated from Table 6.	90
8	St. Mary's Limestone Sorption Results.	92
9	Ba^{2+} Adsorption Data on Calcite Single Crystals.	97
10	Reproducibility with Time and Thermal Effects on XPS Peak Area Intensity Ratios.	103
11	Powdered FeS-Hg^{2+} Sorption Results.	116
12	FeS Surface Area Calculations from Results of Table 11.	125
13	Solution Changes During Hg^{2+} Adsorption.	127
14	Preliminary XPS Study of Adsorption of Hg^{2+} on FeS.	133
15	Effect of pH on Hg^{2+} Adsorption on FeS Plates.	140
16	XPS Study of Mercury Adsorption on Iron Sulphides - Variation with Chloride Concentration.	143
17	XPS Study of Elemental Mercury Adsorption on Iron Sulphides.	148
18	XPS Study, Hg^{2+} Sorption by Iron Sulphides from Chlor Alkali Processing Waters.	151

Table	Description	Page
A.1	Removing Excess Ba^{2+} Solution from Reacted Calcite Surfaces.	162
A.2	Pure Iceland Spar Calcite Crystals - H_2O Induced Surface Reactions (dissolution).	169
A.3	Pure Iceland Spar Calcite Single Crystals - Ar Ion, Thermal, X-ray, Acid and Steam Effects.	172
A.4	Ar Ion Etching Effects on 14, 20 day H_2O Reacted Calcite Crystals.	173
A.5	Effects of Reaction Time (Surface Changes) on the Intensity Ratio $(\frac{Ba}{Ca})$ "Iceland Spar Calcite Crystals in Pure H_2O-Ba^{2+} Solutions."	174
A.6	Calcite-H_2O-CO_2 Equilibria.	183
A.7	Calcite-$Ba(ClO_4)_2$-H_2O-CO_2 Equilibria.	186
A.8	FeS-H_2O Equilibria.	195

LIST OF FIGURES

Figure	Description	Page
1	A.A.S. Mercury Analysis Apparatus (schematic).	10
2	McPherson 36 (ESCA) Instrumentation (schematic).	12
3	Typical Langmuir Adsorption Isotherm Plot.	18
4	Stern Electric Double Layer (schematic).	22
5	ESCA Spectra of the Ba 3d Levels for the Above Amounts of Ba^{2+} Syringed onto Cleaved Calcite Crystals.	37
6	ESCA Spectra of the Pb 4f Levels for the Above Amounts of Pb^{2+} Syringed onto Cleaved Calcite Crystals.	38
7	Representative Ca 2p and C 1s ESCA Spectra.	39
8	The Reproducibility of the Ba $3d_{5/2}$ / Ca $2p_{1/2}$ Ratio for Different Weights of Ba^{2+} Ions on Cleaved Calcite Crystals.	43
9	Calibration Plot for $BaCl_2$ and $Ba(ClO_4)_2$ Spectra: the Area Ratio Ba $3d_{5/2}$ / Ca $2p_{1/2}$ versus Weight of Ba^{2+} Ions on Cleaved Calcite Crystals.	45
10	Comparison of the Pb and Ba ESCA Calibration Plots.	48
11	Mercury ESCA Calibration Plot and Effects of Time on Reproducibility.	56
12	Representative Hg 4f and Cl 2p ESCA Spectra.	57
13	Mercury ESCA Calibration Plot (Data of Table 5).	60
14	Calculation of Mercury 4f Escape Depth.	63
15a	Chlorine ESCA Calibration Plot. Effects of Storage Time on Peak Intensities.	65

Figure	Description	Page
15b	Chlorine ESCA Calibration Plot, Reproducibility.	66
16	Calculation of Chlorine 2p Escape Depth.	67
17	ESCA Calibration Plot for Ba^{2+} and La^{2+} on MnO_2.	69
18	ESCA Calibration Plot for Ni^{2+} on MnO_2.	70
19	Equilibrium of Powdered Calcite in Water, pH vs. Time.	76
20	Pyrex Column, Apparatus Used for Ba^{2+} Crushed Limestone Sorption Study.	79
21	Sorption Plots for Powdered Calcite as a Function of Different Initial Ba^{2+} Concentrations.	82
22	Langmuir Plot, Powdered Calcite - Ba^{2+} Results.	84
23	Langmuir Isotherm, Powdered Calcite - Ba^{2+} Results.	86
24	Ba^{2+} Sorption per Gram Calcite versus Initial Ba^{2+} Concentration.	87
25	Barium Adsorption on St. Marys Limestone.	93
26	Ba^{2+} Adsorption onto Crystalline Calcite Crystals (non-equilibrium conditions).	98
27	Ba^{2+} Adsorption onto Iceland Spar Calcite Crystals (non-equilibrium conditions).	99
28	Ba^{2+} Adsorption onto Crystalline Calcite Crystals (equilibrium conditions).	100
29	Ba^{2+} Adsorption onto Iceland Spar Calcite Crystals (equilibrium conditions).	101
30	Mercuric Ion Adsorption on Powdered FeS.	117
31a	Langmuir Plot, Powdered FeS - Hg^{2+} (nonequilibrium conditions), Data of Table 11a.	118

Figure	Description	Page
31b	Langmuir Plot, Powdered FeS - Hg^{2+} (equilibrium 3 weeks), Data of Table 11b.	119
31c	Langmuir Plot, Powdered FeS - Hg^{2+} (equilibrium 2 hours), Data of Table 11c.	120
32a	Langmuir Isotherm, Powdered FeS - Hg^{2+}, Results of Table 11a.	121
32b	Langmuir Isotherm, Powdered FeS - Hg^{2+}, Results of Table 11b.	122
32c	Langmuir Isotherm, Powdered FeS - Hg^{2+}, Results of Table 11c.	123
33	Preliminary ESCA Results, Hg^{2+} Sorption on Polished FeS Plates.	134
34	Preliminary ESCA Results, Hg^{2+} Sorption on Polished FeS Plates.	135
35	Representative Adsorbed Hg 4f ESCA Spectra.	136
36	Hg 4f ESCA Spectrum Showing Two Oxidation States.	137
37	O 1s ESCA Spectra of FeS, Effects of Adsorption.	139
38	pH Effects of Hg^{2+} Adsorption onto Polished FeS Plates.	141
39a	Hg^{2+} Adsorption onto Polished FeS Plates. Effects of Chloride Concentration.	144
39b	Hg^{2+} Adsorption onto Polished FeS Plates. Effects of Chloride Concentration.	145
39c	Hg^{2+} Adsorption onto Polished FeS Plates. Effects of Chloride Concentration.	146
40	Mechani[illegible]g Adsorption on Non-Stoichiometric FeS.	154

Figure	Description	Page
A.1	Calcite Crystal Dipping Procedure.	163
A.2a	Effects of Water on Calcite Crystal Surfaces (C 1s ESCA Spectra).	170
A.2b	Effects of Barium Solution on Calcite Crystal Surfaces (C 1s ESCA Spectra).	171
A.3	Ni^{2+} Adsorption on MnO_2.	177
A.4	La^{2+} Adsorption on MnO_2.	178
A.5	Ba^{2+} Adsorption on MnO_2.	179
A.6	Calcite Crystal Structure.	187
A.7	FeS Composition Data (a) Composition Range of Pyrrhotite. (b) Plan of the Unit Cell of the Hexagonal Structure of Iron Sulphide. (c) Clinographic Projection of the Same Structure.	196
A.8	FeS_2 Crystal Structure.	196

NOMENCLATURE

e^-	electron
h	Planck's constant (6.625×10^{-27} erg-sec)
ν	frequency of x-ray radiation
E_k	kinetic energy
E_b	binding energy
$\phi_{sp.}$	spectrometer work function
$\phi_{ch.}$	electric potential (charging) of sample
Å	Angstrom, 10^{-8} cm.
λ	escape depth of photoejected electrons
σ	photoexcitation cross section of the atom
pH	$-\log[H^+]$
X	moles metal adsorbed/mole of sorbent
X_m	maximum adsorption capacity (moles metal/mole sorbent)
$C_{equil.}$	equilibrium concentration (moles/ℓ)
b	term related to heat of adsorption
ζ	Zeta Potential (electrical potential across interface)
ψ_o	change in electric potential at double layer
E.D.L.	electric double layer
F	Faraday constant (96,500 coulombs/equivalent)
Z.P.C.	zero point of charge
z	nuclear charge
r	ionic radius
ppm (γ)	parts/million, μg/ml.
μg	10^{-6} gms, microgram
eV	electron volt (~23 kcal/mole)
d	trace metal surface thickness (Å)

CHAPTER 1

1.1 INTRODUCTION

The removal of ions from solution by solid surfaces was studied as early as 1819 by Gazzari[1] and in 1850 by Way[2] for soil-solution interactions. Jenny[3] used the terms "exchange sorption" and "ionic exchange" to describe the removal of cations from solution by colloidal aluminum silicates. Many early soil chemists used the term "adsorption compounds" or "base exchange constituents" to describe the removal of ions from solution by soil.[4]

Today, the solid-solution adsorption reaction is known to be part of a wide range of physical, chemical, geological and biological processes and in regulating many organic and heavy metal micelles in the environment.

From an agricultural and an environmental standpoint the need to understand the factors moderating the partition of ions between solid interfaces and aqueous solutions is of considerable importance.[5] Applications of adsorption for mineral froth flotation, chemical processing, air pollution control and water treatment are known; applications in waste water treatment, nuclear power plant radioactive waste and associated power plant water pollution control are not as well recognized, nor well understood. Therefore there is renewed interest in the adsorption of heavy metals and radioactive nuclides on solid surfaces such as the metal alloys of nuclear power plant reaction vessels and tubing and on the common rock forming minerals calcite[6-16], oxides of iron, silicon, manganese etc.[17-24], silicates[25-27] and metal sulphides.[28-30]

Adsorption of heavy metals, radioactive nuclides and organic species onto minerals must be studied in detail to alleviate pressing environmental problems. Several examples serve to indicate the relevance of this statement.

In limestone deficient areas, e.g. Canadian Shield, lakes and rivers are chemically unbuffered and thus extremely sensitive to pH changes. Large scale sulphur dioxide gas emissions from sulphide ore smelters mixed with atmospheric water vapour create (H_2SO_4) acidic rainfall (i.e. $pH < 5$).

This steady lowering of the ground water pH causes destruction of aquatic life, hinders tree growth and creates increased leaching of trace heavy metals from the country rock. In addition, the increasing acidity enhances desorption of previously adsorbed ions from colloidal and lake sediment surfaces, causing additional heavy metal contamination.[31-34] Thus adsorption reactions may prevent and/or create water pollution problems at the same time.

Mercury pollution in Canadian lakes and rivers[35-37] is a most urgent problem requiring immediate action. Again adsorption processes may well play a dominant role in containing the present pollution and preventing reoccurrences in the future.

Nuclear plant storage/disposal of its radioactive reactor waste and associated water pollution poses a major threat to all life. The adsorption, desorption, leaching and diffusion rates of these nuclides on mineral and metal alloy surfaces must be thoroughly studied, fully understood and safe-guard measures developed if ecological suicide is to be prevented or at least postponed.[38-40]

In addition to these ecological aspects of adsorption, there is an increased geochemical awareness of the ore deposit-adsorption relationship, i.e. manganese nodules, and for understanding the relationships of cation substitution in minerals during crystal growth and subsequent metamorphic reactions.[41]

However, as J.W. Murray[18] states, "adsorption in the marine environment has not yet received the attention it deserves and neither the qualitative nor quantitative aspects of ion adsorption on solids is well established in most cases." For example, there is widespread disagreement on the kinetics of ion sorption on MnO_2.

Morgan and Stumm[42] and Posselt, et al.[21] observed that the rate of sorption at constant pH was rapid (5 minutes). In contrast, Murray[18] found that equilibrium was attained in one hour or less depending on pH, while D.J. Murray[23] and Loganathan and Buran[24] found that the final attainment of equilibrium took hours to days. These discrepancies may well be due to difficulties in obtaining accurate sorbent surface areas, and to the fact that the techniques used to measure sorption do not monitor the actual surface concentration of sorbed ions; but rather monitor decreases in solution concentration of the sorbed ions. Thus, classical chemical[18,43], and instrumental methods such as atomic absorption[18,44], and radioactive tracer techniques[19,44,45] have been used extensively to follow the decrease in sorbate concentration in solution. Recently Sasti and Möller[46], Möller[47] have used the Paneth-Verweck radio tracer method to detect sorbed ^{44}Ca on calcite surfaces.

In this study extensive sorption on mineral surfaces has been examined using the relatively new technique of x-ray photoelectron spectroscopy (ESCA)[48,49], combined with atomic absorption methods as analytical probes. The ESCA technique appeared to have extremely useful properties for fundamental studies of ion sorption on solid surfaces, i.e. qualitative and quantitative trace metal surface analysis. Two mineral systems were studied: (i) Ba^{2+} sorption on single calcite crystals and (ii) Hg^{2+}, Hg^0 sorption on cut and/or polished highly pure slabs of pyrrhotite (FeS) and pyrite (FeS_2) ore.

To get a reasonable measure of the sorption capacity ability of these two sorbents, powdered inorganic calcite and jaw crushed pyrrhotite ore were also studied by monitoring the decrease of sorbate in solution using atomic absorption methods.

These two adsorbate-adsorbent systems (i.e. Ba on calcite and Hg on iron sulphide) were chosen for three major reasons: (i) because of their great geochemical importance; (ii) because of their world wide availability and commercial feasibility for use as a pollution sorbent;and (iii) because any exchange constituents i.e. Ca^{2+}, Fe^{2+}, $CO_3{}^{2-}$, S^{2-} ions would not pose their own pollution hazard if released into the water being cleansed. In addition, large cleaved single crystals of calcite are easily obtained, providing a well defined surface area of reaction and ESCA surface for analysis. Also the sorption ability of iron sulphide ore minerals for removing dangerous heavy metals such as Hg, Cd, etc. from solution had not been studied in detail previously.[50]

1.2 References

1. A. Gazzari (1819); from works of F. Sestini, Landiv. Versuchsst, 16, 409, (1873).
2. J. Way, J. Royal Society, London, 11, 313, (1850).
3. H. Jenny, J. Physical Chemistry, 36, 2217, (1932).
4. W.P. Kelly, W.H. Dore and S.M. Brown, Soil Science, 31, 25, (1931).
5. J.W. Bowden, M.D.A. Bolland, J.P. Posner and J.P. Quirk, Nature (Physical Sci.), 245, 81, (1973).
6. C.W. Correns, Kolloidzachr., 34, 341, (1924).
7. A. Heydemann, Geochim. et Cosmochim. Acta, 15, 305, (1959).
8. (a) E. Canals, R. Marignan and S. Cordier, Trav. Soc. Pharm., Montpellier, 9, 55, (1949).
    (b) E. Canals, R. Marignan and S. Cordier, Ann. Pharm. Franc., 8, 368, (1950).
    (c) E. Canals and R. Marignan, Ann. Pharm. Franc., 7, 502, (1949).
9. J. Jurinak and N. Bauer, Soil Science Society Proceedings, 20, 466, (1956).
10. T. Tamura and E.G. Struxness, Health Physics, 9, 697, (1963).
11. T. Tarutani and S. Misumi, Mem. Fac. Sci. Kyushu, Series C5, 1, 21, (1962).
12. E. Görlich and Z. Görlich, Bull. Acad. Polon. Sci., Sér. Sci., Chim. géol. et géolgraph., 8, 75, (1960).
13. H.B. Mann, Soil Science, 29, 117, (1930).
14. K. Murata, Am. Jour. Sci., 237, 725, (1939).
15. P. Boischot, M. Durroux and G. Sylvestre, Ann. Agr., Series A, 307, (1950).
16. V.I. Spitsyn and V.V. Gromov , Pochvovedeniye, 12, 45, (1959). (transl., Soviet Soil Science)

17. E.A. Jenne, "Trace Inorganics in Water", A.C.S. Adv. Chem. Series 73, (1968).
18. J.W. Murray, Geochim. et Cosmochim. Acta, 39, 505, (1975).
19. B.J. Anderson, E.A. Jenne and T.T. Chao, Geochim. et Cosmochim. Acta, 37, 611, (1973).
20. R.G. Guy, C.L. Chakrabarti and L.L. Schramm, Can. J. Chem., 53, 661, (1975).
21. H.S. Posselt, F.J. Anderson and W.J. Weber Jr., Environ. Sci. Technol., 2, 1087, (1968).
22. J.W. Murray, J. Colloid Interface Sci., 46, 357, (1974).
23. D.J. Murray, T.W. Healy and D.W. Fuerstenau, A.C.S. Adv. Chem. Series, 79, 74, (1968).
24. P. Loganathan and R.G. Burau, Geochim. et Cosmochim. Acta, 37, 1277, (1973).
25. B.H. Bijsterbosch, J. Colloid Interface Sci., 47, 186, (1974).
26. M.G. MacNaughton and R.Q. James, J. Colloid Interface Sci., 47, 431, (1974).
27. J.P. McKaveney, W.P. Fassinger and D.A. Stivers, Environ. Sci. Technol., 6, 1109, (1972).
28. E. Görlich and Z. Görlich, Bull. de L'Acad. Polon. Sci., Sér. des Sci. Chim., 8, 7, 379, (1960).
29. R.O. James and M.G. MacNaughton, Geochim. et Cosmochim. Acta, 41, 1549, (1977).
30. R.O. James and G.A. Parks, A.I.Ch.E. Symposium Series 150, 71, 157, (1975).
31. J.R. Kramer and A.R. Graham, Canadian Mineralogist, 14, 1, (1976).
32. J.R. Kramer, 59th C.I.C., Abstracts of Papers, Symposium on "Chemicals in the Environment", 21, (1976).

33. Toronto Globe and Mail, "Acidic rainfall effects from SO_2, NO_2 air pollution", Feb. 28, 1977.

34. Toronto Globe and Mail, "Increased Air Pollution in Southern Ontario from Michigan electricity generating plants burning sulphur rich coal", Oct. 24, 1977.

35. N. Fimreite, Ph.D. Thesis, Univ. Western Ontario, (1970).

36. R. Bryan, "Much is Taken, Much Remains", Duxbury Press, U.S.A. (1973).

37. Montreal Gazette, "Canadian waterways contaminated with Mercury", June 28, 1977.

38. B.L. Cohen, Scientific American, 236, 21, (1977).

39. Toronto Globe and Mail, "Storage problems associated with Nuclear Waste", Aug. 19, 1976.

40. Financial Post, "Problems of Nuclear waste storage", July 2, 1977.

41. E. Dowty, Geochim. et Cosmochim. Acta, 41, 1643, (1977).

42. J.J. Morgan and W. Stumm, Proceedings 2nd Int. Conf. on Water Pollution Research, Tokyo, Pergamon, Oxford, 103, (1964).

43. (a) E. Suess, Geochim. et Cosmochim. Acta, 34, 157, (1970).
    (b) E. Suess, Geochim. et Cosmochim. Acta, 37, 2435, (1973).

44. J.L. Bischoff, J.J. Clancy and J.S. Booth, Geochim. et Cosmochim. Acta, 39, 559, (1975).

45. G. Michard, C.R. Acad. Sci. Paris, Series D, 269, 1811, (1969).

46. C.S. Sastri and P. Möller, Chem. Phys. Lett., 26, 116, (1974).

47. (a) P. Möller, Inorg. Nucl. Chem. Lett., 9, 759, (1973).
    (b) P. Möller, J. Inorg. Nucl. Chem., 35, 395, (1973).

48. (a) K. Siegbahn, et al., "ESCA - Atomic, Molecular and Solid State Structures Studied by Means of Electron Spectroscopy", Almquist

and Wiksells, Uppsala, (1967).

(b) K. Siegbahn, et al., "ESCA Applied to Free Molecules", North Holland, (1969).

49. K. Siegbahn, J. Electron Spectrosc. Relat. Phenom. 5, 58, (1974).

50. U.S.E.P.A. Publication - R2-72-077, #68-01-0060, Project 16080 G.W.O., (1972). "Various solids, including some minerals were examined to determine their ability to remove mercury from solution."

CHAPTER 2

2.1 ANALYTICAL METHODS

2.1.1 Atomic Absorption Spectrophotometry (A.A.S.)

A model 403 Perkin-Elmer (PE-403) double beam A.A.S. was employed for barium, calcium, mercury and iron trace element analysis. Atomization of mercury species in solution was accomplished either by flameless cold vapour chemical methods[1,2] or by using the PE-2100 heated graphite analyser (HGA).[3,4]

These flameless techniques were found superior to normal flame A.A.S. for mercury giving greater sensitivity, a lower detection limit and fewer interference problems. Optimum working conditions for all elements analysed was as outlined in the P.E. operation manuals[5] and several A.A.S. newsletters.[6,7]

Basic A.A.S. theory and analytical procedures are well referenced and thus omitted here. The apparatus for the cold vapour chemical atomization (Fig. 1) is adapted from an earlier study.[2] Note, the cold vapour chemical atomization procedure seemed easier and gave more reproducible results than the HGA method for mercury analysis.

2.1.2 X-Ray Photoelectron Spectroscopy (XPS)

A McPherson 36 photoelectron spectrometer was available for this research. A concise historical summary of XPS development has recently been published.[8]

K. Siegbahn[9,10] made the major advances in instrumentation and is

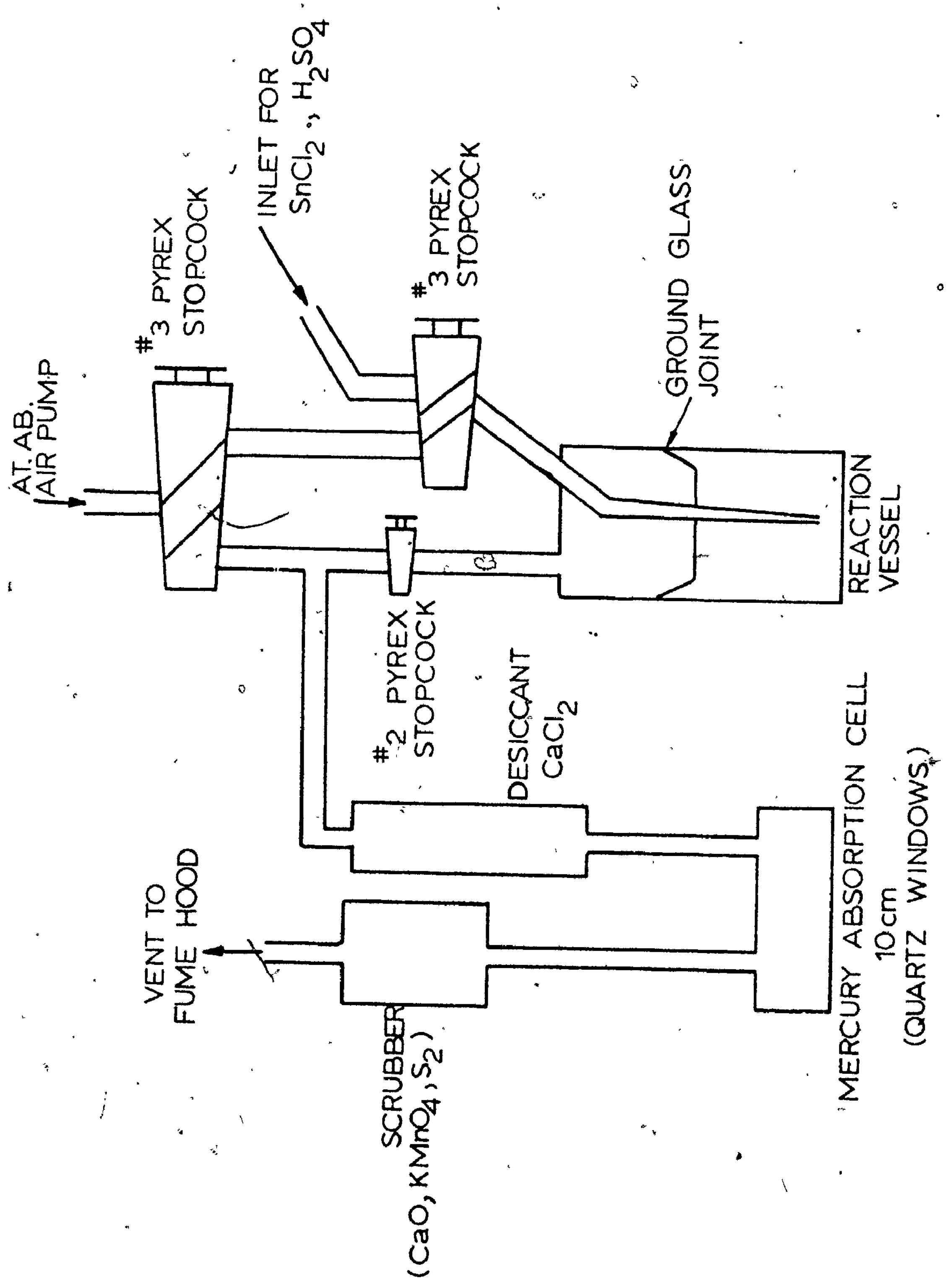

Figure 1. A.A.S. Mercury Analysis Apparatus (schematic).

credited with the development of high resolution XPS and its subsequent use in chemical analysis. Steinhardt[11] however, should also be cited for his many contributions. Theory and detailed instrumentation of XPS is examined ~~by~~ several authorities.[12,13,14]

E.S.C.A. (Electron Spectroscopy for Chemical Analysis) is a spectroscopic technique in which a flux of high energy photons (x-rays) strike a sample in a high vacuum chamber. Core (inner shell) electrons are ejected via the photoionization process $(A + h\nu \rightarrow A^{+*} + e^{-}\uparrow)$ from atoms of this sample and the kinetic energies of these electrons are analysed using a scanning analyser monochromator and electron detector (Figure 2).

Instrumentation required is simple in principle although complex in practice. A detailed explanation of each component is available from the McPherson 36 operation manual[15] and the recent publication of Carlson[14].

The McPherson 36 instrument consists of a x-ray source (magnesium anode), a sample chamber with 8 position sample wheel, a semi-spherical electrostatic analyser for separation of electrons into their range of kinetic energies (0 → 1253.6 eV) and an electron photomultiplier to detect these energetically non-equivalent electrons. To ensure high instrument resolution and prevent surface contamination during analysis, a typical vacuum of 10^{-8} torr. is attained using a turbomolecular pump. In addition, the sample chamber is differentially pumped to approximately 10^{-10} torr. by an auxiliary cryogenic pump. A 10 KeV argon ion gun is attached to the sample chamber for cleaning (etching) the sample surface and/or to depth profile the sample. Data accumulation and operating parameters are controlled by a small computer

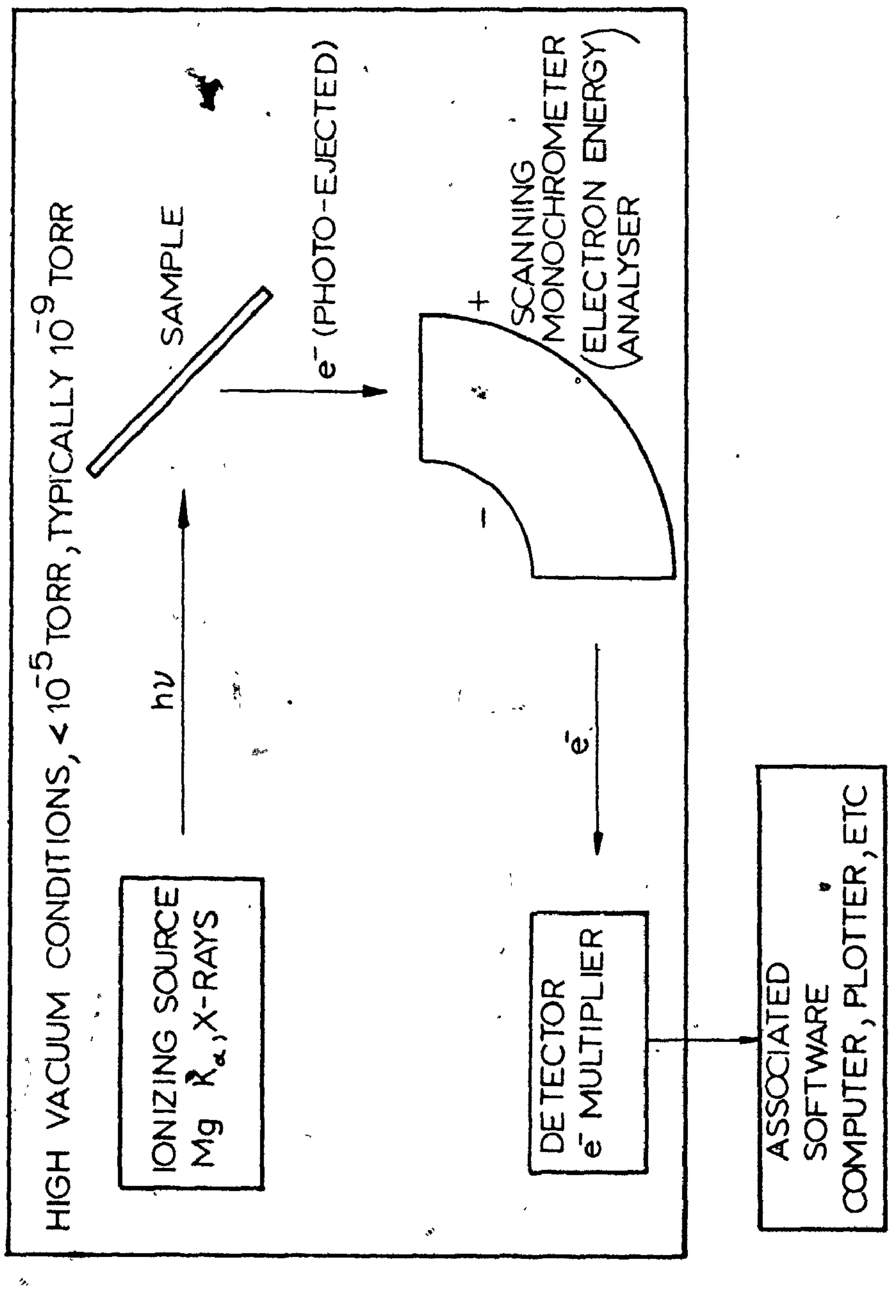

Figure 2. McPherson 36 (ESCA) Instrumentation (schematic).

(PDP8e). These data (i.e. spectra) are computer fit to combination Lorentzian-Gaussian peak shapes using the iterative program compiled at U.W.O.[16]

An ESCA spectrum consists of a plot of number of electrons detected (intensity) per unit time versus the kinetic energy (E_k) of the electrons. Since the kinetic energy is related directly to the ionization potential (binding energy, E_b) by the Einstein equation

$$E_{(x\text{-}ray)} = E_k + E_b = h\nu \qquad (1)$$

and the incident photon energy $h\nu$ ($E_{x\text{-}ray}$) is accurately known for magnesium x-rays (i.e. 1253.6 eV), E_b can be determined. In practice additional energy terms, (i.e. instrument effects) are necessary to balance this 'expression'. Thus equation (1) becomes:

$$E_b = 1253.6 - E_k - \phi_{sp.} - \phi_{ch.} \qquad \text{([illegible])}$$

where $\phi_{sp.}$ is the spectrometer work function (a constant) and $\phi_{ch.}$ is the electric potential (charging) in the sample caused by poor sample conductivity (variable, 0 → 4 eV). The binding energy of each electron is characteristic of the atom from which it was photo-ejected and the chemical environment of that atom (i.e. the atomic structure of each element is unique). The number of electrons analysed with a characteristic binding energy is thus a quantitative measure of that atom's abundance on and near the sample surface because only electrons excited in the first 5 - 15 Å for metals, 15 - 25 Å for inorganic compounds and 50 - 100 Å for organic samples are detected.[17]

This effective depth, the escape depth (λ) of photoejected electrons, is closely related to the square-root of their kinetic energies, i.e.

$\lambda \propto E_k^{1/2}$. Escape depth is defined as a measure of the mean free path length of ejected electrons that leave the sample surface without loss of energy by inelastic scattering. Thus ESCA can be used for structure and bonding studies as well as qualitative and quantitative trace element surface analysis.

2.2 ADSORPTION THEORY - "THE SOLID-SOLUTION INTERFACE"

2.2.1 Introduction

There are two principal concepts used in discussing the control of heavy metals in solution.[18] These are (1) solubility controls, where precipitation and dissolution of solid phases of the metal ion dominate the variation of metal concentration as a function of solution parameters and time; (2) surface chemical controls where the presence of insoluble phases provide sites where adsorption or interfacial reactions can occur. Evidence supporting this latter control was provided during the course of this study. The growth of crystals occurs in successive reaction steps[19] as follows:

(a) transport of solute to crystal interface
(b) adsorption of solute at the surface
(c) incorporation into the crystal lattice.

While dissolution reactions are nearly always diffusion controlled, growth of crystals is frequently controlled by interfacial processes such as adsorption or dislocation steps. As adsorption control mechanisms are also important in many natural waters, a discussion of adsorption and adsorption models best explaining heavy metal uptake by mineral surfaces follows. Ligand concentration, metal concentration and pH are important to both solubility and adsorption mechanisms and a clear distinction between these concepts is thus not always possible. Atoms, ions and molecules bonded to the surface of a solid but differing from the constituents of the lattice and not penetrating the boundary edges of the crystal are said to be adsorbed.[20]

Adsorption is usually subdivided into two categories:

(1) Chemisorption (specific, inner Helmholtz layer, and stern plane adsorption) involves a sharing of electrons between the solid surface and the adsorbate. This chemisorbed layer cannot exceed a single micelle in thickness.

(2) Physisorption (non-specific, outer Helmholtz layer, diffuse layer and limiting Gouy plane adsorption) is caused by van der Waal's (London) dispersion forces aided by coulombic forces. No sharing of electrons occurs. However a displacement of electrons either towards or away from the surface is possible. In solid-solution adsorption, the borderline between these two types is quite blurred and additional reactions may occur. Galwey[20] states "an exclusive division into two classes cannot be made since molecules are capable of being attracted to solid surfaces by bonds within the entire range of strengths of chemical association." In addition, although ion exchange is not considered a true adsorption process[21] there is much evidence indicating exchange occurs during adsorption reactions (e.g. hydrolysable metal - mineral oxide surface).[22] Ion exchange is defined as the process by which the surface loses to the solution an amount of ions electrically equivalent to the ions taken up. For true solution sorption the change in density near the interface is small but the composition of the solution next to the solid may be drastically altered. However, no part of the surface enters the solution.[21] The Fajan-Paneth rule[23]

states that an ion tends to be strongly adsorbed on a solid surface if it forms a difficultly soluble or weakly dissociated compound with the opposite charged ion of the crystal lattice. Where specific chemical effects are not dominant, the ion charge tends to determine the extent of adsorption. Results of Weiser[23] indicated that sorption of ions by $BaSO_4$ correlated more with the solubility of the barium salt rather than ion charge. Adsorbed ions can also become incorporated into the surface lattice when rapid ageing occurs. Thus the amount of sorbate removed from solution no longer corresponds to a simple adsorption process. The term ageing is a process by which surface energy is decreased by elimination of crystal edges, corners, point defects, dislocations, etc. by means of surface diffusion, bulk diffusion and recrystallization. A crystal with a high density of dislocations has a greatly increased free energy. Such crystals tend to "anneal" or recrystallize more readily than crystals with low dislocation densities.[24] In the above ca[illegible] sorption can occur by surface exchange. Thus a simple electrostatic picture is not complete and the kinetics of mixed crystal formation must be examined. Görlich et al.[25] implies that the adsorption process initiates a double exchange on sulphide mineral surfaces. Thus adsorption encompasses a large range of surface reactions; physisorption can initiate chemisorption or vice versa, which can then cause ion exchange and/or surface lattice site substitutions.[19,26] Therefore the more general expression "sorption" processes seems better suited to describe these surface reactions.

2.2.2 Interpretation of Sorption Reactions - "The Langmuir Isotherm"

Sorption results in the removal of ions from solution and their concentration on the surface until the amount remaining in solution is in equilibrium with the surface. Sorption has been found to depend upon adsorbent surface area, adsorbate concentration, time of reaction, solution pH, ionic strength, and temperature. This sorption equilibrium condition is described by expressing the amount of sorbate adsorbed per unit weight of sorbent (X), as a function of the concentration of sorbate remaining in solution at equilibrium ($C_{equil.}$).

If sorption is considered as occurring on specific sites of the surface, then two simple relationships exist between X and $C_{equil.}$ (i.e. the Langmuir (3) and Freundlich (4) adsorption equations.)

$$X = \frac{X_m \cdot b \cdot C_{equil.}}{1 + b \cdot C_{equil.}} \qquad (3)$$

where X_m is the maximum adsorption capacity and b is a constant related to the heat of adsorption; and

$$X = k \cdot C_{equil.}^{1/n} \qquad (4)$$

where k and n are proportionality constants and $n < 1$.

Derivations of the Langmuir and Freundlich gas-solid sorption equations from first principles and their conversion to solid-solution interactions are found in several references.[27-31] Over moderate ranges of solution concentration, either equation gives similar results. However, at low concentrations (e.g. this present study) the Freundlich expression deviates greatly from linearity and thus was not applied in this research.

A plot of X vs. $C_{equil.}$ gives a Langmuir adsorption isotherm of shape shown in Figure 3. This curve plateaus at very low $C_{equil.}$ values and indicates completion of monolayer coverage, a chemisorbed layer.[32]

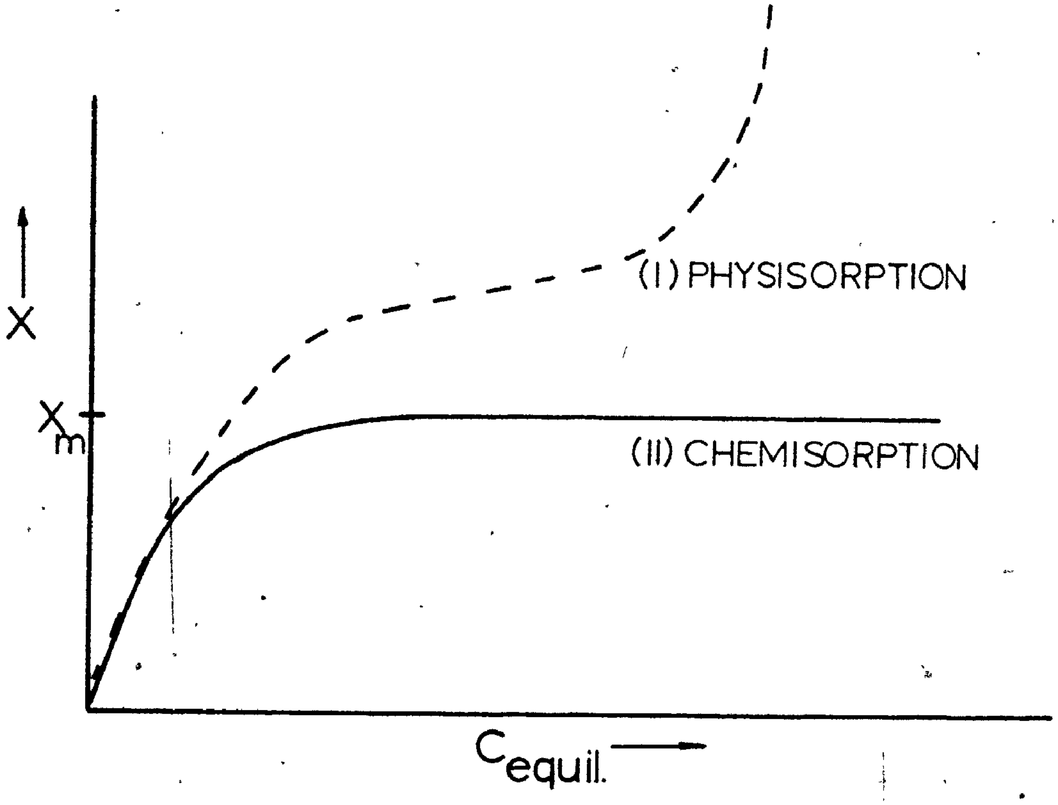

Figure 3. Typical Langmuir Adsorption Isotherm Plot.

The maximum height of this plateau (X_m) denotes the surface adsorption capacity. For physisorption, the plateau continues to rise swiftly at high $C_{equil.}$ values, indicating multilayer coverage. The length of the plateau indicates the difficulty of formation of a second layer because of charge repulsion between the first sorbed layer and those ions still in solution.[33]

In addition, adsorption leads to a reversal of surface charge if no counter ions are adsorbed (the usual case). This charge reversal causes the flattening of the isotherm before all available sites are filled[34] and decreases the X_m value with an increasing solution pH.[35-37]

This classical interpretation of sorption (i.e. specific site type) has been applied to most experimental results. However, many other theories have been developed lately to interpret observations (Section 2.2.3 Sorption Models): from a simple electrostatic surface charge interaction[38] (Gouy-Chapman-Stern) at non-specific sites, ion exchange in several forms[39], to quantum mechanical models[40,41] which apply band theory to sorption on ionic crystals. However, the Langmuir interpretation can describe adequately most experimental results to date and is thus widely applied. Data consistently fitting the Langmuir equation indicate surface selectivity and thus specific chemical sorption.[42] Note, a satisfactory fit of experimental data to the Langmuir equation does not necessarily imply that the conditions which form the basis and mechanism of the Langmuir model are fulfilled.[19]

2.2.3 Other Sorption Models

This section is a summary of current theory and models used to explain sorption from aqueous solution onto ionic surfaces. Adsorption theory and models were initially developed to explain the reaction mechanism on clean and thus more simplistic solid-gas interface.[29,38,40,41] The models became more complex and more speculative when modified to include the solid-solution interface. This is because of the interaction of the solid surface (adsorbent), ions being adsorbed from solution (absorbate) and polar water molecules (the solvent).

Forces acting at interfaces are composed of extensions of forces acting within the two phases; phenomena particular to interfaces result from a non-balance of such forces.

Two broad theories have been advanced to explain colloid stability and adsorption properties at the solid-solution interface. (1) Chemical Theory: a surface charge arises from ionization of complex groups present on the surface, and destabilization of the surface is then due to chemical interactions i.e. complex formation: (2) Physical Theory: emphasizes the concept of an electrical double layer (E.D.L.) and the significance of physical factors such as counter ion sorption, reduction of the Zeta potential and ion-pair formation.

This physical theory has become widely used in interfacial interpretation. However the two theories are not mutually exclusive. It is clear that chemical factors must be considered in addition to the (E.D.L.) to explain many solid-solution phenomena.[19,22,37,42-49]

Solids in natural waters have electrically charged surfaces, one side of the interface assumes a net electrostatic charge, either positive or negative; and an equivalent number of counter ions of opposite charge form a diffuse layer in the aqueous phase. This electric double layer exists at all interfaces in natural waters. The electrical potential across the interface is termed the Zeta Potential (δ).

In the case of ionic crystals, a surface can also acquire an electrical charge through lattice defects, by gross mechanical rupture or by isomorphic ionic replacements within the crystal lattice. Thus either positive or negative charge sites may occur.

The early electrostatic models of Gouy and Chapman were subsequently modified by Stern[38] to include both a sharp and a diffuse layer of ions at this electric double laye[illegible] (Fig. 4).

The electric potential drop ψ_o across the double layer is given by the free energy (ΔG) involved to change the solid-solution junction to $\psi_o = 0$ (i.e. to the zero point of charge (Z.P.C.).

$$-\Delta G = F\psi_o = RT \ln K \qquad (5)$$

and K is the potential determining species at the two electrical potentials (ψ_o and $\psi_o = 0$) and are usually either H^+ or OH^- ions.

$$\text{i.e.} \quad \psi_o = \frac{RT}{F} \ln \frac{[H^+]}{[H_o^+]} = -\frac{RT}{F} \ln \frac{[OH^-]}{[OH_o^-]} \qquad (6)$$

ψ_o = surface potential

F = Faraday (96,500 coulombs/equivalent).

An additional term must be included in expression (5) to indicate the chemical (i.e. non-electrostatic) contribution to adsorption.

$$-\Delta G = F\psi_o + \Phi \qquad (7)$$

This "chemical" term (Φ), includes all chemical interactions such as hydrolysis of the adsorbate, hydroxylation of the sorbent, complex formation of the surface, solvent effects, etc. This expression (7) is basic to the James-Healy Adsorption Model discussed below. The

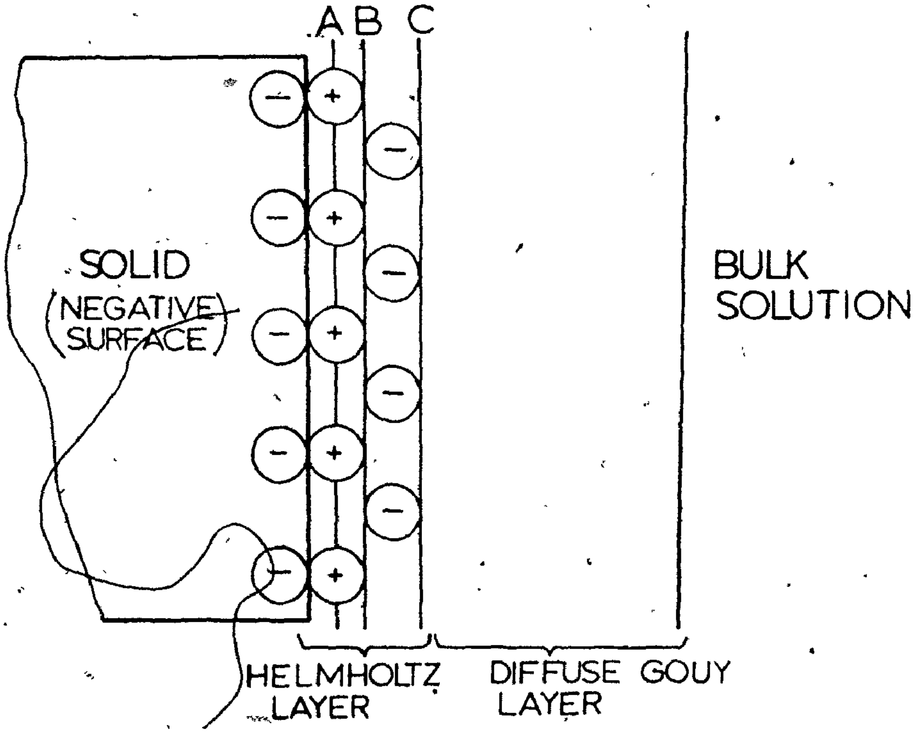

where A is the Stern plane (inner Helmholtz) and B is the limiting Gouy plane (outer Helmholtz).

Figure 4. Stern Electric Double Layer (schematic).

double layer theory predicts that polar water molecules adsorb in a way as to neutralize a solid surface, thus producing a more kinetically favorable state. There is much evidence supporting a thick surface layer of vicinal water on mineral surfaces[50], and this layer is altered or partially removed by specific adsorption. For example, large scale chemical separation of crushed ore from gangue rock by froth flotation has been employed for many years. However, the mechanism of enhanced separation by the addition of organic constituents to the mixture is not well understood.[51] Recent studies indicate that sorption of these organic micelles (xanthates) onto a hydrophilic surface renders it hydrophobic. The colloidal mineral surface and air bubbles are then able to move closer together, enhancing the flotation (separation) rate. If this mechanism is correct, the mineral surface originally holds a thick water layer and a sorption reaction alters this vicinal layer so drastically as to substantially reduce its thickness. Several recent studies [52-54] indicate that strongly adsorbed water on silica (SiO_2) is chemically bound to the surface through hydroxyl groups (OH^-), and there may be three chemisorbed immobilized layers of water at the interface. This sorbed water can be considered as forming a hydroxylated surface. For ionic crystals, surface dissociation of a water molecule causes the proton (H^+) to associate with a surface lattice anion (such as O^{2-} or S^{2-}) forming an acidic $(-O \sim H)^+$ or $(-S \sim H)^+$ group while the dissociated water (OH^-) group becomes associated with a lattice cation (Me^{2+}) forming a basic hydroxyl group.[52,53] $(-Me \sim OH)^-$. The acid $(-O \sim H)^+$ hydroxyl groups are then possible sites of adsorption with hydrated or hydrolyzed metal sorbates (M^{2+}) i.e.

$$(-O-H)^{+}_{surf.} + M^{2+} \overset{k_1}{\rightleftharpoons} (-O-M)^{2+}_{surf.} + H^{+} \qquad (8)$$

$$\text{or} \quad 2(-O-H)^{+}_{surf.} + M^{2+} \overset{k_2}{\rightleftharpoons} (-O-M)^{2+}_{2\ surf.} + 2H^{+} \qquad (9)$$

Additional support for the production of a hydroxylated surface comes from Murray[22], (sorption is pH dependant) and Gregg[55], (methylation of an oxide mineral surface greatly reduces its adsorption ability.)

This simple ion exchange model fits many experimental data. However the expected proton increase in solution is not always observed.[22] Possible counter anion adsorption on the basic hydroxyl group sites occurs, however this is not usually the case. Therefore, "chemical" processes must be active to explain the observations.

Bilinski[42] states "for low charged inorganic surfaces the electrostatic contribution to free energy of adsorption is often smaller than the contributions from covalent, hydrogen bonding or from solvation effects".

Balistrieri[49] found that transition metals adsorbed on hydrous oxides ($FeOOH$, MnO_2) by ion exchange and with the mineral surface both positively and negatively charged, suggesting specific adsorption. i.e.

$$(-XO)H_{surf.} + M^{2+} \rightleftharpoons -XOM^{+}_{surf.} + H^{+} \qquad (10)$$

On the same surfaces, group I and II cations were found to adsorb only after the surface acquired a negative surface suggesting electrostatic adsorption, i.e.

$$(-XO^{-})_{surf.} + M^{2+} \rightleftharpoons -XOM^{+}_{surf.} \qquad (11)$$

The Hohl and Stumm[47] study indicated lead adsorption on Al_2O_3 in a pH region well below that of any hydrolysis and on a positively charged surface and they thus postulated "specific" chemical interactions of (AlO^-) groups with unhydrolyzed lead ions.

The enhanced sorption by hydrolyzed (partial loss of hydration sheath) metal adsorbates on oxides has also been observed and discussed by many workers.[19,22,37,43-46]

In particular, Murray[22], Posselt[37] and Kinnburgh[43] found that sorption followed the series Ba > Sr > Ca > Mg on MnO_2. This sequence follows the Holfmeister classification for the affinity of ions for exchange sorption by cation exchange resins.[56] Holfmeister found the order of affinity for sorption is generally

$$Li^+ < Na^+ < K^+ < Cs^+ < Mg^{2+} < Ca^{2+} < Sr^{2+} < Ba^{2+} < Al^{3+} \quad \text{etc...}$$

The explanation for this order is that affinity is a function of ionic size[56]; i.e. degree hydration $\alpha\ ^{z}/_{r}$. Within a given group of elements, the larger the crystalline ionic radii, the larger is the exchange affinity.

This phenomena is related to the solvation of the ion, i.e. its polarizability. This solvation energy term must be overcome to remove the secondary hydration sheath, thereby enhancing sorption. Note; hydroxyl groups in the mineral surface can lower the effective charge on the hydrated adsorbate, lowering its solvation-energy term, enabling hydrolyzation and thus adsorption.[19] Within a group of elements, the smaller the crystalline radius, the greater is the actual ionic radius of the hydrated ion.[22] The strongly hydrated ions are less likely to undergo sorption because of their increased size, which introduces large steric hindrances. Thus sorption processes are controlled by the interaction of the EDL (i.e. its production of a hydroxylated mineral surface) and hydrated or hydrolyzed adsorbate micelles.

Thus there are two <u>conceptual</u> approaches to the sorption phenomena:[18] (1) Calculation of adsorption isotherms using the electrical double layer (EDL) from an estimation of free energies of adsorption for each hydrolytic species of an adsorbate metal; (2) postulation of ion exchange reactions and derivations of exchange constants without consideration of the physico-chemical structuring of the interface.

Five models based on the above concepts have been proposed and are summarized as follows:[18,45,47]

1. Basic Gouy-Chapman electrostatic sorption at the EDL, modified later by Stern (Figure 4).

2. Surface hydrolysis-ion exchange model of Dugger 1964, where

$$n(S \sim H) + M^{m+} \rightleftharpoons S_nM^{(m-n)+} + nH^+ \qquad (12)$$

This model has been widely used to describe metal sorption on hydrous mineral oxides.[44,57]

3. Adsorption - surface induced hydrolysis

$$S + M^{m+} \overset{k_1}{\rightleftharpoons} S \sim M^{m+} \qquad (13)$$

$$\overset{k_2}{\rightleftharpoons} S \sim M(OH)^{m-1)+} + H^+ \qquad (14)$$

$$\overset{k_3}{\rightleftharpoons} S \sim M(OH)_2{}^{(m-2)+} + 2H^+ \qquad (15)$$

4. Adsorption of hydrolytic complexes using EDL theory "JAMES-HEALY' MODEL[45]

$$\text{hydrolysis} \quad M^{m+} + nH_2O \overset{\beta_n}{\rightleftharpoons} M(OH)_n{}^{(m-n)+} + nH^+ \qquad (16)$$

$$\text{adsorption} \quad S + M(OH)_n{}^{(m-n)+} \overset{K_{ads.}}{\rightleftharpoons} S \sim M(OH)_n{}^{(m-n)+} \qquad (17)$$

$K_{ads.}$ is estimated from $K_{ads.} = \exp[-\Delta G_{ads.}/RT]$

Sorption of metal species from the entire suite of soluble hydrolysis products is estimated from free energies of adsorption of each species. The free energy term from the EDL (Gouy-Chapman) is combined with the "chemical" free energy term (Φ).

$$\Delta G_{ads.} = \Delta G_{coul.} + \Phi, \text{ where } \Phi \text{ is } \Delta G_{chem.} + \Delta G_{solv.} \qquad (18)$$

Equation 18 becomes

$$\Delta G_{ads.} = F\psi_o + F(\frac{z^2e^2}{r}(\frac{1}{\varepsilon_{interface}} - \frac{1}{\varepsilon_{solution}})) + \Delta G_{chem.} \qquad (19)$$

where $\Delta G_{coul.} = F\psi_o$ the simple Gouy-Chapman electrostatic free energy at the interface; $\Delta G_{solv.} = F(\frac{z^2e^2}{r}(\frac{1}{\varepsilon_{int.}} - \frac{1}{\varepsilon_{sol.}}))$, the change in secondary solution free energy as the adsorbing ion moves from the bulk-solution having a dielectric constant ($\varepsilon_{solution}$) to its equilibrium position at the interface with a dielectric constant, ($\varepsilon_{interface}$). The terms z, r are the charge and radius for the adsorbing ion:

$\Delta G_{chem.}$ is the total "specific" sorption free energy for the reaction (i.e. usually 2 → 5 Kcal/mole)[22]

This model in conjunction with the more complete Stern E.D.L. model has recently been proposed.[34,58]

5. Adsorption of hydrolyzable metal ions as a surface complex formation with EDL interactions (hydroxylated surface).[47,48]

Surface reactions

$$S \sim OH_2^+ \xrightleftharpoons{k_1} S \sim OH + H^+ \qquad (20)$$

$$S \sim OH \xrightleftharpoons{k_2} S \sim O^- + H^+ \qquad (21)$$

Coordination reactions

$$S - OH + M^{2+} \overset{k_3}{\rightleftharpoons} S - OM^{+} + H^{+} \qquad (22)$$

and

$$2(S - OH) + M^{2+} \overset{k_4}{\rightleftharpoons} (S - O)_2M + 2H^{+} \qquad (23)$$

In these five models, "S" equals the concentration of surface sites available for adsorption. Models 2 and 3 assume the adsorption interaction is specific and independent of the surface charge, and thus are called "ion exchange" or "chemical" models. Models 1 and 4, however, describe sorption from either a simple or a complex "physical" concept as well as taking into account any "chemical" interaction. These latter models, "physical models", indicate no inner coordination sphere interaction of the adsorbate upon adsorption.

As shown earlier not all experimental observations indicate similar mechanisms and no model adequately explains all phenomena to date. However, model 4[45] (Physisorption model) and model 5[47,48] (chemisorption model) have been widely discussed recently. The above results indicate that sorption is a kinetically favoured, hydroxylated solid surface and hydrated/hydrolyzed metal adsorbate interaction which reduces the electrostatic surface charge to a minimum.[19] Which model chosen to represent this reaction is presently academic, as no verification is presently possible. Note however, the mechanisms can be extended to include other hydrophilic ionic crystal surface reactions, such as calcite and iron sulphides.

2.3 References

1. C. Feldman, Anal. Chem., 46, 1606, (1974).
2. D.C. Manning, At. Absorp. Newslett., 9, 97, (1970).
3. D.C. Manning and F. Fernandez, At. Absorp. Newslett., 9, 65, (1970).
4. J.F. Alder and D.A. Hickmann, Anal. Chem., 59, 339, (1977).
5. Perkin-Elmer, Norwalk, Conn., "Analytical Methods for Atomic Absorption Spectrophotometry", (1973).
6. J.D. Kerber and W.B. Barnett, At. Absorp. Newslett., 8, 113, (1969).
7. G.F. Peterson and H.L. Kahn, At. Absorp. Newslett., 9, 71, (1970).
8. J.G. Jenkin, R.C.G. Leckey and J. Liesegang, J. Electron Spectrosc. Relat. Phenom., 12, 1, (1977).
9. K. Siegbahn, *et al.*, "ESCA - Atomic, Molecular and Solid State Structures Studied by Means of Electron Spectroscopy", Almquist and Wiksells, Uppsala, (1967).
10. K. Siegbahn, *et al.*, "ESCA Applied to Free Molecules", North Holland, (1969).
11. R.G. Steinhardt Jr., Ph.D. Thesis, Lehigh Univ., Pa., (1950); published in abbreviated form in Anal. Chem., 23, 1585, (1951).
12. D.M. Hercules, Anal. Chem., 48, 295R, (1976).
13. C.R. Brundle, J. Vac. Sci. Technol., 11, 212, (1974).
14. T.A. Carlson, "Auger and Photoelectron Spectroscopy", Plenum Press, (1975).
15. GCA/McPherson, Acton, Mass., "ESCA 36 Photoelectron Spectrometer", (1973).
16. G.M. Bancroft, I. Adams, L.L. Coatsworth, C.D. Bennewitz, J.D. Brown and W.D. Westwood, Anal. Chem., 47, 586, (1975).
17. W.M. Riggs and R.G. Beimer, Chem. Technol., 652, (1975).

18. R.O. James and M.G. MacNaughton, Geochim. et. Cosmochim. Acta, 41, 1549, (1977).

19. W. Stumm and J.J. Morgan, "Aquatic Chemistry", Wiley - Interscience, N.Y., (1970).

20. A.K. Galwey, "Chemistry of Solids", Chapman and Hall Ltd., London, (1967).

21. J.J. Bikerman, "Physical Surfaces", Academic, (1970).

22. J.W. Murray, Geochim. et Cosmochim. Acta, 39, 505, (1975).

23. H.B. Weiser, "Colloid Chemistry", Wiley, N.Y., (1950).

24. J. Verhoogen, F.J. Turner, L.E. Weiss, C. Wahrhaftig, and W.S. Fyfe, "The Earth", Holt, Rinehart and Winston, (1970)

25. E. Görlich and Z. Görlich, Bull de L'Acad. Polon. Sci., Séries des Sci. Chim., 8, 7, 379, (1960).

26. R.G. Burns, Geochim. et Cosmochim. Acta, 40, 95, (1976).

27. K. Denbigh, "The Principles of Chemical Equilibrium", Cambridge, (1971).

28. J. de Boer, "Dynamic Character of Adsorption", Oxford, (1968).

29. V. Ponec, Z. Knor and S. Cerny, "Adsorption on Solids", C.R.C., Butterworth, (1974).

30. I. Langmuir, J. Am. Chem. Soc., 40, 1361, (1918).

31. P. Ekwell, "Surface Chemistry", Academic (1965).

32. S.J. Gregg and K. Sing, "Adsorption, Surface Area, Porosity", Academic, Chapters 6, 7, (1965).

33. C.H. Giles, A.P. D'Silva and I.A. Easton, J. Collid Interface Sci., 47, 766, (1974).

34. J.W. Bowden, W.H. Dore and S.M. Brown, Soil Science, 31, 25, (1973).

35. B.J. Anderson, E.A. Jenne and T. Chao, Geochim. et Cosmochim. Acta, 37, 611, (1973).

36. R.G. Guy, C.L. Chakrabarti, L.L. Schramm, Can. J. Chem., 53, 661, (1975).

37. H.S. Posselt, F.J. Anderson, W.J. Weber, Environ. Sci. Technol., 2, 1087, (1968).

38. O. Stern, Z. Elektrochem. 30, 508, (1924).

39. R.O. James, P.J. Stiglich and T.W. Healy, Faraday Discuss. Chem. Soc. 59, 142, (1975).

40. A. Clark, "The Theory of Adsorption and Catalysis", Academic, (1970).

41. A. Clark, "The Chemisorptive Bond", Academic, (1974).

42. H. Bilinski, S. Kozar and M. Brancia, J. Colloid Interface Sci. Symposium, M. Kerker Editor, 3, 211, (1976).

43. D.G. Kinniburgh, J.K. Syers and M.L. Jackson, Soil Sci. Soc. Amer. Proceedings, 39, 464, (1975).

44. M.G. MacNaughton and R.O. James, J. Colloid Interface Sci., 47, 431, (1974).

45. R.O. James and T.W. Healy, J. Colloid Interface Sci., 40, 65, (1972).

46. W. Stumm and J.J. Morgan, J. Amer. Water Works Asso., 54, 971, (1962).

47. H. Hohl and W. Stumm, J. Colloid Interface Sci., 55, 281, (1976).

48. P.W. Schindler, B. Furst, R. Dick and P.V. Wolf, J. Colloid Interface Sci., 55, 469, (1976).

49. L.S. Balistrieri and J.W. Murray, Abstracts from G.S.A. meeting, Seattle, Wash., (1977).

50. C.V. Braun Jr. and W. Drost-Hansen, Colloid Interface Sci. Symposium, M. Kerker, Editor, 3, 533, (1976).

51. J.A. Kitchener, Chemistry and Industry, 2, 54, (1975).

52. H.P. Boehm and M. Herrmann, Zeits. Anorg. Allgem. Chem., 352, 156, (1967).

53. E. McCaffery and A.C. Zettlemoyer, Discuss. Faraday Soc., 52, 239, (1971).

54. W.A. Zisman, A.C.S. Adv. Chem. Series 87, 1 (1968).

55. S.J. Gregg, Phys. Chem. Series 1, "Surface Chem. and Colloids", 6, 188, (1972).

56. R. Kunin, "Ion Exchange Resins", Wiley, N.Y., (1958).

57. R.O. James and G.A. Parks, Chem. Eng. Progr. (1974).

58. J.T. Yates, Chemistry and Engineering News, 8, 19, (1974).

CHAPTER 3

ESCA CALIBRATION STUDIES

3.1 Introduction

The application of ESCA to qualitative and quantitative analysis of surfaces was a major aim of this thesis. Earlier results have indicated its usefulness to this end.[1-13] The literature results show that surface detection of trace elements in the sub-monolayer region is possible $(\lesssim 10^{-8}\text{gm./cm}^2)$[2,5]. This extremely high surface sensitivity has been demonstrated for adsorption studies of gases on metal surfaces[7] and for detection of cations in solution in the low ppb range.[4,5] For quantitative studies of ions on surfaces, for example sorption studies, it is important that reproduceable calibration plots be obtained and that the calibrant surface be similar to the sorbed surfaces. Apart from an earlier study using a ratioing technique[5], there have been few attempts to obtain semi-quantitative or quantitative results using ESCA. These calibrant results are also useful for interpretation of the type of surface coverage, thickness of coverage, and using appropriate equations, can estimate the escape depth of the ion of interest. In addition, effects of carbon surface contamination on spectra intensities can be determined.[2,14]

3.2 Experimental

Semi-quantitative or quantitative chemical analysis require calibration of the spectrometer used. It has been said that calibrant sample surfaces and surfaces of samples used as adsorbents must be chemically and physically similar.[9] Cleaved Iceland Spar grade calcite was therefore used as the calibrant standards in the barium-calcite study; cut and polished FeS and FeS_2 surfaces for the mercury-iron sulphide work, and precipitated MnO_2 on aluminum plates for the barium, lanthanum and nickel - MnO_2 calibration studies. The Iceland spar calcite was cleaved to appropriate dimensions using a hammer and sharp edged steel blades. The iron sulphide plates were cut into thin slabs using a diamond tipped saw, ground on a 30 micron 3M diamond wheel and polished using an 8 micron lead lap using diamond powder. The production of MnO_2 plates is discussed fully elsewhere.[15] In all cases, the calibrant specimens had approximate dimensions of 15 x 10 x 5 mm. This size was appropriate for mounting in the XPS sample holder (8 position carousel). Stock solutions (10,000 ppm) of barium, lead, mercury, lanthanum and nickel were prepared using deionized distilled water and the analytical grade salts $BaCl_2$, $Ba(ClO_4)_2$, $HgCl_2$, $Pb(NO_3)_2$ $LaCl_3$ and $Ni(NO_3)_2$. All calibration solutions, (i.e. the stock and dilutions from these stock concentrations) were stored in polypropylene containers. Chemical analysis of these diluted solutions were done using the model P.E. 403 A.A.S. Aluminum masks with an opening 12.6 mm x 5.0 mm in each, and overall size to exactly fit the sample holder were used to ensure that the analysed area of the surface was constant for each surface. The mask was then placed in the spring loaded sample holder directly over each sample. These masks also acted as holders to keep the sample crystal or plate in place on the 360° rotating holder wheel. It was found using thin threads of teflon that over 95% of the electrons counted by the XPS detector originated from a strip along the middle of the sample, 1.8 mm wide and 12 mm long. This strip is almost the identical size of the entrance slit to the XPS analyser. Thus only one third of the open mask area was actually analysed. XPS calibration curves were produced by evaporating known amounts of barium, lead, mercury, nickel, lanthanum solutions from a 10 ml microsyringe onto the appropriate mineral surface. In the case of the freshly cleaved calcite and the highly polished iron sulphide plates, surface tension created wetting problems. Two methods were examined to minimize this effect. In the first, a large bubble of water was deposited so as to cover the crystal surface and then the trace element droplet was added. This large solution bubble was then carefully stirred using the syringe tip and slowly evaporated using a heat lamp. The poor reproducibility of duplicate calibrants was attributable to islanding of the trace metal on the surface caused by non-uniform surface evaporation of the initial solution bubble. This technique was therefore rejected for accurate calibration studies. The second method consisted of lightly etching the surface with fine crocus cloth before the addition of the trace metal solution. The small droplet was spread evenly over the crystal surface using the syringe tip. Evaporation in air occurred within minutes. Obviously this process may lead to inhomogeneity of the surface on a micro level, but the reproducibility of the results (vide infra) strongly indicates that significant islanding of the metal over the XPS analysed area (12 x 1.8 mm) does not occur.

The precipitated amorphous MnO_2 on Al plates, having a more irregular roughened surface did not require any etching. Spreading of the metal solutions occurred readily. However, the reproducibility of these calibrant MnO_2 plates was reduced somewhat by this irregular surface.

It should be noted that several crystals or plates, with only distilled deionized water evaporated on their surface, were analysed by XPS for the trace elements of interest. These blanks all found to be void of the trace metals indicated that the deionized distilled water and the mineral surfaces were free of these metals.

3.3 Results and Discussion

3.3.1 Barium Analysis on Calcite

Representative barium $3d_{5/2}$, lead 4f, calcium 2p and carbon 1s spectra are shown in Figures 5-7. Each of the barium and lead spectra (50 scans, dwell time 1 sec for 111 points) took approximately two hours to record. Reasonable spectra of these atomic levels could still be obtained into the 10^{-9}gm/cm^2 region. Excellent calcium and carbon spectra were obtained after two scans (~4 min).

All peaks had line widths of about 2.0 eV, and their binding energies (± 0.2 eV), uncorrected taking Au $4f_{7/2}$ = 84.0 eV are: Ca $2p_{1/2}$ 353.2 eV; Ba $3d_{5/2}$ 781.7 eV; Pb $4f_{7/2}$ 146.1 eV; C $1s_{(contamination)}$ 286.6 eV, C $1s_{(CO_3{}^{2-})}$ 291.6 eV.

Figure 5 shows a typical XPS spectrum of a cleaved calcite single crystal of area ~100 mm^2 with 4 x 10^{-8} gms. of barium deposited on its surface. The amount of barium in the mask area (63 mm^2) is then ~2.4 x 10^{-8} gms, while the amount of barium in the actual analysed area (1.8 x 12 mm) is thus ~10^{-8} gms. Since one could detect 2 x 10^{-9} gms.

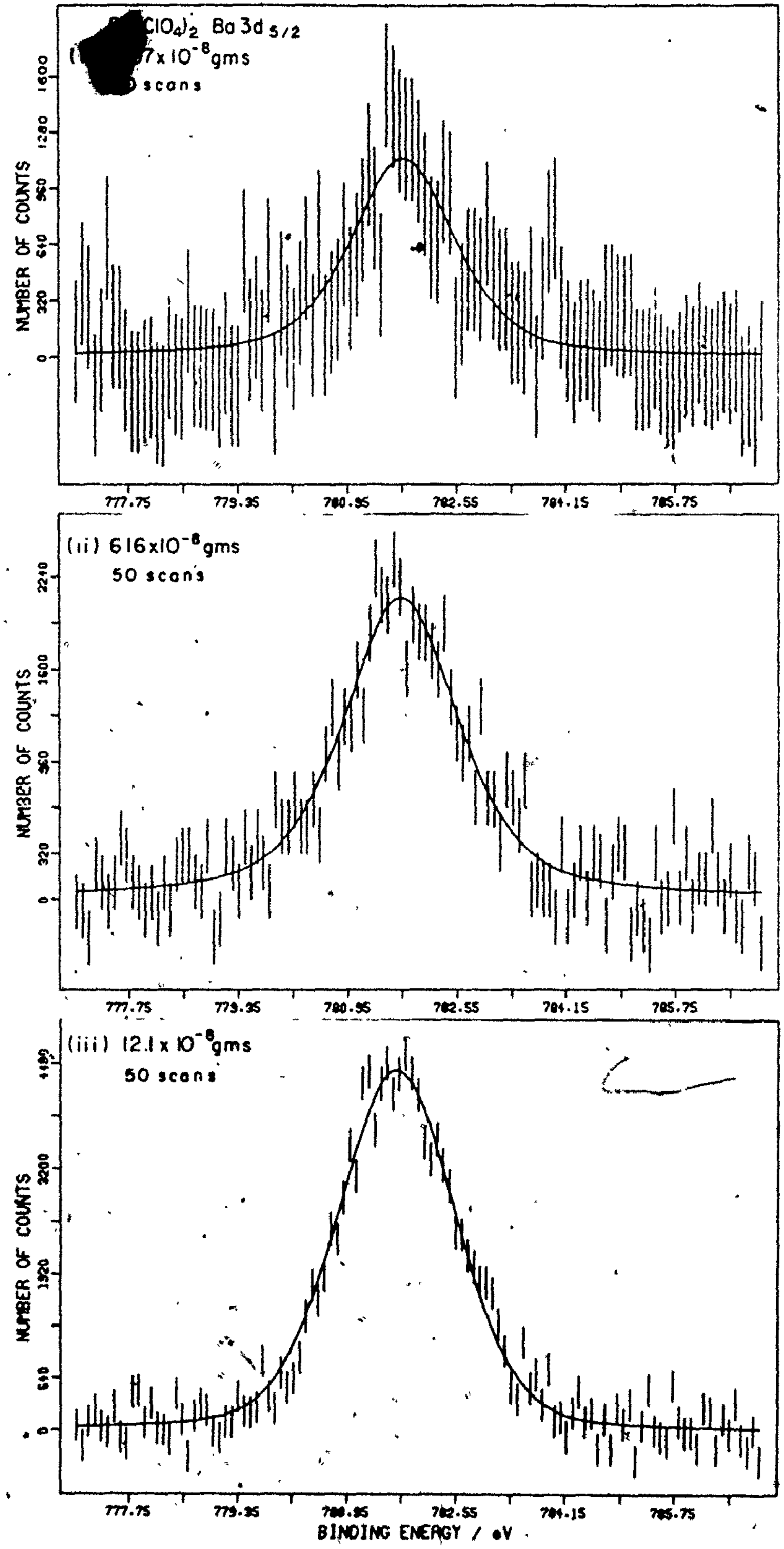

Figure 5. ESCA Spectra of the Ba 3d Levels for the Above Amounts of Ba^{2+} Syringed onto Cleaved Calcite Crystals.

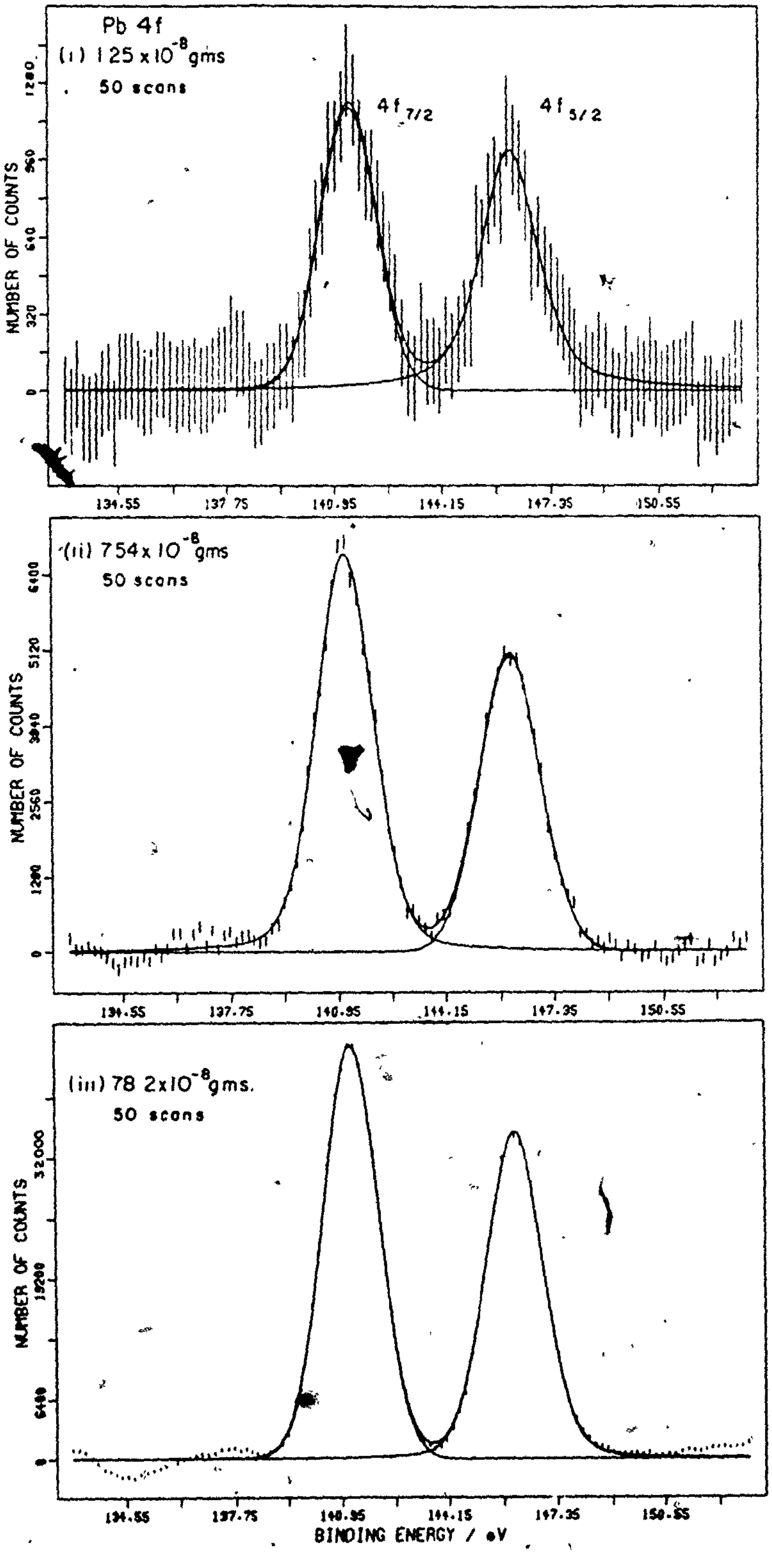

Figure 6. ESCA Spectra of the Pb 4f Levels for the Above Amounts of Pb^{2+} Syringed onto Cleaved Calcite Crystals.

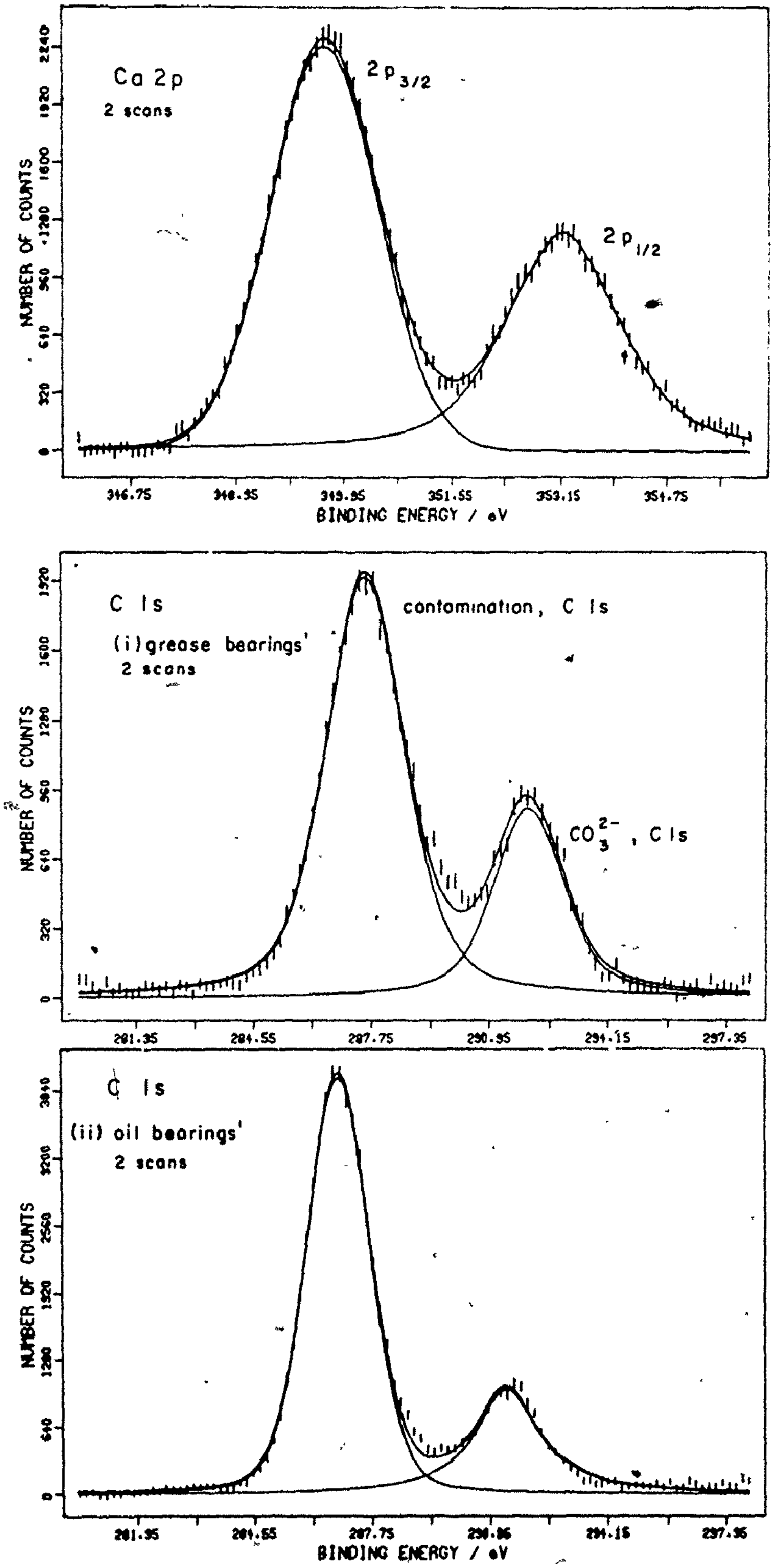

Figure 7. Representative Ca 2p and C 1s ESCA Spectra.

barium on 100 mm^2 of surface, the actual analyzed barium detection level is in the order ~ 5 x 10^{-10} gms. This great sensitivity is still possible, even when there is a large contaminant surface film on the samples. Note, the large C 1s peak, Fig. 7 corresponds to hydrocarbon contamination carbon on the calcite surface. This assignment was confirmed by argon ion etching. It was possible to eliminate this carbon 1s peak (position ~ 287 eV) by Argon etching, for 30 sec. However, this carbon peak builds up again in our 10^{-8} torr. vacuum chamber with time, indicating that the contamination is primarily from the vacuum system (lubrication, filament degassing, etc.) and not from water or air contamination after cleaving of the calcite crystals. In the first calibration study ($Ba(ClO_4)_2$, Table 1), the intensity ratio of contamination C 1s peak to the substrate carbonate C 1s peak ($C_{contam.}/C_{subst.}$) was approximately 4:1. In later studies (Tables 2, 3) this ratio dropped significantly (2 or 3:1). The lower ratio was mostly due to a change from oil bearing lubrication to grease bearings in our vacuum turbomolecular pump.

Extra care was taken to completely clean the sample chamber and to pump the entire vacuum system while empty for several days before analysis. Because of the nature of this study; i.e. mineral surfaces reacted in solution, it would never be possible of course to eliminate all surface contamination. It should be emphasized that as long as the unknown and calibrant samples are analysed together, errors from surface carbon contamination will be minimized. To reduce the effects of such contamination on these barium determinations, the ratio of intensity (area) of barium $3d_{5/2}$ to the calcium $2p_{1/2}$ is always used (i.e. I_{Ba}/I_{Ca}). As the barium coverage is less than a monolayer in most of this work (vide infra) the surface contaminants will decrease the area of both peaks proportionately. The ratio of intensities also largely compensates for non-random effects such as variation in x-ray power, or detector voltage. These intensity area ratios for several experiments are given in Tables 1, 2, 3 along with calculated weights of barium or lead analysed. The results are plotted in Figures 8, 9, 10. It is apparent that linear calibration plots can be obtained and that the reproducibility of the results is rather good considering the potential difficulties of obtaining a homogeneous layer of cations on the calcite surfaces. It should be noted that because the kinetic energy (E_k) of barium $3d_{5/2}$ electrons (~ 470 eV) is much less than the E_k of calcium 2p electrons (~ 900 eV), the barium peak intensity will be decreased more by surface carbon contamination than the calcium peak. However, this effect will cancel, when the contaminant concentration on calibrant and sorbed surfaces are similar.

The results of Table 1 indicate that I_{Ba}/I_{Ca} peak area intensity ratios for calibrant samples analysed, and stored (e.g. in a vacuum desiccator (8 weeks) before re-analysis), are in rather good agreement. The slight decrease in the slope of the plot with storage time (Figure 8) is undoubtedly due to the increase in carbon contamination as indicated by Table 1. These Ba 3d and Ca 2p peak ratios (i.e. slope of plot) were quite reproducible over the three years that barium-calcite samples were analysed; new calibrant samples were produced for re-calibration of the XPS ~~instrument at the~~ beginning of each allowed analysis period (e.g. approx. two week periods, four times a year).

The data for the $BaCl_2$ calibration study (with fresh $Ba(ClO_4)_2$ calibrants for comparison) is given in Table 2 and Figure 9. The slope

TABLE 1 Barium Perchlorate Calibration Data

Wt. Barium (gms.) ±5%	Calcite Crystal Area (mm^2) ±5 mm^2	*Wt. Barium within $63mm^2$ mask (gms.) ±5%	Area Intensity Ratio					
			**$Ba3d_{5/2}/Ca2p_{1/2}$			***C1s/C1s(calcite)		
			1a	2a	3a	1b	2b	3b†
			Initial	24 hrs.	1600 hrs.	Initial	24 hrs.	1600 hrs.
2×10^{-8}	153.0	0.82×10^{-8}	.66	.56	.63	2.68	2.67	3.67
4×10^{-8}	200.1	1.26×10^{-8}	.64	.62	--	7.0††	9.02††	8.07
10×10^{-8}	166.5	3.78×10^{-8}	1.29	1.26	1.72	2.25	2.14	3.00
20×10^{-8}	204.3	6.16×10^{-8}	2.07	1.92	2.13	3.61	3.93	3.95
40×10^{-8}	208.0	12.10×10^{-8}	5.34	5.00	4.55	3.67	4.10	4.17
100×10^{-8}	171.0	36.84×10^{-8}	15.17	13.80	13.04	2.29	2.36	2.83
Blank	202.6	NIL	--	--	--	2.76	2.91	3.08

* Assuming barium cations are evenly distributed over the crystal surface.

** Errors in these values in the range 10-20% due to inhomogeneous surface, poor distribution of barium cations etc. The area ratio quoted is that for 50 scans for the barium peak and two scans for the calcium peak. To obtain the normilized ratio multiply by 0.04.

*** Area ratio quoted is that for two scans of carbon 1s. Errors here quite low <5%.

† Turbo pump vacuum system change over from oil to grease lubrication.

†† Due to this thick carbon film, the corresponding barium ratios are low and have a much larger error.

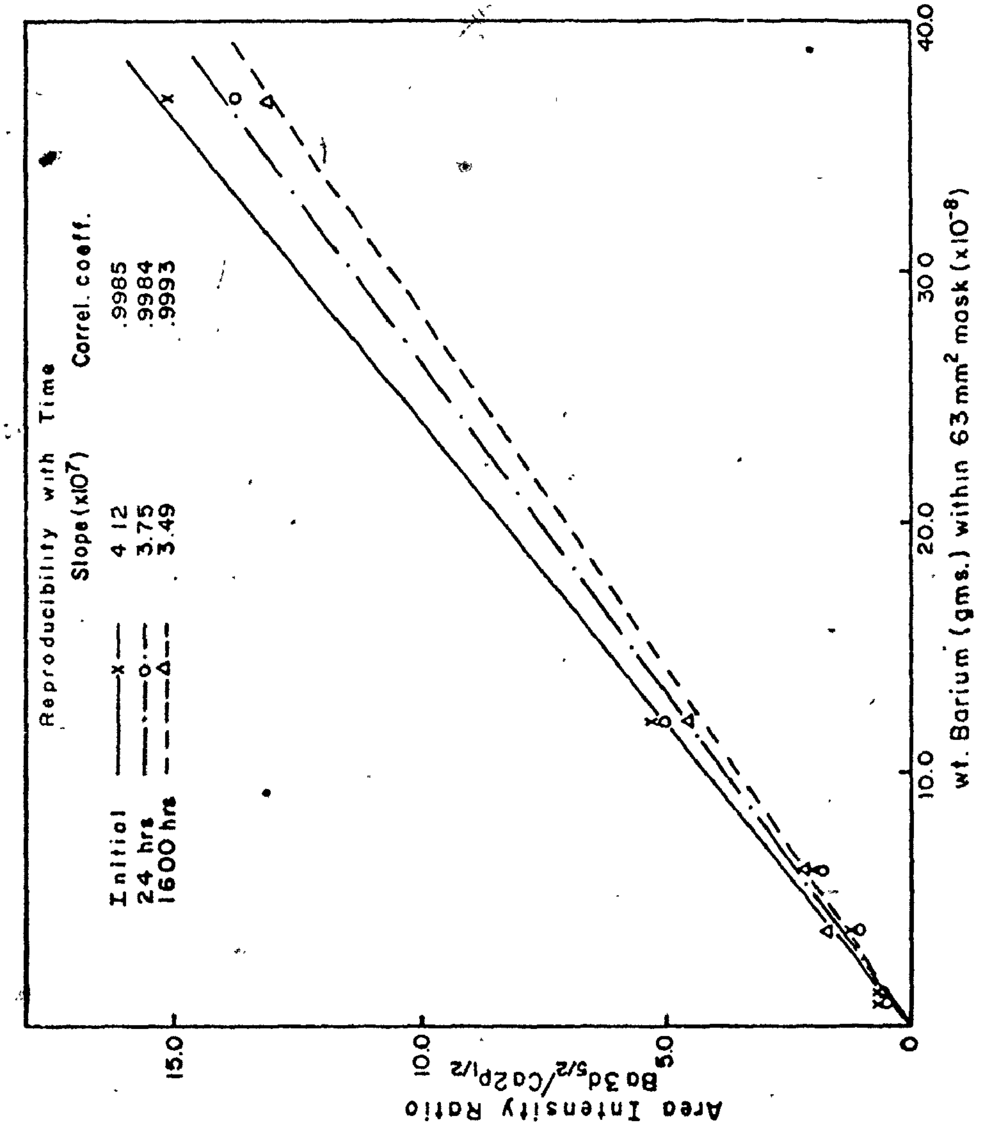

Figure 8. The Reproducibility of the Ba $3d_{5/2}$ / Ca $2p_{1/2}$ Ratio for Different Weights of Ba^{2+} Ions on Cleaved Calcite Crystals.

TABLE 2

Barium Chloride Calibration Data

Wt. Barium (gms.) ±5%	Calcite Crystal Area (mm^2) ±5.0mm^2	*Wt. Barium within 63mm^2 mask. (gms.) ±5%	Area Intensity Ratio†	
			**$\frac{Ba3d_{5/2}}{Ca2p_{1/2}}$	*** $\frac{C\ 1s}{C\ 1s(calcite)}$
(a) $Ba(ClO_4)_2$				
10×10^{-8}	116.6	5.42×10^{-8}	2.50	2.00
20×10^{-8}	99.5	12.66×10^{-8}	5.95	1.81
(b) $BaCl_2$				
Blank	209.2	NIL	—	2.06
2×10^{-8}	239.3	0.53×10^{-8}	0.40	1.67
4×10^{-8}	244.6	1.03×10^{-8}	0.60	1.64
10×10^{-8}	220.2	2.86×10^{-8}	1.50	1.70
40×10^{-8}	204.5	12.35×10^{-8}	5.64	2.22
100×10^{-8}	221.6	28.50×10^{-8}	14.22	2.45

* as per Table 1

** as per Table 1

*** as per Table 1

† as per Table 1

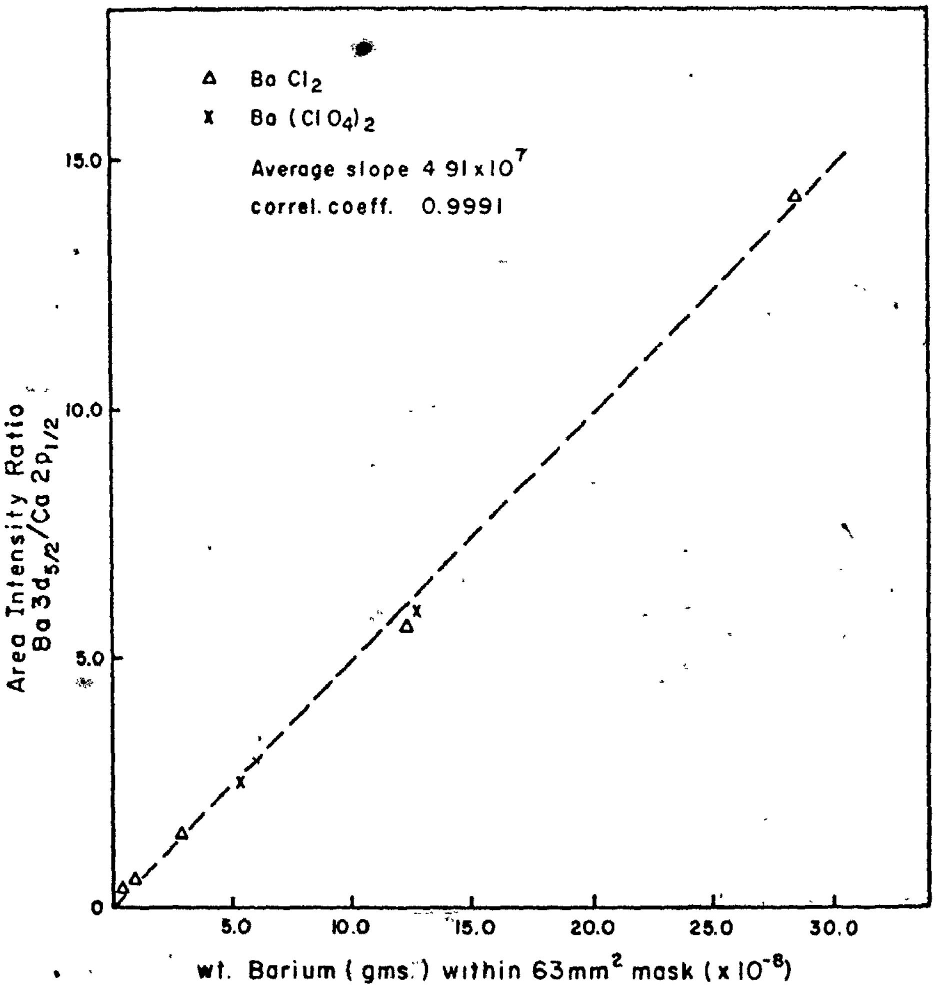

Figure 9. Calibration Plot for $BaCl_2$ and $Ba(ClO_4)_2$ Spectra: the Area Ratio Ba $3d_{5/2}$ / Ca $2p_{1/2}$ versus Weight of Ba^{2+} Ions on Cleaved Calcite Crystals.

of this plot (4.9 x 10^7) is appreciably higher than in Figure 8 i.e. (4.2 x 10^7). This is mainly due to the lower carbon contamination on these surfaces. Note that the anions Cl^- and ClO_4^- appear to have little effect on the peak area intensity ratios. All of the calibration data strongly suggest that errors in the plot slopes (for a given carbon contamination) are less than 10%. A similar result is obtained for the lead calibrant samples, Table 3, Figure 10. However, the slope of this plot is substantially greater than the barium results (vide infra).

All three of these plots are linear beyond monolayer coverage. However, the slope certainly decreases when larger amounts of barium or lead were deposited. In addition, the calcium 2p peaks do not decrease even with ~10^{-6} gm/cm^2 barium or lead on the surface. The above two observations indicate islanding of the barium and lead on the surface with increasing weights.

Considering both the contamination problems, and the problem in spreading the calibrant solutions evenly over the calcite surface, the reproducibility of the results and the linearity of the plots are very satisfying. The result strongly indicates that meaningful quantitative calibration curves for calcite surfaces can be obtained. Further confirmation of the methodology comes from a theoretical analysis of the calibration plots.

Assuming initially that the contaminants affect both Ba (and Pb) and Ca peaks equally, one can write[16,17]

$$I_{Ba} = I_{Ba}^{\infty} \cdot (1 - e^{(-d_{Ba}/\lambda)}) \qquad (24)$$

TABLE 3

Lead Nitrate Calibration Data

Wt. Lead (gms.) ± 5%	Calcite Crystal Area(mm)^2 ±5mm^2	*Wt. Lead within 63mm^2 mask. (gms.) ±5%	Area Intensity Ratio†	
			**Pb4f$_{7/2}$ / Ca2p$_{1/2}$	*** C 1s / C 1s(calcite)
0.4×10^{-8}	108.2	0.23×10^{-8}	0.46	1.90
1.0×10^{-8}	102.4	0.60×10^{-8}	1.14	2.60
2.0×10^{-8}	110.0	1.12×10^{-8}	1.06	2.25
2.0×10^{-8}	98.4	1.25×10^{-8}	1.02	1.76
4.0×10^{-8}	80.4	3.08×10^{-8}	1.60	2.88
4.0×10^{-8}	112.5	2.24×10^{-8}	1.70	2.00
††	112.5	2.24×10^{-8}	2.21	4.38
10×10^{-8}	82.1	7.54×10^{-8}	9.00	2.78
20×10^{-8}	65.5	18.90×10^{-8}	20.10	2.36
40×10^{-8}	104.6	24.1×10^{-8}	22.60	2.57
100×10^{-8}	79.1	78.2×10^{-8}	58.06	2.35

* As per Table 1

** As per Table 1

*** As per Table 1

† As per Table 1

†† Reran after two months in a vacuum dessicator

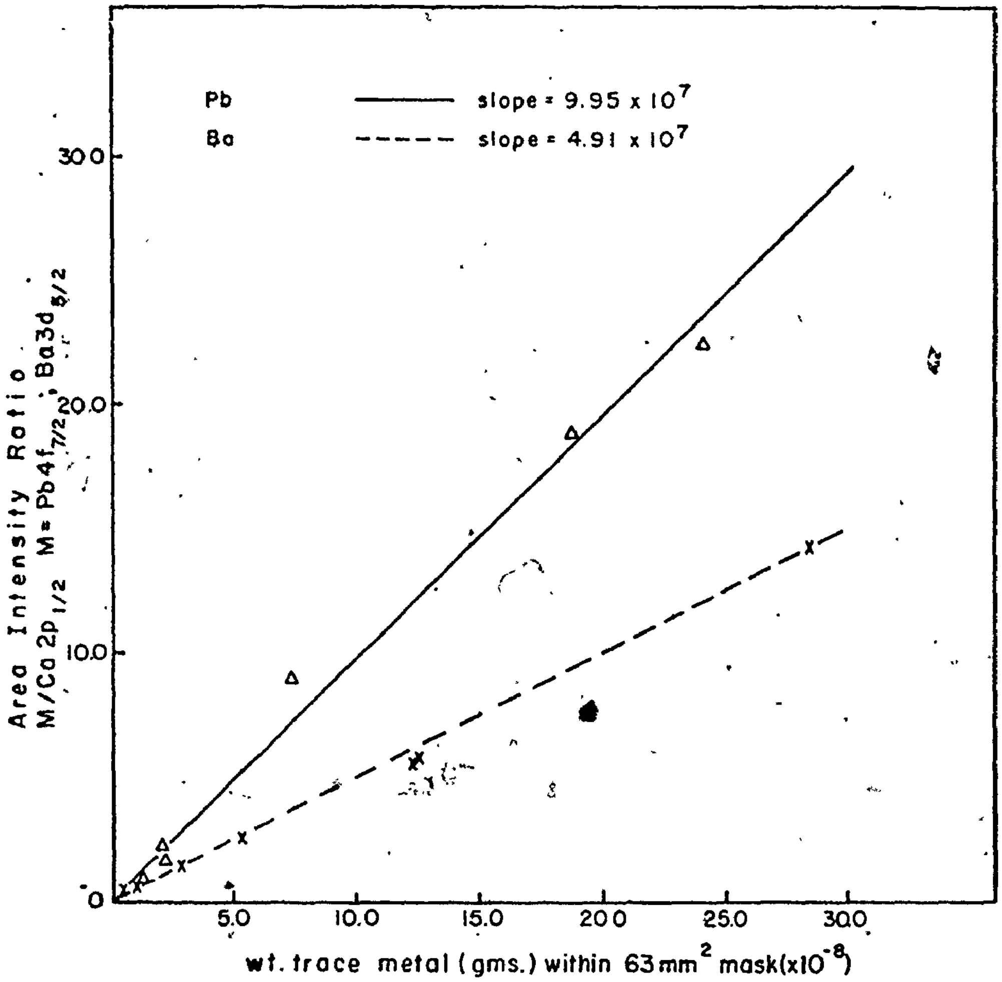

Figure 10. Comparison of the Pb and Ba ESCA Calibration Plots.

$$I_{Ca} = I_{Ca}^{\infty} \cdot e^{(-d_{Ba}/\lambda)} \quad (25)$$

where d_{Ba} is the thickness (Å) of the barium layer, λ are escape depths in the barium layer, I^{∞} are intensities for thick samples and are proportional to cross-sections for excitation of electrons, I are observed intensities (peak areas).

The calculations are simplified because $d_{Ba}/\lambda < 1$. Barium plots (Figures 8, 9) are linear to at least 6×10^{-7} gm/cm^2. This corresponds to $\sim 3 \times 10^{15}$ atoms/cm^2. A monolayer coverage of barium cations on 1 cm^2 surface would total $\sim 2 \times 10^{15}$ atoms ($r_{Ba^{2+}} = 1.34$ Å). Thus these plots are linear to at least one monolayer barium coverage and $d_{Ba} \simeq 2.7$ Å. Compared to the escape depths of $\simeq 12$ Å and 20 Å for Ba 3d and Ca 2p electrons respectively,[18] d_{Ba} then is small. Taking $I_{Ca} \approx I_{Ca}^{\infty}$ [19,20]; $1 - e^{(-d_{Ba}/\lambda)} \simeq d_{Ba}/\lambda$ and $I_{Ba}^{\infty} / I_{Ca}^{\infty} \simeq 10$ [3,19] ratioing equations 24 and 25 we obtain

$$\frac{I_{Ba}}{I_{Ca}} \simeq 10\, d_{Ba}/\lambda \simeq 1.0\, d_{Ba} \quad (26)$$

A linear calibration plot is expected.

In addition, the expected intensity ratio and the observed ratio for the amounts of barium deposited is qualitatively close. For example, 4×10^{-8} gm/cm^2 barium deposited corresponds to ≤ 0.1 monolayer, and d_{Ba} is therefore ~ 0.27 Å. The expected area ratio is thus 0.27 compared to the observed ratio of 0.06 (2/50 x 1.5).

This lack of quantitative agreement can be explained by (1) a large contribution caused by a variation in the transmission linearity of the XPS analyser, i.e. peak intensity varies with E_k, and, (2) a smaller contribution from the surface carbon contaminant layer; both will substantially decrease the barium signal relative to the calcium signal but not alter the lead intensity relative to the calcium.

These two factors are now discussed more fully.

(1) The transmission function (linearity) of the analyser can be a major problem contributing to intensity (peak area variation) from electrons with widely separated E_k[21,22], i.e. Ba $3d_{5/2}$ (470 eV) and Ca 2p (900 eV). The intensity of a photoelectron peak for a sample of uniform composition may be described as follows[23,24],

$$I = I_o \cdot n \cdot \sigma \cdot \lambda_{(\varepsilon)} \cdot T_{(\varepsilon)} \qquad (27)$$

where I_o is the x-ray flux, n the density of atoms, σ photoexcitation cross section of the atom, $\lambda_{(\varepsilon)}$ the mean free path of the electron having energy (ε) in the sample and $T_{(\varepsilon)}$ the analyser transmission efficiency which is proportional to the electrons' E_k.

It can normally be assumed that I_o is a constant during an XPS analysis. The ratio of XPS peak intensities for a given adsorbed atom's atomic level and an ionic solid substrate atomic level can then be written as,

$$\frac{I_{ads.}}{I_{subst.}} = \frac{(n \cdot \sigma \cdot \lambda \cdot T)_{ads.}}{(n \cdot \sigma \cdot \lambda \cdot T)_{subst.}} \qquad (28)$$

The analyser efficiency (T) for the McPherson ESCA 36 is near unity for electrons having E_k differences of a few hundred eV (unpublished result).[25] However for larger variations $\Delta E_k > 200$ eV, the ratio of T may be significant (personal communication).[26]

If one assumes that analyser efficiency is α to E_k for these larger ΔE_k, then an estimate of the intensity ratio, equation 28 can be determined.

For example,

$$\frac{I_{Ba\ 3d_{5/2}}}{I_{Ca\ 2p_{1/2}}} = \frac{(\sigma \cdot \lambda \cdot n \cdot E_k)_{Ba}}{(\sigma \cdot \lambda \cdot n \cdot E_k)_{Ca}} \tag{29a}$$

$$\simeq 3\ n_{Ba}/n_{Ca}$$

and likewise

$$\frac{I_{Pb\ 4f_{7/2}}}{I_{Ca\ 2p_{1/2}}} \simeq 6\ \ n_{Pb}/n_{Ca} \tag{29b}$$

using published values of λ [18,24] and σ [20].

The major reasons for the discrepancy between the I_{Ba}/I_{Ca} and I_{Pb}/I_{Ca} ratios' is due to the escape depth values chosen and/or the transmission function variation of our analyser or to both; this assumes that n_{metal}/n_{Ca} for both barium and lead calibrant weights on a calcite surface are approximately equal (the likely case).

From this calculation, the lead/calcium ratio should be approximately twice that of the barium/calcium ratio in agreement with the experimental results, Figure 10. This agreement indicates that the transmission factor (T) can be largely responsible for the low barium/calcium slope, i.e. the lack of quantitative agreement between the expected area ratio (.27) and observed ratio (.06).

Several assumptions are made in this calculation.

(a) slight changes in the chosen values of escape depths for barium, lead or calcium drastically alter the results.

(b) $T_\varepsilon \propto E_k$ and in turn effects the intensity ratio directly i.e. $$\frac{I_1}{I_2} \quad \alpha \quad \frac{T_{\varepsilon 1}}{T_{\varepsilon 2}} \quad \alpha \quad \frac{E_{k1}}{E_{k2}} \qquad (30)$$

(c) the density of atoms ratios' $\frac{n_1}{n_2}$ for lead on calcite and barium on calcite for similar weights is nearly equal. Note, there is no doubt that the lack of a constant analyser sensitivity across the E_k range of atomic levels can be largely responsible for the observed calibration slopes, Figure 10; but it is also important to realize that another factor could play a significant role in these results as well (i.e. hydrocarbon surface contamination effects).

(2) The effect of the carbon layer can be estimated from the following equation[3] (assuming it affects both layers equally)

$$\frac{I_{Ba}}{I_{Ca}} = \frac{I'_{Ba}}{I'_{Ca}} \cdot e^{d_c\left(\frac{1}{\lambda_{Ba}} - \frac{1}{\lambda_{Ca}}\right)} \qquad (31)$$

where $\frac{I'_{Ba}}{I'_{Ca}}$ is the expected ratio without carbon contamination. The carbon film thickness d_c is estimated from the ratio of the contaminant C 1s peak to the $CO_3{}^{2-}$ carbon 1s peak (Equation 32). Thus

$$\frac{I_C}{I_{CO_3}} = [\, e^{(d_C/\lambda_C \sin\theta)} \,] - 1 \qquad (32)$$

Taking $\lambda_C \simeq 20$ Å for 1000 eV electrons[18,27], $\theta = 45°$ for the McPherson 36 sample holder and the observed $I_C/I_{CO_3} \simeq 3$, Equation 32 gives $d_c \simeq 20$ Å. Solving Equation 31, one obtains $\frac{I'_{Ba}}{I'_{Ca}} \simeq 0.2$ which is in reasonable agreement with the expected 0.27. Thus, the carbon contaminant film decreases the Ba/Ca ratio markedly, and the variation in the slopes from Figure 8 to 9 could be due to the change in carbon contaminant thickness.

The Pb calibration plot further supports this methodology and the above calculations. The slope of the Pb plot is about twice that of the Ba plot (Figure 10), yet the Pb $4f_{7/2}$ cross-section is only 60% of the Ba $3d_{5/2}$ cross-section.[20] However, in contrast to the Ba/Ca ratio, the carbon contaminant layer should barely affect the Pb/Ca ratio (Equation 31) because the E_k of the Pb 4f and Ca 2p electrons are similar.

The lead plot is linear beyond one monolayer coverage and taking $r_{Pb^{2+}} = 1.2$ Å, the monolayer thickness is 2.4 Å. Compared to the escape depth of $\simeq 20$ Å for Pb 4f electrons[18], d_{Pb} is small. Using the earlier substitutions and taking $I^{\infty}_{Pb}/I^{\infty}_{Ca} \simeq 6$ [3,19,20] one obtains:

$$\frac{I_{Pb}}{I_{Ca}} \simeq 0.3\, d_{Pb} \tag{33}$$

Again, a linear plot is expected. However, in this case the expected intensity ratio is closer to the observed ratio, as suggested above. For example, 4×10^{-8} gm/cm² of Pb corresponds to ~ 0.1 monolayers and d_{Pb} is therefore ~ 0.24 Å. The expected area ratio is $(0.3)\cdot(.24) = 0.072$ compared to the observed ratio of 0.10 (2/50 x 2.5).

Considering the many assumptions and the very large possible errors in the escape depths, atom densities, etc. these calculations strongly suggest that our calibration plots are meaningful and that significant islanding is not occurring at the sub-monolayer level. (For example, some of the recently calculated electron escape depths in a recent paper[24] differ from my values by ~ 50%). Penn[24] also mentions that his values for insulators have about a 40% error. The relative slopes of the barium and lead calibration plots, or the carbon attenuation argument, are not affected qualitatively even if the carbon escape depth is ~50 Å (Figure 10). This in no way invalidates the usefulness of this quantitative analysis technique as long as Ba/Ca ratios are compared on calibrant and unknown barium-calcite surfaces.

3.3.2 Mercury Analysis on Iron Sulphide

The results of a mercury chloride calibration study are given in Table 4, Fig. 11. Representative XPS spectra of Hg 4f and Cl 2p are given in Fig. 12. Typical XPS spectra parameters are as follows, Hg 4f: 50 scans, 111 points, 1 sec. dwell time; Cl 2p: 20 scans, 111 points, 1 sec. dwell time.

Reasonable spectra of Fe 2p and S 2p levels were obtained in 20 minutes (10 scans). In addition, O 1s and C 1s levels were obtained in 4 minutes (2 scans). All peaks had linewidths of about 2.0 eV, and the binding energies (±0.2 eV) uncorrected taking Au $4f_{7/2}$ = 84.0 eV) are

Hg $4f_{7/2}$ = 100.8 ; Hg $4f_{5/2}$ = 104.8 ; Cl $2p_{3/2}$ = 198.2 ;
Cl $2p_{1/2}$ = 200.2 ; S $2p_{3/2}$ = 161.3 ; S $2p_{1/2}$ = 162.6 ;
Fe $2p_{3/2}$ = 710.1 ; Fe $2p_{1/2}$ = 712.2 ; C $1s_{\text{(contamination)}}$ = 284.7 ;
O $1s_{\text{(oxide)}}$ = 529.8 ; O $1s_{\text{(contamination)}}$ = 531.9 , 533.2 .

As in the preceeding barium study, the detection level of mercury on iron sulphide (FeS) polished plates was approximately 10^{-9} gms. The detection of Cl^- anions was not as sensitive. The calcite technique of ratioing the metal cation of interest to a substrate atom did not give reproducible results when attempted for mercury on iron sulphide.

Table 4. $HgCl_2$ Calibration Data

(a) Wt. Mercury (gms) (± 5%)	FeS plate Surface Area (mm^2) ± 5.0 mm^2	Wt. Mercury* within 63 mm^2 mask (gms) ± 5%	Area Intensity Ratio** Hg 4f (x 10^4)	
			1 Initial	2 120 days†
2×10^{-8}	117.5	1.07×10^{-8}	0.46	0.3
20×10^{-8}	122.2	10.3×10^{-8}	1.25	---
20×10^{-8}	144.3	8.7×10^{-8}	2.35	1.7
100×10^{-8}	150.7	41.8×10^{-8}	4.3	3.1
100×10^{-8}	74.9	84.0×10^{-8}	11.3	6.0
200×10^{-8}	77.7	162.1×10^{-8}	9.2	---
200×10^{-8}	138.3	91.1×10^{-8}	11.2	7.85
600×10^{-8}	124.6	303.0×10^{-8}	13.1	---
2000×10^{-8}	124.7	1010.0×10^{-8}	19.3	12.8
blank	112.5	~NIL	0.17††	---

(b) Wt. Chlorine (gms) (± 5%)	FeS plate Surface Area (mm^2) ± 5.0 mm^2	Wt. Chlorine* within 63 mm^2 mask (gms) ± 5%	Area Intensity Ratio** Cl 2p (x 10^4)	
			1 Initial	2 120 days†
7.6×10^{-8}	122.2	3.91×10^{-8}	0.32	----
38×10^{-8}	150.7	15.9×10^{-8}	0.63	0.47
38×10^{-8}	74.9	32.0×10^{-8}	0.70	0.52
76×10^{-8}	77.7	61.6×10^{-8}	1.35	0.69
76×10^{-8}	138.3	34.6×10^{-8}	1.03	0.63
228×10^{-8}	124.6	115.0×10^{-8}	1.87	----
760×10^{-8}	124.7	384.0×10^{-8}	3.42	2.06

* assuming mercury cations and chlorine anions are evenly distributed over the surface.

** errors in Hg 4f and Cl 2p peak area intensities are in the range 10-20%. This area intensity is for 50 scans Hg 4f and 40 scans Cl 2p.

† FeS calibrant plates re-analysed 4 months later.

†† This intensity value is due to silicon (Si 2p peak, E_b ~102.9 eV)

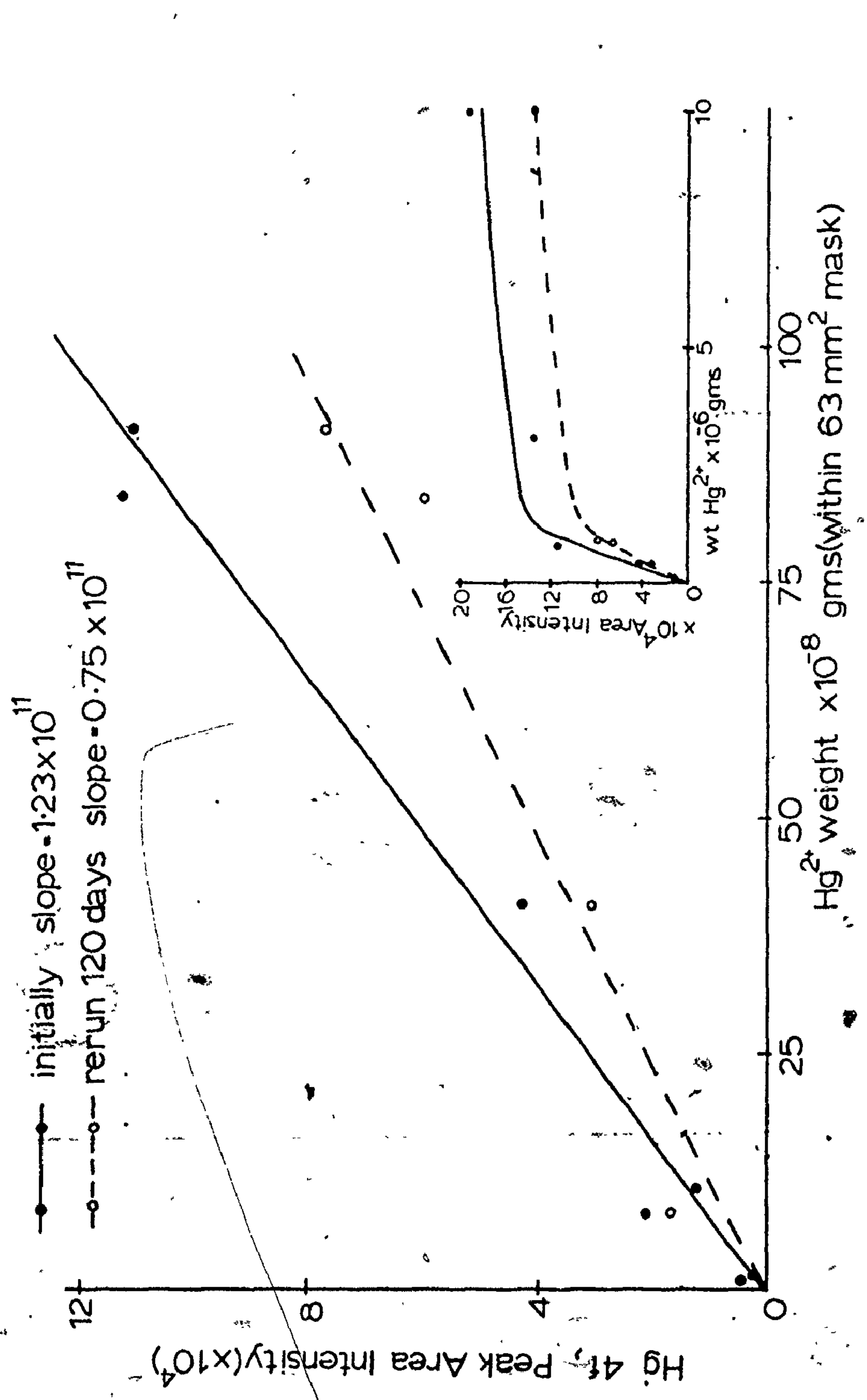

Figure 11. Mercury ESCA Calibration Plot and Effects of Time on Reproducibility.

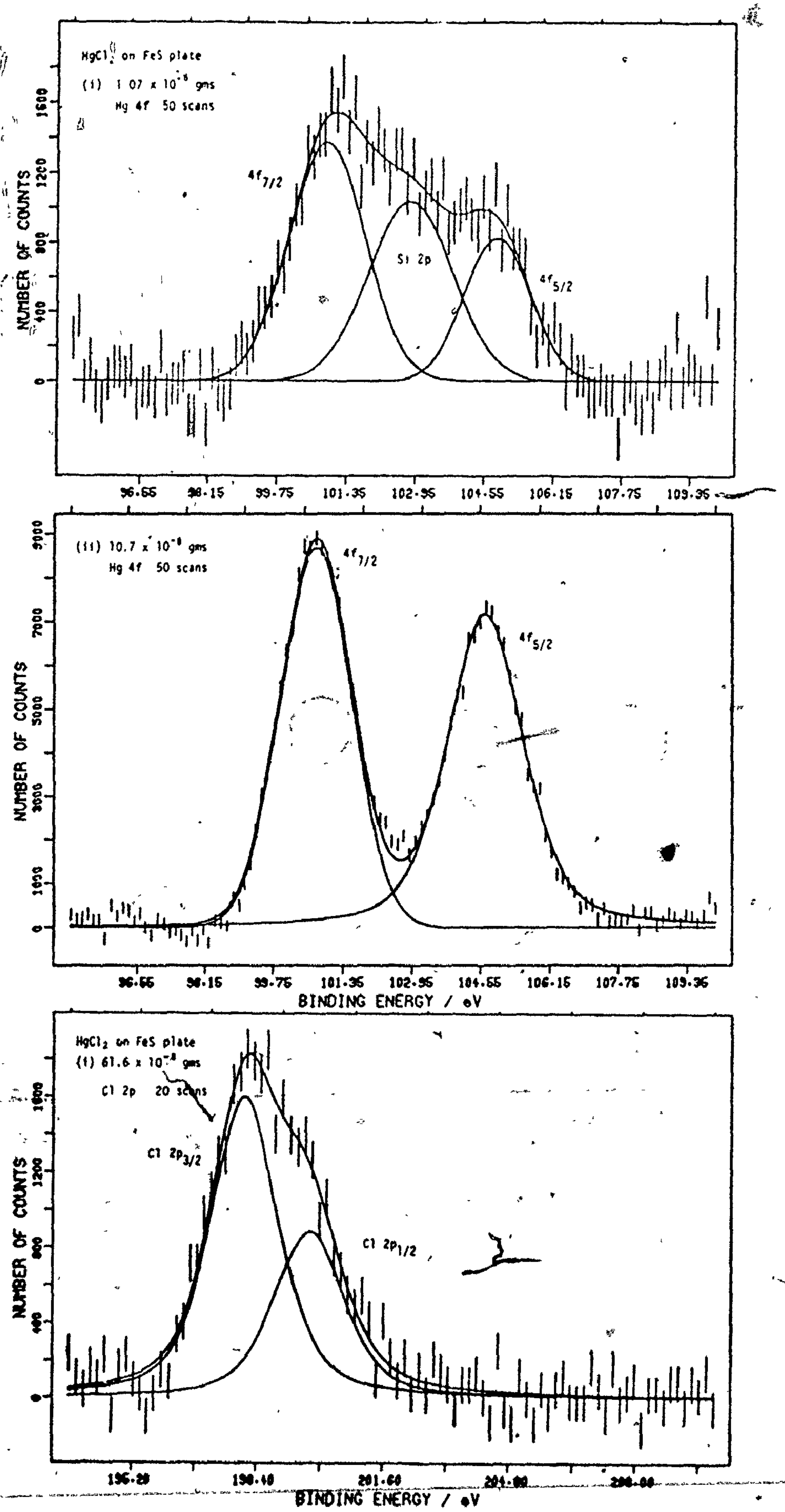

Figure 12. Representative Hg 4f and Cl 2p ESCA Spectra.

The poor agreement stems from a surface lattice viewpoint. Cleaved single crystals of calcite have a stoichiometric surface lattice. Therefore reproducible barium/calcium ratios were possible because the lattice calcium ions are uniformly spaced on the surface. However, the iron sulphide mineral pyrrhotite (FeS) has a non-stoichiometric surface, and thus no substrate atom is useful for a rationing technique. In addition, the sliced and polished sulphide ore surface contained a vast number of small crystals each in a different lattice orientation. Therefore, area intensity values of mercury 4f peaks alone were plotted versus the weight of mercury microsyringed onto the calibrant surfaces. These mercury XPS plots were taken to much larger weights than for the barium-calcite study because it was found, Chapter 5.3, that adsorption of mercury on iron sulphide was very high. The linear region of the mercury plot is approximately the same as the earlier barium and lead study on calcite. However, the flattening of the curve at weights $\gtrsim 1.5 \times 10^{-6}$ gm mercury caused a very difficult problem. Reasons for this flattening of the calibration plot are:

(1) evaporation of a very thick mercury layer when preparing the calibration samples, (i.e. mercury thickness (d) becomes larger than the Hg 4f electron escape depth which is $\simeq 7$ Å).

(2) Islanding of the mercury atoms on the surface during drying (evaporation).

(3) Some loss of the evaporated $HgCl_2$ layer from the surface due to the E.S.C.A. ultra-high vacuum (10^{-8} torr). Note $HgCl_2$ could be volatile under such low pressure due to its low vapour pressure.[28]

The reproducibility of mercury calibrant plots was examined in Table 4, Figure 13 for samples analyzed, then stored for long time

Table 5

Fresh $HgCl_2$ Calibration Data

(a) Wt. Mercury (gms) (± 5%)	FeS plate Surface Area (mm^2) ± 5.0 mm^2	Wt. Mercury* within mask (gms) ± 5%	Peak Area Intensity** Hg 4f ($x 10^4$)
20×10^{-8}	117.5	10.7×10^{-8}	3.06
100×10^{-8}	122.2	51.0×10^{-8}	7.6
100×10^{-8}	144.3	43.6×10^{-8}	7.1
200×10^{-8}	138.3	91.0×10^{-8}	9.6
200×10^{-8}	122.2	103.0×10^{-8}	11.2
2000×10^{-8}	144.3	873.0×10^{-8}	8.7
2000×10^{-8}	74.9	1621.0×10^{-8}	16.7

(b) Wt. Chlorine (gms) (± 5%)	FeS plate Surface Area (mm^2) ± 5.0 mm^2	Wt. Chlorine* within mask (gms) ± 5%	Peak Area Intensity** Cl 2p ($x 10^4$)
38×10^{-8}	122.2	19.6×10^{-8}	0.92
38×10^{-8}	144.3	16.7×10^{-8}	1.03
76×10^{-8}	150.7	31.8×10^{-8}	1.30
76×10^{-8}	138.3	34.6×10^{-8}	1.10
760×10^{-8}	74.9	639.0×10^{-8}	3.84

* as per Table 4.

** as per Table 4.

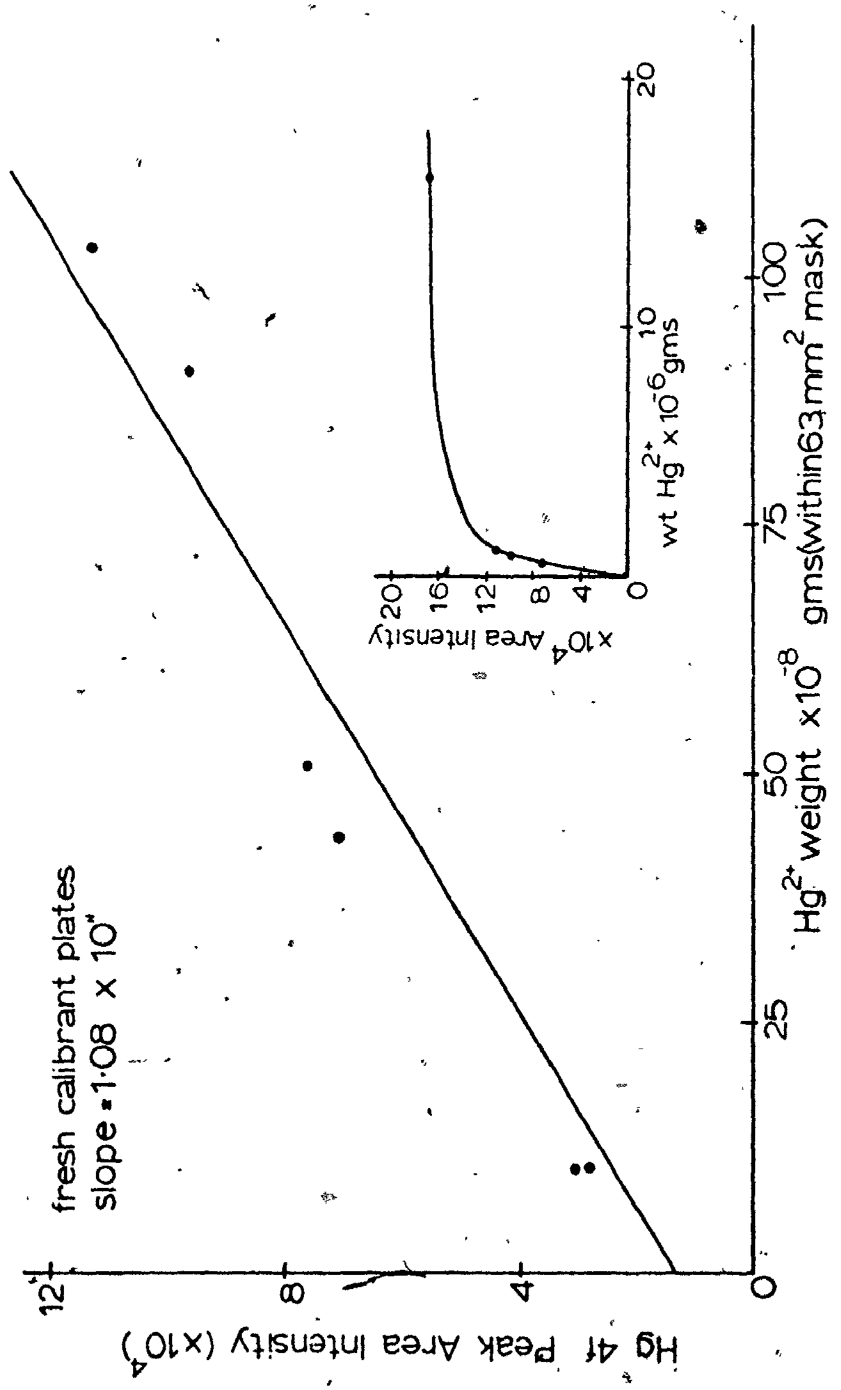

Figure 13. Mercury ESCA Calibration Plot (Data of Table 5).

periods in a vacuum dessicator. The slope of these plots was not as reproducible as for the barium-calcite study. To check the reproducibility of the XPS spectrometer for mercury analysis, fresh calibrant samples were also prepared, Table 5. The slope of this plot agreed very well with the original sample analysis before storage. Carbon contamination was monitored and not found to increase significantly enough to account for this slope variation. This result indicated that a small amount of $HgCl_2$ is lost during vacuum storage. Thus mercury loss from the sulphide surface in the 10^{-8} torr. vacuum XPS chamber is also highly likely to some degree, (i.e. when the evaporated $HgCl_2$ layer is thicker than a monolayer (~3 Å)).

This led to problems when equating the calibrant surfaces to heavily adsorbed mercury - FeS surfaces. The adsorbed surfaces contain mercury strongly bonded to sulphide sites, but with very little or nil Cl^- anion adsorption. Thus little or no Hg loss can be due to the volatility of the $HgCl_2$ salt. Therefore far greater mercury weights can be observed on the adsorbed samples than can be determined using the calibrant method. In many cases, the actual sorbed mercury intensities (Chapter 5.3) are well beyond any calibrant sample. However, a qualitative estimate of mercury sorption is still possible.

Calibrant and Hg reacted (sorbed) FeS surfaces were analysed together, to reduce possible errors caused by instrument variation or surface hydrocarbon contamination.

In addition to estimating adsorbed weights of mercury from solution onto FeS plates, an estimate of the mercury escape depth (λ) was calculated from the calibration plots. Taking the mercuric atom radius as 1.5 Å, the thickness of one monolayer is found to be ~ 3 Å.

Using

$$I_{Hg} = I_{Hg}^{\infty}(1 - e^{-d_{Hg}/\lambda \sin\theta}) \qquad (34)$$

where,

d_{Hg} = thickness of mercury atoms (Å)
λ = the mercury escape depth (Å)
$\sin\theta$ = 0.7071 for the McPherson 36 sample holder ($\theta = 45°$)
I = observed peak area Intensity
I^{∞} = peak area Intensity (i.e. for infinitely thick layer when $d_{Hg} >>> \lambda$)

a theoretical plot of I/I^{∞} versus d_{Hg}, for increasing escape depths (λ) is thus obtained (Fig. 14, Equation 34).

The two major assumptions in this calculation are:

(1) equating the weight of mercury analysed to a mercury thickness (d), (i.e. one monolayer of mercury (3 Å thick) over a 63 mm^2 surface, weighs ≈ 40 x 10^{-8} gms) and

(2) assuming the flattening of the calibration plot was mainly due to the mercury layer thickness (d) being greater than the escape depth of mercury 4f electrons (i.e. approaching I^{∞}).

Re-plotting the mercury calibration data of Figs. 11, 13, using Equation 34, and then comparing the result to the theoretical calculation plot (Fig. 14), it was found that the best fit corresponded to an escape depth (λ) of 6 Å for mercury 4f electrons. Published escape depths found using other techniques indicate values between 7 → 12 Å.[29] The agreement with published values is quite good, considering the

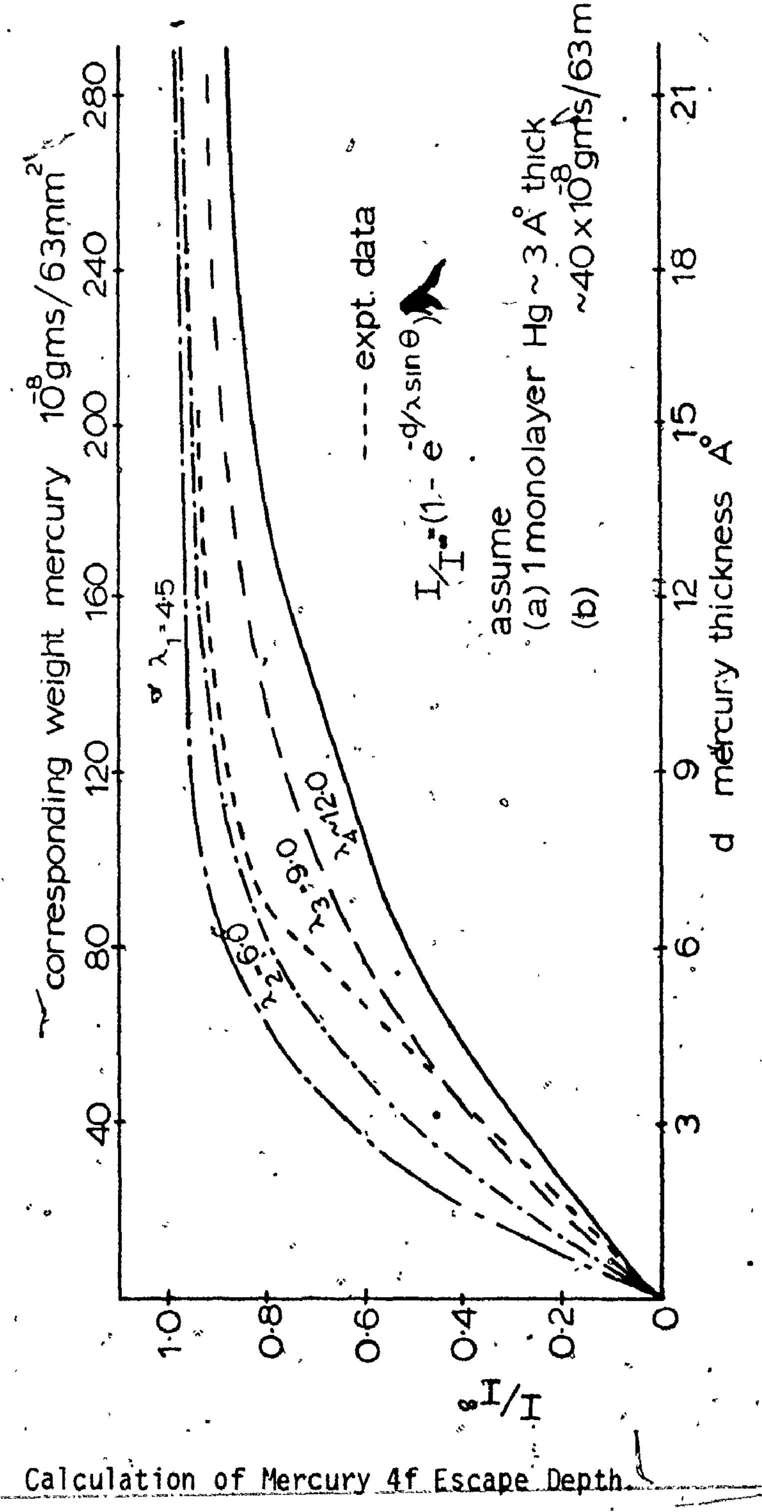

Figure 14. Calculation of Mercury 4f Escape Depth.

assumptions and difficulties previously mentioned.*

Additional support for this technique came from a calculation of the chlorine 2p atomic level escape depth using a chlorine calibration plot (Fig. 15). A monolayer coverage ($\simeq 2$ Å) corresponds to a weight of $\simeq 10^{-7}$ gms/63 mm^2 of surface. The result of this study Fig. 16, using Equation(34) and the calibration plot, Fig. 15, indicated a chlorine 2p escape depth of ≈ 25 Å.

An escape depth of ~ 30 Å is determined from a simple $\lambda \propto E_k^{1/2}$ calculation and other published results.[24]

The experimental errors in these escape depth determinations are large ($\approx 25\%$). However, the qualitative agreement with other determinations lend support to the use of the XPS calibration technique for quantitative trace metal analysis.

3.3.3 Barium, Lanthanum, and Nickel Analysis on MnO_2

The procedure and the results of this calibration study are discussed elsewhere.[15] However, it seems appropriate to include the three calibration plots here to indicate the applicability of this technique. The peak area intensity (50 scans) is related to only that weight of metal actually scanned on the MnO_2 surface (i.e. 63 mm^2); this was not done in the other study.[15] The plots are linear to large weights of metal indicating that even on a roughened surface, (i.e. a

---

*An attempt to determine barium and lead escape depths on the calcite surface using the previous method (Equation 34) met with only limited success. Calibration plots (Figures 9, 10) were extended to cover larger surface weights of lead and barium. This was done so that an estimate of I^∞ for barium and lead ions on the calcite surface could be found. The results indicated that the escape depths were ≈ 12 Å for Ba and ≈ 15 Å for lead. However, the errors in these values were quite large ($\approx 50\%$) and therefore no definite difference in λ could be shown from this study.

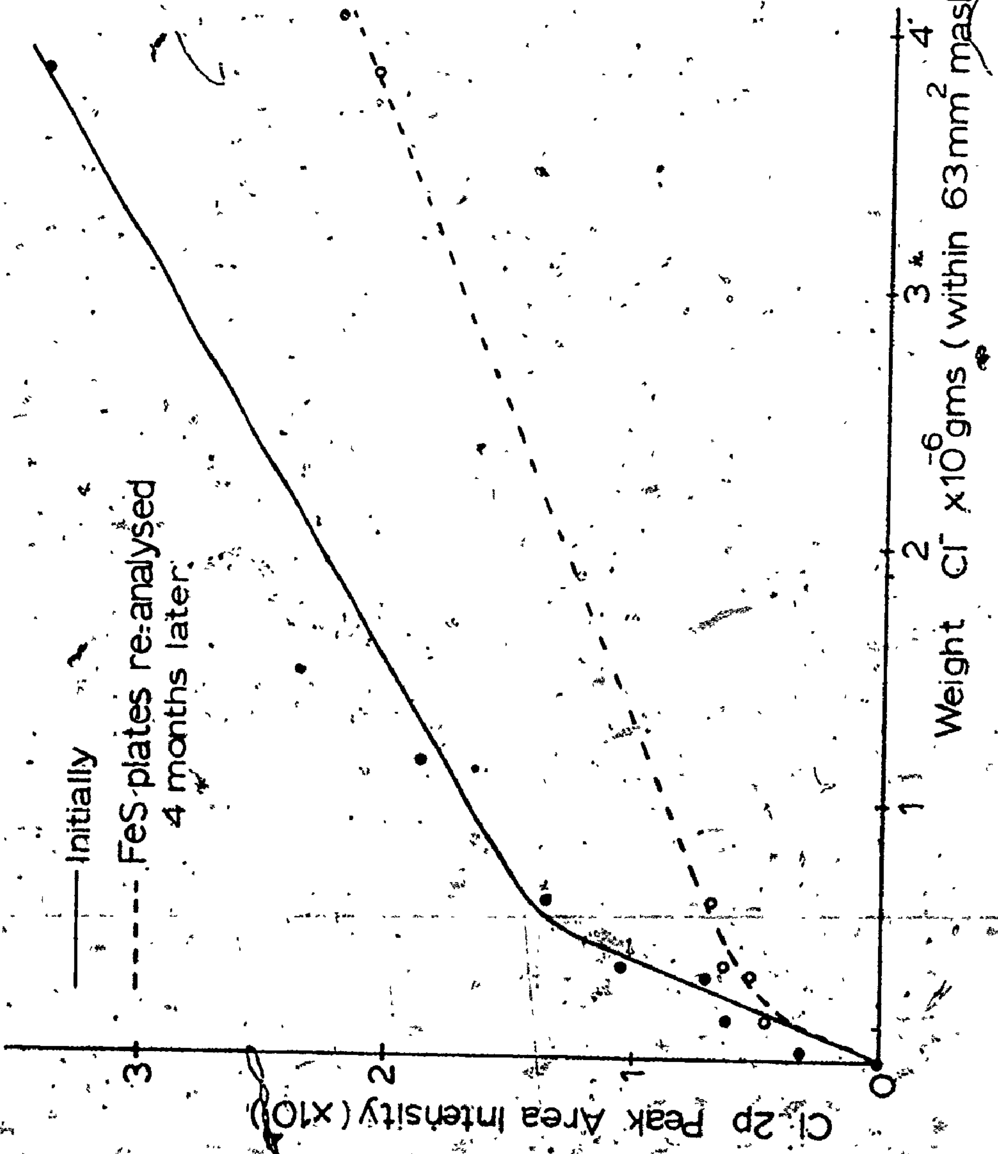

Figure 15a. Chlorine ESCA Calibration Plot. Effects of Storage Time on Peak Intensities.

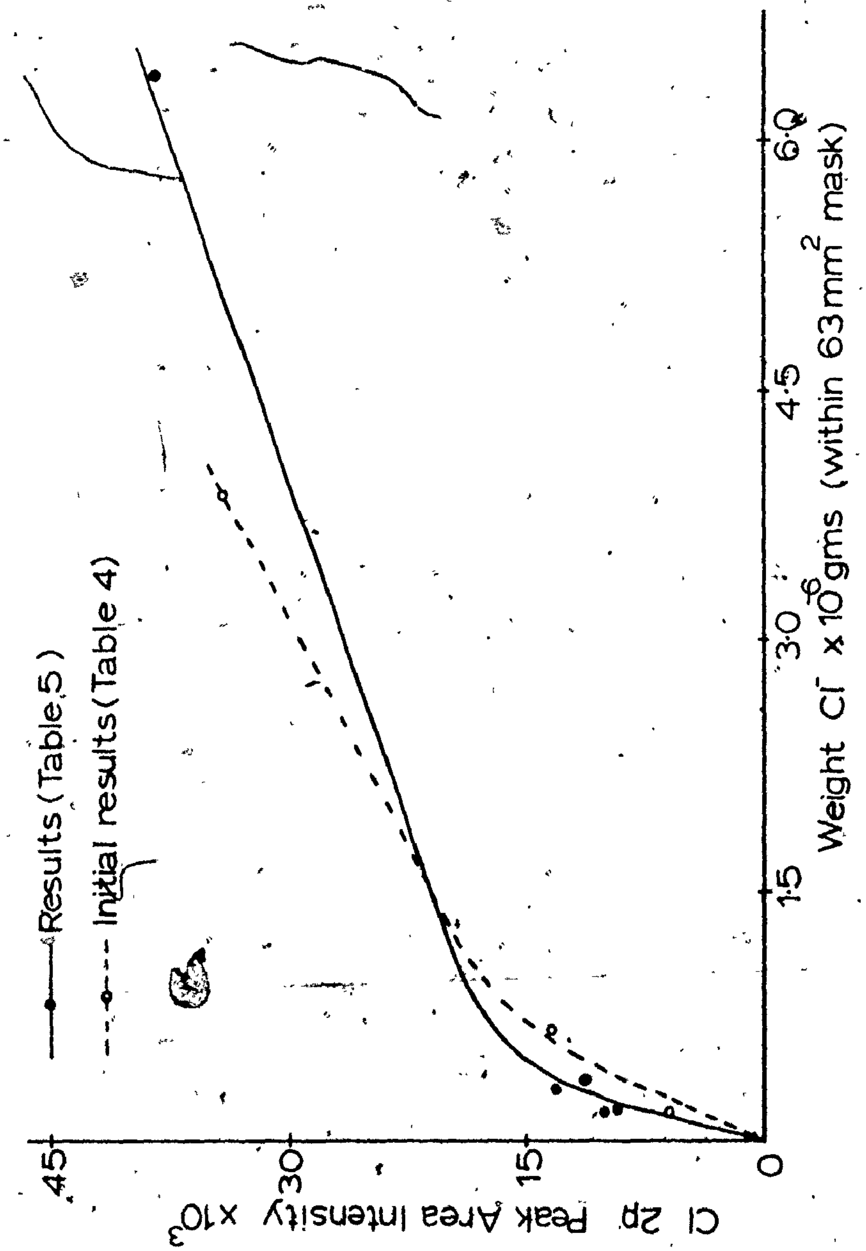

Figure 15b. Chlorine ESCA Calibration Plot, Reproducibility.

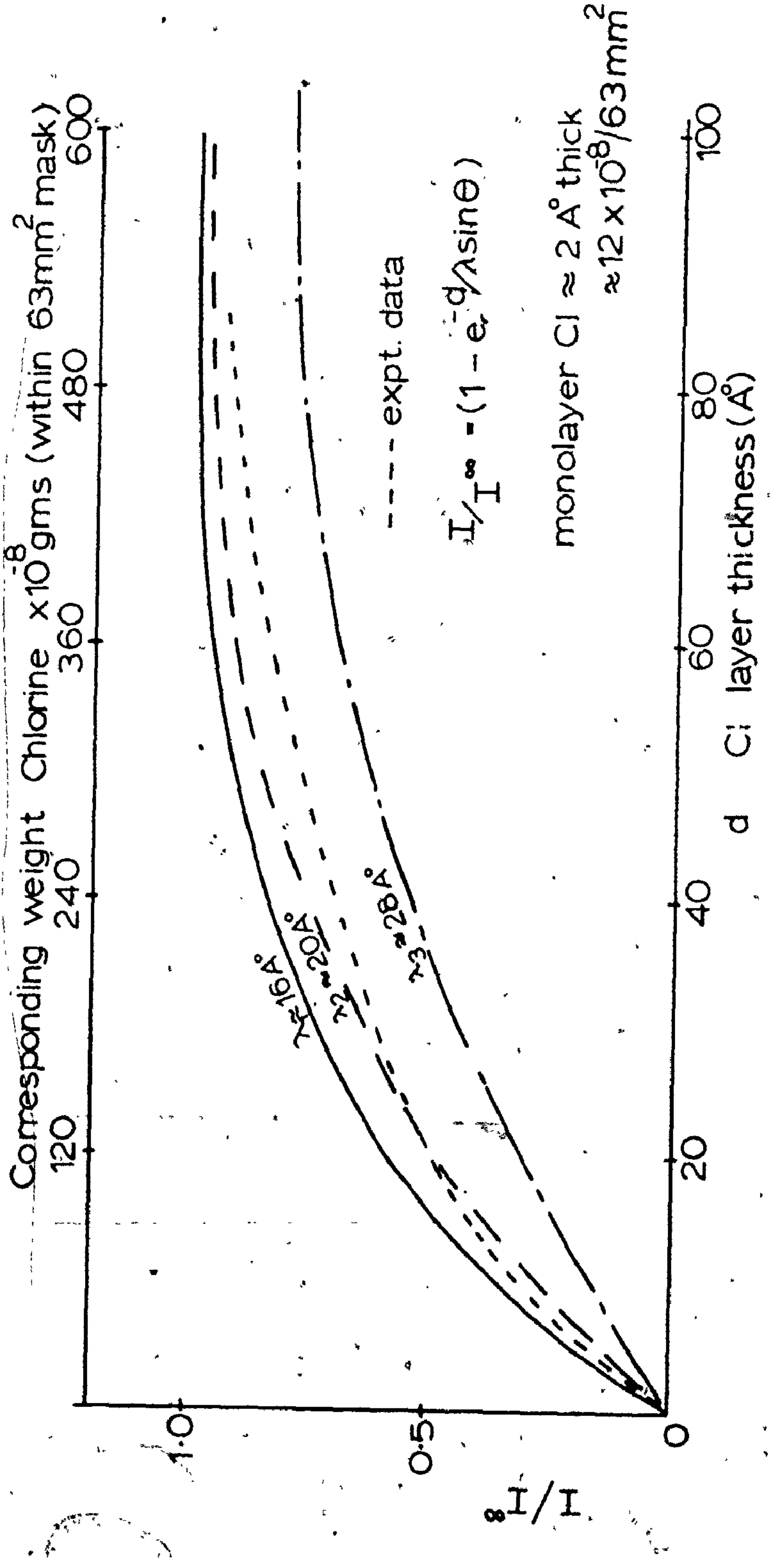

Figure 16. Calculation of Chlorine 2p Escape Depth.

layer of precipitated MnO_2 on Al plates), qualitative results can be obtained (Fig.17,18). These calibration plots were then utilized to determine adsorbed weights of metal on MnO_2 (Appendix A.3).

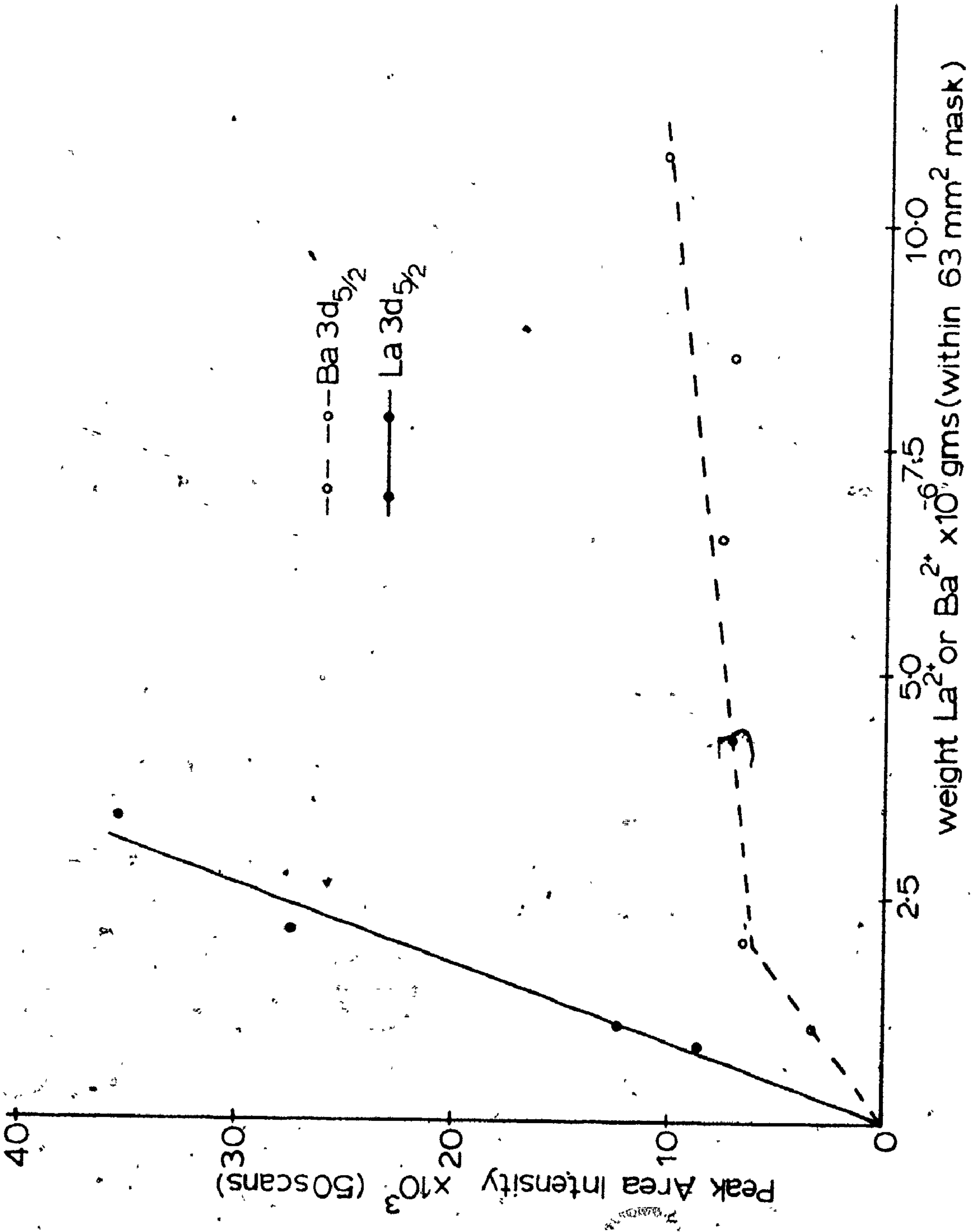

Figure 17. ESCA Calibration Plot for Ba^{2+} and La^{2+} on MnO$_2$.

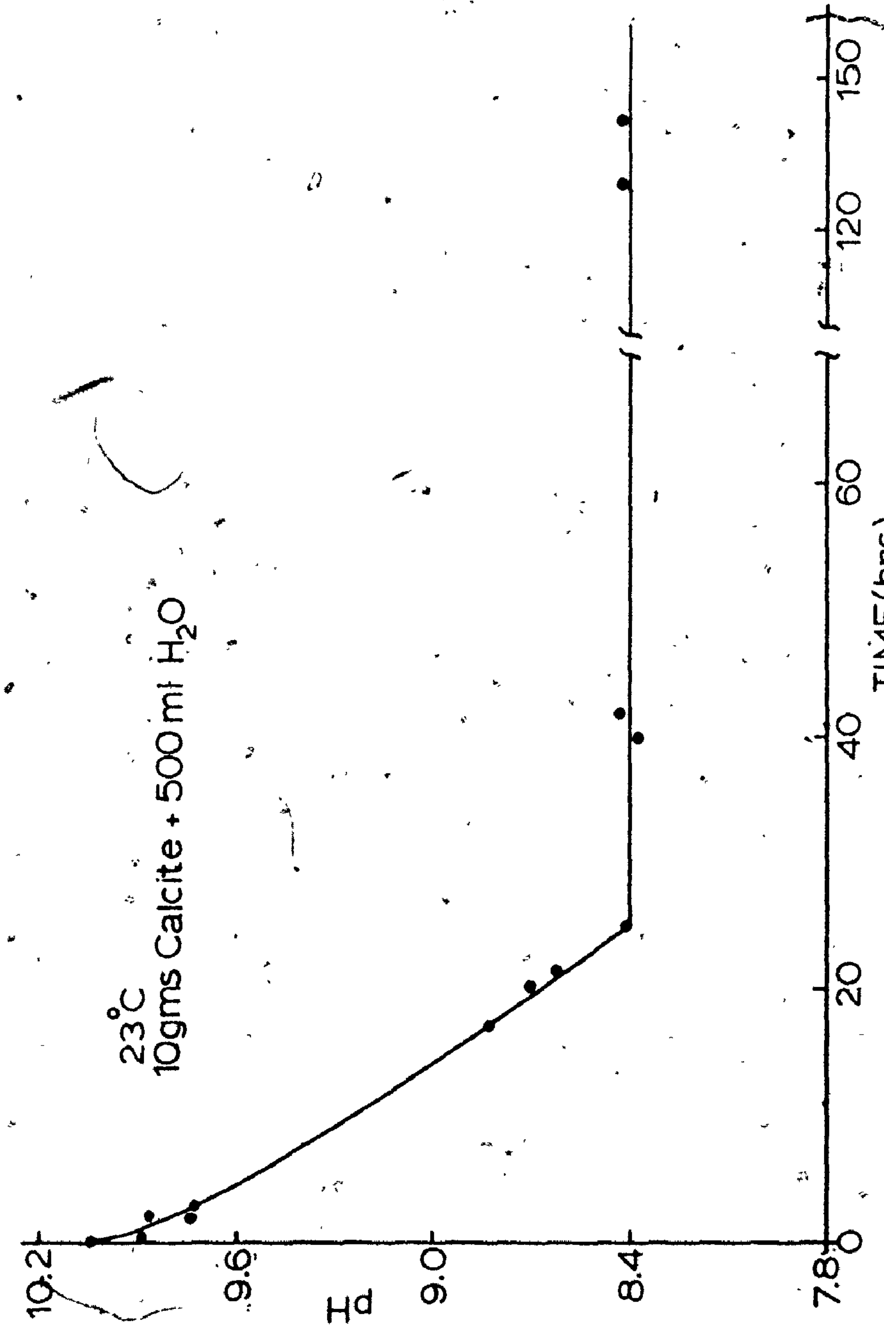

Figure 19. Equilibrium of Powdered Calcite in Water, pH vs. Time.

3.4 References

1. K. Siegbahn, J. Electron Spectrosc., 5, 58, (1974).
2. G.M. Bancroft, J.R. Brown, and W.S. Fyfe, Chem. Geol., 19(2), 131, (1977).
3. W.J. Carter, G.K. Schweitzer, and T.A. Carlson, J. Electron Spectrosc., 5, 827, (1974).
4. M. Czuha and W.M. Riggs, Anal. Chem., 47, 1836, (1975).
5. D.M. Hercules, L.E. Cox, S. Onisick, G.D. Nichols, and J.C. Carver, Anal. Chem., 45, 1973, (1973).
6. P.E. Larson, Anal. Chem., 44, 1678, (1972).
7. P.R. Norton, J. Catal., 36, 211, (1975).
8. W.E. Swartz and D.M. Hercules, Anal. Chem., 43, 1774, (1971).
9. R.S. Swingle, Anal. Chem., 47, 21, (1975).
10. D.M. Wyatt, J.C. Carver, and D.M. Hercules, Anal. Chem., 47, 1297, (1975).
11. M.E. Counts, J.S.G. Jen and J.P. Wightman, J. Phys. Chem., 77, 1924, (1973).
12. G.M. Bancroft and I. Adams, Nature, 250, 219, (1974).
13. R.W. Phillips, J. Colloid Interface Sci., 47, 687, (1974).
14. G.M. Bancroft, J.R. Brown and W.S. Fyfe, Anal. Chem. 49, 1044, (1977).
15. D. Brûlé, M.Sc. Thesis, Univ. Western Ontario, (1977).
16. C.R. Brundle and M.W. Roberts, Chem. Phys. Lett., 18, 380, (1973).
17. M. Klasson, A. Berndtsson, J. Hedman, R. Nilsson, R. Nyholm, and C. Nordling, J. Electron Spectrosc., 3, 427, (1974).
18. I. Lindau and W.E. Spicer, J. Electron Spectrosc., 3, 409, (1974).
19. C.D. Wagner, Anal. Chem., 44, 1050, (1972).
20. J.H. Scofield, J. Electron Spectrosc., 8, 129, (1976).

21. C.D. Wagner, Anal. Chem., 49, 1282, (1977).

22. J.M. Adams, S. Evans, P.I. Reid, J.M. Thomas and M.J. Walters, Anal. Chem. 49, 2001, (1977).

23. R.B. Shalvoy and P.J. Rencroft, J. Electron Spectrosc., 12, 351, (1977).

24. D.R. Penn, J. Electron Spectrosc. 9, 29, (1976).

25. J.R. Brown (unpublished).

26. N.S. McIntyre (personal communication).

27. R.G. Steinhardt, J. Hudis and M.L. Perlman, Phys. Rev., B, 5, 1016, (1972).

28. G.M. Bancroft (personal communication).

29. T.A. Carlson, "Auger and Photoelectron Spectroscopy", Plenum Press (1975).

CHAPTER 4

BARIUM SORPTION ON CALCITE

4.1 Introduction

The more common sedimentary minerals such as the oxides, clays and carbonates are the major adsorbent materials available for geochemical and physical processes in the natural environment. Both the clays and oxides have received intensive study with regard to their sorption abilities of heavy metals and organic micelles from marine, fresh and polluted water. However, the abundance and geological importance of calcite (limestones) as well as its economic value, i.e. for production of building materials, buffering of the oceans, balancing atmospheric CO_2 content, etc. indicated the need for a detailed investigation of its adsorption ability. It is common knowledge that limestone and coral formations improve the taste, colour and odor of water by slow natural filtration processes. A literature survey, indicated both organic$^{1-7}$ and inorganic$^{8-16}$ micelles and ions sorbed from solution by calcite surfaces have been studied (Chapter 1).

The organic sorption studies indicated conclusively that adsorption occurred on the calcite surface and the resulting organic veneer inhibited equilibrium between the solution and the surface. Adsorption of amino acids on aragonite for example, (the high pressure polymorph of calcite) influences its kinetics of recrystallization to calcite.^{7} The adsorption of inorganic species by calcite was originally studied by soil chemists to determine effects of heavy metal uptake by plants from soil types with varying calcite content.[8-10] Mann[11] and Mureta[12] investigated exchangeable manganese in soils and in sediments respectively. Boischot et al.[13] studied calcium, iron and manganese exchange in calcareous soil. Spitsyn's[14] work included strontium 90 sorption on calcareous soils and on calcite crystals. However, no sorption studies of barium ions from dilute barium solution on calcite surfaces was found in the past literature.

Much information is available concerning solid state calcite and calcite surface reactions, using several techniques.[15-20] Thomas[20c] states a correlation between chemical reactivity and crystalline imperfections (point defects, dislocations, substitutions) was noted early in the history of chemistry. He studied these probably enhanced sites of reaction (i.e. adsorption) in detail on calcite. The cleaved calcite surface {100} face was found to contain ~10^3 dislocations /cm^2.[20a] These line defects unlike point defects are thermodynamically unstable. They enhance reactivity (dissolution, adsorption, etc.) because of their extra strain energy and the abnormal stereochemistry in their vicinity. Barium sorption reactions that occurred rapidly on powdered calcite due to its large surface area, (~ .5 m^2/gm, vide infra) and huge dislocation density (> 10^3 defects /cm^2) could be examined as both a time and initial barium concentration dependant reaction by using cleaved single calcite crystals and the XPS surface technique. Highly pure powdered calcite, crushed limestone from a nearby cement quarry and Iceland Spar variety calcite single crystals were studied by atomic absorption and x-ray photoelectron spectroscopy to determine the minerals' ability to remove barium ions from solution. This study was useful in determining if calcite had practical applications to treat waste water or polluted natural waters contaminated in elements such as barium, strontium, etc. In addition, geochemical information could be obtained with respect to the effects of limestone deposits on ore bodies or reactions of these trace elements in the natural environment, etc.

4.2 Powdered Calcite - AAS Study

4.2.1 Experimental

4.2.1.1 Powdered Calcite

The inorganic spec-pure grade calcium carbonate powder was purchased from ROC/RIC (batch CA-32; 99.99%). The surface area of this powder was estimated to be approximately 0.5 m^2/gm. from scanning electron microscope photographs (Appendix A.4.4). Powder x-ray diffraction results confirmed the calcium carbonate polymorph as calcite and analysis by atomic absorption spectrophotometry revealed no trace impurities, such as barium. All experiments were monitored for pH using a Corning 110 digital pH meter and Orion glass electrodes, coupled to a strip chart recorder. All reaction solutions were kept in polypropylene containers at room temperature. Selected weights of powdered calcite (1 to 30 gms) in 500 ml deionized-distilled water were allowed to equilibrate using constant stirring (teflon coated stirring bars and Fisher Flexa-Mix Stirrers). The pH of each solution stabilized at the theoretical value of ~ 8.40 ± .05 after 24 hours (Fig. 19). Theoretical solubility calculations for the systems $CaCO_3 - H_2O - CO_2$ and $CaCO_3 - H_2O - CO_2 - BaCO_3$ are given in Appendix A.4.1, A.4.2. At equilibrium, a 25 ml aliquot of solution was filtered using Whitman #42 filter paper to remove colloidal calcite. This initial solution, analysed for barium and calcium ions, served as a blank, and as a check on the solubility of the calcite in each beaker. The pH was useful as

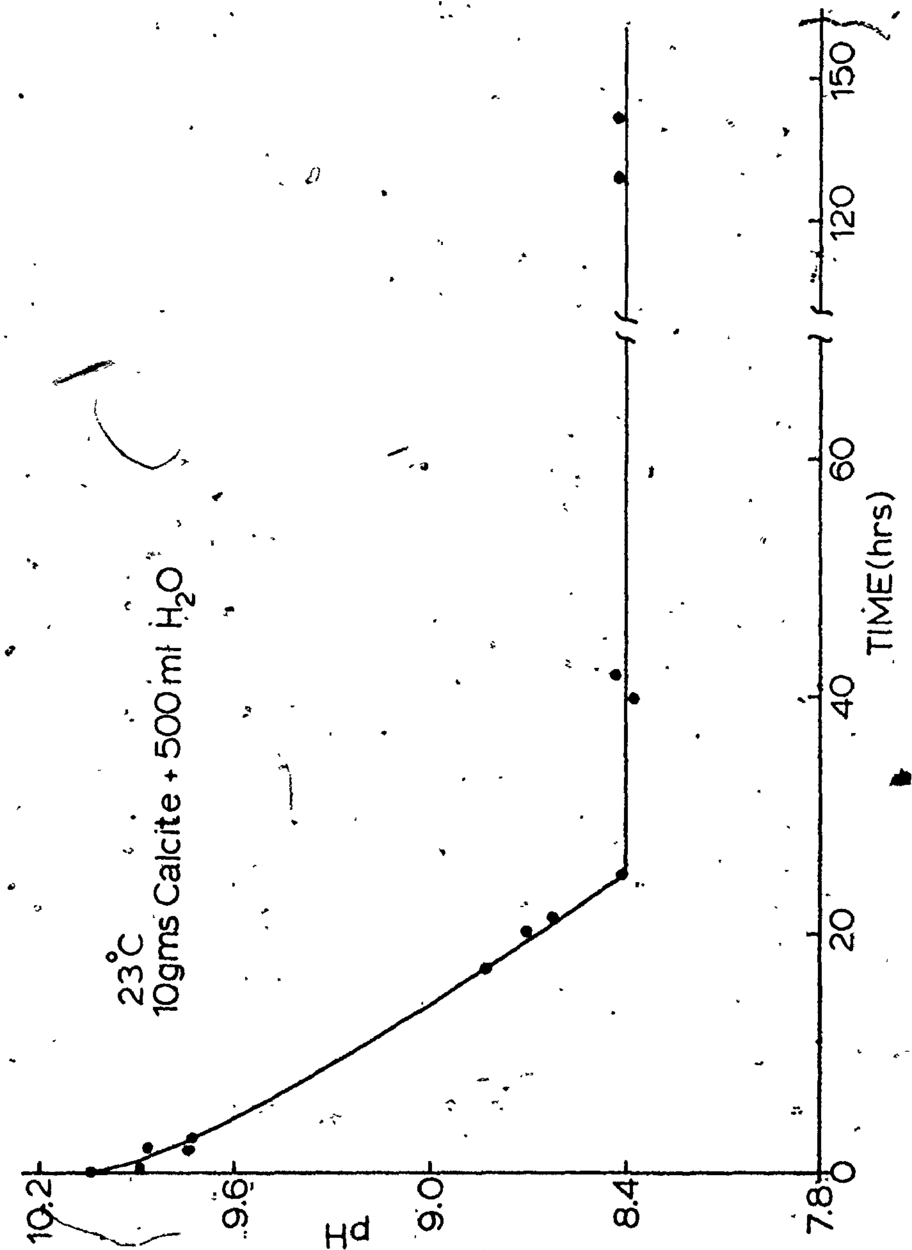

Figure 19. Equilibrium of Powdered Calcite in Water, pH vs. Time.

verification of the accuracy of the calcium concentrations. To produce the necessary barium concentrations, 25 ml of various dilutions of the stock barium solution (10^4 ppm Ba^{2+} as $Ba(ClO_4)_2$) were added to each beaker to obtain initial barium concentrations in the range 25 to 200 ppm, i.e. 1.82×10^{-4} M to 1.46×10^{-3} M. The following example (10 gms calcite powder in 200 ppm barium solution) is given in some detail to illustrate the procedure. 25 ml of a 4000 ppm barium stock solution was added to a 475 ml equilibrium calcite solution. At selected times, 10 ml of this reaction solution was removed by pipette and filtered. The loss of barium from this 10 ml aliquot by the filter paper was checked by dissolving several used filter papers in 1M HCl and analysis by A.A.S. Little or no barium was found in this solution indicating sorption of barium by filter paper is quite small. To prevent A.A.S. chemical interferences, 1 ml of 50,000 ppm lanthanum ($LaCl_2$) was then added to each 10 ml aliquot. All results, i.e. barium concentration values, included this dilution factor of ≈ .0909 (1/11).

The air-acetylene flame combination was used for both calcium and barium analysis[21] (Chapter 2.1). The nitrous oxide-acetylene flame conditions were also examined for barium analysis but rejected because its linear working range was too low for many of the samples examined.[22] Additional dilutions of these samples to fit this reduced linear range would have introduced further errors. The burner head was adjusted to intersect the hollow cathode lamp beam at a 45° angle during calcium analysis to prevent detector saturation. Calibration curves were obtained for both barium and calcium ions using several solutions of $CaCl_2$ and $Ba(ClO_4)_2$ of accurately known concentration. These two solutions were mixed together along with 5000 ppm lanthanum ($LaCl_2$)

2

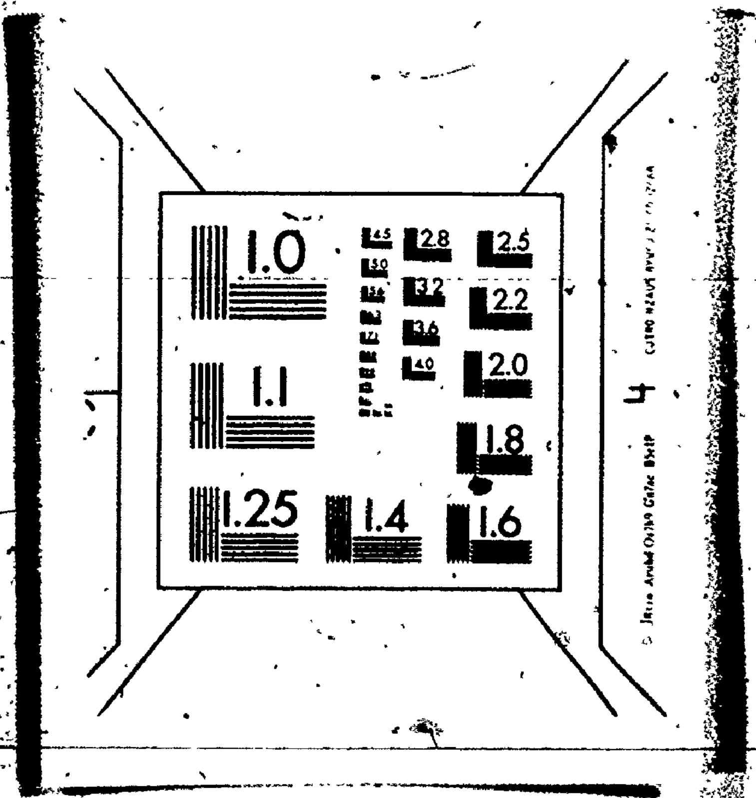

required to prevent matrix and chemical interferences. The barium calibration plot was linear for the entire range studied (0 → 250 ppm), while the calcium curve was slightly non-linear (0 → 100 ppm).

4.2.1.2 "Crushed Limestone"

Two varieties of limestone were collected from the quarry of the St. Mary's Cement Company Ltd., St. Marys, Ontario ; a light coloured limestone from the underlying Detroit River Group and a grey limestone from the overlying Delaware (Dundee) formation.[23,24] Both groups are of Middle Devonian age and are highly pure ($\approx 96\%$ $CaCO_3$). Chemical analysis indicated slightly less magnesium in the underlying Detroit River limestone. The samples from these two groups were washed thoroughly and jaw crushed. The crushed fractions were then sieved, and wet sieved into five size fractions, using a set of Tyler Standard stainless steel mesh sieves. Pyrex glass columns (Fig. 20) were used to study the sorption of barium from solution using 30 gms of these various sieved fractions of both varieties of limestone. Each glass column was fitted with a removable 400 mesh nylon screen to hold the crushed limestone but allow the solution to pass unobstructed. Each limestone sample was placed in the column and eluted with deionized distilled water till the eluted water was colourless, (≈ 250 ml); 100 ml of deionized distilled water (pH $\approx$ 5.5) was then eluted and stored for later analysis.

Next, a 100 ml aliquot of 100 ppm (7.3×10^{-4} M) barium solution (pH $\approx$ 4.8) was eluted and saved. Finally, three, 50 ml portions of deionized distilled water were eluted and stored. All solutions were analysed for calcium and barium, as previously, by A.A.S. In addition, all solution pH measurements and the time required to elute each 100 ml

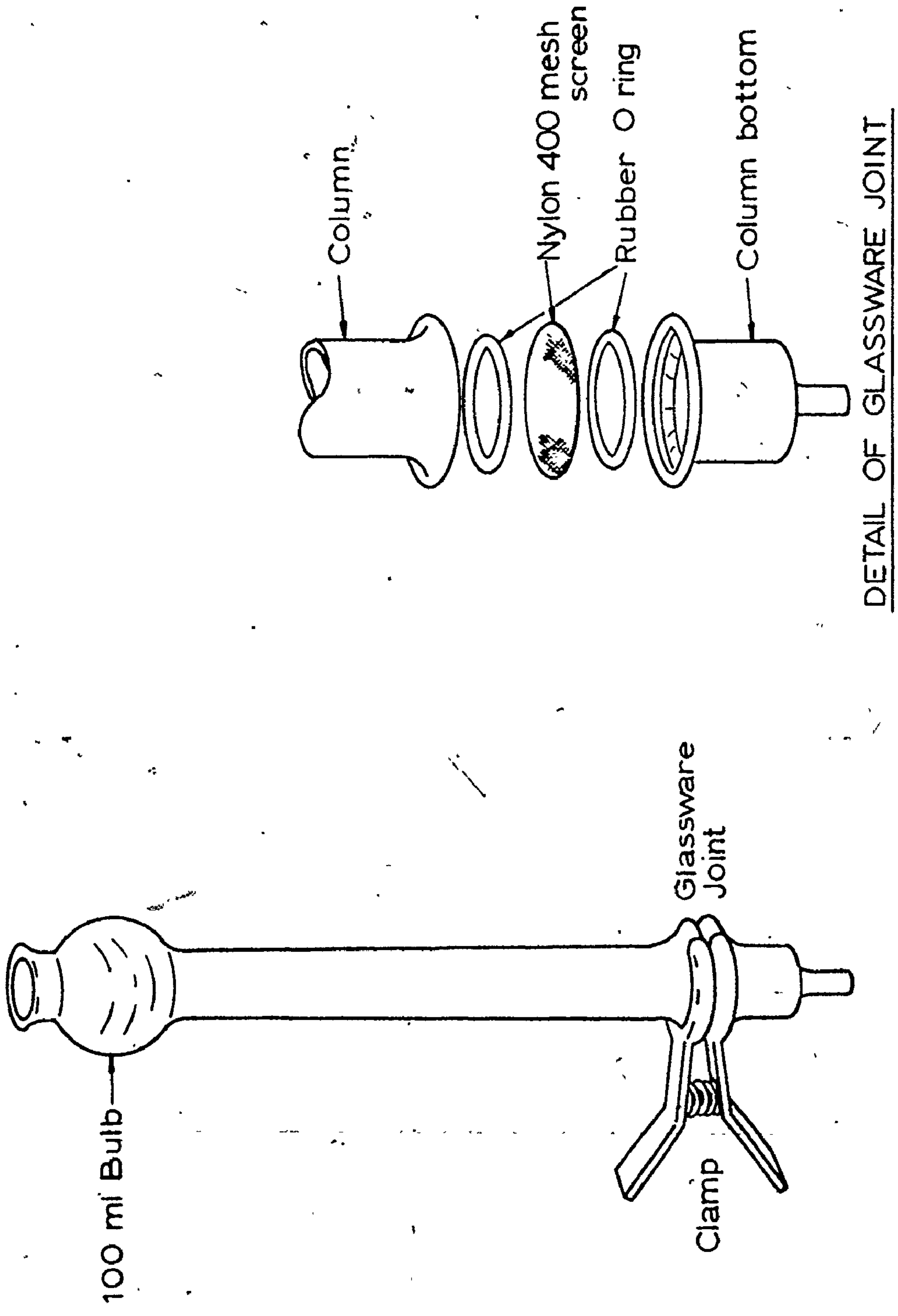

Figure 20. Pyrex Column, Apparatus Used for Ba^{2+} Crushed Limestone Sorption Study.

aliquot of barium solution through each limestone fraction was recorded.

4.2.2 Discussion

4.2.2.1 Powdered Calcite

A summary of the A.A.S. results for barium and calcium concentrations in the powdered calcite experiments is given in Table 6. The barium ion concentration decreased rapidly after its addition to the stirred calcite solution. In most reactions, the majority of barium had been removed after only a few minutes, i.e. the time to ensure mixing. For the 200 ppm solution, the final barium concentration levelled out completely after 30 minutes and did not measurably decrease in the next 24 hours. Table 6 shows immediately that the final concentration of barium is dependent on the initial barium concentration and on the amount of calcite powder in the solution - as expected for a sorption process. It is also apparent from Table 6 that the amount of barium ions sorbed is very closely equal to the amount of calcium entering solution. This result verifies that an exchange process is the major mechanism of barium sorption on calcite powder, i.e.

$$\mathrm{Ba}^{2+}_{\mathrm{sol'n}} + \mathrm{Ca}_{\mathrm{surf.}} \overset{K}{\rightleftharpoons} \mathrm{Ba}_{\mathrm{surf.}} + \mathrm{Ca}^{2+}_{\mathrm{sol'n}} \qquad (35)$$

where

$$K = \frac{[\mathrm{Ba}_{\mathrm{surf.}}][\mathrm{Ca}^{2+}_{\mathrm{sol'n}}]}{[\mathrm{Ba}^{2+}_{\mathrm{sol'n}}][\mathrm{Ca}_{\mathrm{surf.}}]} \qquad (36)$$

More extensive results for this sorption is found in Fig. 21. These curves are characteristic of a sorption process where the decrease in barium in solution at each original concentration is proportional to the weight (surface area) of calcite powder used. Of course, for a simple precipitation process, the barium concentration would be expected

Table 6

Powdered Calcite-Ba^{2+} Adsorption Results

	Wt. Calcite used (gms)	Ba^{2+} in initial 500 ml solution		Ba^{2+} loss from 500 ml Ba^{2+}-calcite solution (reacted 100 minutes)		% Ba^{2+} sorbed	Ca^{2+} increase in 500 ml solution		$C_{equil.}$ (moles Ba^{2+}/ litre at equilibrium)	X (moles Ba^{2+}/ mole $CaCO_3$)
	(±0.01)	ppm (±0.5)	Moles ($x10^{-4}$)	ppm (±0.5)	Moles ($x10^{-4}$)		ppm (±0.5)	Moles ($x10^{-4}$)	$x10^{-4}$	$x10^{-4}$
(a)	10	10	0.364	9	0.33	90	1.0	0.125	0.073	3.28
(b)	5	20	0.728	10	0.37	50	1.0	0.125	0.728	7.20
	10	20	0.728	17	0.62	85	1.5	0.19	0.218	6.50
(c)	5	50	1.82	24	0.88	48	4.0	0.50	1.820	1.80
	10	50	1.82	41	1.5	82	9.0	1.125	0.660	14.76
	20	50	1.82	49	1.79	98	12.0	1.50	0.073	8.20
(d)	10	100	3.64	45	1.64	45	10.0	1.25	4.000	16.40
(e)	5	200	7.28	31	1.13	16	6.0	0.75	12.400	22.00
	10	200	7.28	60	2.18	30	12.0	1.50	10.200	21.80
	20	200	7.28	100	3.64	50	37.0	4.75	7.280	18.00

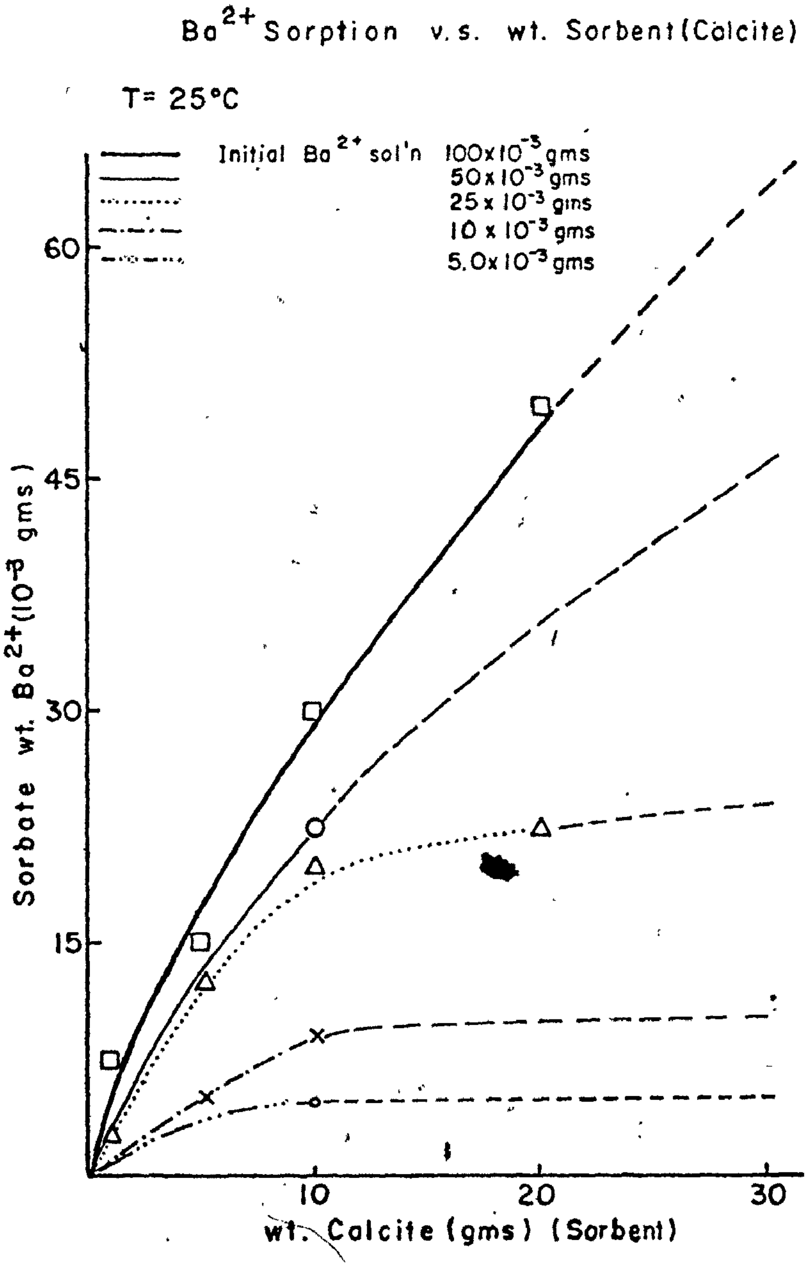

Figure 21. Sorption Plots for Powdered Calcite as a Function of Different Initial Ba^{2+} Concentrations.

to level out at a constant value regardless of the initial concentration of barium in solution. Solubility calculations (Appendix A.4.2) indicate that the equilibrium concentration of calcium and barium should remain in the ratio 0.933 for all cases. (i.e.

$$K_{sp}(CaCO_3) \simeq 10^{-8.32} \; ; \; K_{sp}(BaCO_3) \simeq 10^{-8.80}$$

The data from these calcite adsorption experiments were fitted to the Langmuir equation (Chapter 2.2) in the re-written form for adsorption from solution.[25]

(i.e. $y = ax + b$)

$$\frac{C_{equil.}}{X} = \frac{1}{X_m \cdot b} + \frac{C_{equil.}}{X_m} \qquad (37)$$

where

$C_{equil.}$ = number of moles Ba^{2+}/litre remaining in solution at equilibrium.

X = quantity of Ba^{2+} sorbed, in moles Ba/mole calcite.

X_m = maximum sorption capacity of calcite, moles Ba^{2+}/mole calcite.

b = quantity related to the energy of sorption which is related to the heat of sorption, Q by an equation of the type; $b \propto e^{Q/RT}$ (Gabano et al.).[26]

Plotting $\frac{C_{equil.}}{X}$ versus $C_{equil.}$ (Equation 37), one obtains a straight line of slope $\frac{1}{X_m}$ and y-axis intercept $\frac{1}{X_m \cdot b}$ (Figure 22).

Thus, the calcite maximum sorption capacity for barium at 22°C and a measure of its sorption energy, is determined.

Using these values of X_m and b found from a linear least squares

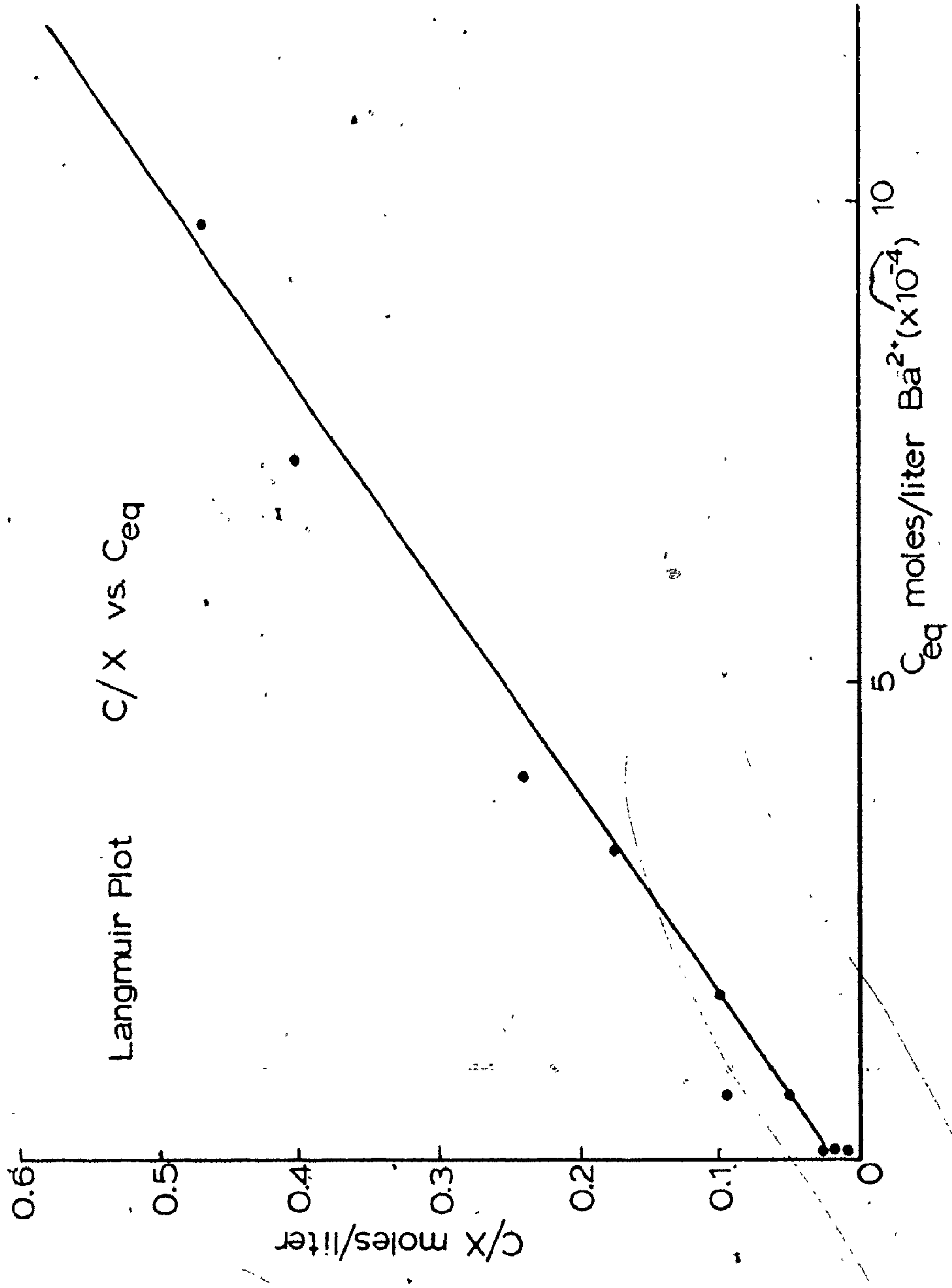

Figure 22. Langmuir Plot, Powdered Calcite - Ba^{2+} Results.

computer program calculation, a theoretical sorption isotherm plot was calculated from the following:

$$X = \frac{X_m \cdot b \cdot C_{equil.}}{(1 + b \cdot C_{equil.})} \tag{38}$$

Substituting a given set of $C_{equil.}$ values into expression (38), a set of X values was calculated and plotted (Fig. 23). The experimental data plotted using this same expression follows the theoretical curve rather well; indicating the values of X_m(2.1×10^{-3} moles Ba/mole calcite) and b(2×10^4) calculated from the Langmuir plot are of proper dimensions.

The sorption isotherm has an H-type curve dependence (See Chapter 2.2 also). Giles[27] states this shape indicates an ionic element sorbing on an oppositely charged surface. The length of the plateau indicates the difficulty of formation of a second layer due to charge repulsion between the first layer and those ions still in solution.

The amount of barium sorbed/gm of calcite versus original barium concentration was plotted to test that only a monolayer of barium was actually sorbed (Fig. 24). For each set of results, the curves plateau at about 2.5×10^{-3} gms barium/gm of calcite. Taking the surface area of the powdered calcite as 0.5 m^2/gm, the above amount of barium corresponds to 1.6×10^{15} atoms barium/cm^2 of surface. If 30% of the calcite surface lattice is assumed to be occupied by calcium, (a reasonable estimate), then 1 cm contains $\simeq 1.0 \times 10^{15}$ atoms of exchangeable sites. Once again considering the errors in the surface area measurement, these results are in very good agreement with monolayer coverage. Using the following equation[28],

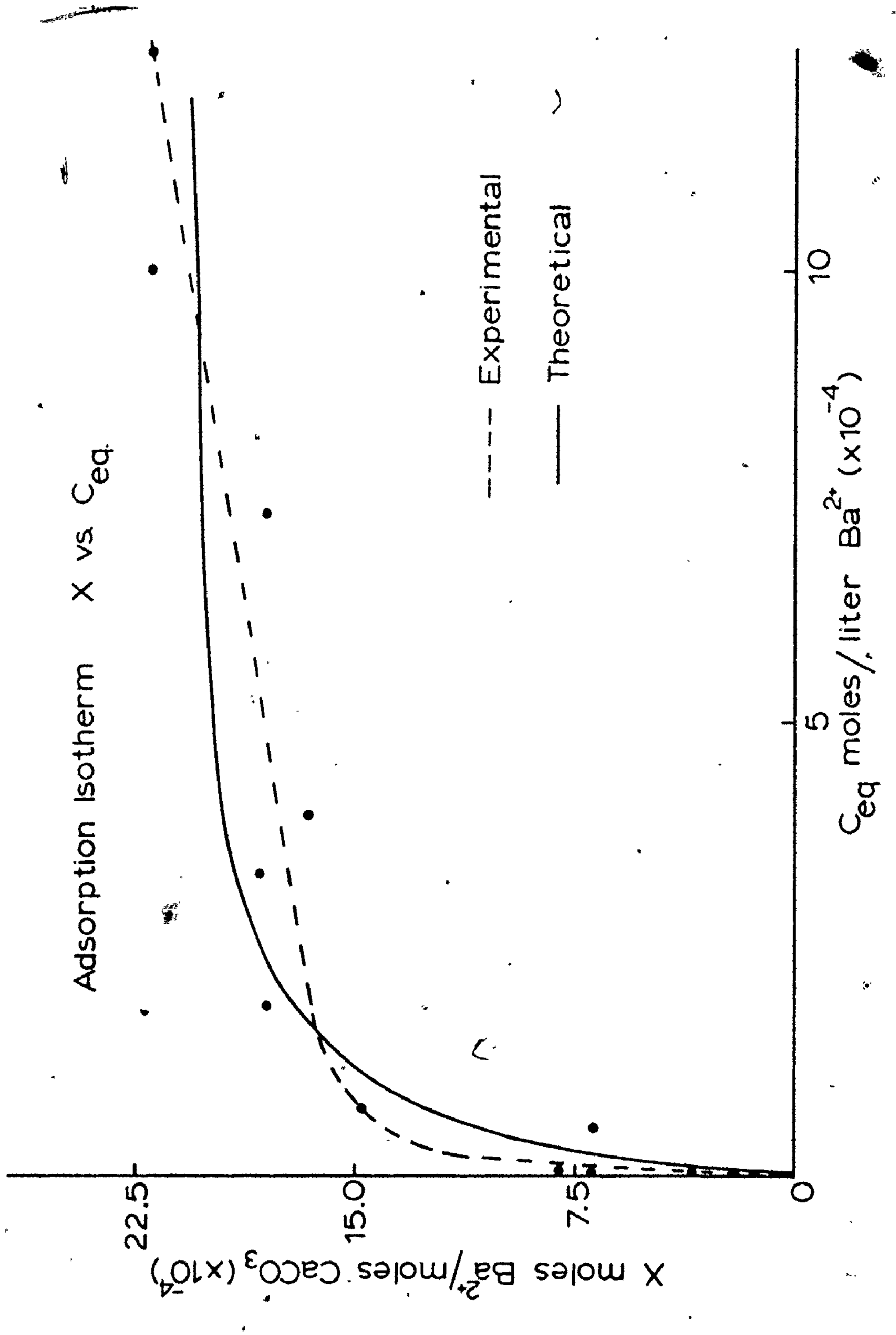

Figure 23. Langmuir Isotherm, Powdered Calcite - Ba^{2+} Results.

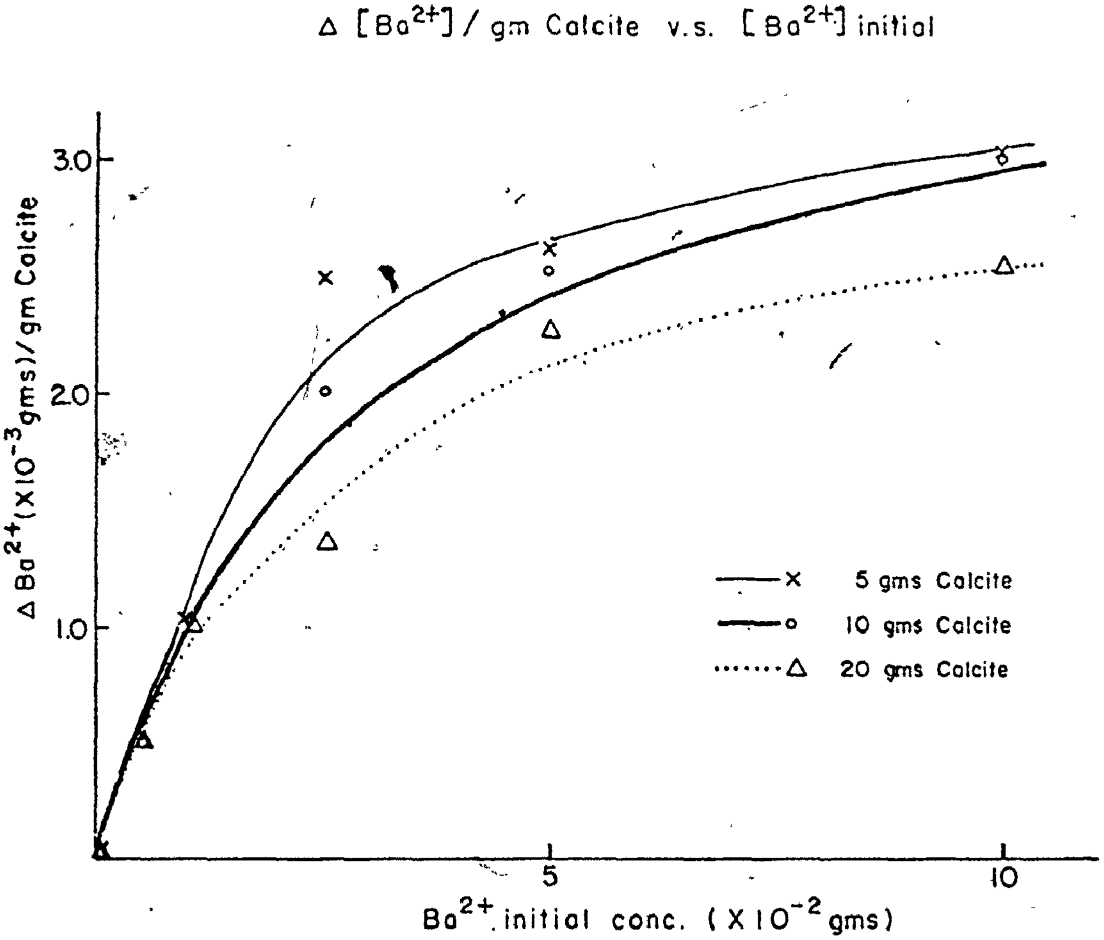

Figure 24. Ba^{2+} Sorption per Gram Calcite versus Initial Ba^{2+} Concentration.

$$S = \frac{X_m \cdot N \cdot A_m}{M} \qquad (39)$$

where

N = Avagadro's number (6.023×10^{23})

A_m = barium atom area ($5.75\ \mathring{A}^2$)

M = molecular weight of barium (137.2 gm/mole)

X_m = the maximum sorption capacity (3×10^{-3} gms Ba/gm calcite)

the surface area of the powdered calcite was calculated to be 0.73 m^2/gm. This area agrees quite well with the earlier estimate of 0.5 m^2/gm from the scanning electron microscopy method. These results also indicate that a sorption-exchange process occurs on the calcite surface (See Chapter 2.2 - Sorption Theories).

The results of this adsorption study can also be used to determine the equilibrium constant (K) and hence the free energy of sorption (ΔG) for barium exchange. This is done by re-arranging the well known expression (40),

$$\Delta G = -RT \ln K \qquad (40)$$

into the form

$$K = e^{-\Delta G/RT} = \frac{[Ba_{surf.}][Ca^{2+}_{sol'n}]}{[Ba^{2+}_{sol'n}][Ca_{surf.}]} \qquad (41)$$

Note, only the $[Ca_{surf.}]$ term in expression (41) is not easily determined experimentally. Fortunately, two methods can be used to estimate its value. The first method assumed that the value of $X_m \sim 2.1 \times 10^{-5}$moles/gm (determined above) also gave a qualitative measure of the total number of calcium ion surface sites. The second method, a theoretical calculation (vide infra) indicated $\simeq 1 \times 10^{15}$ calcium ions/cm^2 of surface. Using the experimentally determined calcite surface area (.73 m^2/gm), a value of $[Ca_{surf.}] \simeq 1.5 \times 10^{-5}$ moles/gm is found. Both methods give reasonably similar results. Values of K and ΔG were calculated and are reported in Table 7. It is most interesting that the calculated free energy of formation for Equations 42, 43, i.e. $BaCO_3$ and $Ba,Ca(CO_3)_2$,

$$CaCO_3 + Ba^{2+} \rightleftharpoons BaCO_3 + Ca^{2+} \qquad \Delta G° = -0.6 \text{ Kcal/mole} \qquad (42)$$

$$2CaCO_3 + Ba^{2+} \rightleftharpoons Ca,Ba(CO_3)_2 + Ca^{2+} \qquad \Delta G° = -1.42 \text{ Kcal/mole} \qquad (43)$$

and the results of Table 7, ($\Delta G° \simeq -0.5$ Kcal/mole) are quite similar. It is highly probable this type of study has great potential in determining thermodynamic parameters for surface exchange reactions.

4.2.2.2 Crushed Limestone

Table 8 and Figure 25 indicate the results of this sorption study on crushed limestone from the Dundee and Detroit River Formations. It is interesting to note that the Dundee limestone sorbs double that of the other type. Several factors, other than calcium carbonate composition must be responsible for this large different, as both varieties of limestone contain approximately 95% $CaCO_3$. In addition, there was little difference in sorption rates from non-washed and washed Dundee limestone fractions.

It was observed that the softer Detroit River limestone powdered more readily than the Dundee limestone, but it was more prone to caking when water was eluted through it (Note the elution time rates are for 100 ml of solution). The Dundee limestone contained more cherty material and this is probably responsible for its extra hardness and freedom from caking.

Table 7

Thermodynamic Data Calculated from Table 6

	Wt. Calcite (gms) ±0.01	* $\Delta Ba^{2+}_{sol'n}$ (moles/500 ml) $(x10^{-5})$	** $\Delta Ca^{2+}_{sol'n}$ (moles/500 ml.) $(x10^{-5})$	† $Ba^{2+}_{surf.}$ moles $(x10^{-5})$	†† $\Delta Ca^{2+}_{surf.}$ moles $(x10^{-5})$	K	ΔG Kcal/mole
(a)	10	0.33	12.25	3.3	14.75	0.845	+0.10
(b)	5 10	3.65 1.09	1.25 1.90	3.65 6.21	6.75 14.1	0.185 0.77	+0.99 +0.15
(c)	5 10 20	9.4 3.2 0.3	5.0 11.25 15.0	8.80 15.0 17.[illegible]	3.0 4.75 17.0	1.56 10.75 52.65	-0.26 -1.40 -2.34
(d)	10	20.0	12.5	16.4	3.5	2.93	-0.64
(e)	5 10 20	61.5 51.0 36.4	7.5 15.0 47.5	11.3 21.8 36.4	0.5 1.0 0.0	2.76 6.41 ∞	-0.60 -1.10 --
						Average	-0.57

* $\Delta Ba^{2+}_{sol'n} = Ba^{2+}_{initial} - Ba^{2+}_{sorbed}$

† $Ba^{2+}_{surf.} = Ba^{2+}_{sorbed}$

** $\Delta Ca_{sol'n}$ = solution Ca^{2+} increase.

†† $\Delta Ca_{surf.}$ = Initial Ca^{2+} ions on surface - Ca^{2+} into solution, where

Initial Ca^{2+} ions on Surface α surface area (wt. calcite)

For this case, Initial Ca^{2+} content = 2×10^{-5} moles/gm (from X_m data using complete monolayer exchange of $Ba^{2+} \longrightarrow Ca^{2+}$)

or = 1.6×10^{-5} moles/gm (from surface lattice estimate of Ca^{2+} ions/gm calcite; assuming surface area calcite - 1.0 m^2/gm.)

The caking problem would decrease the Detroit River limestone surface area substantially, thus reducing available sorption sites. A particle size of approximately 50 mesh was found best as this size gave nearly optimum sorption at fast elution times. Beyond 50 mesh, the sorption rate increase was low while elution time increased sharply.

As in the powdered calcite study (Chapter 4.2.2.1), nearly equal moles of barium and calcium ions are exchanged using these columns (Table 8). The maximum weight of barium sorbed (6.5×10^{-3} gms) on 30 gms of limestone having a particle size of 100 mesh (calculated surface area ≃ .015 m^2/gm (Appendix A.4.4.1) also indicated a monolayer exchange process.

The maximum exchange capacity of powdered calcite having a surface area of ≃ .75 m^2/gm (Chapter 4.2.2.1) was found to be 3.0×10^{-3} gms barium/gm calcite. The column sorption results indicated a sorption capacity of 2.2×10^{-4} gms barium/gm Dundee limestone. Because the sorption capacities are in a ratio 14:1, the surface areas can be assumed to be probably near this ratio also; i.e. 0.75 : .054 m^2/gm. From Equation (39), a surface area of 0.06 m^2/gm was calculated using the maximum sorption capacity (2.2×10^{-4} gm/gm) of the Dundee crushed limestone. Note, this value 0.06 m^2/gm and the crude approximation for 1 gm of 100 mesh limestone (.015 m^2/gm) are in qualitatively good agreement. These calculations give further support to the monolayer exchange mechanism, i.e ≃ 30% exchangeable surface sites. In addition, these results indicated that approximately 50 mesh crushed limestone could be of major use as an economical method to remove metal cations from aqueous solution either by elution through packed columns or by

Table 8

St. Mary's Limestone Sorption Results

LIMESTONE (30 gms)		+I		++II				+++III						
								(i)		(ii)		(iii)		(iv)
FORMATION	PARTICLE SIZE (Tyler-mesh) size	Ca^{2+} content ($x10^{-4}$gms) (±5%)	pH (±0.1)	ΔBa^{2+} (decrease) ($x10^{-4}$gms) (±5%)	ΔCa^{2+} (increase) ($x10^{-4}$gms) (±5%)	pH (±0.1)	ELUTION TIME (sec.)	ΔBa^{2+} content ($x10^{-4}$gms) (±5%)	pH (±0.1)	ΔBa^{2+} content ($x10^{-4}$gms) (±5%)	pH (±0.1)	ΔBa^{2+} content ($x10^{-4}$gms) (±5%)	pH (±0.1)	Total Ba^{2+} desorbed ($x10^{-4}$gms) (±5%)
A) DUNDEE														
1. Unwashed column	10-16	14.2	7.2	19.6	6.1	8.4	15	NIL	7.3	NIL	7.1	NIL	7.3	NIL
	16-35	20.9	7.7	35.2	13.8	8.2	20	0.56	7.9	NIL	7 8	NIL	7.7	0.56
	35-60	15.4	7.8	52.8	23.1	8.1	50	6.60	7.8	2.2	7.9	1.7	7.7	10.5
	60-70	17.0	8.0	53.0	23.2	8.6	80	11.6	7.8	5.0	7.8	4.4	7.6	21.0
	80-100	16.5	7.6	69.3	26.4	8.0	250	11.6	7.5	7.7	7.6	5.0	7.5	24.3
2. Washed column (100 ml. water)*	10-16	8.8	7.5	12.0	6.6	6.5	15	1.1	6.7	0 55	6.9	NIL	6.9	1.65
	16-35	13.8	7.6	37.2	12.1	7.1	25	1.7	7.5	1.1	7.9	1.1	7.9	3.90
	35-60	8.5	8.1	50.4	15.4	7.8	60	7.7	8.6	2.7	8.6	2.3	8.6	12.70
	80-100	6.8	7.5	63.4	16.6	7.1	260	12.7	8.5	6.1	7.9	5.0	7.9	23.80
B) DETROIT RIVER														
Washed column (100 ml. water)*	0-16	8.25	8.1	8.6	7.7	7.6	30	1.1	7.1	NIL	7.1	NIL	7.4	1.1
	16-35	7.7	8.1	17.4	8.4	7.4	50	3.3	8.1	1.1	7.4	0.5	7.2	4.9
	35-60	7.4	7.2	27.3	10.5	7.3	65	7.7	8.1	1.6	8.0	1.1	7.3	10.4
	60-70	6.6	7.4	31.7	11.0	7.0	190	12.7	8.6	3.3	9.0	1.7	8.8	17.7
	80-100	5.5	7.5	31.8	8.3	7.4	315	18.2	8.7	3.3	8.7	1.7	8.6	23.2

* This initial wash water discarded.

\+ Results of 100 ml deionized distilled water, (pH ~ 5.5) eluted through limestone filled column. No Ba^{2+} was detected in any eluted water sample.

++ Results of 100 ml Ba^{2+} solution (10^{-2} gms, pH ~ 4.8) eluted through column. At. Ab. analysis of the initial solution indicated, 98.9 ppm Ba^{2+} (7.2×10^{-4} M) and 2.6 ppm Ca^{2+} (6.5×10^{-5} M), ΔBa^{2+} = Ba decrease in this solution; ΔCa^{2+} = Ca increase in this solution.

+++ Analysis of three separate 50 ml elutions ((i), (ii), (iii)) of deionized distilled water (pH ~ 5.5) through column after Ba^{2+} elution (Part II). ΔBa^{2+} = Ba increase in this 50 ml of pure water.

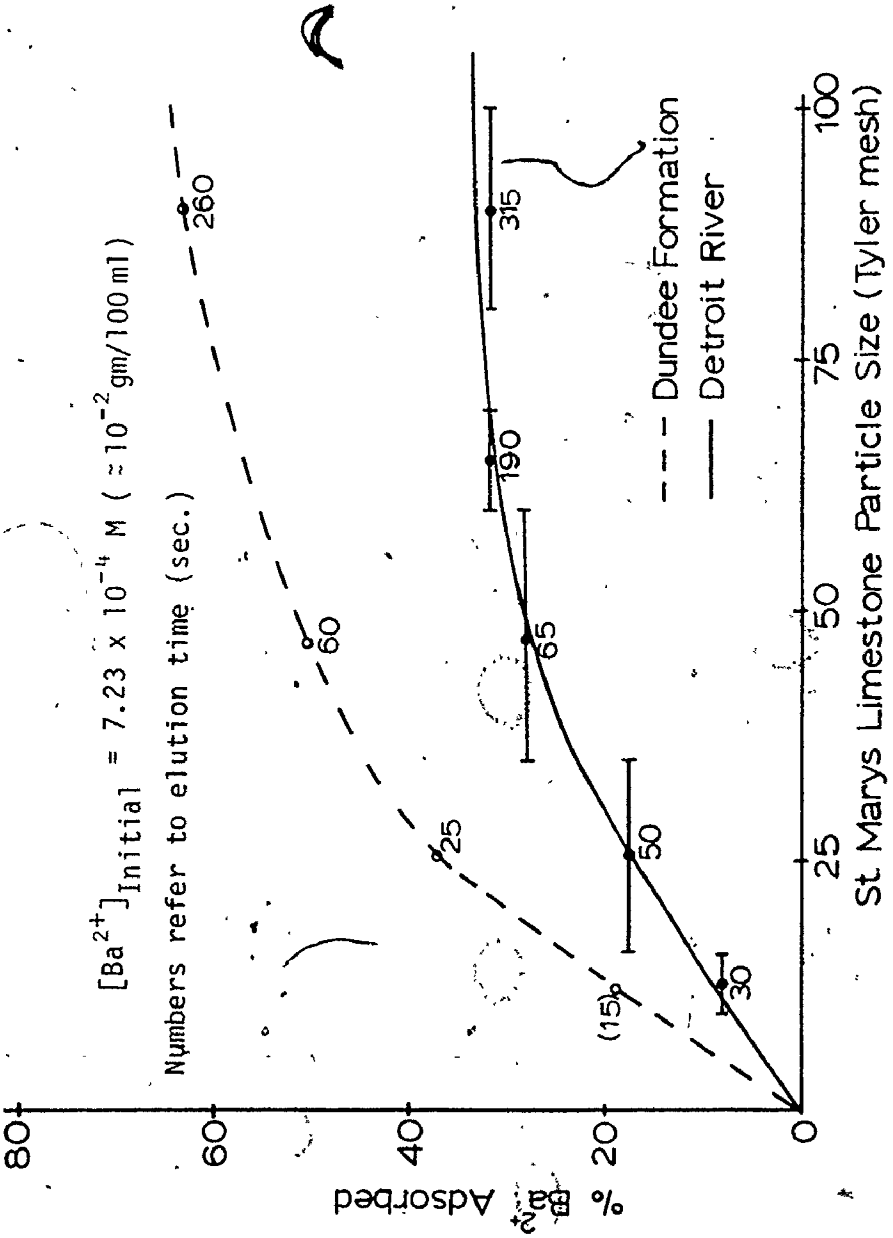

Figure 25. Barium Adsorption on St. Marys Limestone.

flow bed processes.

4.3 Single Crystal Calcite - XPS Study

4.3.1 Experimental

Two varieties of calcite crystals, Iceland Spar calcite and milky (opaque) crystalline calcite, were studied for their ability to adsorb barium from dilute solution. These solutions were of two types: barium ions in solution at (1) non-equilibrium and (2) equilibrium conditions with respect to calcium carbonate at 22 ± 2°C. Barium solutions were prepared using $Ba(ClO_4)_2$ and deionized distilled water. The calcite crystals were cleaved as in Chapter 3. The milky calcite variety was highly fractured, containing large visible internal cracks while the Iceland Spar calcite was optically clear and free of visible internal fractures, creating a smooth, mirror-like surface when cleaved.

For the first type of reactions (non-equilibrium), crystals of both varieties of calcite were place in polypropylene beakers with 500 ml. of deionized distilled water varying from 20 to 200 ppm (1.46×10^{-4} M to 1.46×10^{-3} M) in barium. No attempt was made to allow the calcite crystals to attain equilibrium with the water prior to barium sorption. The initial pH of these solutions was approximately 5.5 ± .2.

For the second type of reaction, (equilibrium), the cleaved calcite crystals were placed in 500 ml of deionized distilled water, pre-saturated with powdered calcium carbonate for 48 hours (pH ≃ 8.4). Appropriate aliquots of stock barium solutions were then added to each beaker to obtain the final required solution concentration of 1.46×10^{-4}M to 1.46×10^{-3} M barium. Crystals were removed from solution after reaction-times varying from a few hours to over a month and immediately dipped (washed) five times in separate beakers of deionized distilled water to remove original barium solution adhering to the surface (See Appendix A.1 for details). Dipping five times was chosen after several experiments were performed to determine the best method to remove excess solution. For example, several calcite crystals were placed in 200 ppm barium solutions for thirty days, removed and each crystal dipped from one to twenty times, in fresh water. Additional fresh crystals were dipped in concentrated barium solutions for 10 seconds, removed and then rinsed in the above manner. In this second type of experiment, no barium was detected on the surfaces analysed. All of these calcite surfaces were analysed using the XPS technique outlined in Chapter 3.

ESCA spectra of Ba $3d_{5/2}$, Ca 2p, C 1s, O 1s and Cl 2p were recorded for each calcite crystal. In addition, unreacted calcite crystals were also examined and used as reference blanks.

Many of these barium sorbed crystals were stored for periods up to 18 months, and re-analysed to determine reproducibility of the ESCA technique and to check on diffusion rates at the calcite surface.

It was observed during these studies that the carbon 1s spectra changed with the time of reaction. Several experiments were performed to determine what surface changes may have occurred. Cleaved Iceland Spar calcite was reacted in pure water at 22°C for selected times (0 - 50 days, (Appendix A.2)). The surface of these crystals and the barium reacted crystals were examined by Ar ion etching using the 10 K eV Ar gun assembly. Depth profiling of these reacted surfaces made it possible to estimate the effects of water and sorption of barium on the surface with time of reaction. In addition, reactions of the calcite surface by other processes were studied. They included heating to 500°C for

15 minutes, reaction in 1 M HCl acid for 30 seconds, exposure to the XPS 10^{-9} torr. vacuum for several days, exposure to x-ray radiation (200 watts) for 36 hours, and variable reaction times in steam vapour. In these cases, the C 1s and Ca 2p spectra levels were examined with increasing Ar ion etch time.

4.3.2 Discussion

The weights of barium sorbed on cleaved calcite crystal surfaces at equilibrium and non-equilibrium conditions (22°C) as a function of initial barium concentration and reaction time were determined using the ESCA calibration plots from Chapter 3. These results shown in Table 9, Fig. 26-29 strongly indicate that exchange adsorption (rather than precipitation) is occurring; the amount of barium on the surface increases both with increasing barium concentration in solution and with time of reaction. Crystals from the non-equilibrium solutions shown in Figures 26, 27 (i.e. barium-pure water at a pH ≈ 5.5) are sorbed more strongly than crystals from the equilibrium solution, Figures 28, 29 (i.e. barium-saturated calcium carbonate solutions at a pH ≈ 8). Two factors would seem to explain the enhanced sorption rate of crystals in the non-equilibrium solutions. They are, an initial acidic solution pH and a need for attainment of solution equilibrium with the crystals; both factors would cause a greater dissolution of the calcite surface, hence a greater sorption rate. The exchange of barium for calcium would be kinetically more favoured for surfaces undergoing dissolution (recrystallization).[20C,29]

In the equilibrium solutions, the sorbed amounts of barium is

Table 9. Ba^{2+} Adsorption Data on Calcite Single Crystals

SINGLE CRYSTAL CALCITE			INITIAL Ba^{2+} CONCENTRATION (500 ml solution)							
			I		II		III		IV	
			20ppm(7.28×10^{-5} moles)		50ppm(1.82×10^{-4} moles)		100ppm(3.64×10^{-4} moles)		200ppm(7.28×10^{-4} moles)	
Reaction type (25°C)	Variety	Reaction TIME* (days)	$\frac{I_{Ba}}{I_{Ca}}$**	Weight*** adsorbed ($\times 10^{-8}$gms)	$\frac{I_{Ba}}{I_{Ca}}$**	Weight*** adsorbed ($\times 10^{-4}$gms)	$\frac{I_{Ba}}{I_{Ca}}$**	Weight*** adsorbed ($\times 10^{-8}$gms)	$\frac{I_{Ba}}{I_{Ca}}$**	Weight*** adsorbed ($\times 10^{-4}$gms)
(A) Pure Ba^{2+} solution (non-saturated w.r.t. calcite)	crystalline (opaque)	10	4.2	15.0	7.13	25.0	8.0	28.0	9.1	32.0
		20	3.75	13.0	6.36	23.0	8.1	28.5	12.4	44.0
		30	4.32	15.3	8.60	31.0	11.1	40.0	11.2	40.0
	Iceland spar	10	1.35	4.6	4.4	15.6	5.3	20.0	9.1	32.0
		20	3.0	10.0	6.1	22.0	5.1	18.0	7.5	27.0
		30	2.6	9.0	4.3	15.5	8.8	31.5	10.0	36.0
		50	2.4	8.7	5.8	21.0	8.1	28.5	---	---
(B) Ba^{2+} solution (pre-saturated† w.r.t. calcite)	crystalline (opaque)	1	NIL	NIL	NIL	NIL	NIL	NIL	1.25	2.5
		4	0.36	>1.0	0.6	1.0	2.3	5.5	2.0	4.5
		10	0.70	1.5	2.2	5.4	---	---	---	---
		15	0.50	>1.0	2.5	6.0	---	---	---	---
		20	1.50	4.0	4.3	12.0	---	---	6.7	18.0
		30	---	---	---	---	---	---	8.2	22.0
	Iceland spar	10	NIL	NIL	1.15	4.0	1.7	6.0	7.2	22.5
		15	1.0	3.0	2.90	11.0	6.3	22.0	---	---
		25	2.0	8.0	3.0	11.4	(6.7 7.0	(24.0 25.6	7.5	25.5

* each crystal dipped 5 times in deionized distilled water (Appendix A 1).

** I_{Ba}/I_{Ca} refers to Peak Area Intensity ratio of $\frac{Ba\ 3d_{5/2}}{Ca\ 2p_{1/2}}$ ($\frac{50\ \text{scans}}{2\ \text{scans.}}$).

*** weight (gms) of Ba^{2+} sorbed; errors = ± 20%, values computed from appropriate calibration plot (Chapter 3).

† pre-saturated using enough spec. pure calcite powder to saturate 500 ml water (≈ 7×10^{-3} gms).

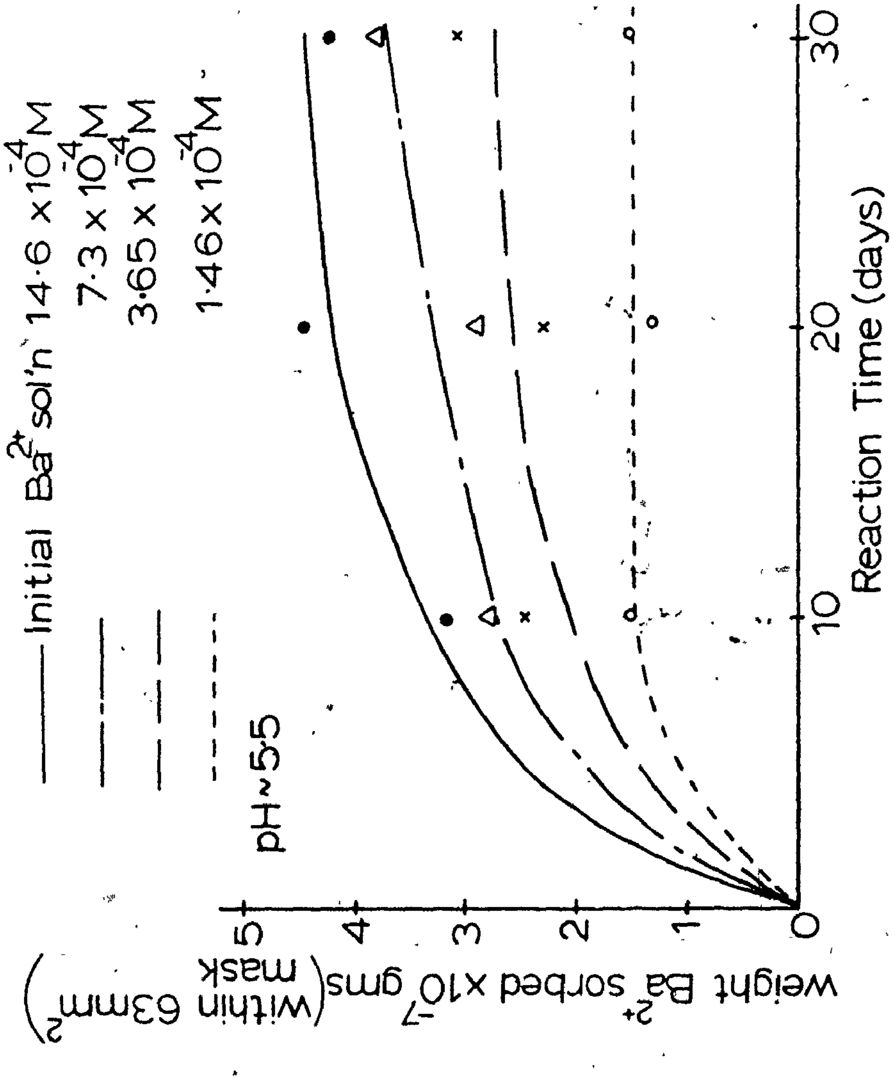

Figure 26. Ba^{2+} Adsorption onto Crystalline Calcite Crystals (non-equilibrium conditions).

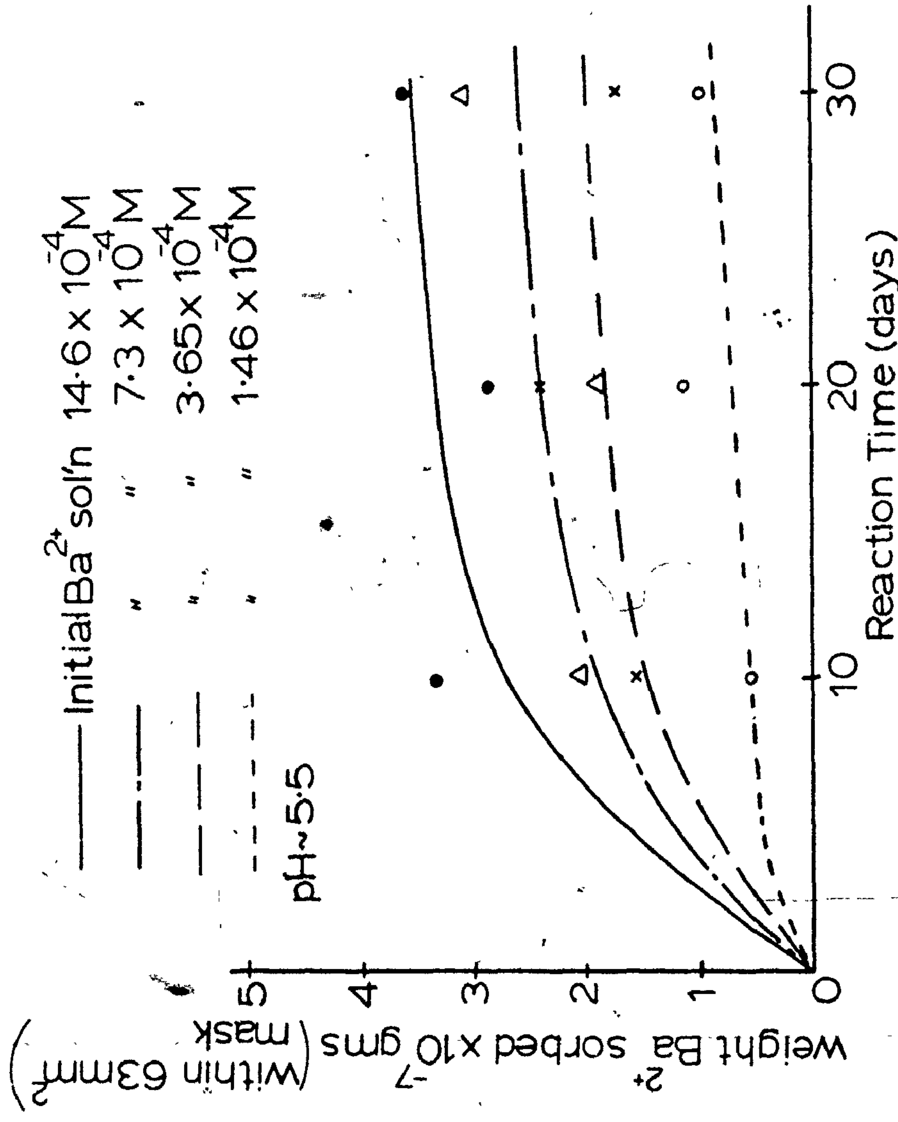

Figure 27. Ba^{2+} Adsorption onto Iceland Spar Calcite Crystals (non-equilibrium conditions).

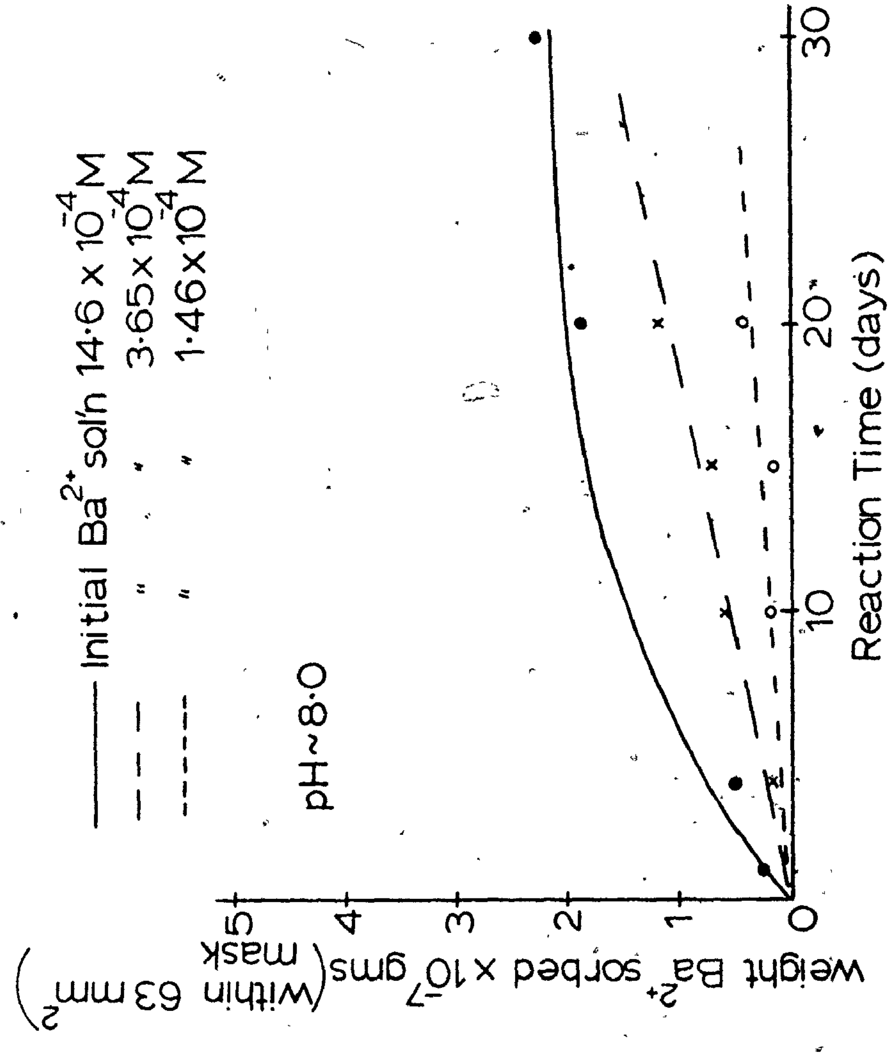

Figure 28. Ba^{2+} Adsorption onto Crystalline Calcite Crystals (equilibrium conditions).

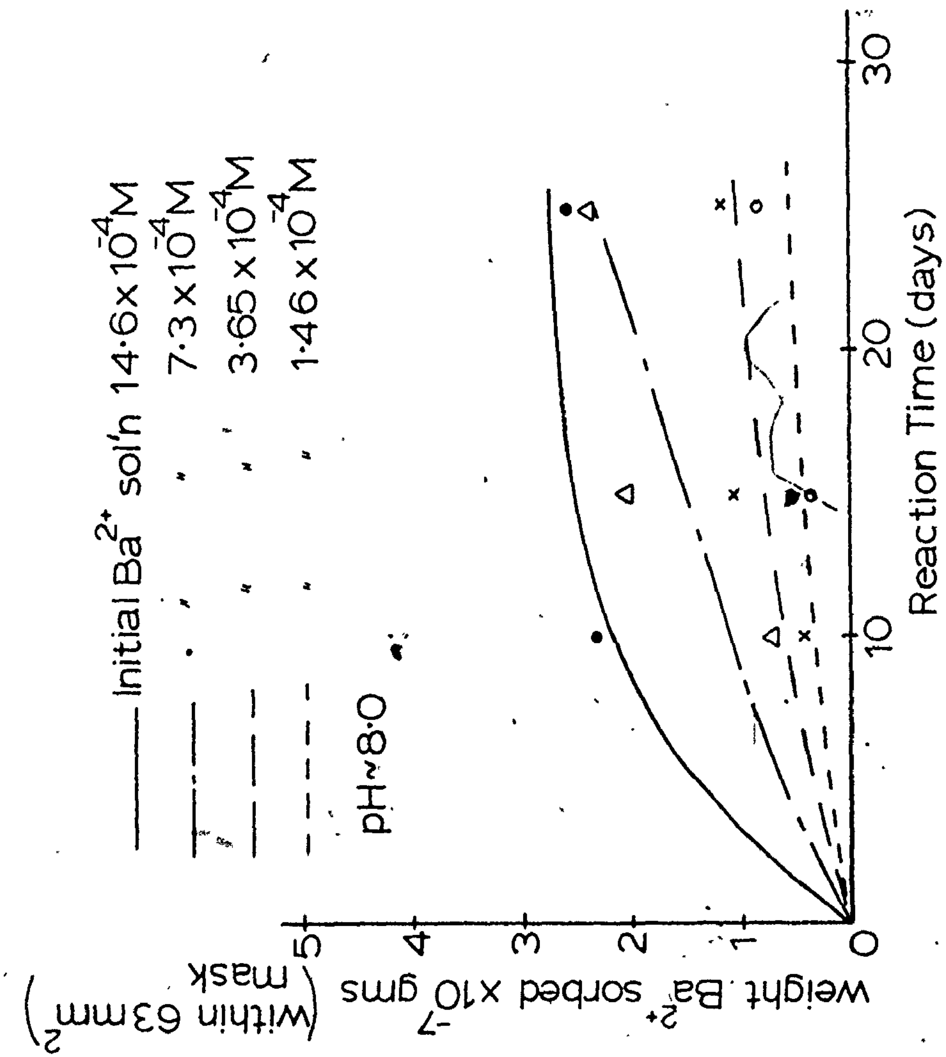

Figure 29. Ba^{2+} Adsorption onto Iceland Spar Calcite Crystals (equilibrium conditions).

similar for both Iceland Spar and the milky calcite, indicating a similar type calcite surface. This effect would be expected because the surface of both varieties of calcite had several days to age in the pre-saturated calcium carbonate solution before addition of barium. This long time period allowed ageing processes to decrease surface imperfections and reduce charge sites. The milky calcite variety was found to have a greater sorption ability than the Iceland Spar calcite. This was especially noted in the non-equilibrium solutions. The best explanation for this effect is related to differences in the surface properties of these two types of calcite. The Iceland Spar calcite cleaved surface is quite smooth and free of surface fractures. This good cleavage produces few reaction sites which in turn hinders a sorption exchange.

It should be emphasized that the qualitative aspect of Figures 26-29 are not dependant on the absolute accuracy of the XPS calibration plot's slope (Chapter 3).

The time scale (i.e. days) of adsorption (exchange) on these calcite single crystals in dilute barium solutions was ideal for following these types of reactions by XPS. The reproducibility of XPS barium 3d/calcium 2p spectra ratios' are shown in Table 10 when surfaces were re-analysed 18 months apart. Such good agreement verifies the stability of the XPS spectrometer, accuracy of the technique and also indicates diffusion to be nil at 22°C. Upon heating to 500°C for one day, Ba 3d/Ca 2p ratios' became essentially zero as barium ions could not be detected. However, heating at 100°C and 200°C increased the ratio, possibly because surface hydrocarbon contamination was removed. (Table 10)

Table 10

Reproducibility with Time and Thermal Effects on XPS Peak Area Intensity Ratios

Reacted Sample* (non-saturated w.r.t. calcite)	$I_{Ba\ 3d_{5/2}} / I_{Ca\ 2p_{1/2}}$**		
	Initially	150 days	heated 24 hours (500°C)
(A) Iceland spar crystals			
1. 10 days in 200 ppm Ba^{2+} solution	8.86	10.60	0.71
2. 30 days in 200 ppm Ba^{2+} solution	9.95	10.27	NIL
3. 20 days in 100 ppm Ba^{2+} solution	5.11	6.77	0.70
4. 10 days in 50 ppm Ba^{2+} solution	4.15	4.04	6.02†
5. 10 days in 100 ppm Ba^{2+} solution	5.87	5.20	6.60††
(B) Crystalline (opaque) Crystal			
1. 10 days in 200 ppm Ba^{2+} solution	10.80	9.92	NIL

* Calcite crystal reacted in stated Ba^{2+} concentrations for stated reaction time; each crystal dipped (washed) 5 times in water (Appendix A.1).

** as per Table 9.

† heated 24 hours at 100°C;

†† heated 24 hours at 200°C;

Note C 1s contamination peak intensity reduced in both cases. Thus expect increase in $\frac{I_{Ba}}{I_{Ca}}$ ratio.

(See chapter 3.3.1)

It is interesting to note the amount of barium sorbed on calcite, (4×10^{-7} gm/cm^2 $\approx 1.8 \times 10^{15}$ atoms/cm^2) from the 1.46×10^{-3} M solution, after reacting 20 days, (Figure 26) is consistent with monolayer coverage.

Little or no chloride or perchlorate anions were detected using the XPS technique (i.e. Cl 2p) on any reacted calcite crystals placed either in $Ba(ClO_4)_2$ or $BaCl_2$ solutions, regardless of the barium sorption measured. However, chlorine was always detectable on the calibrant samples and in intensity proportions representative of the evaporated solution concentration. This is very strong evidence that anion specific adsorption (i.e. Cl^- or ClO_4^-) does not occur on the ionic calcite crystal surface.[15a] This result is also consistent with other studies which indicated no anion adsorption on oxides.[30,31]

4.4 Conclusion

The explanation of barium sorption on calcite surfaces is to be found in the adsorption theory discussed in Chapter 2. For example, the concepts of electrical charge (EDL theory), lattice defect consequences (ageing processes) and the Fajan-Paneth rule effects seem best to explain barium sorption on calcite. Briefly, an EDL of water is anticipated because calcite in aqueous solution is hydrophilic[32], and the point of zero charge (PZC) for calcite is pH $\approx$ 8.2.[6] Using the many variations of hydrolysis-exchange sorption (Chapter 2), a picture of barium, calcium exchange is seen. Hydrated barium ions attracted to the EDL see localized sites of negative charge caused by the ageing processes (recrystallization). Specific sorption occurs once the barium cation enters the stern plane. Rearrangement at these sites is then possible, with incorporation of barium into the lattice.

A possible mechanism then is

$$CaCO_{3(surf.)} + H_2O \overset{k_1}{\rightleftharpoons} Ca - OH_{(surf.)} + CO_3 - H_{(surf.)} \tag{44}$$

(i) hydroxylation of surface

$$Ca - OH_{(surf.)} + CO_3 - H_{(surf.)} + Ba^{2+}_{(aq.)} \overset{k_2}{\rightleftharpoons} CO_3 - Ba_{(surf.)} + Ca^{2+}_{(surf.)} + H_2O \tag{45}$$

(ii) sorption

$$Ca_{(surf.)} + CO_3 - Ba_{(surf.)} \overset{k_3}{\rightleftharpoons} BaCO_{3(surf.)} + Ca^{2+}_{(aq.)} \tag{46}$$

(iii) exchange

Thus

$$CaCO_{3(surf.)} + Ba^{2+}_{(aq)} \overset{K}{\rightleftharpoons} BaCO_{3(surf.)} + Ca^{2+}_{(aq.)} \tag{47}$$

(iv) overall

(i.e. $K = k_1 + k_2 + k_3$)

Another possible mechanism is

$$2CaCO_{3(surf.)} + Ba^{2+}_{(aq.)} \overset{K}{\rightleftharpoons} CaBa(CO_3)_2 + Ca^{2+}_{(aq.)} \tag{48}$$

For this type of mechanism, no pH changes upon sorption-exchange are anticipated as an H^+ release into solution quickly reacts either with OH^- or CO_3^{2-} or CO_2. The powdered calcite results Chapter 4.2.2.1, the lack of anion sorption and the single crystal rate effects (Chapter 4.3.2) all suggest a specific chemical exchange reaction occurs for the barium-calcite system. Unlike oxide-metal cation sorption, the calcite sorption rate is slow. This may well be due to large differences in their points of zero charge (Chapter 2) and unlike calcite, oxide minerals are free of complex equilibria reactions in solution. Note the pH (Z.P.C.) is ≃ 8.2 for calcite but is only ≃ 3 for oxide minerals.

The observation that water reacted surfaces of Iceland Spar calcite which are initially transparent (i.e. a stoichiometric lattice) become opaque and white in time, (i.e. a non-stoichiometric lattice) suggest that ageing (recrystallization) is the major mechanism for barium reaction at the surface.

Note the lower (bottom) side of these reacted crystals (face down against beaker bottom) showed no surface changes after reacting fifty days. (Appendix A.2)

It is thus postulated that normal sorption processes, on the hydroxylated calcite surfaces, attract the positively charged, hydrated/hydrolyzed barium ions to the surface region while slow ageing of the surface allow the exchange reaction observed. As previously stated, simple solubility (precipitation) considerations cannot apply to these reactions, remembering that barium loss from solution (Chapter 4.2) is proportional to the calcite surface area, initial barium concentration in solution and time of reaction.

The surface areas of the powdered calcite and crushed limestone calculated from maximum adsorption capacities (X_m) agreed very well with surface area estimates calculated using other methods and thus provide further support to a monolayer exchange mechanism.

In addition the single crystal calcite results, combined with the earlier powdered calcium carbonate study, both indicating monolayer coverage, lend strength to the quantitative significance of the XPS calibration plots (Chapter 3).

4.5 References

1. K.E. Chave, Science, 148, 1723, (1965).
2. K.E. Chave and E. Suess, Limnol. Oceanogr. 15, 633, (1970).
3. E. Suess, Geochim. et Cosmochim. Acta, 34, 157, (1970).
4. P. Mayers and J. Quinn, Limnol. Oceanogr. 16, 992, (1973).
5. E. Suite and M. Arakawa, J. Chem. Soc. Japan, 75, 596, (1954).
6. P. Somasundaran, J. Colloid Interface Sci., 31, 557, (1969).
7. T. Jackson and J. Bischoff, J. Geology, 79, 493, (1971).
8. a) E. Canals, R. Marignan and S. Cordier, Trav. Soc. Pharm., Montpellier, 9, 55, (1949).
   b) E. Canals, R. Marignan and S. Cordier, Ann. Pharm. Franc., 8, 368, (1950).
   c) E. Canals and R. Marignan, Ann. Pharm. Franc., 7, 502, (1949).
9. T. Tamura and E.G. Struxness, Health Physics, 9, 697, (1963).
10. T. Tarutani and S. Misumi, Mem. Fac. Sci. Kyushu, Series C5, 1, 21, (1962).
11. H.B. Mann, Soil Science, 29, 117, (1930).
12. K. Murata, Am. Jour. Sci., 237, 725, (1939).
13. P. Boischot, M. Durroux and G. Sylvestre, Ann. Agr., Series A, 307, (1950).
14. V.I. Spitsyn and V.V. Gromov, Pochvovedeniye, 12, 45, (1959). (transl., Soviet Soil Science)
15. a) P. Möller and G. Weir, Radiochimica Acta, 144, (1972).
    b) P. Möller and G. Rajagopalan, Zeitschrift für Phys. Chem. 81, 547, (1972).
    c) P. Möller, J. Inorg. Nucl. Chem., 35, 395, (1973).
    d) P. Möller, Inorg. Nucl. Chem. Lett., 9, 759, (1973).

16. E. Görlich and Z. Görlich, Bull. Acad. Polon. Sci., Sér. Sci., Chim. géol. et géolgraph., 8, 75, (1960).

17. E. Görlich, Z. Görlich and T. Szwaja, Bull L'Acad. Polon. Sci., Sér. Sci., géol. et géolgraph., 7, 669, (1958).

18. J.D.H. Williams, J.K. Syers, R.F. Harris and D.E. Armstrong, Environ. Sci. Technol., 4, 517, (1970).

19. C.V. Cole, S. Olsen and C. Scott, Soil Sci. Soc. Am., 17, 352, (1953).

20. (a) J.M. Thomas and G. Renshaw, Trans. Faraday Society, 61, 791, (1965).
(b) J.M. Thomas and G. Renshaw, J. Chem. Soc., A, 2753, (1969).
(c) J.M. Thomas, Chem. in Britain, 6, 60, (1970).
(d) J.M. Thomas, Phil. Trans. Royal Society, 277, 251, (1974).

21. J.D. Kerber and W.B. Barnett, At. Absorp. Newslett., 8, 113, (1969).

22. G.F. Peterson and H.L. Kahn, At. Absorp. Newslett., 9, 71, (1970).

23. D.F. Hewitt, "The Limestone Industries of Ontario", O.D.M. Publication #5, (1960).

24. Field Trip Excursion Guide Book, Part B: Phanerozoic Geology, G.A.C. Publication, Editor, P.G. Telford (1975).

25. B.J. Anderson, E.A. Jenne and T.T. Chao, Geochim. et Cosmochim. Acta, 37, 611, (1973).

26. J.P. Gabano, P. Étienne and J.F. Laurent, Electrochim. Acta, 10, 947, (1965).

27. C.H. Giles, A.P. D'Silva and I.A. Easton, J. Colloid Interface Sci., 47, 766, (1974).

28. S.J. Gregg and K. Sing, "Adsorption, Surface Area, Porosity", Academic, Chapters 6, 7, (1965).

29. J. Verhoogen, F.J. Turner, L.E. Weiss, C. Wahrhaftig, and W.S. Fyfe, "The Earth", Holt, Rinehart and Winston, (1970).

30. P. Ney, "Zeta-Potentiale und Flotierbarkeit von Mineralen", Springer-Verlag (1973).

31. R.T. Shuey, Developments in Economic Geology, Vol. 4, "Semi-Conducting Ore Minerals", (1975).

32. S.J. Gregg, Phys. Chem. Series 1, "Surface Chem. and Colloids", 6, 188, (1972).

CHAPTER 5

MERCURY SORPTION ON IRON SULPHIDES

5.1 Introduction

As discussed in Chapter 1, mercury pollution of natural waters by industrial chemical processes[1,2] has created severe problems in many countries of the world. In addition, an increased use of coal and geothermal steam for electrical energy generation will cause a further strain on technology to prevent additional widespread mercury contamination of the atmosphere and hydrosphere. Besides the huge sulphur dioxide and nitrous oxide emissions, these energy sources contain large concentrations of heavy metals including mercury, cadmium, etc.[3] Economical and efficient methods must be devised to eliminate present mercury pollution as well as to reduce these future hazardous conditions.

The uptake of heavy metals, including mercury, have been examined previously using cellulose[4], silicon alloys[5], peat moss[6], and selected agricultural products and by-products.[7] From a geochemical viewpoint, adsorption of mercury ions by mineral surfaces seemed quite feasable as well.

The common sulphide minerals, pyrrhotite ($Fe_{1-X}S$) and pyrite (FeS_2) warranted study to determine their sorbent properties in decreasing or entirely removing mercuric ions and elemental mercury from aqueous solution. Sorption of mercury onto these mineral surfaces should also give some indication of their ability to remove mercury from contaminated atmospheric samples as well. But no gas sorption studies are attempted in this thesis. Mercuric ion sorption on silica[8,9] and heated pyrite[10], i.e. $FeS_2 \xrightarrow{\Delta} FeS$, have been studied previously, but not in detail.

As in the calcite work, Chapter 4, preliminary studies using powdered (crushed) pyrrhotite were necessary to determine mercury sorption properties under various conditions, eg. time of reaction, surface area (weight) of sorbent, initial mercury (sorbate) concentration, pH, etc., before a detailed XPS study on small cut and polished mineral sections could be initiated.

Pyrrhotite and pyrite ores were chosen for three reasons. They are common and thus economical minerals to mine throughout the world and are usually quite accessible in localities where mercury contamination is dominant. For example, most massive sulphide mining operations (Pb, Zn, Ni) separate and discard huge amounts (thousands of tons) of iron sulphides yearly. Secondly, these ores pose no large pollution threat of their own if dumped into contaminated waterways. They are highly insoluble and if exchange of mercury for iron ions occurred, the iron and/or sulphur is easily precipitated by natural processes. Finally, any sorbed mercury product (probably HgS or HgO) is highly insoluble and if properly disposed, precludes large desorption rates with time. This is essential if large scale water treatment projects are to be done economically and efficiently.

5.2 Powdered Iron Sulphide - AAS Study

5.2.1 Experimental

The absorption of mercuric ions from solution using several weights of crushed, sieved iron sulphide (pyrrhotite) was examined. Highly pure Sudbury pyrrhotite ($Fe_{1-X}S$), obtained from the Geological Collection (UWO) was crushed and sieved using Tyler stainless steel sieves. The

> 1000 mesh fraction was collected and used in the following study.

Two reaction mechanisms were studied, (1) reactions involving non-equilibrium conditions, that is addition of crushed FeS directly to various concentrations of mercuric chloride and (2) equilibrium conditions, where concentrated mercuric chloride aliquots were added to the crushed FeS at equilibrium with water. All of these experiments followed similar procedures as outlined in Chapter 4.2. Only deionized distilled water (pH $\simeq$ 5.5) and polypropylene beakers and storage bottles were used. Stirring of each solution and pH determinations were done using equipment previously discussed (Chapter 4.2). Analytical grade mercuric chloride ($HgCl_2$) was purchased from J.T. Baker and used to prepare a 10,000 ppm stock solution. Dilutions of this stock solution were used to prepare each 500 ml reaction solution.

The initial pH of mercuric chloride solutions (i.e. non-equilibrium reactions) before addition of powdered iron sulphide, is controlled by the salt concentration. Because of pH variations in these solutions, it was difficult to compare sorption rates for mercury ions on the FeS. Therefore an equilibrium study was initiated, having the iron sulphide powder equilibrate in water at pH = 4 prior to mercury ion addition. For these equilibrium type reactions, 0.25 to 1.0 gm of crushed iron sulphide ore was stirred in water approximately two hours to attain equilibrium.

$$FeS + H_2O \overset{\text{fast}}{\rightleftharpoons} Fe^{2+} + HS^- + OH^- \qquad (49)$$

$$2FeS_{(\text{black})} + H_2O \underset{\text{slow}}{\overset{O_2}{\rightleftharpoons}} Fe_2O_{3(\text{brown})} + 2SO_4{}^{2-} + 2H^+ \qquad (50)$$

Long reaction times (> 24 hours) posed problems because colloidal iron oxide was produced. This was noted by the colour change of the powder and a pH drop in solution (Equation 50).

Additional study indicated the iron sulphide reached equilibrium (Equation 49) in approximately one hour, with no appreciable production of iron oxide. At selected times after addition of mercury ions to each reaction solution, 10 ml aliquots were removed and centrifuged 30 minutes at 3600 rpm to remove any iron sulphide powder. This method was found superior to filtering the aliquots with #42 Whitman filter paper as mercury retention by the filter paper was avoided. One ml of 5% nitric acid was added to each 10 ml aliquot to prevent mercury sorption on the walls of the polypropylene bottles. The samples were then analysed by cold vapour chemical or graphite furnace flameless Atomic Absorption methods.

Mercury analysed by the cold vapour method involved reacting either 20 ml or 50 ml of sample solution and 10 ml of water, with 1 ml of 10% sulphuric acid and 1 ml of 5% stannous chloride to produce mercury vapour. This vapour was then detected using normal Atomic Absorption methods. The graphite furnace method gave a lower detection level, but because of the volatility of mercury even at 100°C, 25 μl of 10%, sodium sulphide had to be added to each 50 μl sample placed in the graphite tube. The sodium sulphide acted as a fixing agent preventing premature loss of mercury during the drying stage, but it is very hazardous due to escaping hydrogen sulphide gas. Recently an improved Heated Graphite Analyser (HGA) technique has been proposed which eliminates the sodium sulphide step.[11] Both techniques offer reliable analysis.to less than 1 ppb and can be used to check on each other'saccuracy. However, the linear working (calibration) range is quite small for the graphite furnace method and extra dilutions of standards and samples was required. Therefore the chemical cold vapour method seems better suited for analysis of trace mercury in solution.

5.2.2 Discussion

The results of the mercury ion interaction with powdered iron sulphide surfaces is given in Table 11. This mercury ion loss from solution was determined for the three reaction types discussed in section 5.2.1. The data for the mercury ion uptake on increasingly greater weights of FeS at pH ≈ 4 (Table 11c) is plotted in Figure 30. Note, this plot indicates an adsorption process because the mercury loss from solution is proportional to the weight of powdered FeS(sorbent) and the initial mercury ion concentration (sorbate). The Langmuir adsorption expression (Equation 37) was then used to determine the maximum adsorption capacity (X_m) and the adsorption constant (b) for the FeS powder at the three reaction types listed in Table 11. The resulting linear adsorption plots are shown in Figure 31. Using these experimentally determined X_m and b values and Equation 38, the three corresponding adsorption isotherms, Figure 32, were calculated. The rather poor reproducibility of the non-equilibrium reaction results (Table 11a, Figure 32a) can be explained as being due to the solution pH dependance on the initial mercuric chloride content (adsorption is pH dependant). The variations in adsorption isotherms indicated the effect of pH and solution equilibrium on the Hg^{2+}-FeS sorption rates.

In the second reaction type (Table 11b), the iron sulphide powder was stirred three weeks in water before addition of mercury. The conversion of FeS to iron oxide was very high in this study. This was easily observed due to the colour change of the powdered FeS (black →

Table 11. Powdered FeS-Hg^{2+} Sorption Results

Reaction Conditions	Weight FeS (gms) (± 5%)	Hg^{2+} in initial 500 ml solution		Hg^{2+} loss from 500 ml Hg^{2+}-FeS sol'n reacted 30 min.		% Hg^{2+} sorbed	C_{equil} (moles Hg^{2+}/ℓ. at equil'm) $x10^{-5}$	X ($\frac{\text{moles } Hg^{2+} \text{ sorbed}}{\text{mole FeS}}$) $x10^{-2}$
		ppm ±5%	moles $x10^{-4}$	ppm ±5%	moles $x10^{-4}$			
(A) Non-Equilibrium (FeS powder added directly to Hg^{2+} solutions) pH ~ 5 → 3.5	0.10	0.1	0.0025	0.1	0.0025	100%	0	0.022
	0.10	1.0	0.025	1.0	0.025	100%	0	0.22
	0.10	10.0	0.25	10.0	0.25	100%	0	2.2
	0.10	20.0	0.50	15.0	0.38	75%	2.5	3.3
	0.10	50.0	1.25	40.0	1.00	80%	5.0	8.8
	0.10	100.0	2.50	50.0	1.25	50%	25.0	11.0
	0.50	50.0	1.25	50.0	1.25	100%	0	2.2
	0.50	100.0	2.50	100.0	2.50	100%	0	4.4
	0.50	500.0	12.5	150.0	3.75	30%	175.0	6.6
(B) Equilibrium (3 wks) (FeS powder in water before Hg^{2+} added pH ~ 5 → 3.5) i.e. possibility Fe_2O_3 produced.	0.5	50.0	1.25	50.0	1.25	100%	0	2.2
	0.5	100.0	2.50	94.0	2.35	94%	3.0	4.12
	0.5	100.0	2.50	91.0	2.28	91%	4.5	3.99
	0.5	200.0	5.0	120.0	3.0	60%	40.0	5.2
	0.5	200.0	5.0	112.0	2.8	56%	44.0	4.7
(C) Equilibrium (2hrs) (FeS powder in water before Hg^{2+} added pH ~ 4.0)	0.25	0.5	0.0125	0.47	0.0118	99%	0.015	0.042
	0.25	1.0	0.025	1.0	0.025	100%	0.0	0.088
	0.25	10.0	0.25	9.9	0.248	99%	0.04	0.87
	0.25	60.0	1.50	30.0	0.75	50%	15.0	2.63
	0.25	200.0	5.0	40.0	1.00	20%	80.0	3.51
	0.50	0.5	0.0125	0.475	0.0120	99%	0.010	0.021
	0.50	10.0	0.25	9.5	0.2375	95%	0.25	0.42
	0.50	60.0	1.50	54.0	1.35	90%	3.0	2.37
	0.50	200.0	5.0	80.0	2.00	40%	60.0	3.51
	1.0	1.0	0.025	0.98	0.0245	98%	0.01	0.022
	1.0	10.0	0.25	9.8	0.245	98%	0.10	0.22
	1.0	60.0	1.5	58.5	1.463	98%	0.75	1.28
	1.0	200.0	5.0	140.0	3.50	70%	30.0	3.07

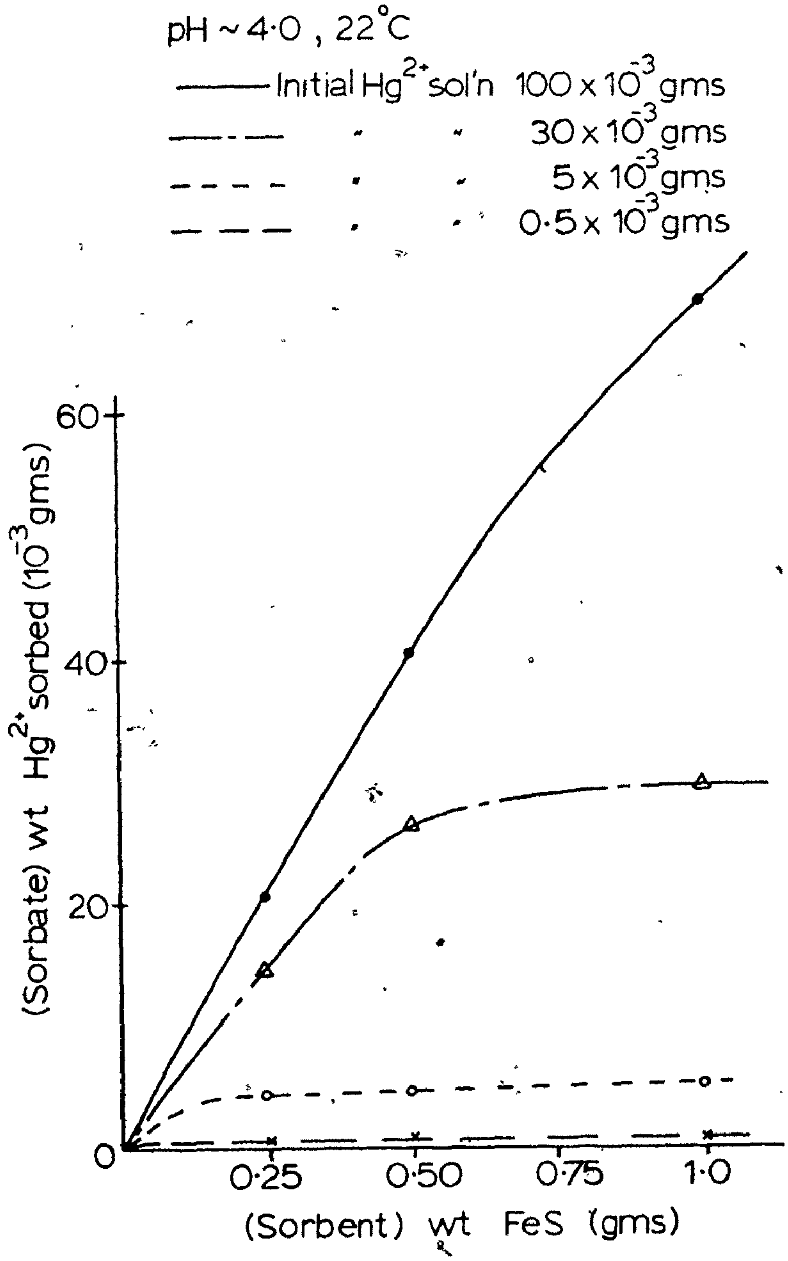

Figure 30. Mercuric Ion Adsorption on Powdered FeS.

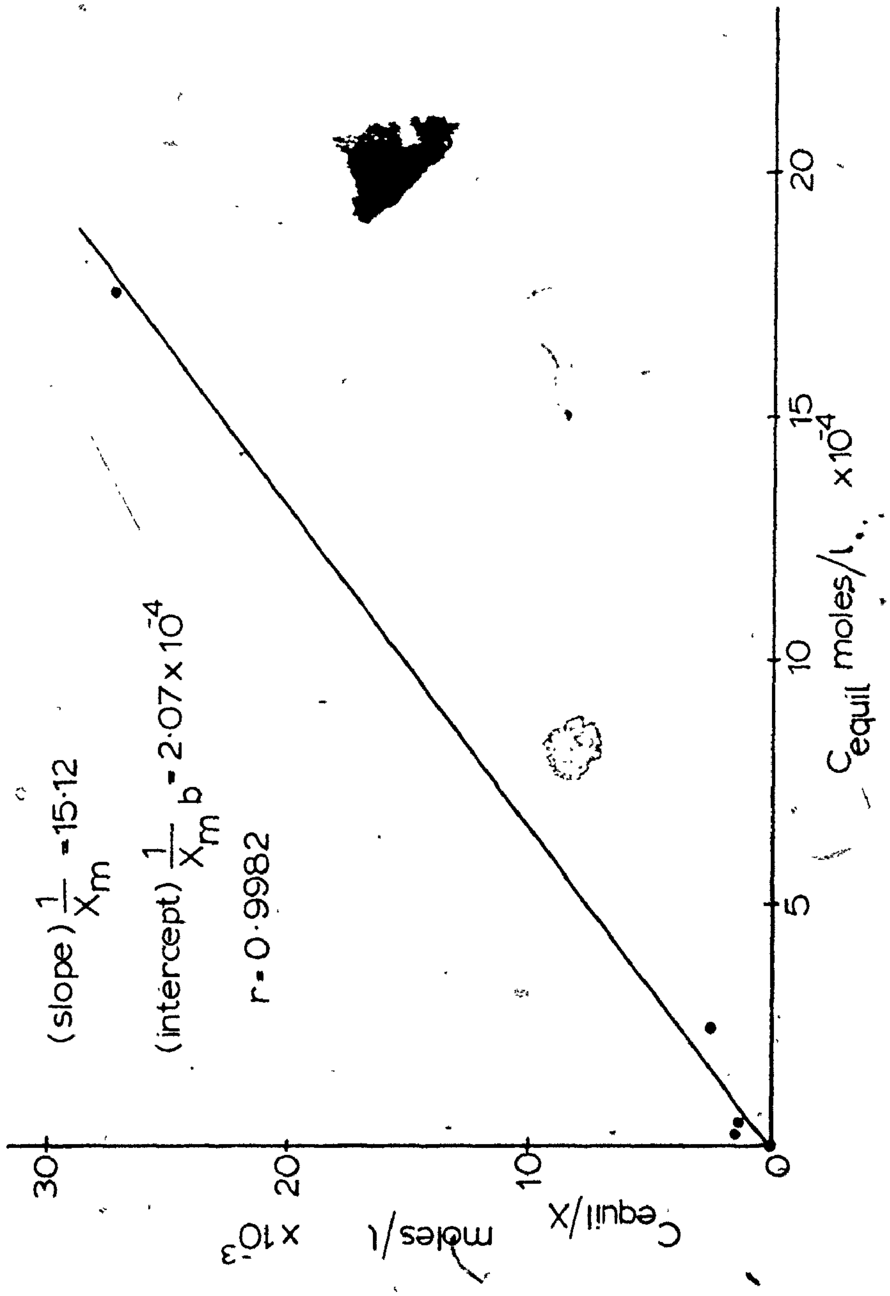

Figure 31a. Langmuir Plot, Powdered FeS - Hg^{2+} (nonequilibrium conditions), Data of Table 11a.

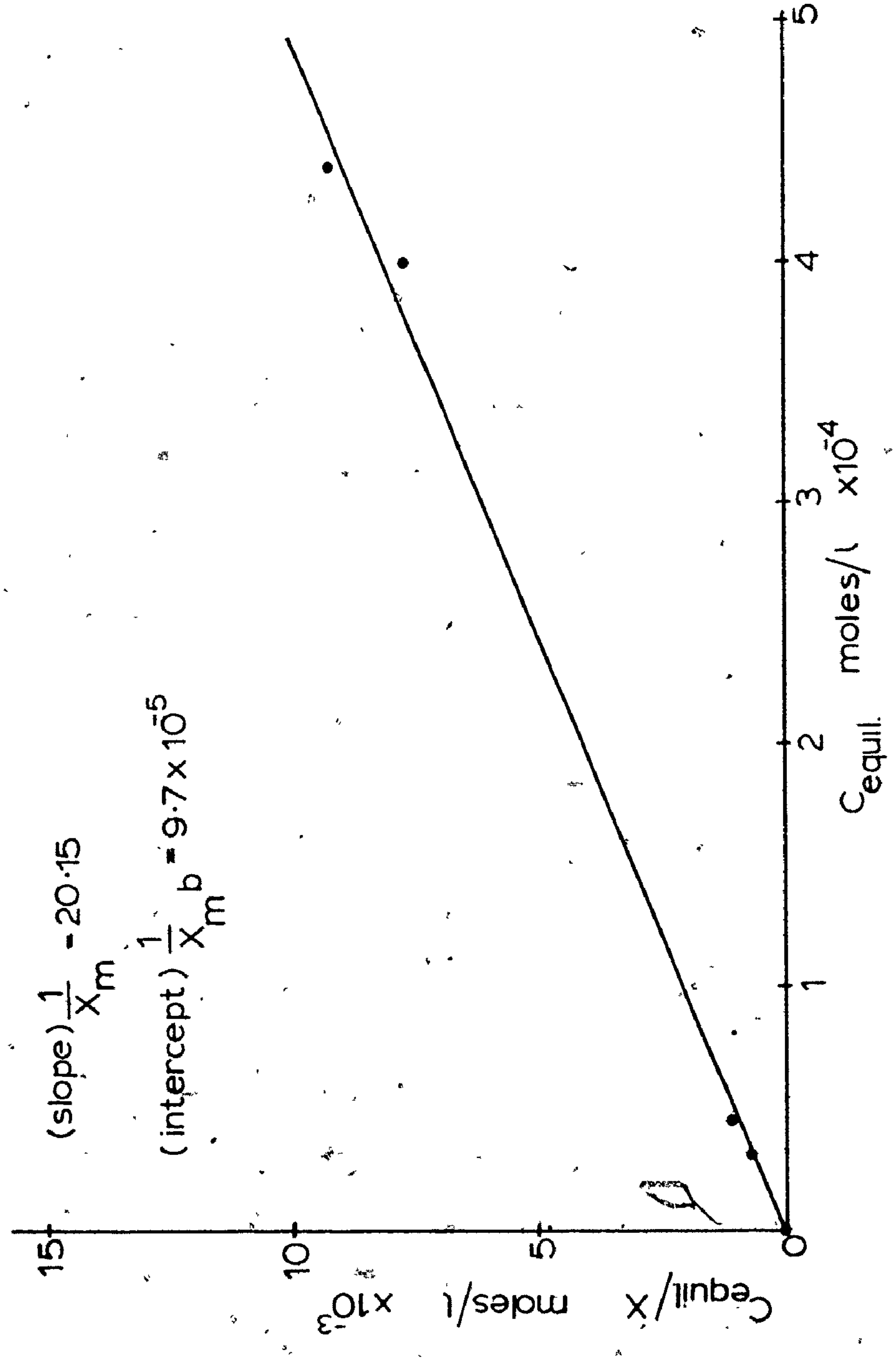

Figure 31b. Langmuir Plot, Powdered FeS - Hg^{2+} (equilibrium 3 weeks), Data of Table 11b.

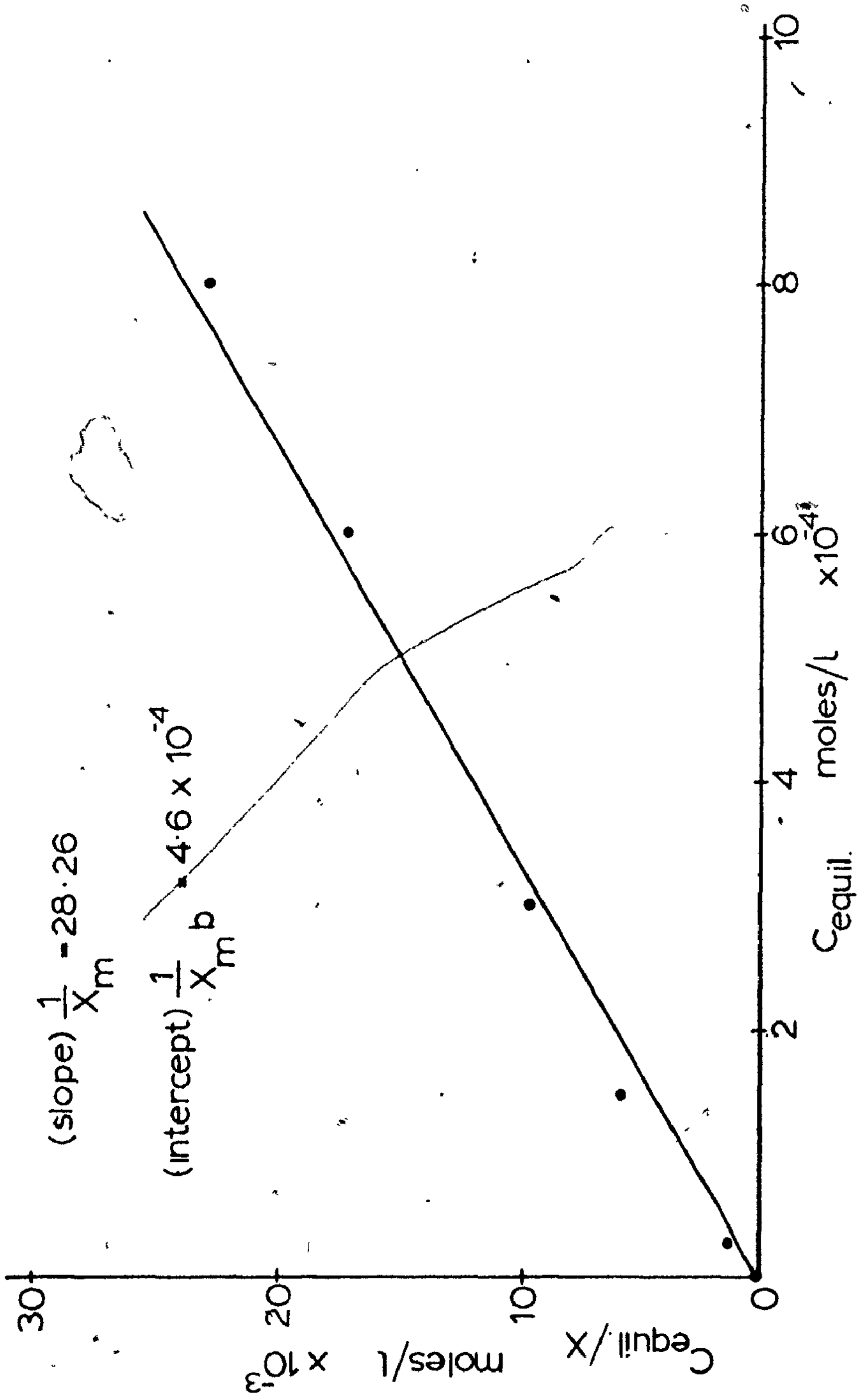

Figure 31c. Langmuir Plot, Powdered FeS - Hg^{2+} (equilibrium 2 hours), Data of Table 11c.

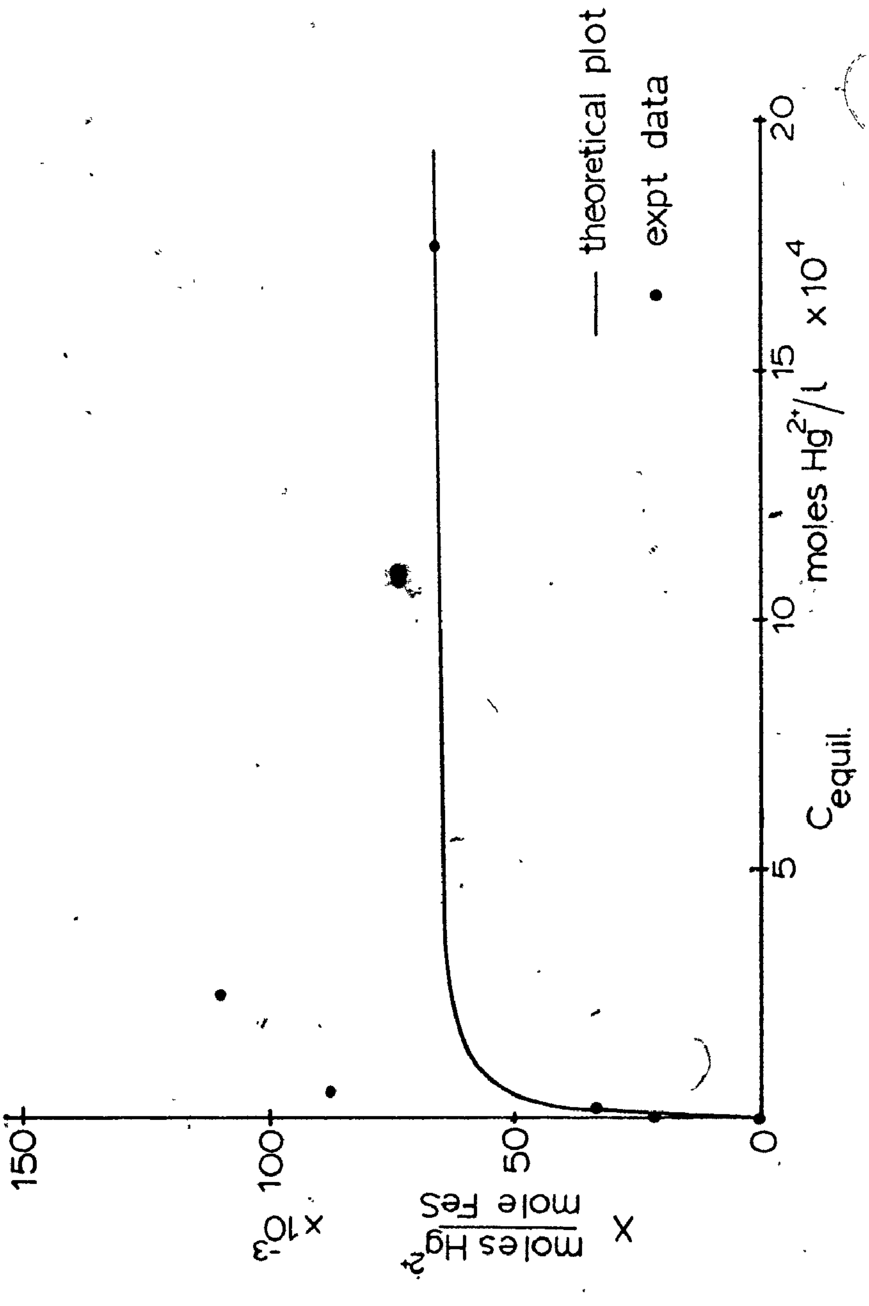

Figure 32a. Langmuir Isotherm, Powdered FeS - Hg^{2+}, Results of Table 11a.

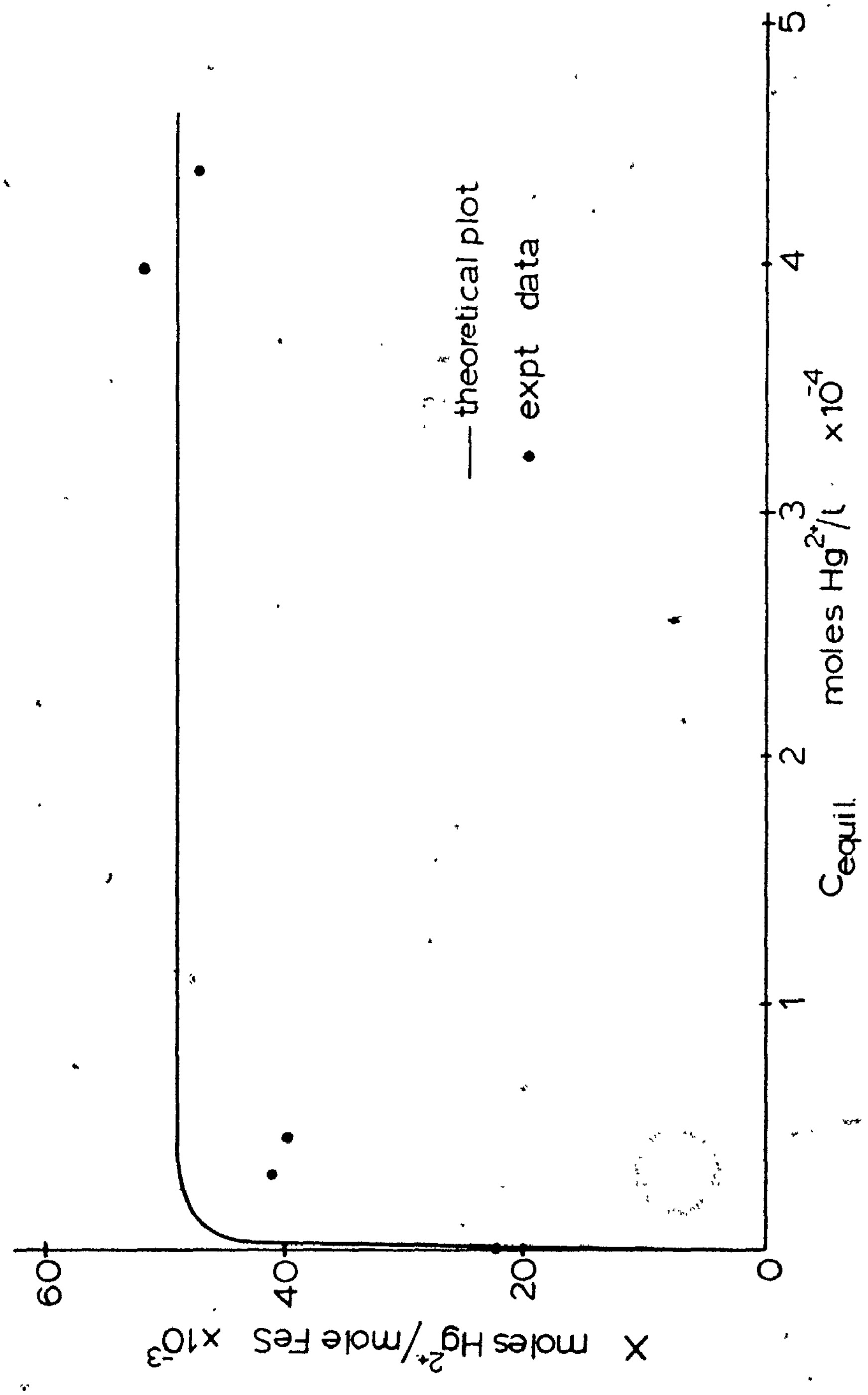

Figure 32b. Langmuir Isotherm, Powdered FeS - Hg^{2+}, Results of Table 11b.

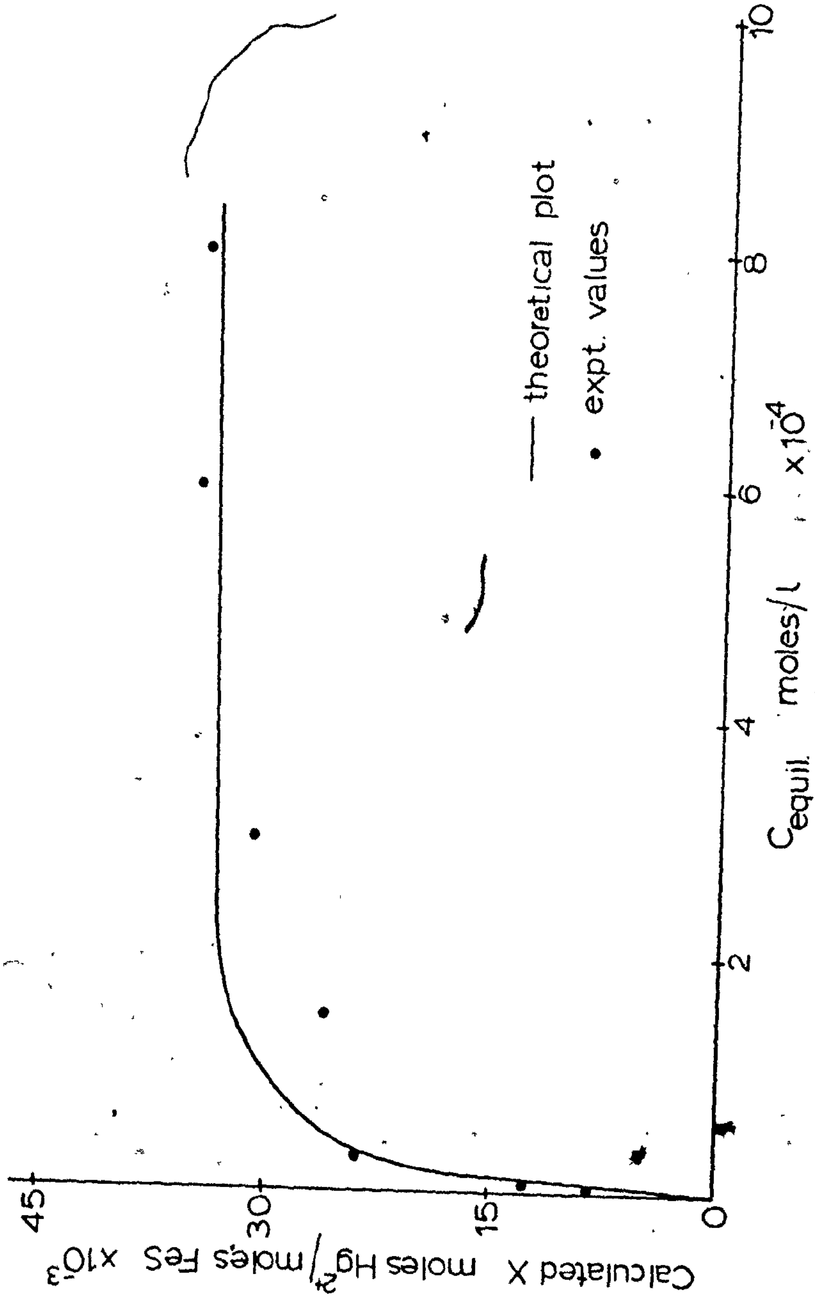

Figure 32c. Langmuir Isotherm, Powdered FeS - Hg^{2+}, Results of Table 11c.

reddish brown). Using the X_m values determined from the Langmuir plots and Equation 39, an estimate of the surface area of the powdered FeS was also found (Table 12).

Experiments in which iron sulphide was equilibrated in water two hours and then adjusted to pH ~ 4, gave the most reproducible sorption data and surface area determinations, (Table 12). These equilibrium results fit well to the Langmuir adsorption equation and adsorption isotherm. The good linear fit indicated a sorption process which was proportional to sorbent surface area and sorbate concentration at constant pH.

These results and the non-equilibrium results do not vary significantly however. Adsorption of mercuric ions by iron sulphide surfaces occurred very quickly (minutes) over a pH range of 3.5 → 5.5, and occurred regardless of solution-mineral thermodynamics. It is most satisfying that even in non-equilibrium conditions, the iron sulphide ore sorbs mercuric ions quickly and to a large degree. For large scale applications to treat water polluted with mercuric ions, the crushed ore could be placed in either ion exchange type columns or used in fluidized-bed type processes.

The calculated solubility reaction of FeS in water, (Appendix A.5.1) indicates that the concentration of iron and sulphur increases with solution acidity. A simple precipitation of mercury sulphide (HgS) is not the dominant reaction causing mercuric ion loss from solution. The results of Table 11 indicated that sorption of mercuric ions is proportional to initial mercury concentration and surface area (weight) of sorbent present in solution. No mercury ion and lattice iron ion exchange was noted for these adsorption reactions because no iron increase in solution was seen. Thus no comparisons with the barium-

Table 12

FeS Surface Area Calculations from Results of Table 11.

	$\frac{1}{X_m}$[†]	X_m[††]	$\frac{1}{X_m b}$[‡]	b[‡‡]	S[†††]
	(slope)	$\frac{\text{moles Hg}^{2+}}{\text{mole FeS}}$ x 10^{-2}	Y Intercept x 10^{-4}	Adsorption Constant x 10^{4}	Surface Area m^2/gm.
(A) Non-Equilibrium Results	15.12	6.6	2.07	7.32	17.1
(B) Equilibrium Results (3 weeks)	20.15	4.96	0.97	20.8	12.9
(C) Equilibrium Results (2 hours)	28.26	3.55	4.67	6.05	9.24

[†] from Langmuir plots; Figures 31, 32; also see Equation 37.

[††] X_m, the maximum adsorption capacity.

[‡] from Langmuir plots; Figures 31, 32 and Equation 37.

[‡‡] b, constant related to the heat of adsorption (energy of sorption).

[†††] See Equation 39.

calcite exchange sorption mechanism should be made in this case. Sorption of mercury on iron sulphide would seem to obey a similar mechanism as sorption of metal cations on various mineral oxides of manganese, iron, silicon, titanium, etc. (Chapter 2), i.e.

$$XO \sim H + M^{2+} \rightleftharpoons XO \sim M + H^+ \quad (51a)$$

$$\text{and} \quad 2(XO \sim H) + M^{2+} \rightleftharpoons 2(XO) \sim M + 2H^+ \quad (51b)$$

where "X" refers to a surface lattice cation. In the case of mercuric ion sorption on iron sulphides, possible reactions are then

$$-FeS \sim H + Hg^{2+} \rightleftharpoons FeS \sim Hg + H^+ \quad (52a)$$

$$\text{and} \quad 2(-FeS \sim H) + Hg^{2+} \rightleftharpoons (FeS)_2 \sim Hg + 2H^+ \quad (52b)$$

The results of the powdered pyrrhotite study indicate the above reactions may be possible. From the results of Table 13, the decrease in Hg^{2+} concentration in solution caused by sorption onto the various weights of pyrrhotite is usually balanced by a corresponding increase in solution pH (i.e. in moles H^+).

In each example, the adsorbed Hg^{2+} and released H^+ content is proportional to initial sulphide weight. Note, H^+ increase in solution is always less than the corresponding drop in Hg^{2+} concentration. Possible errors in pH measurement and analysis of Hg^{2+} concentration in solution may account for this discrepancy. Parallel reactions of pyrrhotite in solution (i.e. $FeS + H_2O \rightarrow OH^- + HS^- + Fe^{2+}$) producing OH^- during adsorption, however, could account for the observed $[H^+]_{\text{released}} < [Hg^{2+}]_{\text{sorbed}}$ reaction i.e. via neutralization, ($OH^-_{\text{produced}} + H^+_{\text{released}} \rightarrow H_2O$).

Table 13

Solution Changes During Hg^{2+} Adsorption

*Wt. FeS reacted (gms) ±5%	Initial Hg^{2+} content in 500 ml sol'n moles($\times 10^{-4}$)	Solution pH		$[H^+]_{released}$	$[Hg^{2+}]_{sorbed}$
		Initial	Final (30 minutes)	moles ($\times 10^{-4}$)	moles ($\times 10^{-4}$)
0.25	0.25	4.02	3.86	0.21	0.25
0.25	1.50	4.04	3.81	0.32	0.75
0.25	5.00	4.00	3.71	0.48	1.00
0.50	1.50	3.98	3.64	0.62	1.35
0.50	5.00	4.05	3.51	1.10	2.00
1.00	1.50	3.92	3.59	0.68	1.46
1.00	5.00	4.02	3.47	1.22	3.50

* Results of Table 11c.

Evidence supporting this reaction comes from several reaction samples where the initial Hg^{2+} concentration in solution was very low (0.1 and 1.0 ppm). In these cases, the solution pH actually decreased upon sorption. Thus, when the parallel reactions producing OH^- are larger than release of H^+ caused by sorption processes, a drop in pH is seen ($[H^+]_{released} < [OH^-]_{produced}$). At large initial Hg concentrations, the sorption rate is enhanced; hydrogen ions are released in excess of hydroxyl ions produced by other reactions, and a pH increase in solution is observed.

Investigators studying sorption of metal cations on mineral oxide surfaces also observed this pattern, i.e. $[H^+]_{released} \lesssim [M^{2+}]_{sorbed}$.

Thus, exchange reactions of Hg^{2+} on iron sulphide may be written as

$$[FeSH^-]_{surf.} + Hg^{2+} \rightleftharpoons [FeSHg]_{surf.} + H^+ \quad (53a)$$

$$\text{or} \quad [FeOH \cdot SH]_{surf.} + Hg^{2+} \rightleftharpoons [FeSHg]_{surf.} + H_2O \quad (53b)$$

Calculations of mercury ion coverage on the crushed iron sulphide surfaces, using the data of (Table 11) indicate monolayer coverage. For example, a calculated average estimate of available adsorption sites on the non-stoichiometric $Fe_{1-X}S$ surface was found to be ~ 8×10^{14} sites/cm^2. The data of Table 11, indicated a maximum surface coverage of ~ 2×10^{15} ions/cm^2, assuming the iron sulphide surface area is ≃ 10 m^2/gm, (Table 12). The surface area of the powdered FeS using S.E.M. methods was found to be approximately 1.9 m^2/gm (Appendix A.5.3). This value and the surface area determined experimentally (10m^2/gm) are in qualitatively good agreement considering the errors and assumptions made in this calculation.

A simple calculation follows which indicates the possible use of crushed pyrrhotite in mercury pollution abatement work. If a polluted water supply containing 10 ppb mercury was eluted at a flow rate of 1000 litres/minute through a column containing 1 ton of 100 mesh crushed pyrrhotite, it would take ~ 15 years to attain monolayer coverage (saturation of the FeS). This surface saturation time estimate assumes that all mercury is removed from solution during elution.

From these preliminary sorption results, it is highly probable that an economical and efficient mode of mercury ion removal from solution (and atmosphere) is possible using crushed pyrrhotite. The XPS study, to follow, collaborated this result and provided additional information because much lower mercury concentrations in solution and other solution variables, such as counter-ion effects, could be examined.

5.3 Polished Iron Sulphide Plates - XPS Study

5.3.1 Experimental

High grade pyrrhotite ($Fe_{1-X}S$) and pyrite (FeS_2) ores were studied using the XPS technique to determine their ability to adsorb mercury ions from trace mercury chloride solutions. The Sudbury pyrrhotite was highly pure but had trace silica and chalcopyrite as impurities. Two varieties of pyrite, a high grade massive ore from Tennessee and large single cubic crystals (1" x 1") from Spain were examined. These sulphide ores were cut to a size which easily fit the XPS sample holder. The pyrrhotite slabs were then epoxyed onto identically sized aluminum plates and ground and polished using a 30 micron diamond platter followed by diamond powder on a lead lap. A final 8 micron mirror-like finish was attained. Several of the pyrrhotite plates were not polished and several of the polished plates were roughened using fine grade crocus cloth and used in a study of adsorption rates with surface roughness. The cut pyrite slabs were not polished in this study. But many of the naturally grown outer surfaces of these large single cubic crystals were compared to cut surfaces for variation in sorption rates.

Each sulphide plate was washed thoroughly in acetone and distilled deionized water and air dried prior to XPS analysis for surface trace impurities of silica (SiO_2), mercury, chlorine, etc. These plates were then reacted in 500 ml of various concentrations of mercuric chloride or in elemental mercury (Hg°). All stock solutions and dilutions were prepared using analytical grade mercuric chloride and sodium chloride supplied by BDH chemicals and freshly produced distilled deionized water. Solutions containing mercuric ions were stored and reacted in polypropylene storage containers and beakers. Preliminary studies involved the reaction of FeS plates in various mercuric ion eoncentrations without regard to initial solution pH (i.e. solution pH regulated by mercuric chloride only). More extensive experiments were then undertaken with better controlled and monitored reaction conditions. Small additions (drops) of concentrated HCl (12 M) or NaOH (16 M) were used to control the solution pH at constant values of either 4 or 7. These sorption reaction rates were also monitored with time and sodium chloride concentration. Several sulphide plates were also placed in beakers of Hg°, pre-equilibrated with water for 2 days (10 ml Hg° + 500 ml H_2O) or directly face down on the Hg° (4 days), to determine Hg° adsorption rates on iron sulphide.

Practical applications of these results were then attempted using waste water effluent collected at a chlor-alkali pulp and paper complex. These solutions contained both trace elemental mercury atoms (Hg°) and mercuric ions as contaminants. Analysis using spark source mass spectroscopy[12] (unpublished) indicated a large sodium and chlorine content as well. Two one gallon aliquots were collected and stored in polypropylene containers: (a) a chemically treated portion leaving the plant site (returning to the natural environment) with a pH ~ 6.2, mercury concentration ≈ 5 ppb and sodium, chlorine concentration ≈ low 100's ppm and (b) a non-treated process solution used only within the plant site having a pH ~ 5.5, mercury concentration ≈ 2 ppm and sodium, chlorine content > 2000 ppm.

Using procedures discussed above, sulphide plates were reacted in 500 ml of these two solutions for various time periods at their natural pH and at a constant pH ~ 4 (controlled by small additions of concentrated hydrochloric acid).

After a specific period of reaction, each plate was carefully removed from its reaction solution and washed (dipped) five separate times in fresh distilled deionized water to remove unadsorbed, adhering mercury ions (Appendix A.1). Each plate was then air dried and analysed using XPS. Spectral parameters for all elements examined, Hg 4f, Cl 2p, S 2p, Fe 2p, C 1s, O 1s, are given in Chapter 3.3.2. In addition, Na 1s spectra, E_b = 1072 eV, for 10 scans using 111 points and 1.0 sec. dwell time; and complete wide scan spectra (0 → 1,000 eV) for 5 scans using 1,000 points and 1.0 sec. dwell time were analysed for many of the sulphide surfaces. Each spectrum was computer fit and interpreted using calibration plots produced previously (Chapter 3.3.3).

5.3.2 Discussion

The preliminary XPS analysis of sorbed mercuric ions on pyrrhotite polished plates is given in Table 14, Figures 33, 34. Several representative Hg 4f spectra are shown in Figure 35. These spectral peak areas were referred to appropriate calibration plots (Chapter 3.3.2) to determine weights (gms.) of mercury adsorbed. It is interesting that the weight of mercury sorbed decreases with increasing $HgCl_2$ solution content. A likely explanation for this odd behaviour is that the solution pH increases with increasing $HgCl_2$ content, and sorption is pH dependent.[13] At pH values less than 7, the major mercuric ion species in solution is $HgCl_2^\circ$, however at greater pH values or when no chloride ions are present, the dominant species is $Hg(OH)_2^\circ$.[9] If as suggested by McNaughton et al. studies[9], the $HgCl_2^\circ$ species is not sorbed on silica, then it is apparent that Hg^{2+} and/or $Hg(OH)_2^\circ$ species will be preferentially sorbed. The results of my preliminary iron sulphide study usually indicated low chloride ion sorption at any initial $HgCl_2$ solution concentration. This observation is not consistent with the known mercuric species (i.e. $HgCl_2^\circ$) in acidic solution. Obviously the reaction between the surface and mercuric ions (Hg^{2+}) is very specific or more likely, the $HgCl_2^\circ$ species reacts with the surface sulphur sites upon sorption and liberates chloride ions into solution.

Several of the XPS spectra from Table 14 indicated two distinct mercuric 4f peaks as shown in Figure 36. XPS analysis of $HgCl_2$ and Hg_2Cl_2 powder, (pressed into pellets) indicated only a small chemical shift of approximately 0.2 eV between the two oxidation states. Thus the large

Table 14. Preliminary XPS Study of Adsorption of Hg^{2+} on FeS

*Initial Hg^{2+} conc. (ppm) (as $HgCl_2$)	**Reaction Time (min.)	Mercury 4f Peak Area Intensity ($\times 10^3$)	***Wt. Hg^{2+} (gms) ($\times 10^{-8}$)
(a) Polished FeS plates			
1.0	30	15.0	10.0
	240	100.0	>100.0
10.0	30	13.0	8.0
	240	20.0	15.0
50.0	0.2	NIL	NIL
	30	8.0	5.0
	240	28.0	20.0
	360	50.0	42.0
(b) Scratched FeS plates			
1.0	360	56.0	30.0
10.0	360	16.0	10.0
50.0	360	92.0	50.0
(c) Polished FeS plates			
0.2	5	6.5	4.0
	30	14.0	11.0
	360	26.0	22.0
	1440	55.0	46.0
1.0	30	22.0	17.0
	360	27.0	23.0
	1440	37.0	31.0
10.0	5	22.0	17.0
	10	42.0	35.0
	30	48.0	41.0
	360	28.0	23.0
	1440	61.0	52.0
50.0	5	26.0	22.0
	10	25.0	21.0
	30	23.0	20.0
	360	42.0	36.0
	1440	64.0	55.0

* 500 ml Hg^{2+} solution used.

** FeS plates dipped 5 times in fresh water to remove adhering Hg^{2+} solution (Appendix A.1).

*** Equivalent weight of Hg^{2+} estimated from Hg^{2+} calibration plots (Chapter 3).

+ Peak Area Intensity for 50 scans Hg 4f.

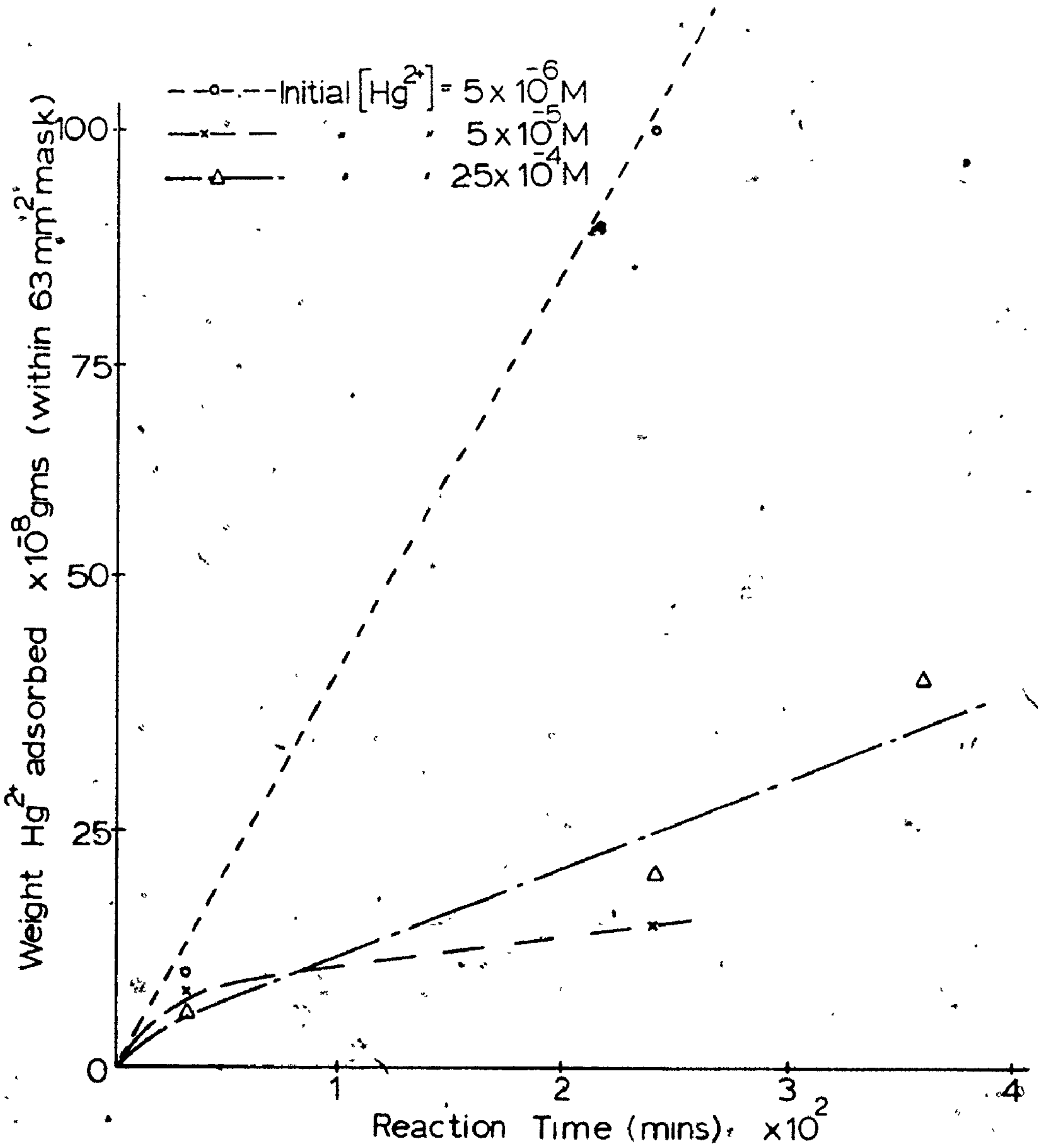

Figure 33. Preliminary ESCA Results, Hg^{2+} Sorption on Polished FeS Plates.

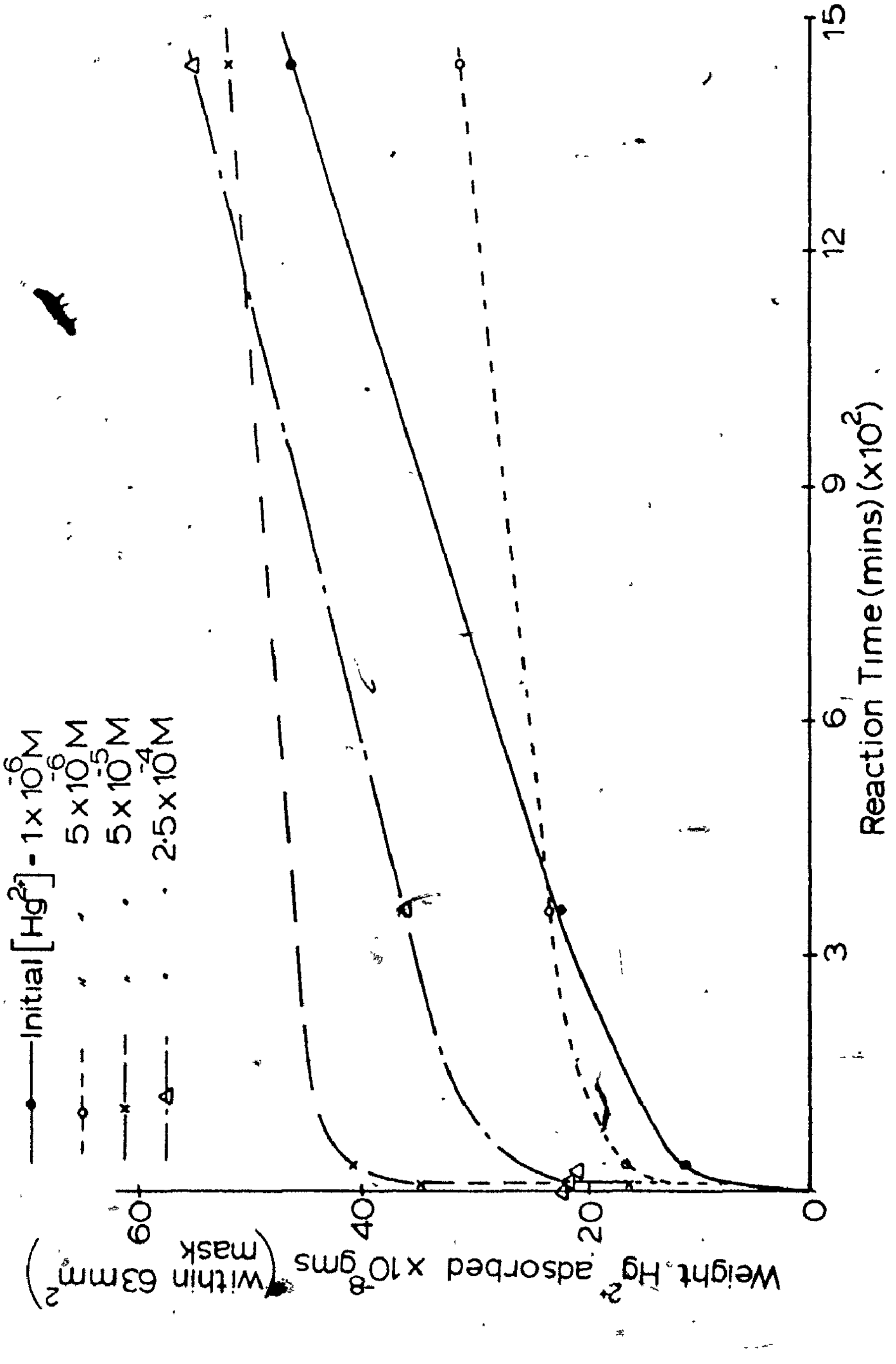

Figure 34. Preliminary ESCA Results, Hg^{2+} Sorption on Polished FeS Plates.

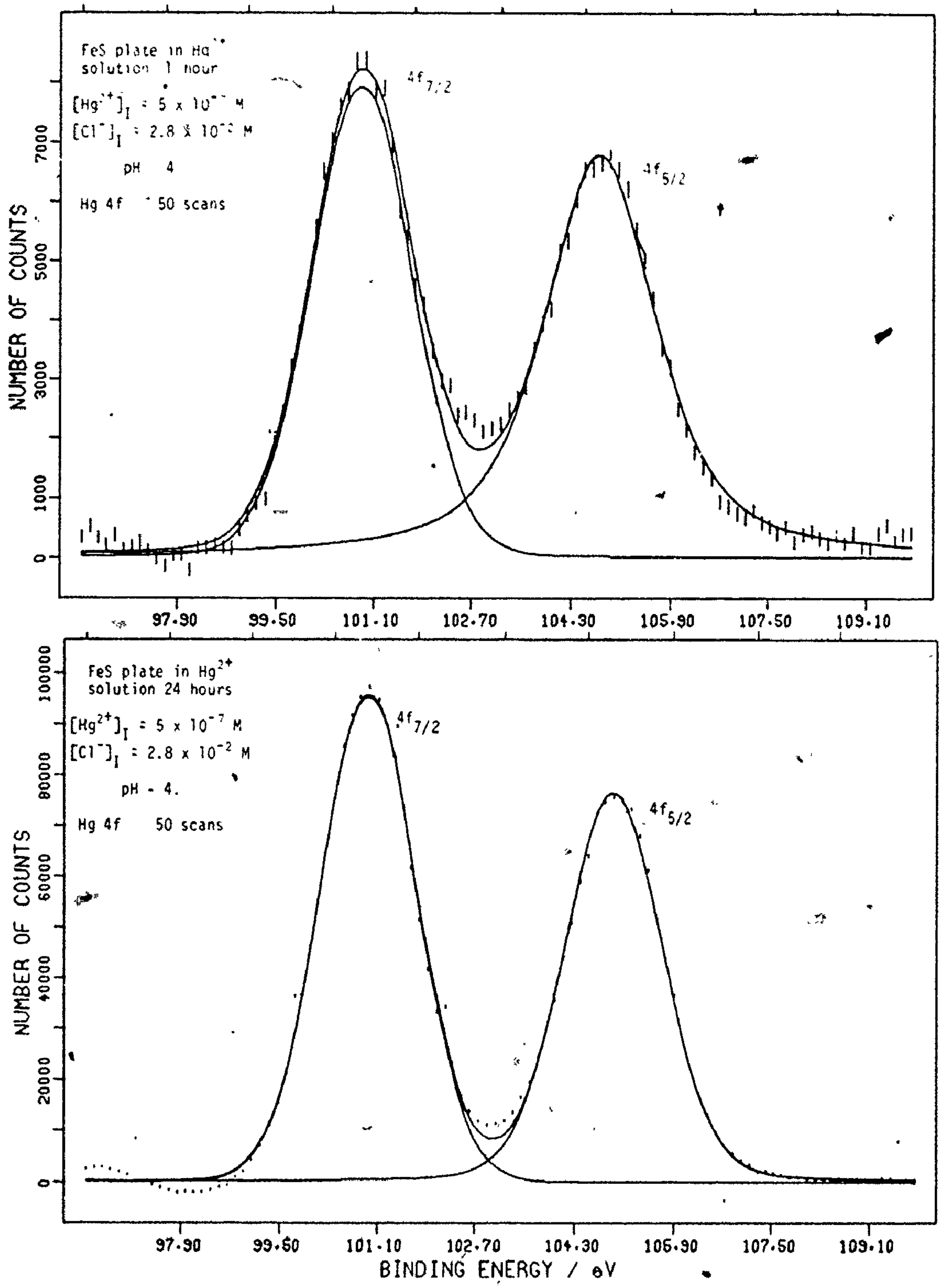

Figure 35. Representative Adsorbed Hg 4f ESCA Spectra.

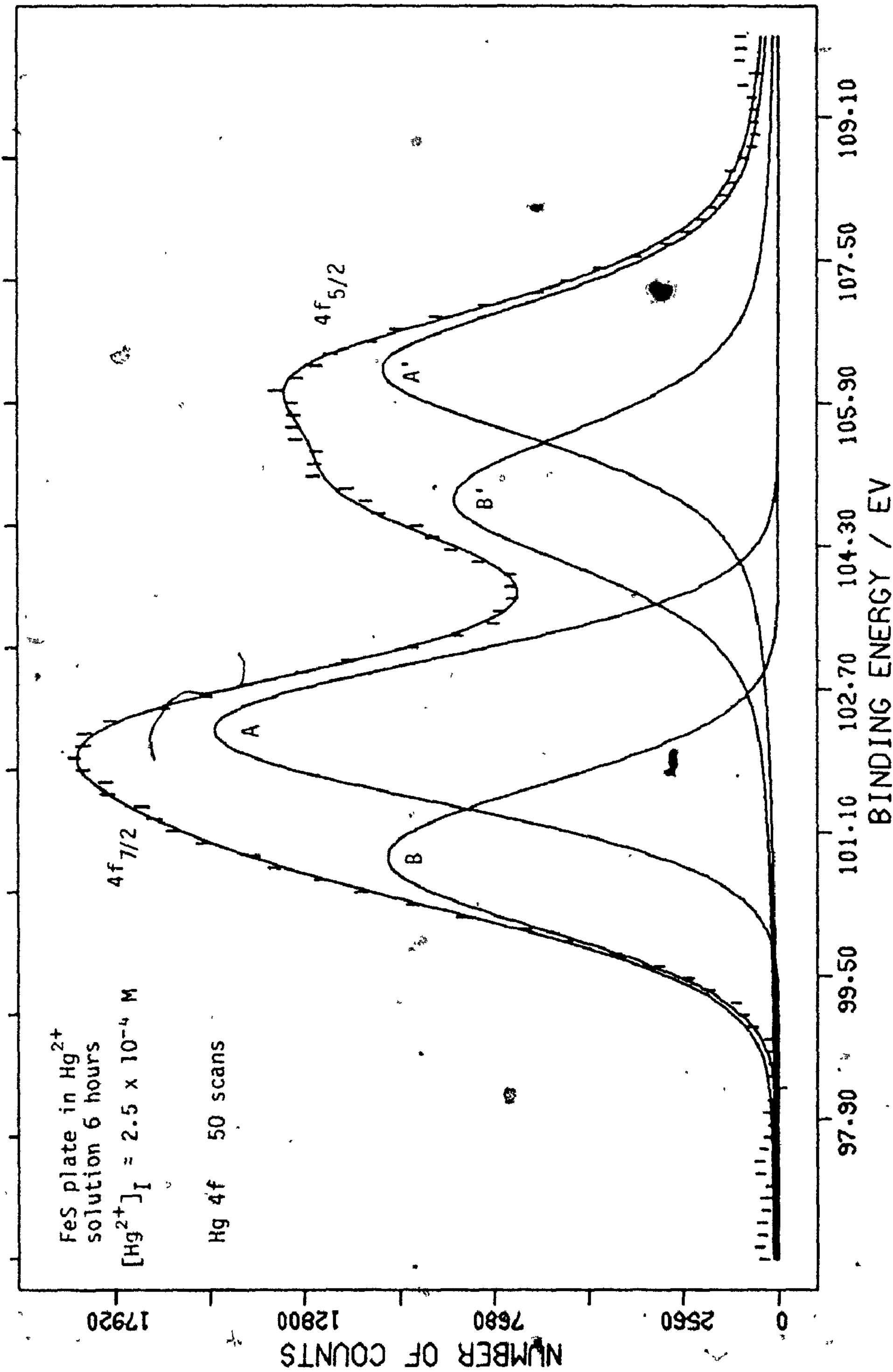

Figure 36. Hg 4f ESCA Spectrum Showing Two Oxidation States.

observed shift (Figure 36) of approximately 1.0 eV cannot be explained as simply due to the two mercury oxidation states. Mercuric ion sorption at both sulphur ($S^=$) and oxygen ($O^=$) sites on the mineral surface is possible. The O 1s spectra of all pyrrhotite and pyrite plates (Figure 37) indicated three oxygen species on the surface.

The O 1s peak at E_b ~ 530 eV is due to oxygen (O^{2-}) bonded to iron as an oxide and is caused by oxidation of the sulphide surface during cutting, polishing and reaction in aqueous solution. The O 1s peak located at E_b ~ 532 eV is due to contamination water vapour or hydroxyl groups from the XPS vacuum system and/or reaction in water. The third O 1s peak at E_b ~ 533 eV is attributable to physically adsorbed O_2 gas from the reaction solution.[14,15] Ney[16] found that sulphide minerals adsorbed dissolved oxygen from aqueous solution to a much larger degree than for most minerals.

It should be noted that oxide peak (a) decreases with reaction time, eg. as the surface becomes covered with sorbed mercury ions; peak (b) at 532 eV usually remained unchanged regardless of reaction time and peak (c) at 533 eV increased with reaction time. Therefore sorption of mercury ions onto both sulphide and oxide sites is a reasonable assumption.

Effects of pH upon sorption rates, Table 15, Figure 38, were then studied. These results indicated again that small initial mercuric chloride concentrations produced large weights of mercury sorbed on the pyrrhotite surface. It was found that adsorption of mercuric ions is large at pH ~ 4 while at pH ~ 8, the amounts are very much reduced. Solubility considerations of FeS may be key to this sorption behaviour. The dissolution of iron and sulphur ions from the surface lattice

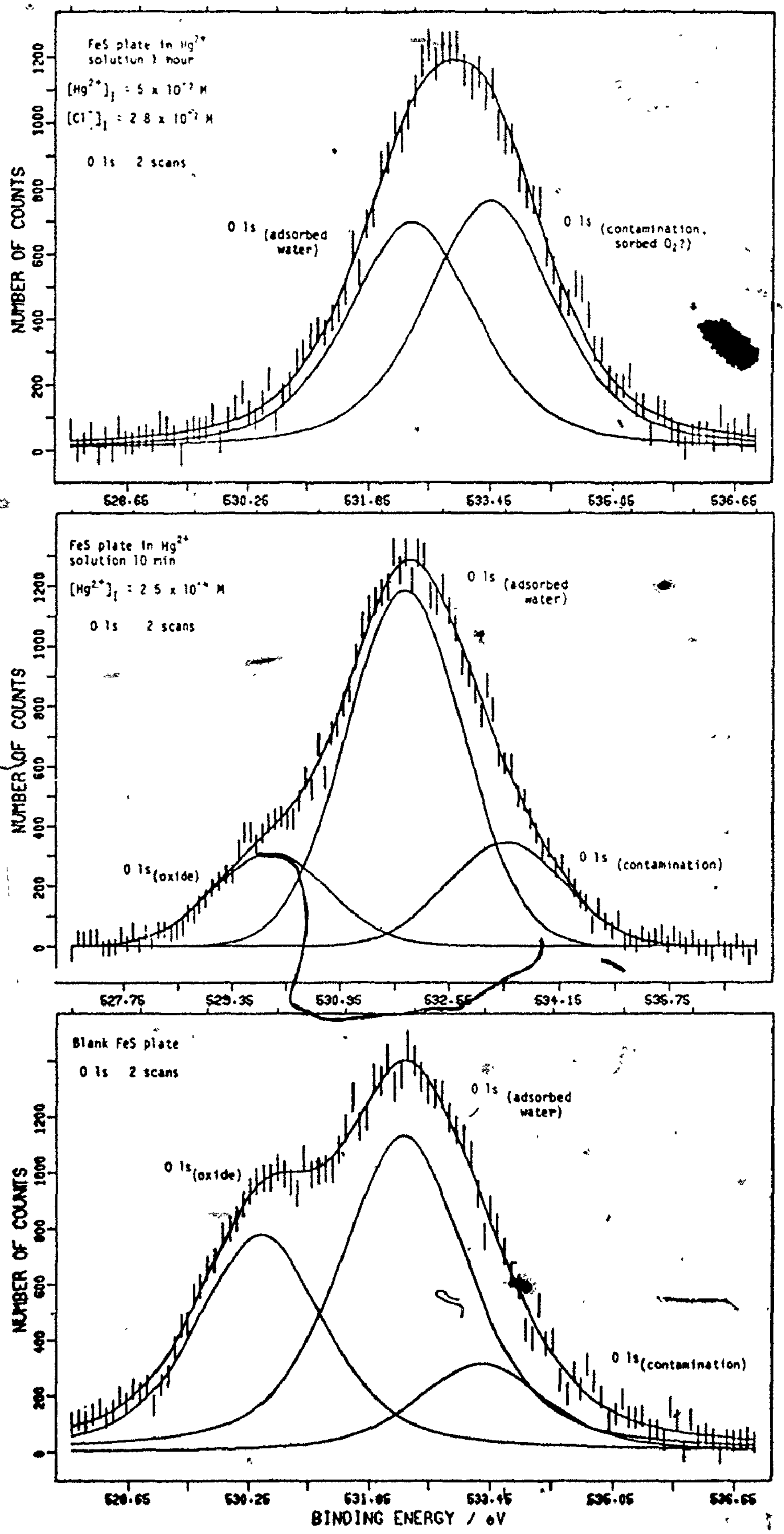

Figure 37. 0 1s ESCA Spectra of FeS, Effects of Adsorption.

Table 15. Effect of pH on Hg^{2+} Adsorption on FeS Plates

*Initial Hg^{2+} concentration (ppm)	**Reaction time (min.)	†Mercury 4f Peak Area Intensity ($\times 10^{4}$)	***Equivalent Weight of mercury adsorbed ($\times 10^{-8}$)
Polished FeS plates			
(a) pH ~ 4.0			
1.0	100 1440	28.6 45.0	>>200.0 >>>200.0
10.0	100 1440	8.6 13.0	90.0 150.0
50.0	100 1440	4.8 23.0	50.0 >>>200.0
(b) pH ~ 8.0			
1.0	100 1440	1.0 2.7	10.0 27.0
10.0	100 1440	2.6 3.2	25.0 30.0
50.0	100 1440	1.6 7.0	15.0 65.0

* as per Table 14.

** as per Table 14.

*** as per Table 14.

† as per Table 14.

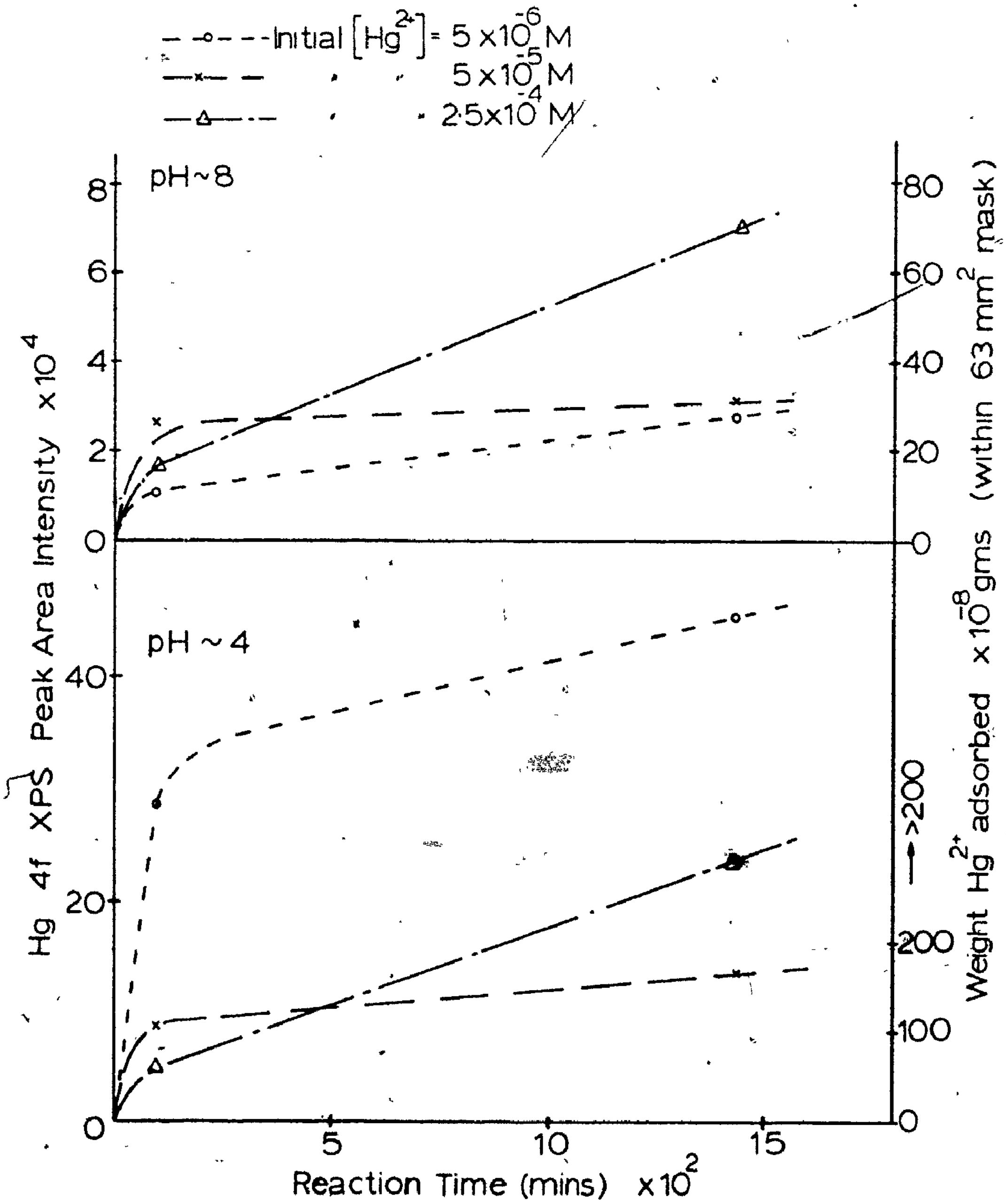

Figure 38. pH Effects of Hg^{2+} Adsorption onto Polished FeS Plates.

increases in acidic conditions.

As previously noted, in basic conditions the $Hg(OH)_2^{\circ}$ species dominates and thus at pH ~ 8 and low chloride content, large mercuric ion sorption rates should be observed if a simple hydrolysis mechanism for sorption was in operation.[9] Obviously for sulphide minerals, other factors dominate the sorption rates.

More intensive studies using both pyrrhotite and pyrite plates, Table 16, at a solution pH ≃ 4 ($HgCl_2^{\circ}$ species dominant) and variable sodium chloride content (0, 100, 1000 ppm), were then undertaken. These results indicated that for each initial mercuric ion concentration and constant time of reaction, the sorption rate of mercury increased with increasing chloride concentration (Figure 39). Mercury sorption rates on iron sulphide minerals do not follow a simple cation hydrolysis relationship as previously suggested for oxides.[9]

In the present XPS studies, little chloride and nil sodium ions were detectable although the initial solution concentrations of NaCl was as large as 1000 ppm Cl^-. The large sorption of mercury ions from these highly electrolytic but initially low concentrations of mercury solutions, indicated that sorption is highly specific. Possibly the addition of a large salt content into dilute mercury concentration creates a positive pressure so to speak, forcing the neutral/positive mercury species towards the negative sulphide surface.[17] The point of zero charge (P.Z.C.) for pyrrhotite occurs at pH ~ 3.[18] The surface and mercury ion collision rate and thus rate of adsorption is therefore enhanced. At larger initial mercury concentrations, the salt's influence is less pronounced, as expected, because the surface and mercury ion collision rate is initally very large.

Table 16. XPS Study of Mercury Adsorption on Iron Sulphides - Variation with Chloride Concentration

*Initial Hg^{2+} concentration ppm	**Reaction Time (min.)	†Mercury 4f Peak Area Intensity (x10^4)			***Equivalent weight mercury adsorbed gms (x10^{-8})		
		Initial Chlorine concentration (ppm)			Initial Chlorine concentration (ppm)		
		0	100	1000	0	100	1000
(A) pH - 4.0							
1. FeS polished plates							
0.02	1440	3.6	29.4 23.0	38.7	30.0	>100.0	>>100.0
0.10	5 60 1440	--- 0.82 30.6	0.42 2.12 56.9	0.47 7.30 69.5	--- 6.0 >100.0	3.0 16.0 >>100.0	3.0 56.0 >>>100.0
1.0	60 1440	53.0 40.6	43.8 40.6	38.2 52.4 47.0	>>100.0 >>100.0	>>100.0 >>100.0	>100.0 >>100.0
2. FeS scratched plate							
0.10	1440	---	26.6	54.0	---	>100.0	>>100.0
3. Spanish FeS$_2$ (single crystals)							
0.02 (a) natural surfaces	1440	---	7.3	6.3	---	55.0	50.0
(b) cut surfaces	1440	.66	3.0	6.0	5.0	20.0	45.0
0.10 (a) cut surfaces	1440	18.9 22.6	11.1	10.9 12.4	>100.0	90.0	-100.0
(b) bottom side of crystal(a)	1440	---	0.0	1.1	---	0.0	7.0
4. Sudbury Massive FeS$_2$ ore							
0.02 cut plate	1440	1.0	7.4	9.4	8.0	50.0	70.0
0.10 cut plate	1440	---	14.0	10.0	---	100.0	80.0
(B) pH - 7.0							
5. FeS polished plate							
0.10	1440	2.3	6.0	2.3	20.0	50.0	20.0

* as per Table 14.

** as per Table 14.

*** as per Table 14.

† as per Table 14.

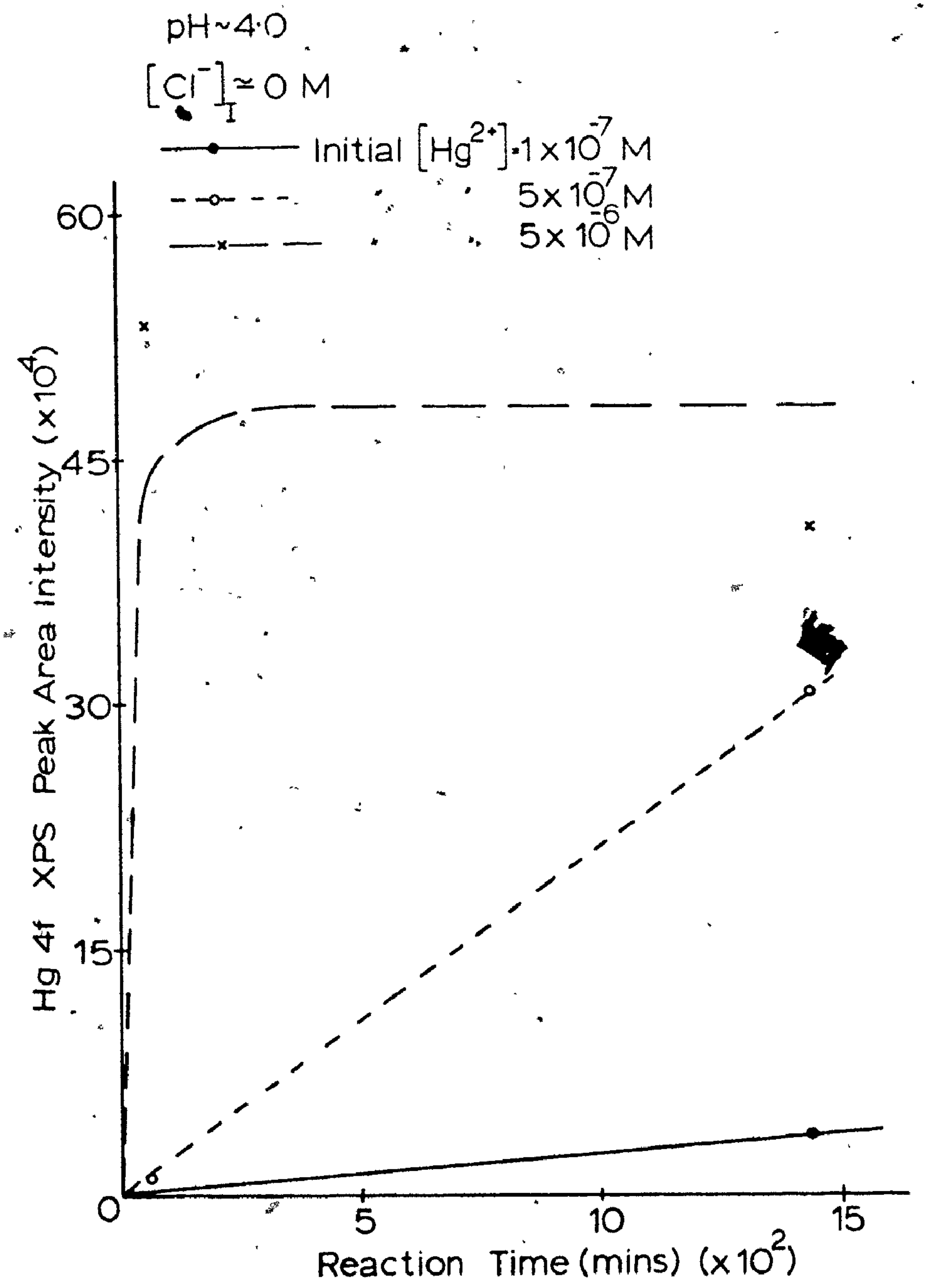

Figure 39a. Hg^{2+} Adsorption onto Polished FeS Plates. Effects of Chloride Concentration.

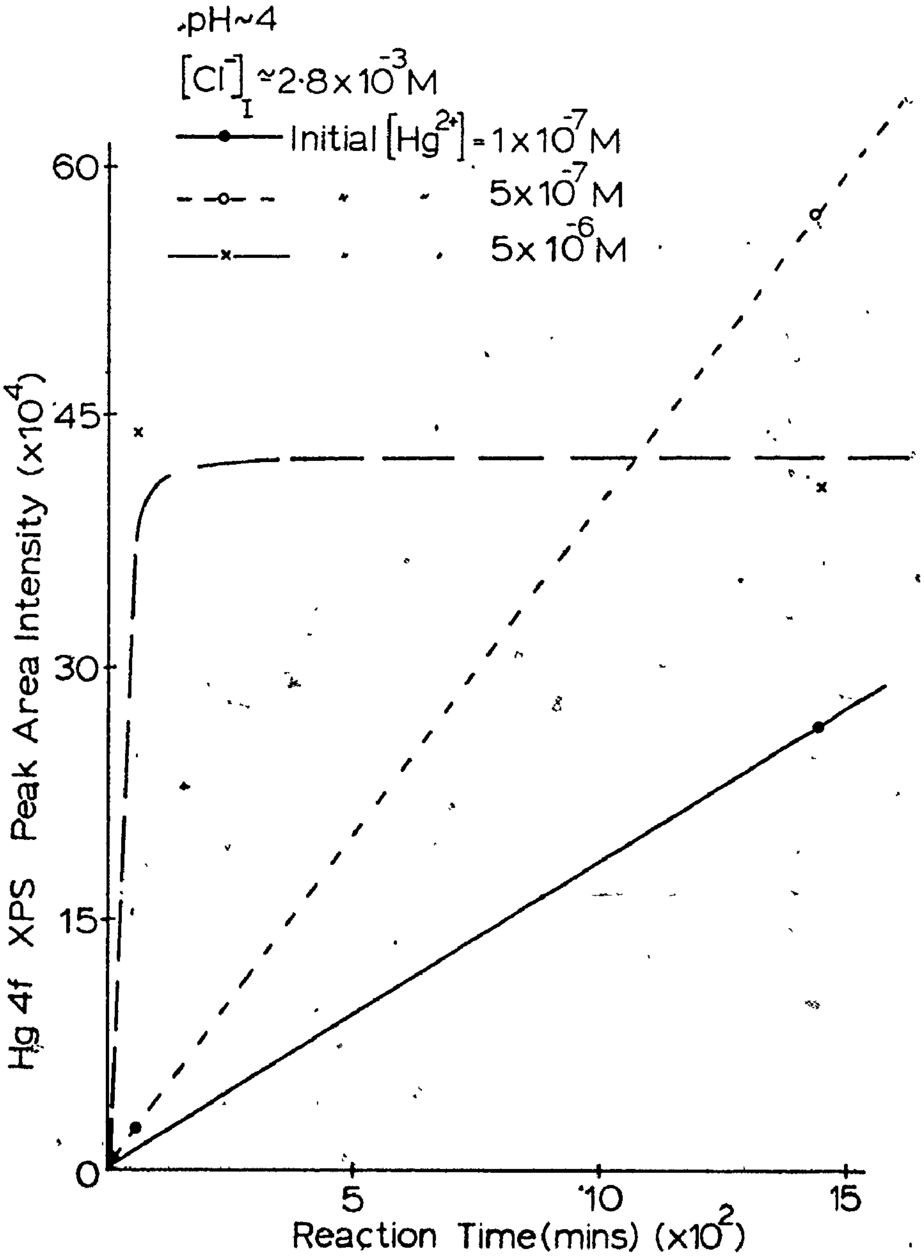

Figure 39b. Hg^{2+} Adsorption onto Polished FeS Plates. Effects of Chloride Concentration.

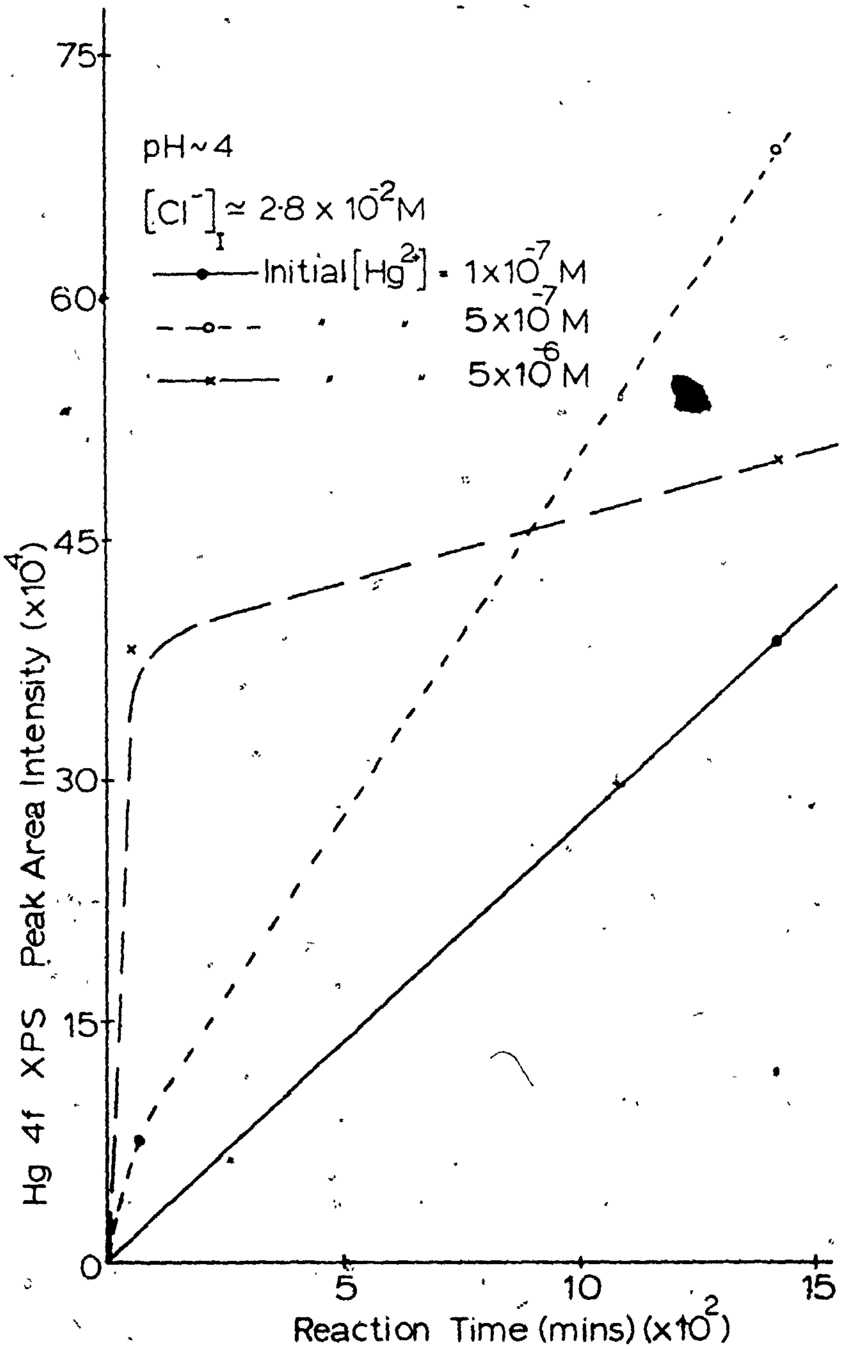

Figure 39c. Hg^{2+} Adsorption onto Polished FeS Plates. Effects of Chloride Concentration.

Sulphide plates studied at pH ≃ 7, Table 16 produced a much lower sorption rate with respect to the results at pH ~ 4. This indicated again the pH influence upon sorption rates. It was also found that pyrrhotite sorbed much larger weights of mercury ions than pyrite assuming equivalent initial mercury, sodium and chloride ion concentrations. Thus surface lattice sites and solubility differences are important sorption reaction parameters.

The actual lattice arrangement of iron and sulphur ions in pyrrhotite indicates vacancies at iron sites (i.e. pyrrhotite is not sulphur rich, but is iron deficient). These vacant iron sites would be readily accessible to adsorbing mercury ions. Mercury adsorption (substitution) could then occur without the addition of iron to the solution and without invoking the hypothesis that hydroxylation of surface sites and/or exchange of hydrogen ions is a pre-requisite to adsorption. Of course, dissolution of the pyrrhotite surface to attain solution equilibrium would increase available adsorbing sites as well. Pyrrhotite, unlike pyrite is soluble in concentrated HCl.[19] Thus in acidic solutions containing a large Cl^- content, surface dissolution of pyrrhotite would be greatly enhanced. This important characteristic of pyrrhotite plus the previously discussed inherent iron site vacancies (creating a large negative surface charge) can be used to explain its greater rate of adsorption of mercury ions/atoms.

Several pyrrhotite and pyrite plates reacted in elemental mercury (Hg^o) and in elemental mercury in water, Table 17, were also studied by XPS for sorption rates. Both sulphide mineral surfaces proved to be excellent elemental mercury adsorbents. An earlier study of Hg°

Table 17. XPS Study of Elemental Mercury Adsorption on Iron Sulphides

*Mercury reaction type	**Reaction Time (min.)	†Mercury 4f Peak Area Intensity ($\times 10^4$)	***Weight of Mercury adsorbed (gms) $\times 10^{-8}$
(A) Elemental mercury-water equilibrium			
1. FeS polished	2880	2.54	20.0
2. FeS_2 (Spain)			
(i) natural surface	5760	22.2	>200.0
(ii) cut surface	5760	18.6	>200.0
3. FeS_2 (Sudbury massive ore)	5760	16.0	~200.0
(B) Elemental mercury			
1. FeS polished	2880	31.3	>>200.0
2. FeS_2 (Spain)			
(i) natural surface	5760	31.6	>>200.0
(ii) cut surface	5760	29.4	>>200.0
3. FeS_2 (Sudbury massive ore)	5760	32.8	>>200.0

* as per Table 14.

** as per Table 14.

*** as per Table 14.

† as per Table 14.

solubility in water at 22°C indicated an equilibrium mercury content of ≈ 25 ppb.[20] It is very apparent, that iron sulphide minerals concentrate mercury ions and atoms from extremely dilute mercury solutions, efficiently and very specifically.

Using these results (Table 14 → 17), estimates of surface coverage were determined. For example, a sorbed mercury weight of $\simeq 10^{-6}$ gm/cm^2 of surface is approximately 3×10^{15} atoms/cm^2. Calculated monolayer mercury coverage on the sulphide surface is $\approx 1 \times 10^{15}$ atoms/cm^2 (vide infra). The XPS results once again indicate that sorption on the mineral surface proceeds till monolayer coverage occurs. Factors such as chloride concentration, mercury ion concentration, pH and time of reaction dictate completion of this layer. In most cases examined, the limiting weight of mercury adsorbed is $\simeq 10^{-6}$ gms/cm^2. Unfortunately, as discussed in Chapter 3, the XPS calibration plots could not be extended to the peak area intensitites observed on many of the adsorbed sulphide plates. No technique was therefore available to compare these large peak intensities to mercury weights (gms). It is most interesting that both elemental mercury and mercuric ions were adsorbed by iron sulphide mineral surfaces and more importantly from aqueous solutions of extremely low mercury concentration. In addition, large chloride ion concentrations enhanced sorption rates (e.g. chloride ions may catalyse the sorption reaction rate). These promising results prompted further studies of practical significance.

Process water samples containing mercury were collected at a large chlor-alkali plant in Canada and studied using iron sulphide plates and methods discussed above. These results, Table 18, indicated significant sorption onto the mineral surfaces and an enhanced sorption rate with increasing pH.

A recent study[2] has indicated mercury pollution from chlor-alkali plants and their associated dump sites, both active and closed, is an extremely dangerous ecological problem. High mercury levels in sludge ponds contribute approximately equally to atmospheric and water pollution in the vicinity of the plant. A value, ranging from 150 → 1500 kg/yr mercury loss to the environment by Swedish chlor-alkali plants is reported. In Canada, with more alkali producing plants[21], a correspondingly larger loss is therefore expected. Lindberg[2] states "the most significant mercury waste problem in this industry involves disposal of large quantities of solid waste materials" and "given the common disposal practice of ponding these solid wastes, along with the residence time of mercury in existing large scale waste deposits, (≃ 100 years) it becomes apparent that the role of such residual waste deposits in local mercury cycles will continue to grow". An excellent review of mercury equilibrium in the environment has been prepared by Kothny.[22]

The results found in the present thesis indicate that iron sulphides, pyrrhotite in particular, sorb monolayer amounts of mercury atoms and ions from dilute solution. Crushed pyrrhotite would thus seem ideal as an insulating jacket to store solid chlor-alkali plant wastes and cleanse process waters containing mercury. A thick layer of pyrrhotite surrounding these wastes could then drastically reduce mercury loss to the environment. Pilot studies are therefore required to improve and better define commercial applications of this sorption mechanism.

Table 18

XPS Study of Mercury Sorption by Iron Sulphides from Chlor Alkali Processing Waters

*Chlor Alkali Processing Solution Type (500 ml)	Iron Sulphide Ore	**Reaction Time (hours)	†XPS Peak Area Intensity Hg 4f ($x10^4$)	***Weight of Mercury Adsorbed (gms) x 10^{-5}
1. ††C-A-1				
(a) pH ~ 5.5	FeS (polished)	1.	1.11	2.0
		1.	2.10	3.5
	"	24.	2.95	6.0
		24.	4.70	12.0
	"	48.	6.92	40.0
	"	120.	7.45	65.0
		120.	6.80	43.0
(b) ‡pH ~ 4.0	FeS (polished)	4.	----	----
	"	24.	4.5	11.0
	"	48.	27.5	>>>100.0
	FeS_2 (a) Sudbury massive ore.	24.	7.0	45.0
	(b) Spanish Single crystal natural surface	24.	2.6	5.0
2. ‡‡C-A-2				
(a) pH ~ 6.2	FeS (polished)	6.	0.83	1.0
	"	24.	2.12	3.5
(b) ‡pH ~ 4.0	FeS (polished)	4.	27.3	>>>100.0
	"	24.	7.1	45.0
	"	48.	19.3	>>>100.0
	FeS_2 (a) Sudbury	24.	2.7	5.0
	(b) Spain	24.	5.1	15.0

* as per Table 14.

** as per Table 14.

*** as per Table 14.

† as per Table 14.

†† non-treated chlor alkali processing water, initial pH-5.5, Hg^{2+}-2 ppm and high NaCl.

‡ pH adjusted to ≈4 (dropwise addition of 1 M HCl).

‡‡ treated chlor alkali processing water initial, pH-6.2, Hg^{2+}-5 ppb and low NaCl.

5.4 Conclusion

The explanation of mercury sorption on iron sulphide surfaces is to be found in the adsorption theory discussed in Chapter 2.

As in the calcite study, Chapter 4, concepts of the electric double layer (E.D.L.) theory, surface hydroxylation, ageing processes and mineral solubility can explain the specific adsorption of mercury on sulphide minerals. Using these previously discussed sorption factors and invoking models of James et al.[8,23] possible sorption mechanisms can be written (Equations 52a,b).

A specific type sorption reaction is postulated as no increase in iron concentration was observed in solution, little or no chloride, and sodium ions were adsorbed; and hydrogen ions released to solution nearly always approached the amount of mercury adsorbed.

Polished and partially oxidized sulphide surfaces contain S^{2-} and O^{2-} adsorption sites. Both S-Hg and O-Hg adsorption reactions may therefore occur. Note, the dominant mercury species in solution will be $HgCl_2^{\circ}$.

Sulphide

$$FeS + HgCl_2^{\circ} \rightleftharpoons FeS \sim Hg + 2Cl^- \qquad (54a)$$

$$2(FeS) + HgCl_2^{\circ} \rightleftharpoons (FeS)_2 \sim Hg + 2Cl^- \qquad (54b)$$

Oxide

$$FeO + HgCl_2^{\circ} \rightleftharpoons FeO \sim Hg + 2Cl^- \qquad (55a)$$

$$2(FeO) + HgCl_2^{\circ} \rightleftharpoons (FeO)_2Hg + 2Cl^- \qquad (55b)$$

Possible mechanisms of the above reactions can be written, assuming initial hydroxylation of the mineral surface.

$$FeS_{(s)} + H_2O \rightleftharpoons [FeOH \cdot SH]_{surf.} \qquad (56)$$

Thus, for reaction 54a (see Figure 40a)

$$[FeOH \cdot SH]_{surf.} + HgCl_2^{\circ} \rightleftharpoons [FeOH \cdot SHg]_{surf.} + 2Cl^- + H^+ \qquad (57a)$$

$$\rightleftharpoons [FeSHg]_{surf.} + 2Cl^- + H_2O \qquad (57b)$$

and for reaction 54b (see Figure 40b)

$$2[FeOH \cdot SH]_{surf.} + HgCl_2^{\circ} \rightleftharpoons [(FeOH \cdot S)_2Hg]_{surf.} + 2Cl^- + 2H^+ \qquad (58a)$$

$$\rightleftharpoons [FeOH \cdot FeS_2Hg]_{surf.} + 2Cl^- + H^+ + H_2O \qquad (58b)$$

$$\rightleftharpoons [(FeS)_2Hg]_{surf.} + 2Cl^- + 2H_2O \qquad (58c)$$

The oxide mechanism (Equations 55a,b) is identical in nature to the above equations for iron sulphide-mercury adsorption. Because of the excess iron site vacancies on the mineral's surface, a net negative charge is created with exchangeable hydrogen ions associated with the surface anions. Filling of the empty iron sites by mercury ions/atoms from solution is possible and possibly can explain the observed behaviour. For example, a variation of the reaction mechanisms represented by equations 57a,b and 58a,b,c with/without invoking surface hydroxylation can be written as 59a,b and 60a,b respectively (Figure 40c).

$$[\bigcirc_{Fe} \cdot S]_{surf.} + HgCl_2^{\circ} \rightleftharpoons [HgS]_{surf.} + 2Cl^- \qquad (59a)$$

or $$[\bigcirc_{Fe} SH]_{surf.} + HgCl_2^{\circ} \rightleftharpoons [HgS]_{surf.} + H^+ + 2Cl^- \qquad (59b)$$

$$[Fe, \bigcirc_{Fe} S]_{surf.} + HgCl_2^{\circ} \rightleftharpoons [Fe, HgS_2]_{surf.} + 2Cl^- \qquad (60a)$$

or $$[Fe, \bigcirc_{Fe} (SH)_2]_{surf.} + HgCl_2^{\circ} \rightleftharpoons [Fe, HgS_2]_{surf.} + 2H^+ + 2Cl^- \qquad (60b)$$

(a) Reaction Mechanism 54a

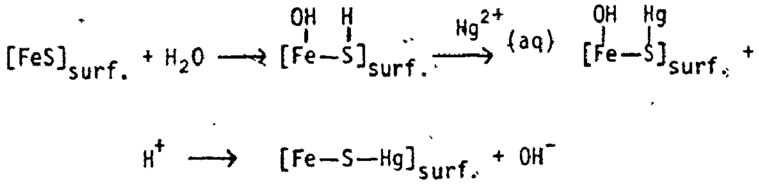

$$[FeS]_{surf.} + H_2O \longrightarrow [\overset{OH}{Fe}-\overset{H}{S}]_{surf.} \xrightarrow{Hg^{2+}(aq)} [\overset{OH}{Fe}-\overset{Hg}{S}]_{surf.} + H^+ \longrightarrow [Fe-S-Hg]_{surf.} + OH^-$$

(b) Reaction Mechanism 54b

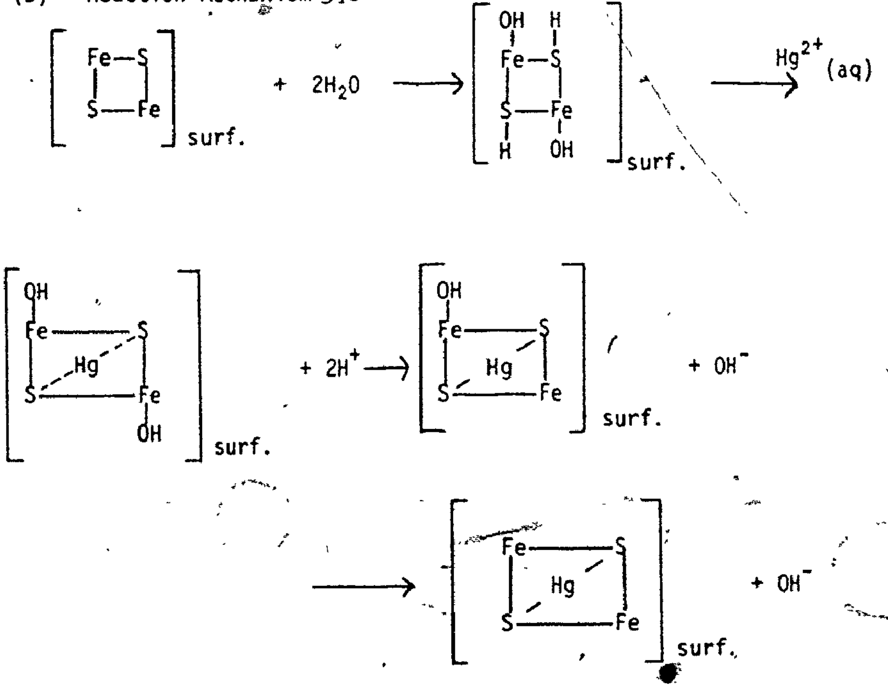

(c) Reaction Mechanism 59 (0_{Fe} refers to iron site vacancy)

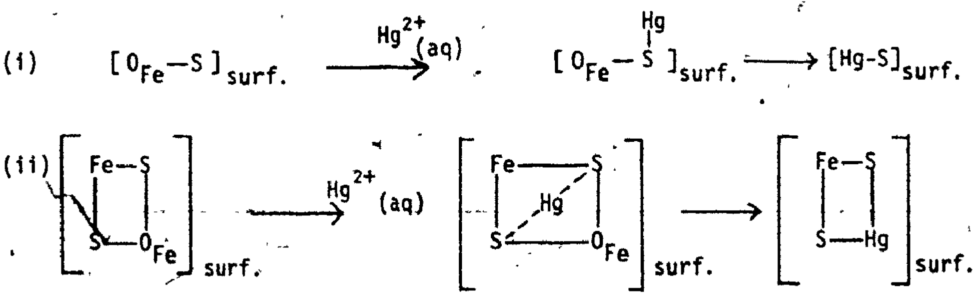

$$\text{(i)}\quad [0_{Fe}-S]_{surf.} \xrightarrow{Hg^{2+}(aq)} [0_{Fe}-\overset{Hg}{S}]_{surf.} \longrightarrow [Hg\text{-}S]_{surf.}$$

Figure 40. Mechanism of Hg Adsorption on Non-Stoichiometric FeS.

$\bigcirc_{Fe}$ represents an empty iron site at the lattice surface.

But other sorption mechanisms (Chapter 2), e.g. EDL theory, surface hydroxylation, ageing, dissolution, etc. must still be used to explain the extent and speed of surface mercury coverage and the increase in hydrogen ion concentration in solution.

There are many difficulties in explaining all observations and interpreting the results found in terms of the adsorption models available. One should remember that the present knowledge of colloidal stability, complex solubilities, complex ion formation, indeed adsorption itself is still at an early stage of development. Hopefully, future work can unravel many of the unknowns and uncertainties discussed here.

5.5 References

1. N. Fimreite, Ph.D. Thesis, Univ. Western Ontario, (1970).
2. S.E. Lindberg and R.R. Turner, Nature, 268, 133, (1977).
3. D.E. Robertson, E.A. Crecelius, J.S. Fruchter and J.D. Ludwick, Science, 196, 1094, (1977).
4. W.N. Marchant, Environ. Sci. Technol., 8, 993, (1974).
5. J.P. McKaveney, W.P. Fassinger and D.A. Stivers, Environ. Sci. Technol., 6, 1109, (1972).
6. B. Coupal and J.M. Lalancette, Water Research, 10, 1071, (1976).
7. M. Friedman and A.C. Waiss, Environ. Sci. Technol., 6, 457, (1972).
8. R.O. James and G.A. Parks, A.I.Ch.E. Symposium Series 150, 71, 157, (1975).
9. M.G. MacNaughton and R.O. James, J. Colloid Interface Sci., 47, 431, (1974).
10. U.S.E.P.A. Publication R2-72-077, #68-01-0060, Project 16080 G.W.O., (1972).
11. J.F. Alder and D.A. Hickman, Anal. Chem., 49, 336, (1977).
12. B.I. Kronberg, (Personal communication).
13. J.W. Murray, Geochim. et Cosmochim. Acta, 39, 505, (1975).
14. a) C.R. Brundle, T.J. Chung and D.W. Rice, Surface Sci., 60, 286, (1976).
    b) K.S. Kim and R.E. Davies, J. Electron Spectrosc. 1, 251, (1972).
15. a) M.K. Oku and S. Ikeda, J. Electron Spectrosc., 7, 465, (1975).
    b) G. Schon and S.T. Lundin, J. Electron Spectrosc., 1, 105, (1972).
16. P. Ney, "Zeta-Potentiale und Flotierbarkeit von Mineralen", Springer-Verlog, (1973).
17. V.L. Snoeyink and W.J. Weber, Jr., A.C.S. Adv. Chem. Series 79, 125, (1968).

18. R.T. Shuey, Developments in Economic Geology, Vol. 4; "Semi-Conducting Ore Minerals", (1975).

19. W.A. Deer, R.A. Howie and J. Zussman, "An Introduction to the Rock-Forming Minerals", Longman, (1975).

20. A. Stock, F. Cucuel, F. Gerstner, H. Köhle and H. Lux, Z. Anorg. Chem., 217, 241, (1937). From works of W.F. Linke, "Solubilities of Inorganic Chemicals", A.C.S. Vol. 1, 1179 (1958).

21. R. Bryan, "Much is Taken, Much Remains", Duxbury Press, U.S.A. (1973).

22. E.L. Kothny, A.C.S., Adv. Chem. Series 123, 48, (1973).

23. R.O. James and T.W. Healy, J. Colloid Interface Sci., 40, 65, (1972).

CHAPTER 6

CONCLUDING REMARKS

X-ray photoelectron spectroscopy has been shown to be useful for quantitative analysis of trace metal ions adsorbed onto mineral surfaces. The detection level is estimated to be greater than 10^{-9} gm/cm^2. Surface reactions (dissolution) of calcite crystals in water were also detected by monitoring the C 1s spectra region using the XPS technique. Linear reproducible calibration plots were obtained for barium, lead, mercury, lanthanum, nickel and chlorine ions micro-syringed on various mineral surfaces. It would thus seem that most elements can be analysed and give reproducible linear calibration plots using this technique. It is important, however, that these calibrant surfaces be chemically and physically similar to the unknown surfaces to be analysed.

The calcite and iron sulphide powdered adsorption studies gave estimates of their sorption uptake and rates; using appropriate equations an estimate of the powders' surface area was found. These powder studies were also useful in verifying the adsorbed weights determined from the XPS calibration plots and gave further validity to these XPS calibration procedures. These powdered mineral adsorption results also verified that precipitation was not significant for the metal concentration ranges used in these experiments.

Both the atomic absorption and XPS results indicated monolayer coverage for these ion-mineral surface reactions. It was also determined that counter-ions such as Cl^- or ClO_4^- were not sorbed to any degree on the mineral surfaces studied.

The results of mercury adsorption on iron sulphides indicate the potential use in eliminating both mercuric ions and elemental mercury atoms from polluted natural waters, industrial waste and process waters. A more detailed investigation involving the most efficient design of a pilot plant and related chemical parameters to best use iron sulphide ore should be examined.

In addition, this work should involve in situ treatment of polluted water on a large scale so that problems associated with a bulk application can be eliminated. The use of iron sulphide ore for adsorption of mercury vapour should also be studied to determine its effectiveness on an industrial scale.

The XPS technique has great potential in examining other adsorption systems such as the actinide elements and radioactive nuclides on metal alloys and geologically important surfaces. These surfaces include the oxides, sulphides, phosphates and large chain and sheet silicates. These future studies would be of great practical application in understanding our fragile environment and correcting past and future indiscretions.

APPENDIX A.1

WASHING (DIPPING) PROCEDURE USED FOR ESCA STUDIES

To ensure no initial barium solution was adhering to calcite crystal surfaces after removal from reaction solutions (Chapter 4.3), a washing (dipping) procedure using deionized distilled water was developed. Table A.1, Figure A.1 indicates the results of this study. Figure A.1 also indicates more barium is sorbed onto crystals placed in non-equilibrium barium solutions, (i.e. not pre-saturated with respect to calcium carbonate). Dipping each crystal into fresh water made little difference in the XPS Ba/Ca intensity ratio results and indicated that barium is strongly bonded to the calcite surface. The small decrease in these ratios with increasing dipping indicated a small amount of desorption into the wash water. Even after one dip in water, adhering barium solution should be greatly diluted and lost from the surface. As further evidence to support the usefullness of this technique, several calcite crystals were first dipped into 200 ppm barium solutions for ten seconds, removed and washed as above. In each case, no barium adhering to the surface was detected using XPS techniques.

Table A.1

Removing Excess Ba^{2+} Solution From Reacted Calcite Surfaces

(1) Calcite Crystals in Saturated (CaCO$_3$ Equilibrium Solution) 200 ppm Ba^{2+} for 30 days			(2) Calcite Crystals in Non-Saturated (CaCO$_3$ Solution) 200 ppm Ba^{2+} for 30 days		
*Number of Dips in Pure Water	**Area Intensity Ratio (I)	***Wt. Ba^{2+} sorbed (x10^{-8}gms)	*Number of Dips in Pure Water	**Area Intensity Ratio (I)	***Wt. Ba^{2+} sorbed (x10^{-8}gms)
1	7.3	18.0	1	13.4	33.0
4	6.9	16.5	3	13.3	33.0
8	6.1	16.0	5	12.3	30.0
10	5.8	15.0	15	10.5	23.0
15	5.3	14.5			

* 50 ml fresh water used for each dip.

** $I = \dfrac{\text{Peak Area Ba } 3d_{5/2} \text{ (50 scans)}}{\text{Peak Area Ca } 2p_{1/2} \text{ (2 scans)}}$

*** From appropriate ESCA Ba^{2+} calibration plots (Chapter 3), Errors in wts. ≈ ± 20%.

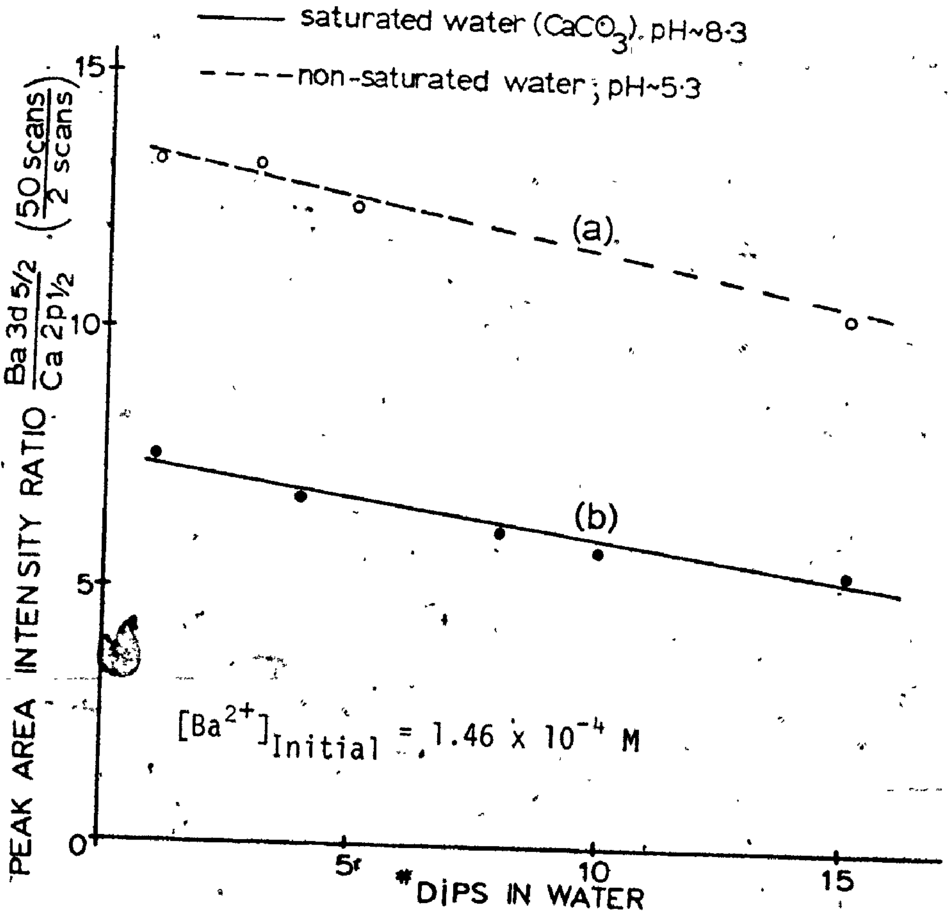

Figure A.1. Calcite Crystal Dipping Procedure.

APPENDIX A.2

CALCITE SURFACE REACTIONS STUDIED BY ESCA

The carbon 1s XPS spectra of barium reacted calcite crystals indicated significant changes with time of reaction. Therefore, effects of water contact time on the calcite surface were examined. It is apparent that the calcite-water interaction causes a third surface carbon species at a binding energy of ~ 289 eV (Table A.2, A.3, Figure A.2). This peak increases in size with reaction time. The peak at ~ 287 eV is assigned to vacuum hydrocarbon contamination, Table A.3. Sample charging is thus ~ 2.0 eV for calcite, an insulator. Notice that Ar ion etching decreases the contamination peak intensity but it increases when the crystal is left in the XPS vacuum for additional time. The C 1s peak seen at ~ 292 eV can then be assigned to the carbonate (CO_3^{2-}) carbon species.

Evaporation of two microlitres of water onto the calcite surface produced this third carbon species as well (Table A.2). Analysis of this same water supply evaporated on aluminum and stainless steel plates did not produce this third carbon species to any degree. Contaminant organics in the water is thus unlikely. In addition, it was found that for a calcite crystal in water 28 days only the upper (top) exposed surface was greatly altered while the lower (bottom) side, resting against the beaker bottom, was not affected (Table A.2).

XPS C 1s spectra binding energies indicated this third peak (~289 eV) is either a C-O or CO_2 species. Argon ion etching of the surface reduced this third peak to a minimum very quickly, (Table A.4) and, it did not increase when left in the vacuum system for an additional day. Notice, also that the C 1s peak at 284.6 (i.e. uncharged hydrocarbon contamination on the aluminum mask) did not increase during this time in the vacuum.

This observation indicates the hydrocarbon contamination preferentially coats the calcite crystal, possibly due to electrostatic considerations. Argon ion re-etching after this one day, again removed the hydrocarbon layer from the calcite surface. The C 1s peak (289 eV) intensity did not increase after its quick removal by the Ar ion etching, supporting the claim it is situated only on the outer surface of the calcite surface and is caused by the reaction with water e.g. is a CO or CO_2 species. This carbon species could originate two ways. [illegible]rstly, the hydrocarbon contamination from the vacuum system could interact with the greatly perturbed (aged) calcium carbonate surface lattice, e.g. C(hydrocarbon) + O_X(surface). Secondly, the perturbed calcite lattice generates this new C 1s peak. Because it does not reappear after Ar ion etching and it's intensity increases with water reaction time, one may conclude that we are seeing the recrystallized surface (non-stoichiometric) which contains, sorbed CO_2, H_2O and a recrystallized, hydroxylated calcite surface lattice.

It is interesting that heating to 500°C does not alter the C 1s spectra, (Table A.3) although the calcite surface is greatly altered visually. The Ca 2p spectra however indicated surface decomposition of calcite (i.e. $CaCO_3 \xrightarrow{\Delta} CaO + CO_2$).

The effects of x-ray bombardment on the calcite were also examined (Table A.3). These (C 1s) results indicated increasing hydrocarbon contamination during 36 hours exposure to 200 watt x-rays but no new carbon species were observed. The Ca 2p spectra, again indicated surface decomposition to calcium oxide. No decomposition of the surface was observed using only the 10^{-8} torr. vacuum, even after 36 hours.

Reaction of calcite in acid (1M HCl) and in steam vapour (Table A.3) indicated no surface decomposition but the C 1s spectra indicated the production of the CO type carbon species (i.e. the ageing product at E_b ~ 289 eV).

These results, especially the calcite reaction results in water, (i.e. development of a non-stoichiometric surface) indicated care must be taken to ensure that greatly altered barium sorbed calcite surfaces be rejected as no accurate weight of sorbed barium could be determined using the Ba/Ca ratio method. The greatly altered (aged) sorbed samples cannot be related to the cleaved stoichiometric calibration samples.

The results of Table A.5 indicate the aforementioned potential problems. For example, a calcite crystal surface in a 50 ppm barium solution for ten days was not greatly altered by the reaction. Thus Ar ion etching for 120 seconds indicated no Ba/Ca intensity ratio changes. However another crystal in 100 ppm barium solution for 50 days showed large Ba/Ca ratio differences before and after Ar ion etching for 120 seconds. In the above case, the surface was drastically affected by the solution. This was observed from the Ca $2p_{\frac{1}{2}}$ and C 1s spectra peak intensities and peak envelopes. After Ar etching, the Ba/Ca ratio was greatly reduced due to a large increase in the Ca $2p_{\frac{1}{2}}$ peak intensity, because the etching exposed fresh surface lattice calcium ions. Therefore, there is an upper time limit in which barium reacted calcite crystals can be equated to the XPS calibration plots and still have a qualitative meaning. In many cases, crystals reacted for extended periods of time (30 → 50 days) did not undergo severe surface destruction as indicated from their nearly normal Ca 2p and C 1s spectra. Generally, the reacted crystal Ba/Ca ratios and calibration crystal results could be equated for reaction times of ~ 30 days for equilibrium (i.e. pre-saturated calcite solutions) type reactions and ~ 21 days for the non-equilibrium (i.e. pure water, barium) solutions. Longer reaction time results were less accurate due to the surface ageing processes and hence omitted.

Table A.2

Pure Iceland Spar Calcite Crystals - H_2O Induced Surface Reactions (dissolution)

Electronic level		Peak Position†† eV	PEAK AREA INTENSITY (2 scans)									
			2ml H_2O evap. on surface			Calcite in H_2O (days)						
			before	after	*Ar etched 20 sec.	Initial	5	14	20	Initial	28 (faceup)	28 (facedown)
Ca	$2p_{1/2}$	353.0 ± .2	3700	3300	3900	3400	2800	2600	2200	3700	2500	4100
	$2p_{3/2}$	349.5 ± .2	7500	6400	8000	7000	5900	5500	5000	6700	4100	8200
†C 1s	(1)	287.0 ± .5	3720	2610	1830	5800	6500	5100	5200	7500	11400	9900
	(2)	289.0 ± .5	--	1060	--	--	2100	1800	1400	--	3700	--
	(3)	292.0 ± .5	2418	1340	2072	3100	1350	900	950	4200	2400	4600

* Ar ion etching power 30 μA x 10 KeV

† C 1s (1) hydrocarbon contamination.
(2) unknown carbon species.
(3) CO_3^{2-} species.

†† w.r.t. Au 4f, 84 eV; estimated error is average deviation from all like spectra analysed. Note C 1s spectra line-widths computer constrained at 2.1 eV.

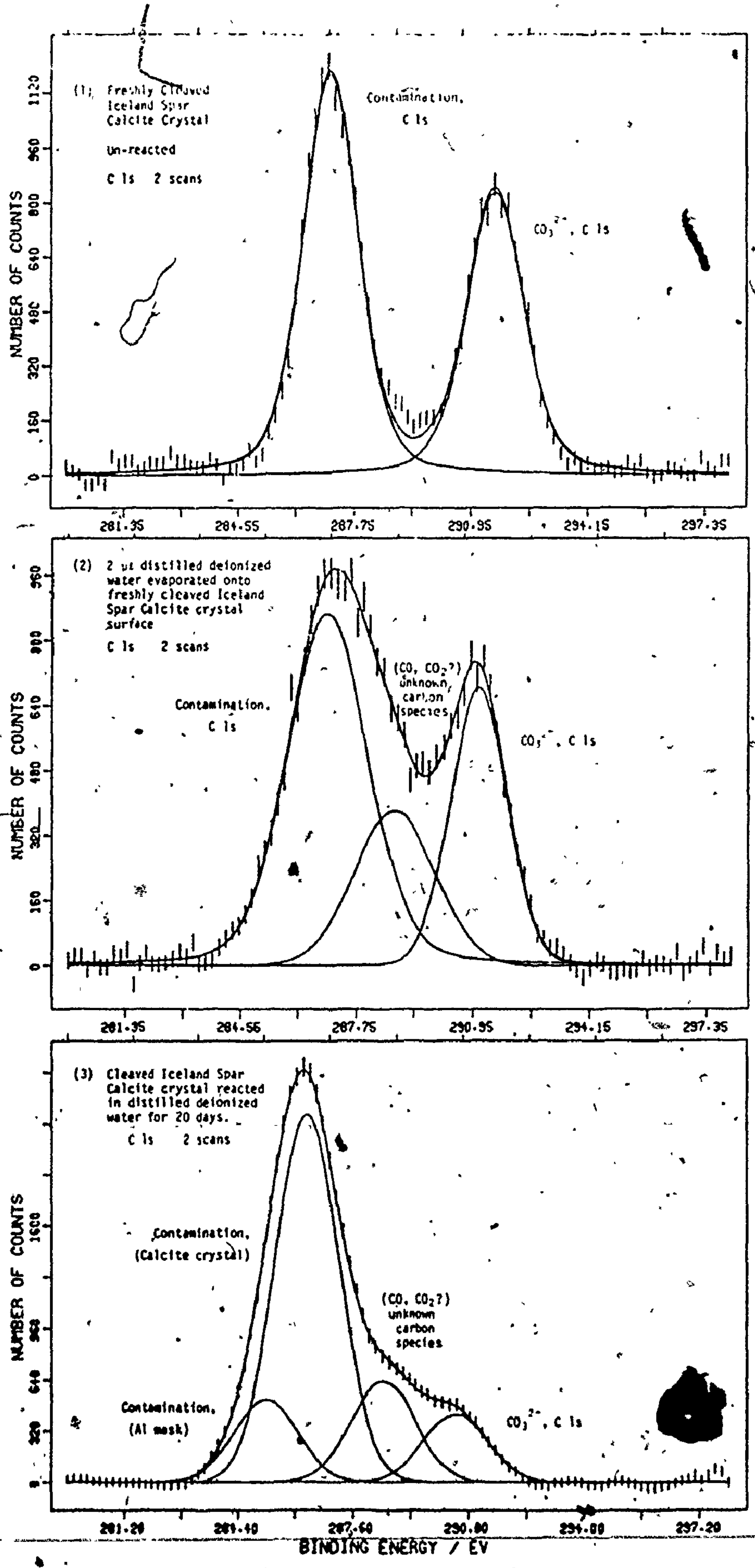

Figure A.2a. Effects of Water on Calcite Crystal Surfaces (C 1s ESCA Spectra).

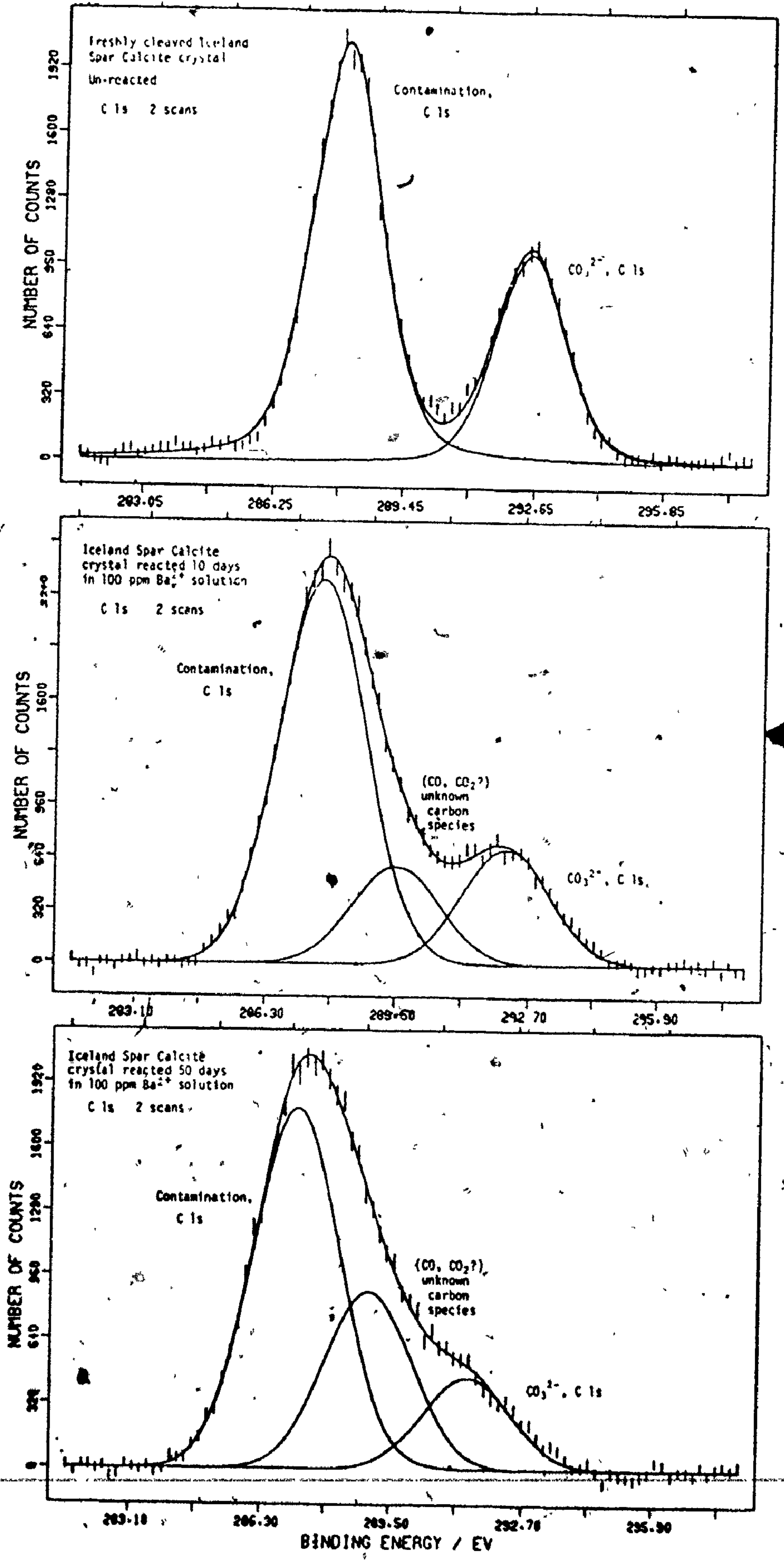

Figure A.2b. Effects of Barium Solution on Calcite Crystal Surfaces

Table A.3

Pure Iceland Spar Calcite Single Crystals - Ar ion, Thermal, X-ray, Acid and Steam Effects. Induced Surface Decomposition Effects.

Electronic Level	††Peak Position eV	PEAK AREA INTENSITY (2 scans)															
		1				2				3		4		5			
		*Ar Ion Etching Effect				Thermal Effects (15 min.)				X-ray Effects (200 watts)		1M HCl Effect		Steam Vapour (hr.)			
		Initial	30 sec. etch	1 day later	re-etch 60 sec.	Initial	200°C	Initial	500°C	Initial	36 hours	Initial	30 sec.	Initial	0.5	1.0	96
Ca $2p_{1/2}$	353.0 ± .2	3200	3400	3300	3500	2700	2200	4200	3400	2800	1600	---	---	2300	---	470	400
(CaCO$_3$) $2p_{3/2}$	349.5 ± .2	6500	7000	6800	7100	5500	4440	8900	7000	5300	3300	---	---	4700	---	1020	850
Ca** $2p_{1/2}$	352.1 ± .3	---	---	---	---	---	---	---	1500	---	700	---	---	---	---	---	---
$2p_{3/2}$	348.4 ± .3								3100		1300						
+C 1s (1)	286.7 ± .5	4430	1320	2850	475	3720	3350	3300	3600	2000	7800	1050	1320	2600	5200	2420	5700
(2)	289.0 ± .5	---	---	---	---	---	---	---	---	---	---	---	1250	---	530	300	570
(3)	291.6 ± .5	3300	25[illegible]0	2780	2190	2418	1330	2900	600	1900	1000	1680	800	1885	---	---	---

* as per Table A.2.

** $CaCO_3 \xrightarrow{\Delta} CaO + CO_2\uparrow$.

\+ as per Table A.2.

†† as per Table A.2.

Table A.4

Ar Ion Etching Effects on 14, 20 day H_2O Reacted Calcite Crystals

Sample in H_2O	*Ar ion etching Time (sec.)	C 1s†,†† PEAK AREA INTENSITY (2 scans)			
		1	2	3	4
		284.6 ± .5eV	286.5 ± .5eV	289.0 ± .5eV	291.5 ± .5eV
1. 14 days	Initial	700	5100	1800	900
	10	2450	1900	400	1300
	20	2600	1350	400	1500
	55	2400	900	350	1450
	115	2200	600	350	1450
	1 day later	2050	1800	400	1300
	re-etch 60 sec.	1700	650	300	1400
2. 20 days	Initial	1150	5200	1400	950
	10	3050	1700	500	1250
	20	3100	1300	300	1150
	55	3000	900	400	1300
	1 day later	3075	1700	400	1050
	re-etch 60 sec.	2475	650	300	1250

* as per Table A.2.

† C 1s 1) hydrocarbon contamination deposited on Aluminum mask by Ar ion etching of calcite surface.
2) hydrocarbon contamination on calcite surface.
3) unknown carbon species; probably CO or CO_2.
4) Carbonate (CO_3^{2-}) species.

†† as per Table A.2.

Table A.5

Reaction Time Surface Change Effects on Intensity Ratio $(\frac{Ba}{Ca})$ "Iceland Spar Calcite Crystals in Pure H_2O-Ba^{2+} Solutions."

Ba^{2+} conc.	REACTION TIME	*Ar Ion Etch Time	††PEAK AREA INTENSITY					
			Ba $3d_{5/2}$	Ca $2p_{1/2}$	†††Intensity Ratio	†C 1s (2 scans)		
			(50 scans)	(2 scans)		1	2	3
ppm	(Days)	(sec.)	782.0 ± .5 eV	353.0 ± .2 eV	(I)	(286.5 ± .5 eV)	(289.0 ± .5 eV)	(291.5 ± .5 eV)
(1) 50	10	0	9100	2100	4.4	4200	1600	1800
		10	9100	2100	4.4	3000	1150	1600
		120	8100	2300	3.5	2600	800	1500
(2) 100	10	0	8150	1500	5.3	5000	1300	1500
	20	0	7750	1510	5.1	4000	1000	1400
	30	0	7000	680	8.8	3600	520	750
	50	0	5400	650	8.1	4700	2300	1200
		10	5400	650	8.1	3600	1350	1250
		120	7500	1800	4.2	2000	1850	1350

* as per Table A.2.

† as per Table A.2.

†† as per Table A.2.

††† $I = \frac{Ba\ 3d_{5/2}}{Ca\ 2p_{1/2}} \left(\frac{50\ scans}{2\ scans}\right)$

3 OF/DE 3

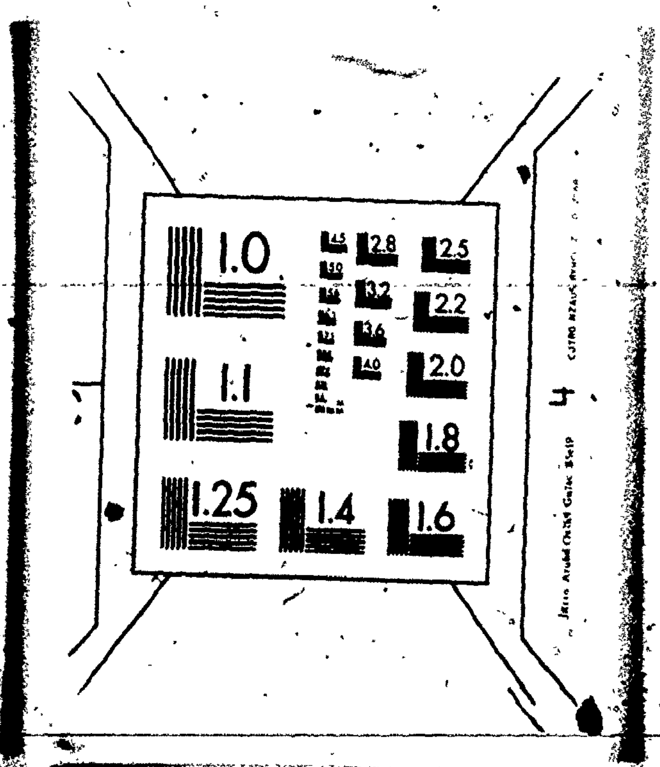

APPENDIX A.3

ADSORPTION OF METAL IONS ON MnO_2

The removal of barium, lanthanium, and nickel species from dilute solution by the sorption process was examined using the XPS technique. A detailed account of this study has recently been prepared.[1] A short summary of those results, with some modifications, are included here for completeness.

Precipitated MnO_2 deposited onto aluminum plates of the proper size to fit the ESCA sample wheel (Chapter 3.2) were placed in various concentrations of the chosen metals. After selected periods of time, these plates were removed from solution, rinsed (dipped as in Appendix A.1) and analysed by XPS for the appropriate metal (La, Ba, Ni) adsorbed on their surface.

All XPS spectra were computer fit using previously discussed methods (Chapter 3.2). The computed peak area intensities were then equated to a corresponding calibration plot (Chapter 3.3.3). The results of this work are shown in Figures A.3 → A.5. Briefly, the results indicated an adsorption process occurred dependent upon initial solution metal ion concentration and time of reaction. Calculations of adsorbed surface weights, indicated monolayer coverage.[1] As in other oxide mineral-metal ion sorption studies, an exchange sorption mechanism is proposed for the MnO_2 surface reaction.[1→4] Note the XPS surface technique gave semi-quantitative results in this study, once again indicating the usefulness and accuracy of the XPS calibration plots of Chapter 3.

---

1. D. Brûlé, M.Sc. thesis, Univ. Western Ontario, (1977).
2. J.W. Murray, J. Colloid Interface Sci., 46, 357, (1974).
3. R.O. James and T.W. Healy, J. Colloid Interface Sci., 40, 65, (1972).
4. R.O. James, P.J. Stiglich and T.W. Healy, Faraday Discuss. Chem. Soc. 59, 142, (1975).

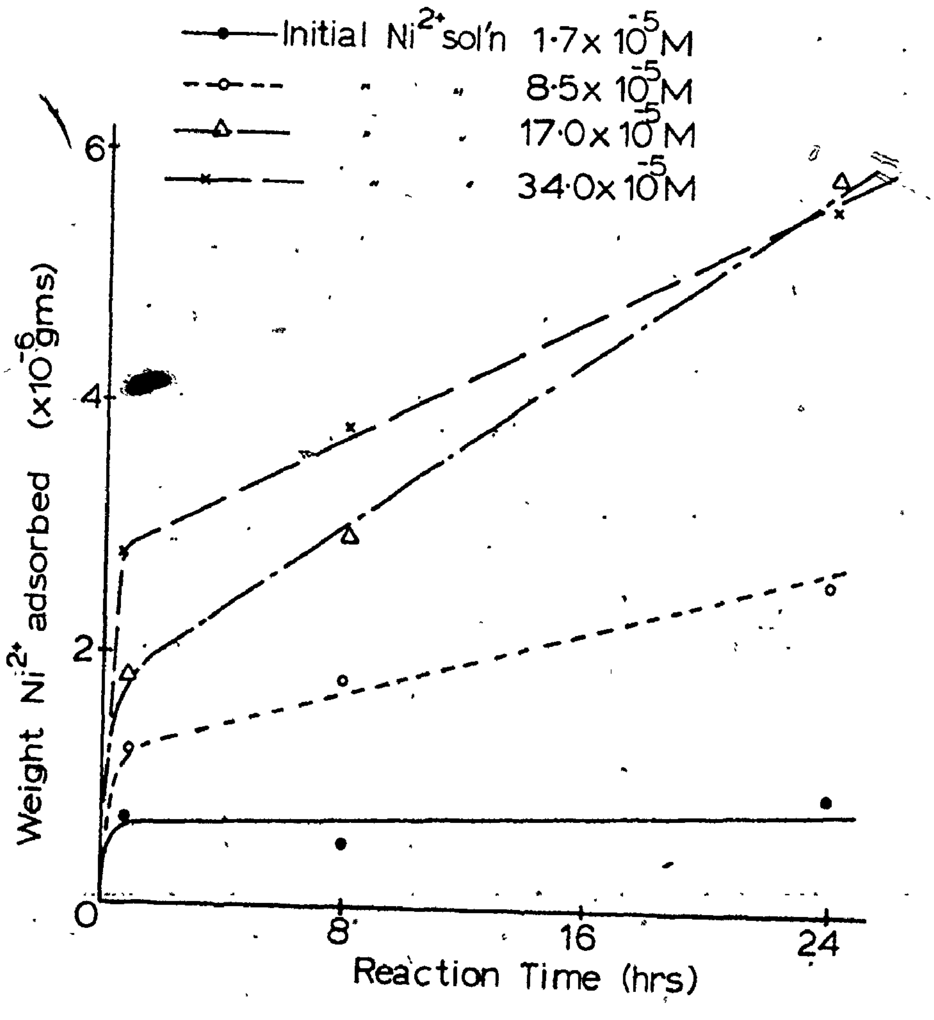

Figure A.3. Ni^{2+} Adsorption on MnO_2.

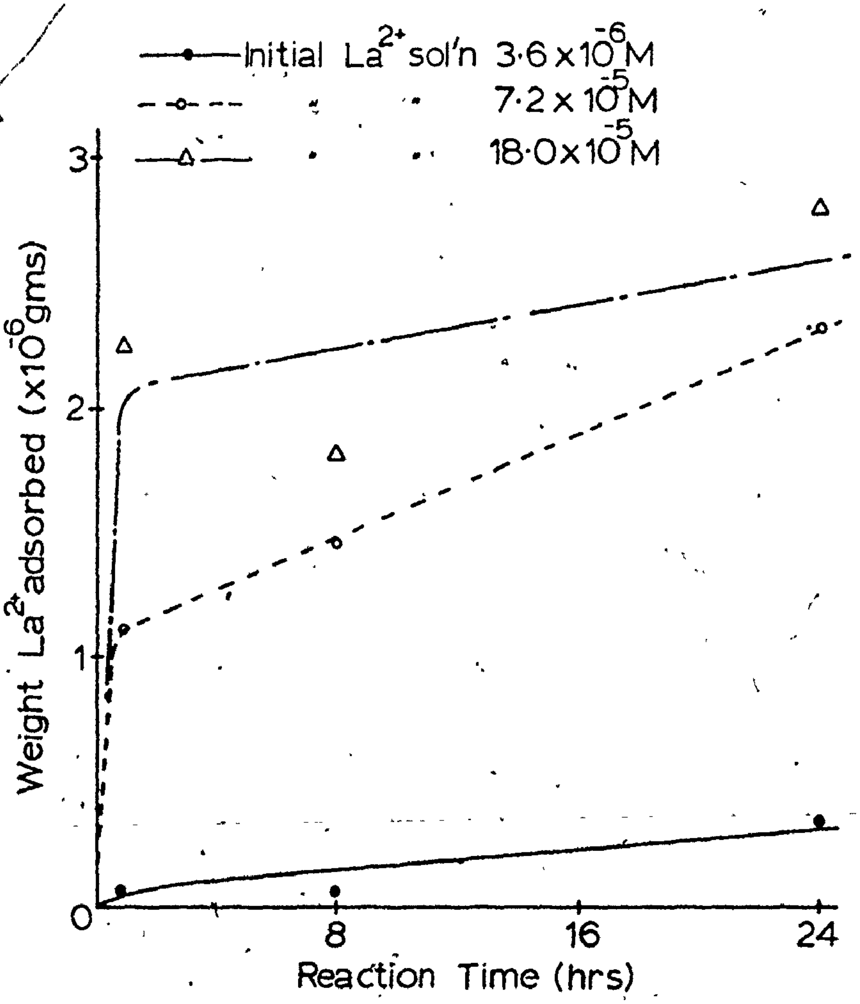

Figure A.4. La^{2+} Adsorption on MnO$_2$.

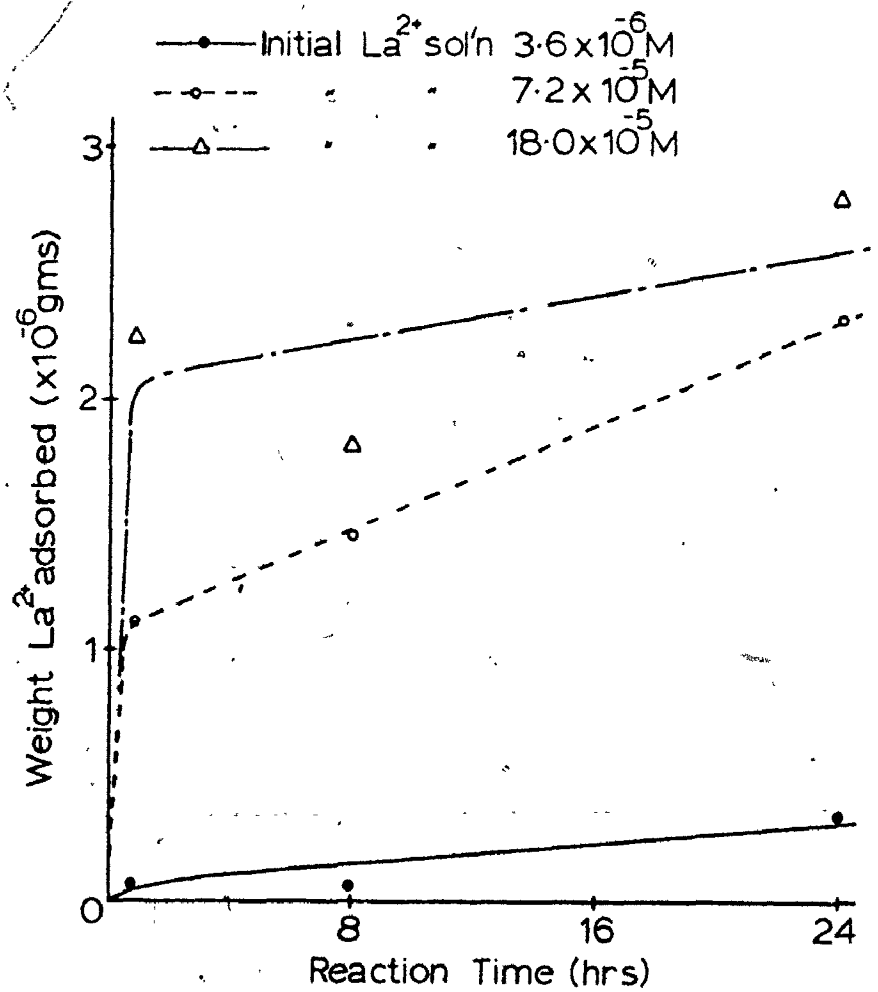

Figure A.4. La^{2+} Adsorption on MnO_2.

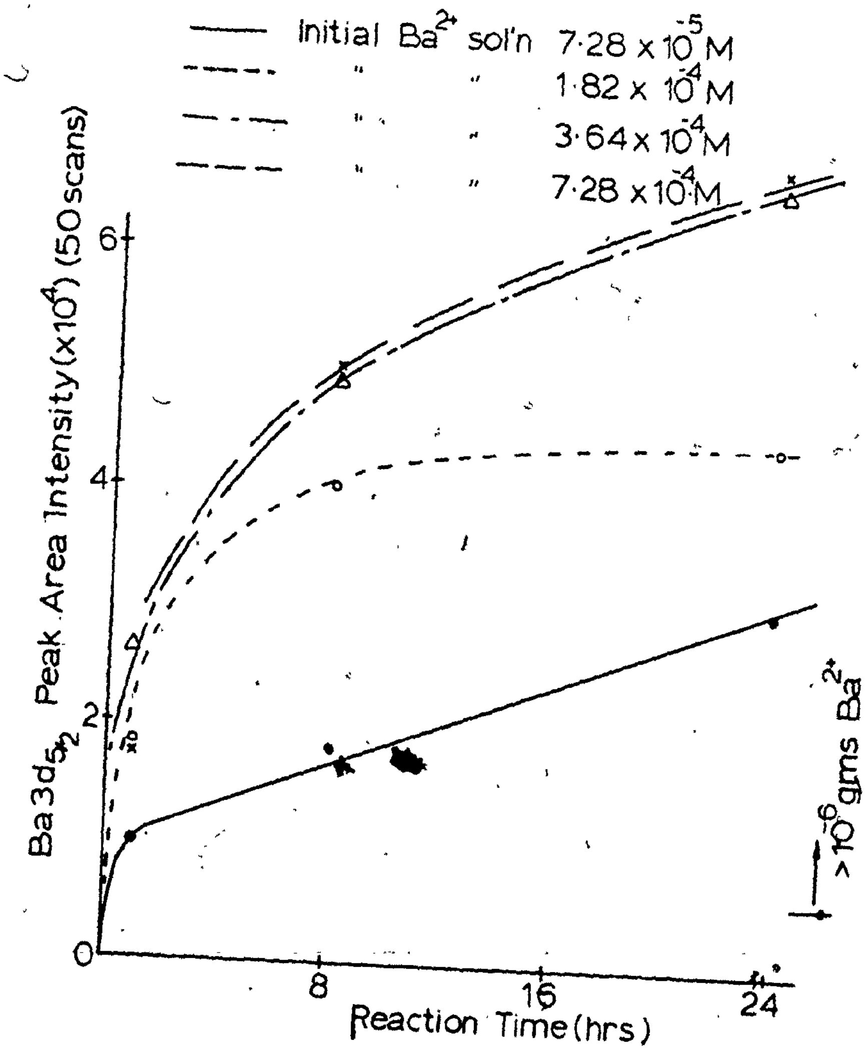

Figure A.5. Ba^{2+} Adsorption on MnO_2.

APPENDIX A.4

CALCITE DATA

A.4.1 Calcite - H_2O - CO_2 Equilibria

The simultaneous equilibrium of powdered calcite ($CaCO_3$) and distilled deionized water open to the atmosphere (i.e. containing CO_2; $P_{CO_2} = 10^{-3.5}$) is calculated using the method of Garrels and Christ.[1] (See references 2, 3 also)

Important reactions in this equilibria are written as follows:

$$CaCO_3 \rightleftharpoons Ca^{2+} + CO_3^{2-} \qquad K_{sp} = 10^{-8.3} \qquad (A.1)$$

$$H_2CO_3 \rightleftharpoons H^+ + HCO_3^- \qquad K_{H_2CO_3} = 10^{-6.4} \qquad (A.2)$$

$$HCO_3^- \rightleftharpoons H^+ + CO_3^{2-} \qquad K_{HCO_3^-} = 10^{-10.3} \qquad (A.3)$$

$$CO_2 + H_2O \rightleftharpoons H_2CO_3 \qquad K_{CO_2} = 10^{-1.47} \qquad (A.4)$$

$$H_2O \rightleftharpoons H^+ + OH^- \qquad K_W = 10^{-14} \qquad (A.5)$$

The charge balance for the reaction is

$$2[Ca^{2+}] + [H^+] = 2[CO_3^{2-}] + [HCO_3^-] + [OH^-] \qquad (A.6)$$

For a constant pressure of $P_{CO_2} \sim 10^{-3.5}$ and using Equation (A.4), $[H_2CO_3]$ can be calculated, i.e.

$$[H_2CO_3] = 10^{-3.5} \times 10^{-1.47} = 10^{-5.0} \qquad (A.7)$$

Rearranging Equations (A.1 → A.5) into terms of $[H^+]$ (Equations A.8 → A.11), and then substituting into Equation (A.6), a value of the $[H^+]$ (i.e. the pH) at equilibrium is found. (Equation A.12, 13) Substituting this $[H^+]$ value back into Equations A.8 → A.11, the other species concentrations at equilibrium are then calculated.

$$[HCO_3^-] = 10^{-11.4} / [H^+] \tag{A.8}$$

$$[CO_3^{2-}] = 10^{-10.3}[HCO_3^-] / [H^+] = 10^{-21.7}/[H^+]^2 \tag{A.9}$$

$$[OH^-] = 10^{-14} / [H^+] \tag{A.10}$$

$$[Ca^{2+}] = 10^{-8.3}/[CO_3^{2-}] = 10^{13.4}[H^+]^2 \tag{A.11}$$

Substituting into Equation (A.6)

$$2(10^{13.4}\cdot[H^+]^2) + [H^+] = 2\left(\frac{10^{-21.7}}{[H^+]^2}\right) + \frac{10^{-11.4}}{[H^+]} + \frac{10^{-14}}{[H^+]} \tag{A.12}$$

multiplying both sides by $[H^+]^2$,

$$10^{13.7}[H^+]^4 + [H^+]^3 - 10^{-11.4}[H^+] = 10^{-21.4} \tag{A.13}$$

$$\therefore [H^+] = 10^{-8.34}$$

At equilibrium (22°C), the pH is ≈ 8.34. Concentration of each species in solution at equilibrium is shown in Table A.6. Note the derivation of this simultaneous equilibria is only valid when $m_i \approx a_i$ (i.e. if $\gamma_i \approx 1.0$). This is because in Equations A.1 → A.5, concentrations are measured in activities (a_i) while in Equation A.6, concentrations are measured in molarities (m_i). The ionic strength of this solution at equilibrium was calculated from Equation A.14.

$$I = \frac{1}{2}\sum_i m_i z_i^2 \tag{A.14}$$

and found to be ≈ .0015.

Using the Debye-Hückel limiting expression, (Equation A.15), a solution activity co-efficient of 0.84 was calculated

$$-\log \gamma_i = A z_i^2 I^{\frac{1}{2}} \tag{A.15}$$

$$\gamma_{soln.} = 0.84$$

Table A.6

Calcite-H_2O-CO_2 Equilibria

Species in Solution at Equilibrium	Species Concentration at Equilibrium	
	moles/ℓ.	ppm
$[H^+]$	$10^{-8.34}$	---
$[Ca^{2+}]$	$10^{-3.28}$	21.0
$[CO_3{}^{2-}]$	$10^{-5.02}$	0.60
$[HCO_3{}^-]$	$10^{-3.06}$	53.1
$[OH^-]$	$10^{-5.66}$	0.04
$[H_2CO_3]$	$10^{-5.0}$	0.62

Thus the assumption that $m_i \simeq a_i$ is justified for the calcite - CO_2 - H_2O equilibria.

---

1. R.M. Garrels and C.L. Christ, "Solutions, Minerals and Equilibria", Harper and Row, 100, (1965).
2. K.H. Wedepohl, "Geochemistry", Holt, Rinehart and Winston, 144, (1971).
3. R.A. Horne, "Marine Chemistry", Academic Press, 203, (1969).

A.4.2 Calcite - $Ba(ClO_4)_2$ - H_2O - CO_2 Equilibria

Simultaneous equilibria of barium perchlorate reacted with calcite and water open to the atmosphere is calculated.

The method is similar to that of Appendix A.4.1, but the barium and perchlorate ions must now be included in the charge balance expression of Equation A.6. In addition the solubility product (K_{sp}) of $BaCO_3$ must also be known (Equation A.16).

$$BaCO_3 \rightleftharpoons Ba^{2+} + CO_3^{2-} \qquad K_{sp} \quad 10^{-8.80} \qquad (A.16)$$

$$[Ba^{2+}] = 10^{-8.8}/[CO_3^{2-}] = 10^{12.9}[H^+]^2 \qquad (A.17)$$

Equation 6 then becomes

$$2[Ca^{2+}] + 2[Ba^{2+}] + [H^+] = 2[CO_3^{2-}] + [HCO_3^-] + [OH^-] + [ClO_4^-] \quad (A.18)$$

Substituting Equations A.8 → A.11, and A.17 into expression A.18, results in the following

$$2(10^{13.4}\cdot[H^+]^2) + 2(10^{12.9}\cdot[H^+]^2) + [H^+] = 2\left(\frac{10^{-21.7}}{[H^+]^2}\right) + \frac{10^{-11.4}}{[H^+]} + \frac{10^{-14}}{[H^+]} + [ClO_4^-] \quad (A.19)$$

multiplying through by $[H^+]^2$

$$10^{13.82}[H^+]^4 + [H^+]^3 - [ClO_4^-][H^+]^2 - 10^{-11.4}[H^+] - 10^{-14}[H^+] = 10^{-21.4} \qquad (A.20)$$

In this study, the perchlorate ion concentration, $[ClO_4^-]$, varied from $0 \rightarrow \simeq 3 \times 10^{-3}$ M.

Thus Equation A.20 can be solved for $[H^+]$ throughout that $[ClO_4^-]$ range. (Table A.7) It was found that the $[H^+]$ increased from $10^{-8.41}$ to $10^{-8.15}$ as the $[ClO_4^-]$ was increased from $0 \rightarrow \simeq 3 \times 10^{-3}$ M.

For equilibrium conditions, the concentration ratio of barium/calcium would be $\simeq 0.925$. (Table A.7) This ratio <u>should</u> remain constant for the $Ba(ClO_4)_2$ concentrations studied. Take the case when calcite and a solution of $\simeq 1.46 \times 10^{-4}$ M $Ba(ClO_4)_2$ (20.0 ppm Ba^{2+}) open to the atmosphere, equilibrate. The resulting solution should be ~ 1.38×10^{-4} M barium (19 ppm) and ~ 4.37×10^{-4} M calcium (17.5 ppm) Table A.7. Calculations of ionic strength ($I \simeq .004$) and activity coefficient ($\gamma_i \simeq 0.75$) again verified the assumption that $a_i \simeq m_i$ for this reaction. (See A.4.1 for method of calculation) Note in the adsorption studies of Chapter 4, the barium and calcium equilibrium concentrations did not nearly approximate these solubility calculations. Other factors (e.g. sorption) must then be responsible for overruling simple solution thermodynamics.

A.4.3 Calcite Crystal Chemistry

Extensive literature is available describing the crystal structure of calcite and it's physical and chemical properties.[1→5] The crystal structure is shown in Figure A.6. Calcite has a $\{10\bar{1}1\}$ perfect cleavage (more commonly labelled {100}). It has a trigonal (face-centred

Table A.7

Calcite-$Ba(ClO_4)_2$-H_2O-CO_2 Equilibria

Species in Solution at Equilibrium	Species Concentration at Equilibrium for $[ClO_4^-]$ shown					
	moles/ℓ.	ppm	moles/ℓ.	ppm	moles/ℓ.	ppm
$[ClO_4^-]$	NIL	---	$10^{-3.5}$	31.5	$10^{-2.5}$	315.0
$[H^+]$	$10^{-8.41}$	---	$10^{-8.38}$	---	$10^{-8.15}$	---
$[Ca^{2+}]$	$10^{-3.42}$	15.2	$10^{-3.36}$	17.5	$10^{-2.9}$	50.4
$[Ba^{2+}]$	$10^{-3.92}$	16.5	$10^{-3.86}$	19.0	$10^{-3.4}$	54.7
$[CO_3^{2-}]$	$10^{-4.88}$	0.79	$10^{-4.94}$	0.69	$10^{-5.4}$	0.24
$[HCO_3^-]$	$10^{-2.99}$	62.4	$10^{-3.02}$	58.2	$10^{-3.25}$	34.3
$[OH^-]$	$10^{-5.59}$	0.04	$10^{-5.62}$	0.04	$10^{-5.85}$	0.02
$[H_2CO_3]$	$10^{-5.0}$	0.62	$10^{-5.0}$	0.62	$10^{-5.0}$	0.62
$[Ca^{2+}]/[Ba^{2+}]$	3.16	0.921	3.16	0.921	3.16	0.921

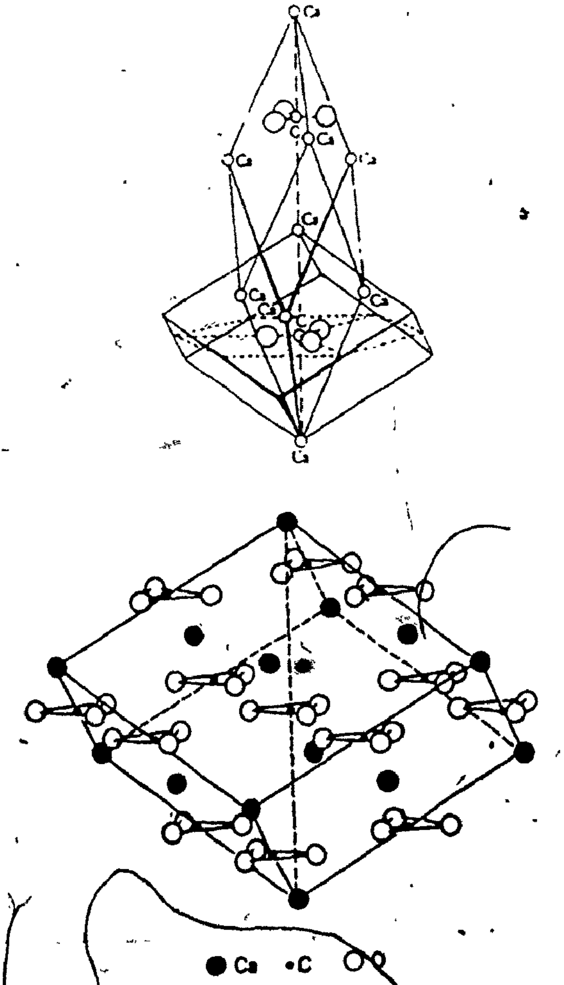

Figure A.6. Calcite Crystal Structure.

rhombohedral) unit cell lattice. The calcium ions are in six coordination with oxygen ions of the planar sp^2 hybrid CO_3^{2-} groups. Dissolution reactions of calcite in solution have been examined in detail by Thomas[4,5].

---

1. W.A. Deer, R.A. Howie and J. Zussman, "An Introduction to the Rock-Forming Minerals", Longman, (1975).
2. R.C. Evans, "Crystal Chemistry", Cambridge Press, 220, (1966).
3. J. Verhoogen, F.J. Turner, L.E. Weiss, C. Wahrhaftig, and W.S. Fyfe, "The Earth", Holt, Rinehart and Winston, (1970).
4. J.M. Thomas and G. Renshaw, Trans. Faraday Society, 61, 791, (1965).
5. J.M. Thomas and G. Renshaw, J. Chem. Soc., A, 2753, (1969).

A.4.4 Calcite Surface Area Calculations

A.4.4.1 Crushed St. Mary's Limestone (100-120 mesh)

The average limestone particle size was taken from the 100-120 mesh sieve screen size (i.e. 100 mesh = 0.149 mm). Therefore the average particle had a radius of $\approx 7.5 \times 10^{-3}$ cm. The surface area of one gram of 100 mesh limestone could then be estimated from Equations A.21, A.22 below

$$S = 4\pi r^2 = 7 \times 10^{-4}\,\text{cm}^2 \qquad \text{(surface area of one particle)} \qquad \text{(A.21)}$$

$$V = \frac{4}{3}\pi r^3 = 1.8 \times 10^{-6}\,\text{cm}^3 \qquad \text{(volume of one particle)} \qquad \text{(A.22)}$$

From the known density of limestone (2.71 gm/cm^3) and the estimated volume of one particle, the number of 100 mesh particles is found to be $\sim 2.1 \times 10^5$ particles/gram.

This number of particles (one gram) is therefore equivalent to $\approx .015$ m^2, the surface area.

A.4.4.2 The RIC/ROC Spec-Pure Calcite (< 1000 mesh)

The chemically precipitated spec-pure grade calcite was found to contain particles of much less than 1000 mesh (Tyler standard size). Scanning electron microphotographs, taken at 1000 X magnification indicated an average particle length of ≈ 5×10^{-4} cm. The particles are rhombohedral in shape, allowing a simple calculation to find an average particle volume (1.25×10^{-10} cm^3) and surface area (1.5×10^{-6} cm^3). The volume of one gram of calcite (.369 cm^3) is taken from its known density. Using this data, the surface area of one gram of this calcite was estimated. One gram of calcite contains ~ 3×10^9 particles of the above size. The surface area of ~ 3×10^9 particles (1 gm) is ≈ 4.5×10^3 cm^2 or 0.45 cm^2.

APPENDIX A.5

IRON SULPHIDE DATA

A.5.1 FeS-H2O Equilibria

Important reactions are as follows,

$$FeS \rightleftharpoons Fe^{2+} + S^{2-} \qquad K_{sp} \sim 10^{-17.3} \qquad (A.23)$$

$$*H_2S \rightleftharpoons HS^- + H^+ \qquad *K_1 \sim 10^{-7} \qquad (A.24)$$

$$HS^- \rightleftharpoons S^{2-} + H^+ \qquad *K_2 \sim 10^{-12.92} \qquad (A.25)$$

$$H_2O \rightleftharpoons OH^- + H^+ \qquad K_W = 10^{-14} \qquad (A.26)$$

*The values of K_1, K_2 deviate two orders of magnitude in recent literature.[1] Thus, solubility calculations can only be estimates for this reaction.

In addition, FeS oxidizes in water containing dissolved oxygen to produce Fe_2O_3 as follows,

$$FeS + H_2O \overset{fast}{\rightleftharpoons} Fe^{2+} + HS^- + OH^- \qquad (A.27)$$

$$2FeS + H_2O + 5O_2 \overset{slow}{\rightleftharpoons} Fe_2O_3 + SO_4^{2-} + 2H^+ \qquad (A.28)$$

Thus the reaction of FeS in water is not a simple equilibrium problem.

For example, electrochemistry considerations of the reaction are important, i.e.

$$Fe^{2+} + H_2O \rightleftharpoons FeOH^+ + H^+ \qquad (A.29)$$

$$FeOH^+ + \frac{1}{2}O_2 \rightleftharpoons FeO(OH) \quad E^\circ \simeq .771 \text{ eV} \qquad (A.30)$$

Hydrogen ions are consumed by this oxidation process. Note that 2[FeO(OH)] can be re-written in the form $(Fe_2O_3 \cdot H_2O)$. However, when only the initial (fast)reaction A.27 is considered, calculations of species solubilities are possible.

The equilibria species of Reaction A.27, can be determined from Equations A.23 → A.26 and the mass and charge balance expressions given below (A.31, 32).

$$[Fe^{2+}] = [S^{2-}] + [HS^-] + [H_2S] \qquad (A.31)$$

$$2[Fe^{2+}] + [H^+] = 2[S^{2-}] + [HS^-] \qquad (A.32)$$

Rearranging in terms of $[S^{2-}]$ in Equation A.31, A.32, and then substituting A.32 into A.31, a 5th order quadratic equation in the $[S^{2-}]$ species is produced i.e.

$$10^{-17.3} = [S^{2-}]^2 + [S^{2-}]\left(\frac{2[S^{2-}]^2 - 2\times 10^{-17.3}}{10^{-12.92} - [S^{2-}]}\right) + 10^{-5.92}\left(\frac{2[S^{2-}]^2 - 2\times 10^{-17.3}}{10^{-12.92} - [S^{2-}]}\right)^2 \qquad (A.33)$$

Solving,

$$[S^{2-}] \simeq 10^{-11} \rightarrow \simeq 10^{-11.5}$$

Therefore

$$[H^+] \simeq 10^{-7.9} \rightarrow \simeq 10^{-6.9} \qquad [Fe] \simeq 10^{-6.3} \rightarrow \simeq 10^{-5.8}$$

$$[HS^-] \simeq 10^{-5.99} \rightarrow \simeq 10^{-5.48} \qquad [H_2S] \simeq 10^{-6.9} \rightarrow \simeq 10^{-5.38}$$

Note, this calculated hydrogen concentration ($10^{-7.9}$) is not initially observed experimentally when FeS is placed in water. Instead a sudden increase in pH is seen, indicating that a mineral surface - H_2O reaction may initially dominate. i.e. ionic hydrolysis or surface hydroxylation etc. With increasing reaction time, the solution pH decreased, approaching the above calculated value.

A.5.2 FeS - $HgCl_2$ - H_2O Equilibria

Equilibria of $HgCl_2$ in water is first discussed.

$$HgCl_2 \rightleftharpoons Hg^{2+} + 2Cl^- \qquad K_{sp} = 10^{-13.79} \qquad (A.34)$$

$$\rightleftharpoons HgCl^+ + Cl^- \qquad K_1 = 10^{-7.05} \qquad (A.35)$$

$$\rightleftharpoons HgCl_3^- \qquad K_2 = 1.9[Cl^-] \qquad (A.36)$$

$$\rightleftharpoons HgCl_4^{2-} \qquad K_3 = 19[Cl^-]^2 \qquad (A.37)$$

The species solubility results for the salt, $HgCl_2$ added to water are given below. These values are taken from the calculations of Butler.[1]

$$[HgCl_2^\circ] \simeq 10^{-.57} \qquad [Hg^+] \simeq 10^{-6.34}$$

$$[HgCl^-] \simeq 10^{-3.33} \qquad [HgOH^+] \simeq 10^{-5.93}$$

$$[HgCl_3^-] \simeq 10^{-3.44} \qquad [Hg(OH)_2] \simeq 10^{-4.41}$$

$$[HgCl_4^{2-}] \simeq 10^{-6.17} \qquad [Cl^-] \simeq 10^{-3.72}$$

$$[H^+] \simeq 10^{-4.11}$$

Figure 8-12 in Butler[1] also indicated the dominant species in solution is $[HgCl_2^\circ]$ for Cl^- concentrations between 10^{-7} and 10^{-2} M.

The addition of dissolved $HgCl_2$ to equilibrium FeS solutions is now discussed.

The solubility product of HgS is given below.

$$HgS \rightleftharpoons Hg^{2+} + S^{2-} \qquad K_{sp} \sim 10^{-52.4} \qquad (A.38)$$

This equilibria reaction (FeS - $HgCl_2$ - H_2O) can be simplified because of this extremely low K_{sp} value (A.38). The methods discussed in A.5.1 can then be applied to this equilibria, and concentration values determined are as in A.5.1.

Obviously the equilibrium concentration of HgS is dependant on the sulphide species concentration in solution. The method of Krauskoft[2] was used to determine equilibrium values of sulphur species at the pH values used in this study.

For reaction A.27 the following expression can then be written,

$$[Fe^{2+}] = (K_{sp}(1 + \frac{[H^+]}{K_2} + \frac{[H^+]^2}{K_1K_2})^{\frac{1}{2}} \qquad (A.39)$$

Expression (A.39) was solved to determine the species concentration at pH ~ 4, 5, 6 respectively (Table A.8). Note the dominant sulphide species is H_2S at these pH values. Thus the solution mercury ion concentrations will be extremely low (not measurable) in an equilibrium FeS - H_2O - $HgCl_2$ solution ($<10^{-20}$ M). The experimental results (Chapter 5), however, indicated values of mercury in solution greater than calculated here and, mercury ion loss from solution dependant on surface area of FeS (weight) and reaction time. Processes of adsorption are thus dominant and overrule simple solubility considerations discussed above.

---

1. J.N. Butler, "Ionic Equilibrium", Addison-Wesley, 300, (1964).
2. K.B. Krauskoft, "Introduction to Geochemistry", McGraw-Hill, N.Y., 486, (1967).

A.5.3 Iron Sulphide Crystal Chemistry

A.5.3.1 $Fe_{1-x}S$ Crystal Chemistry

The composition of pyrrhotite is bounded by FeS and Fe_7S_8. The majority of terrestrial pyrrhotite is an intergrowth of hexagonal Fe_9S_{10} with monoclinic Fe_7S_8 (Fig. A7). This solid solution equilibria produces

Table A.8

FeS-H_2O Equilibria

Species in Solution*	Species Concentration at pH shown (moles/ℓ.)		
	6	5	4
$[H^+]$	~ 10^{-6}	~ 10^{-5}	~ 10^{-4}
$[Fe^{2+}]$	~ $10^{-4.69}$	~ $10^{-3.69}$	~ $10^{-2.69}$
$[S^{2-}]$	~ $10^{-12.61}$	~ $10^{-13.61}$	~ $10^{-14.61}$
$[HS^-]$	~ $10^{-5.69}$	~ $10^{-5.69}$	~ $10^{-5.69}$
$[H_2S]$	~ $10^{-4.69}$	~ $10^{-3.69}$	~ $10^{-2.69}$

* based on method of Krauskoft.

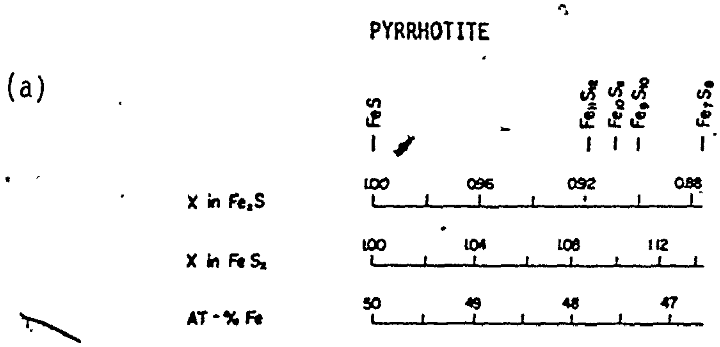

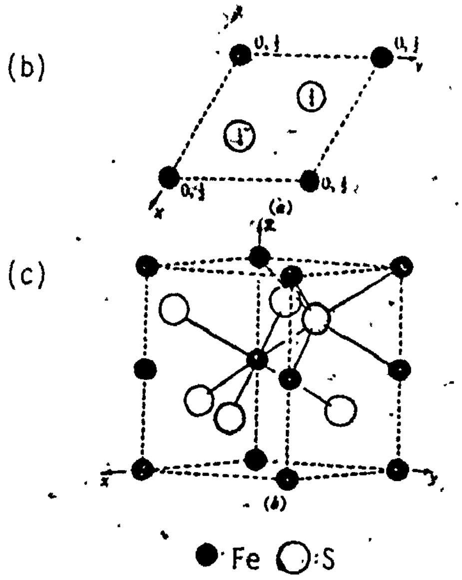

Figure A.7. FeS Composition Data.

(a) Composition Range of Pyrrhotite.

(b) Plan of the Unit Cell of the hexagonal structure of iron sulphide.

(c) Clinographic Projection of the Same Structure.

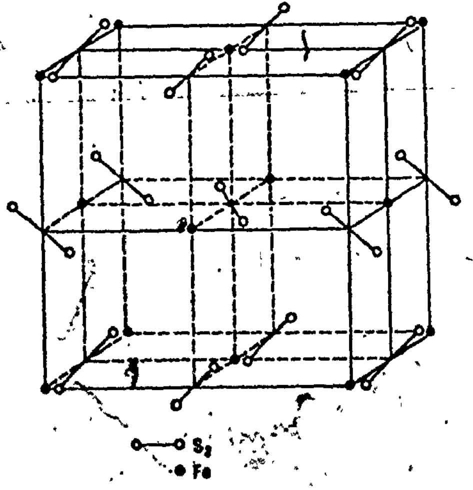

Figure A.8. FeS_2 Crystal Structure.

a non-stoichiometric mineral structure because of iron atom vacancies.

$Fe_{1-x}S$ is usually considered to be ionic with composition

$$[Fe^{2+}_{1-3x} \quad Fe^{3+}_{2x} \quad \bigcirc_{x} \quad S^{2-}]$$

where $\bigcirc$ represents an iron vacancy and $x < .334$. Pyrrhotite is also a good conductor. Unlike pyrite (FeS_2), pyrrhotite is attacked by concentrated HCl.

More detailed discussions of $Fe_{1-x}S$ can be found in Shuey[1], Evans[2] and Deer et al.[3]

A.5.3.2 FeS_2 Crystal Chemistry

Pyrite has the cubic halite structure with the S_2^{2-} anion taking the place of Cl^-; hence its reduced symmetry. Like diamond, the pyrite structure is thought of as a single giant molecule held together by strong covalent bonding (d^2sp^3). Pyrite has poor cleavage planes and is insoluble in concentrated HCl. A detailed description of pyrite bonding and structural properties can be found in several texts.[1→4]

---

1. R.T. Shuey, Developments in Economic Geology, Vol. 4, "Semi-Conducting Ore Minerals", (1975).
2. R.C. Evans, "Crystal Chemistry", Cambridge Press, 220, (1966).
3. W.A. Deer, R.A. Howie and J. Zussman, "An Introduction to the Rock-Forming Minerals", Longman, (1975).
4. J. Verhoogen, F.J. Turner, L.E. Weiss, C. Wahrhaftig, and W.S. Fyfe, "The Earth", Holt, Rinehart and Winston, (1970).

A.5.4 Crushed FeS Surface Area Calculation

The crushed iron sulphide was found to contain particles of less than 1000 mesh (.0149 mm). Scanning electron microphotographs, taken at 3000 X magnification indicated an average particle size of $\sim 7 \times 10^{-5}$ cm.

The particles are spherical in shape. Equations A.21, A.22 were then used to determine the surface area (1.54×10^{-8} cm^2) and volume (1.8×10^{-13} cm^3) of one such particle. The known density of FeS is ~ 4.7 gms/cm^3. Therefore 1 gram would contain ~ 1.2×10^{12} particles. This number of particles (1 gm.) is thus equivalent to ~ 1.83 m^2, the surface area.

The experimentally determined surface area of FeS using mercury adsorption coverage was ≈ 10 m^2/gm. (Chapter 5.2). Qualitatively good agreement is apparent in these measurements.

APPENDIX A.6

PREVIOUSLY COPYRIGHTED MATERIAL,

IN APPENDIX A.6, LEAVES 200-219,

NOT MICROFILMED.

QUANTITATIVE X-RAY PHOTOELECTRON SPECTROSCOPY (ESCA): STUDIES OF B^{2+} SORPTION ON CALCITE, by G. Michael Bancroft, James R. Brown and W.S. Fyfe, Departments of Chemistry and Geology, University of Western Ontario, London, Ontario, Canada, N6A 5B8. Chemical Geology, 19 (1977) 131-144. Copyrighted by Elsevier Scientific Publishing Company, Amsterdam - Printed in the Netherlands.

CALIBRATION STUDIES FOR QUANTITATIVE X-RAY PHOTOELECTRON SPECTROSCOPY OF IONS, by G. Michael Bancroft, James R. Brown, and W.S. Fyfe, Departments of Chemistry and Geology, University of Western Ontario, London, Ontario, Canada, N6A 5B8. Reprinted from Analytical Chemistry, Vol. 49, Page 1044, June 1977. Copyright 1977 by the American Chemical Society and reprinted by permission of the copyright owner.